Geochemical Effects on Natural Convection in Porous Media

Lindsey T. Corson
Department of Mathematics & Statistics
University of Strathclyde
Glasgow, U.K.

September 2012

This thesis is submitted to the University of Strathclyde for the degree of Doctor of Philosophy in the Faculty of Science.

This thesis is the result of the author's original research. It has been composed by the author and has not been previously submitted for examination which has led to the award of a degree.

Signed:

Date:

Acknowledgements

This thesis started out life as a six month Final Honours project, and even though I tried to run away from it for eighteen months, the lure of the unanswered questions eventually drew me back. Much of the blame for this lies with my supervisor, Dr David Pritchard, whose enthusiasm was strangely infectious. I am eternally grateful for his support throughout my PhD studies and for his patience whilst allowing me the freedom to work in my own way. I am also indebted to the Carnegie Trust for the Universities of Scotland for their financial support.

The best way to procrastinate is with good friends, and my thanks go to all of you who have distracted me, whether over a gin and tonic, a good meal, or simply in their office for a chat. I am also extremely grateful for the support and encouragement of my family.

My final thanks go to my husband, Stephen, who somehow managed to keep me (relatively) sane, especially during the writing-up phase, and who always managed to make me laugh at the end of the day. I couldn't have done this without you.

Abstract

We describe a model of buoyancy-driven flow in a saturated reactive porous medium, the porosity and permeability of which evolve through precipitation and dissolution as a mineral is lost or gained from the pore fluid. We consider two scenarios: convection driven solely by solutally induced buoyancy effects with a vertically varying equilibrium solubility, and convection driven by a combination of thermally and solutally induced buoyancy effects where the solubility of the dissolved component depends on the temperature. In both cases we characterise the onset of convection using linear stability analysis, and explore the further development of the coupled reaction–convection system numerically.

For solutal convection, at low Rayleigh numbers the effect of the reaction–permeability feedback is shown to be destabilising, while at higher Rayleigh numbers the porosity evolution has a stabilising effect. Over longer timescales, reaction–permeability feedback triggers secondary instabilities in quasi-steady convective circulation, leading to rapid reversals in the direction of circulation. Over very long timescales, characteristic patterns of porosity emerge, including horizontal layering as well as the development of vertical chimneys of enhanced porosity.

For thermosolutal convection we find that, when the system is solutally unstable, the behaviour of the system is qualitatively the same as for solutal convection, regardless of whether the system is thermally stable or unstable. However, new, interesting behaviour is seen when the system is solutally stable. The long-term evolution of the porous layer depends on whether the underlying thermal or solutal gradient dominates. When the solutal gradient dominates, the reaction-permeability feedback triggers a secondary instability, resulting in the lateral migration of the concentration and temperature fields and rapid reversals in the direction of circulation. However, when the thermal gradient dominates, the reaction-permeability feedback tends to suppress the circulation, although it re-emerges after a long quiescent period.

Contents

Chapter 1

Introduction

The circulation of fluid under the influence of buoyancy forces is believed to occur in many geological settings (Nield and Bejan 2006; Phillips 1991, 2009), although it has been directly observed only occasionally (e.g. Stevens *et al.* 2009). Such fluid usually contains a rich cocktail of dissolved minerals, however, the amount of solute in the fluid is unlikely to be conserved: it may be dissolved from or precipitated onto the rock matrix as its solubility varies with temperature, pressure and the local rock chemistry. The role of such processes in controlling the structure of rocks and the characteristic patterns of mineral deposition is still not fully understood.

In this thesis we examine two idealised models of reactive convection in a porous medium where the rock matrix is allowed to evolve through precipitation and dissolution as a mineral is lost or gained from the fluid. Rather than studying a detailed geochemical model of a particular system we consider a simple, but physically founded, model with the aim of elucidating the fundamental mechanisms which control the evolution of the porous matrix.

The thesis is structured as follows. In chapter 2 we present a review of the literature pertaining to reactive convection in porous media. We also introduce our mathematical model of flow and transport in a reactive porous medium with evolving porosity.

In chapter 3 we consider the simplest model in which reaction-convection inter-

actions can occur: convection driven solely by solutally-driven density effects, where precipitation and dissolution strive to restore the local concentration to some equilibrium value that varies with depth. We carry out a linear stability analysis of the onset of convection and then validate the stability results using a numerical model. Further numerical simulations are carried out to examine the longer-term behaviour of the system and to identify the mechanisms which control the evolution of the porous matrix.

In chapter 4 we consider the same model as in chapter 3, but change the boundary conditions at the top and bottom of the layer from Dirichlet to Neumann conditions. We carry out a linear stability analysis to examine what effect this change in boundary conditions has on the onset of reactive convection. The stability analysis results are verified using a numerical model, and numerical simulations are carried out to investigate the longer-term evolution of the system.

In chapter 5 we extend the model presented in chapter 3 to consider reactive convection driven by a combination of thermal and solutal density effects, and perform a linear stability analysis of the onset of convection. In chapter 6 we validate the results of the stability analysis using a numerical model and perform simulations to investigate the long-term behaviour of the system.

Finally, in chapter 7 we summarise the work contained in this thesis and discuss the most promising directions for future work.

Chapter 2

Literature review and model description

In this chapter we present a review of the literature pertaining to reactive convection in porous media. We also introduce the governing equations of our models along with some caveats concerning their use.

2.1 Porous media

A porous medium is a material consisting of both solid and fluid phases, where the solid phase consists of a solid matrix with an interconnected void in which the fluid phase is found. This matrix can be formed either from a single solid with holes (e.g. a sponge), or a number of smaller solids packed closely together with small gaps between them (e.g. sand). For our purposes, the prototypical porous media are porous rocks such as sandstone or limestone. The interconnectedness of the pores allows fluid to flow through the material, and in the simplest configuration the pore space is filled with a single fluid (single-phase flow), whereas with two-phase flow a liquid and a gas share the pore space (Nield and Bejan 2006; Phillips 1991, 2009).

Naturally occurring porous media contain an irregular distribution of pores which vary in both shape and size. At the microscopic pore scale the flow quantities

(velocity, pressure, etc.) are irregular, and study at this level requires detailed knowledge of the internal structure of the porous medium. The computational resources required to consider a sufficiently large domain will almost always exceed reasonable limits. For example, recent numerical pore scale simulations of reactive multiphase flow, on a cuboidal domain consisting of approximately $20 \times 20 \times 30$ pores, had running times ranging from 12 to 60 h on 2000 processors (Parmigiani *et al.* 2011). The alternative is to use a macroscopic approach, in which the flow quantities are averaged over volume elements with a length scale large enough to contain many pores, but shorter than the length scale of the macroscopic flow domain (Nield and Bejan 2006, §1.1).

The porosity ϕ of a porous medium is defined as the volume fraction of connected voids that allow fluid movement (Phillips 1991, §2.1). Hence, $1 - \phi$ is the volume fraction occupied by solid if all the void space is interconnected. If the void space is not all connected then we must consider an effective porosity, defined as the ratio of connected void to total volume (Nield and Bejan 2006, §1.2).

In naturally occurring porous media the porosity ϕ rarely exceeds 0.6, but higher porosities can occur when the porosity is due to dissolution, particularly in carbonates. In massive fractured carbonates ϕ can be as low as 0.01, and igneous and metamorphic rocks almost always have $\phi < 0.01$. Typical values for sandstone lie in the range $0.08 < \phi < 0.38$ (Nield and Bejan 2006, Table 1.1).

2.2 Natural convection in a porous medium

Natural, or free, convection is a fluid motion generated by density differences between different regions of a fluid as a result of temperature or solutal gradients. When acted upon by gravity these density differences result in buoyancy forces: lighter, less dense fluid seeks to rise relative to heavier, more dense fluid, while heavier fluid sinks relative to its lighter surroundings. If the buoyancy forces are strong enough to overcome the viscous forces that act to dissipate fluid motion, then the fluid will be susceptible to instability and convective motion will occur.

The ratio of buoyancy forces to viscous forces acting on a fluid in a porous medium

is given by the dimensionless Rayleigh-Darcy number, or Rayleigh number for short,

$$\mathcal{R}a = \frac{\hat{\rho}_0 \hat{g} \hat{\beta}_T \hat{K} \hat{h} \Delta \hat{T}}{\hat{\mu} \hat{\kappa}_T}. \tag{2.1}$$

Here, $\hat{\rho}_0$ is some reference density of the fluid, $\hat{g}$ is the gravitational acceleration, $\hat{\beta}_T$ is the thermal expansion coefficient, $\hat{K}$ is the permeability of the porous medium, $\hat{h}$ is the thickness of the porous layer, $\hat{\mu}$ is the dynamic viscosity of the fluid, $\hat{\kappa}_T$ is the thermal diffusivity, and $\Delta\hat{T}$ is the temperature difference across the layer. See §2.6 for further discussion of these parameters. Throughout this thesis, a caret $\hat{}$ will denote a dimensional variable, while dimensionless variables are unadorned.

The study of fluid convection in a horizontal layer began with the quantitative experiments of Bénard in 1900 (Drazin 2002, §6.1). He melted a 1 mm deep layer of wax in a metal dish by heating the base. When the base was hot enough to melt all the wax, there was, at first, no motion in the wax, but once the base was heated past some critical temperature, a hexagonal pattern developed on the surface of the wax. Bénard deduced that this pattern was a result of the presence of convection cells below.

Lord Rayleigh (1916) modelled this problem by assuming an infinite layer of fluid, bounded above and below by stationary horizontal plates which are maintained at constant uniform temperatures, with the bottom plate hotter than the top plate. He found that once the temperature difference across the layer exceeded some critical value, an instability appeared in the form of cellular convection.

More than four decades later, it was determined that the main cause of Bénard cells in thin liquid films was the surface tension gradient rather than the buoyancy force (Pearson 1958). Regardless, the problem of density driven convection has come to be known as Rayleigh-Bénard convection. It remains a fundamental paradigm for nonlinear dynamics including instabilities and bifurcations, pattern formation, chaotic dynamics and developed turbulence (Bodenschatz *et al.* 2000; Kadanoff 2001).

The theoretical study of natural convection in a porous medium dates back to the independent linear stability analyses of Horton and Rogers (1945) and Lapwood

(1948). It is considered the porous media analogue to Rayleigh-Bénard convection in a pure fluid layer; that is, convection in a fully saturated, infinite horizontal porous layer as a result of a vertical temperature gradient so that cooler, denser fluid lies above warmer, less dense fluid.

When the upper and lower boundaries are taken to be impermeable and isothermal, both Horton and Rogers (1945) and Lapwood (1948) found that the critical Rayleigh number required for convection to occur is $\mathcal{R}a^{\text{crit}} = 4\pi^2$, with corresponding critical horizontal wavenumber $m^{\text{crit}} = \pi$. Therefore, when the temperature difference across the layer is such that $\mathcal{R}a < 4\pi^2$ the conductive base state remains stable, but when the temperature difference is increased such that $\mathcal{R}a > 4\pi^2$ an instability appears in the form of cellular convection which, at the stability threshold, has horizontal wavenumber π.

As well as two impermeable and isothermal boundaries, Lapwood (1948) also considered various combinations of impermeable, free (constant pressure), constant temperature and constant heat flux boundaries. The critical Rayleigh number and corresponding critical wavenumber for various combinations of boundary conditions were given by Nield (1968) (see Table 2.1). As the boundary conditions are relaxed, the critical Rayleigh number decreases as expected, along with the critical wavenumber.

In the late 1960s and early 1970s, four sets of authors (Elder 1967; Katto and Masuoka 1967; Combarnous and LeFur 1969; and Buretta 1972), each using different experimental set-ups, measured critical Rayleigh numbers which were generally within about 20% of the theoretical critical value $\mathcal{R}a^{\text{crit}} = 4\pi^2$ (Murray and Chen 1989). The major contributions to the error in $\mathcal{R}a^{\text{crit}}$ are errors in the precise determination of the permeability and the heat conductivity of the medium (Elder 1967; Murray and Chen 1989).

Many authors have considered variations on the classical Horton-Rogers-Lapwood problem. The effect of nonlinear basic temperature profiles was investigated by Nield (1975), who found that it is possible for the critical Rayleigh number to be lower with a curved temperature profile than with a linear profile. The effect of the Coriolis force on linear and nonlinear convection has been studied (see, for example, the review of Vadasz 2000) motivated by practical applications in

Fluid		Thermal			
lower	upper	lower	upper	$\mathcal{R}a^{\text{crit}}$	m^{crit}
IMP	IMP	CTP	CTP	$4\pi^2 \approx 39.48$	$\pi \approx 3.14$
IMP	IMP	CTP	CHF	27.10	2.33
IMP	IMP	CHF	CHF	12	0
IMP	FRE	CTP	CTP	27.10	2.33
IMP	FRE	CHF	CTP	17.65	1.75
IMP	FRE	CTP	CHF	$\pi^2 \approx 9.87$	$\pi/2 \approx 1.57$
IMP	FRE	CHF	CHF	3	0
FRE	FRE	CTP	CTP	12	0
FRE	FRE	CTP	CHF	3	0
FRE	FRE	CHF	CHF	0	0

IMP: impermeable. FRE: free.
CTP: constant temperature (isothermal). CHF: constant heat flux.

Table 2.1: Values of the critical Rayleigh number $\mathcal{R}a^{\text{crit}}$ and the corresponding critical wavenumber m^{crit} for various boundary conditions (after Nield 1968). The subscripts l and u refer to lower and upper, respectively. Reproduced from Nield and Bejan (2006, §6.2).

engineering, for example in centrifugal filtration processes and rotating machinery. However, in geophysical settings the effect of the Coriolis force is generally negligible. Furthermore, the external constraint of a magnetic field on linear and nonlinear magnetoconvection, with its applications in the study of convection in the Earth's interior as well as in the study of bifurcation and chaotic phenomena, has been investigated (see Rudraiah (1984), and references therein).

At intermediate Rayleigh numbers, the patterns of convection become less regular and much more complicated as newly unstable modes grow to larger amplitudes than the original roll cells and supplant them (Palm *et al.* 1972; Rudraiah and Srimani 1980). The dynamics and bifurcation structure of convection for intermediate Rayleigh numbers ($600 \leq \mathcal{R}a \leq 1250$) have been thoroughly explored both theoretically and computationally by Graham and Steen (1994). They found that this Rayleigh number regime is characterised by thermal plumes that emerge from thin thermal boundary layers at the top and bottom of the domain. These plumes drive resonant instabilities that lead to periods of quasi-periodic, subharmonic or weakly chaotic behaviour.

As the Rayleigh number is increased further the dynamics of the convection become increasingly complicated as we enter a regime of convective turbulence in which the fluid swirls in highly structured but never-repeating patterns. The dynamics of high Rayleigh number convective turbulence and the associated enhancement of the heat transport still present many challenges for theory and experiment (Otero *et al.* 2004).

2.3 Thermosolutal convection

In many geological settings the circulating fluid often contains minerals in solution, and therefore it is of interest to consider the onset of convection in a porous medium where the density gradients that provide the driving buoyancy force are induced by the combination of temperature and solutal gradients. As with single-diffusive convection, the dimensionless Rayleigh number provides an indication of the potential for instability, and thus for convective heat transfer. However, since there are two sources of buoyancy in thermosolutal convection, we need to consider two Rayleigh numbers: the thermal Rayleigh number $\mathcal{R}a$, as defined in the previous section, and the solutal Rayleigh number $\mathcal{R}a_C = NLe\mathcal{R}a$, where $Le = \hat{\kappa}_T/\hat{\kappa}_C$ is the ratio of the thermal diffusivity to the molecular diffusivity of the solute, known as the Lewis number, and $N = \hat{\beta}_C\Delta\hat{C}/\hat{\beta}_T\Delta\hat{T}$ is the buoyancy ratio (Nield and Bejan 2006, §9.1).

While a stratified layer of a single-component fluid is stable if the density decreases upwards, a similar layer of a fluid containing two components, which can diffuse relative to each other, may be dynamically unstable. In a fluid layer, the interesting effects in thermosolutal convection arise because heat diffuses more rapidly than a dissolved substance. Hence, this process is often called double-diffusive convection. In a porous medium the system is also double-advective; because heat is shared between the fluid and rock matrix, while the solute is confined to the pore space, heat is advected more slowly than the solute. This difference in advection and diffusion rates is crucial to the stability properties of the thermosolutal system (Phillips 1991, §5.2).

The onset of double-diffusive convection in a porous medium was first studied

theoretically by Nield (1968) who considered the double-diffusive generalisation of the Horton-Rogers-Lapwood problem: convection in a fully saturated, infinite horizontal porous layer as a result of linear vertical temperature and concentration gradients. Using a linear perturbation analysis and considering the limiting case where the transport is isoadvective, he derived critical conditions bounding the onset of convection.

When both the thermal and solutal gradients are destabilising the double-diffusive situation is qualitatively the same as the single-diffusive one. However, interesting new phenomena occur when the thermal and solutal gradients contribute in opposite senses to the stability of the system.

If the thermal gradient is stabilising, but the solute gradient is destabilising, an upwardly displaced particle will end up lighter than its surroundings, since heat diffuses more rapidly than the solute, and therefore continue to move upwards. Similarly, a downwardly displaced particle will be heavier than its surroundings and continue to move downwards. This results in monotonic instability. The stability boundary given by Nield (1968) in this regime has been verified by experiments in a Hele-Shaw cell by Cooper *et al.* (1997).

The resulting flow pattern in this regime is known as 'fingering', since the same instability in a pure fluid layer appears in the form of 'fingers' that grow downward from the upper part of the layer (Turner 1985). The linear stability analysis of Nield (1968) was extended by Taunton *et al.* (1972) to determine the conditions under which fingers develop in a porous medium. However, the question arises as to whether fingers can form fast enough in a porous medium before they are destroyed by dispersive effects. Visualisation and flux experiments conducted by Imhoff and Green (1988) using a salt-sugar system found that fingering did occur, but it was unsteady in contrast to the quasisteady fingering found in a pure fluid layer. Many authors have highlighted the importance of fingering in the vertical transport of contaminants in groundwater (Imhoff and Green 1988; Van Dam *et al.* 2009 and references therein) however, it was only recently that field evidence of fingering associated with natural free convection was found (Van Dam *et al.* 2009).

Alternatively, when the thermal gradient is destabilising, but the solute gradient

is stabilising, an upwardly displaced particle will lose heat and end up heavier than its surroundings and therefore begin to sink. Similarly, a downwardly displaced particle will end up lighter than its surroundings and therefore will rise again. The restoring forces acting on the particle may return it to its equilibrium state at a speed greater than its original outward speed, resulting in a growing oscillatory motion. This is known as overstable behaviour (Nield and Bejan 2006, §9.1). In this regime the resulting flow pattern can ultimately be either penetrative, where convection cells penetrate upwards and occupy the entire layer, or layered, where convection occurs as a series of stacked convection cells (Oldenburg and Pruess 1998). Both experiments in a Hele-Shaw cell (Griffiths 1981), and numerical experiments (Oldenburg and Pruess 1998) have shown that layered double-diffusive convection is possible, with the numerical results suggesting that this state is favoured in an anisotropic porous medium where the vertical permeability is smaller than the horizontal permeability.

Rudraiah *et al.* (1982) applied nonlinear stability analysis to the case of a porous layer with isothermal and isosolutal boundaries. They found that when the solutal gradient is stabilising and the thermal gradient is destabilising, a finite amplitude solution to the system is possible for subcritical values of the thermal Rayleigh number $\mathcal{R}a$. The minimum values of $\mathcal{R}a$ for which a steady solution is possible lie below the critical values for the linear instability of the base state; consequently there is a range of Rayleigh numbers for which nonlinear instability and subcritical convection are possible.

The linear stability theory was extended by Murray and Chen (1989) to include the effects of a nonlinear basic salinity profile and temperature-dependent viscosity and volumetric expansion coefficients. It is seen that with variable viscosity and volumetric expansion coefficients, both the critical thermal Rayleigh number $\mathcal{R}a$ and the critical wavenumber are reduced. Their experiments with glass beads in a box with rigid isothermal upper and lower boundaries agreed with the new reduced critical $\mathcal{R}a$ to within 10%. Furthermore, in the presence of a stabilising solutal gradient, they found that the onset of convection was marked by a dramatic increase in the heat flux at the critical Rayleigh number, and as the temperature difference was reduced to subcritical values, the heat flux curve established a hysteresis loop.

Further linear and nonlinear stability analyses, analytical and numerical studies were undertaken by Mamou and Vasseur (1999) for both Dirichlet and Neumann thermal and solutal boundary conditions. Using both linear and nonlinear perturbation theories they investigated the onset and development of convection. Depending on the boundary conditions and the governing parameters of the problem (the thermal and solutal Rayleigh numbers, the Lewis number, and the aspect ratio of the porous enclosure), four different regimes were found to exist: the pure diffusive regime, the subcritical convective regime, the overstable regime and the supercritical regime. Their numerical results also indicated the existence of multiple solutions which depend on the initial conditions, as well as suggesting the possible occurrence of travelling waves in infinite horizontal enclosures.

2.4 Reactive convection in a porous medium

The models describing single- and double-diffusive convection in a porous medium have many applications in environmental and geophysical fluid dynamics. These include the dolomitisation of carbonate platforms, in which original calcium carbonate rock is converted into calcium magnesium carbonate, either wholly or in part, by percolation of fluids through the rock. This process usually, but not always, improves the reservoir quality of the rock by increasing porosity and permeability (Kaufman 1994). Large-scale convective circulation of groundwater containing dissolved minerals in sandstone aquifers has also been proposed to explain the location of uranium-ore deposits (Raffensperger and Garven 1995a,b). Furthermore, models of double-diffusive convection have been used to explain convection patterns and heat transfer in geothermal reservoirs (Oldenburg and Pruess 1998). The exchange of dissolved species with the porous medium is believed to be important in many of these settings. However, the effect these processes might in turn have on the convective motion has received relatively little attention.

When a nonisothermal chemical reaction takes place, the heat generated (or consumed) by the exothermic (or endothermic) reaction creates density gradients, which can drive instabilities. The first study of reactive convection in a porous

medium was undertaken by Steinberg and Brand (1983, 1984) who presented a linear and weakly nonlinear analysis of the chemically-driven instability of a reactive binary mixture in a porous medium. However, they restricted their analysis to the regime where the first order reaction occurred over much shorter timescales than solutal diffusion, i.e. a fast reaction, so solutal diffusion could be neglected. They found that an endothermic reaction leads only to monotonic instability when the system is heated from below, while an exothermic reaction leads to monotonic instability if the system is heated from above, but oscillatory instability if the system is heated from below. Furthermore, the presence of a reaction affects the critical wavenumber at which the onset of convection occurs.

Gatica *et al.* (1989) and Viljoen *et al.* (1990) considered a more complicated exothermic reaction term with the purpose of describing how reactive flow affects the stability boundaries of the system. They assumed that the Lewis number $Le = 1$, so the solutal and thermal diffusion rates were identical and overdamped behaviour was impossible. However, Subramanian and Balakotaiah (1994) showed that the Lewis number has a pronounced effect on the stability boundaries. They considered an exothermic first order reaction and examined the stability of the conduction solution with respect to convective perturbations. It was found that increasing Le shifts the stationary stability boundary towards higher values of the thermal Rayleigh number.

More recently, Pritchard and Richardson (2007) investigated the effect of a thermally-controlled reaction on the onset of thermosolutal convection in a porous medium, using a model based on that of Steinberg and Brand (1983), but where solutal diffusion is not neglected. Unlike that study, however, they neglected any thermal contribution from the reaction, and considered the case where the dominant contribution to buoyancy comes from the change in solute concentration rather than from changes in temperature. They also found that the critical wavenumber depends on the reaction rate, although the dependence is qualitatively different from that found by Steinberg and Brand (1983). When the solutal gradient is destabilising, the reaction tends to stabilise the system. If the system is weakly solutally destabilised then the reaction can stabilise the system even in the absence of diffusion, but for strongly destabilised systems, diffusion is essential to the stability.

2.5 Flow–reaction feedback

A particular feature of reactive flow in a porous medium, including convective flow, is the possibility of feedback as the exchange of minerals alters the permeability of the medium, which in turn alters the patterns of flow: inhomogeneous permeability may even control whether large-scale flow is able to occur (Sharp and Shi 2009). A general discussion of flow-reaction feedback has been presented by Phillips (1991, 2009). Some specific problems which have received particular interest are detailed in this section.

2.5.1 Reaction-infiltration instability

Perhaps the most thoroughly studied topic is the reaction-infiltration, or wormholing, instability. In this process, fluid is forced through a porous medium and, if the fluid is undersaturated with respect to the porous medium, dissolution of the porous medium will commence. As the reaction protrudes into the unaltered region, the flow of the undersaturated fluid tends to be focussed to the tip of the protrusion, forming fingers of relatively high permeability, which further dissolve the medium in these channels, thus enhancing the permeability still further.

Chadam *et al.* (1986) developed a nonlinear model of flow–reaction feedback for the reaction-infiltration instability, under the assumption that the porous medium contains only a single reactive mineral and the fluid contains only a single reactive chemical species. Making a thin reaction front approximation, they performed a linear stability analysis of the dissolution fingers and found that there is a critical wavelength above which disturbances may become linearly unstable. These predictions were confirmed by numerical simulations.

Chadam *et al.* (1991) extended this model to allow for the possibility that the dissolved solute can increase the viscosity of the fluid. This set-up corresponds to the unstable situation of forcing a less viscous fluid into one with a higher viscosity, as with the Saffman-Taylor instability. However, unlike the Saffman-Taylor instability, chemical reactions are central to the reaction-infiltration instability, where instabilities result from porosity/permeability changes. Therefore, the front ve-

locity is slower than the fluid velocity, in contrast to the Saffman-Taylor instability where they are identical. They found that, with this coupling of the Saffman-Taylor and reaction-infiltration instabilities, as the viscosity change increases and as the porosity/permeability change increases, the number of modes that lose stability also increases. A further extension to include velocity-dependent hydrodynamic dispersion was proposed by Chadam *et al.* (2001), who found that the inclusion of this dispersion truncates the interval of unstable modes with large wavenumbers.

A simpler model was proposed by Hinch and Bhatt (1990). They used simpler reaction equations than Chadam *et al.* (1986), and ignored large-scale hydrodynamic dispersion. Furthermore, they kept the porosity of the medium fixed, but allowed its permeability to vary as a function of the concentration of the dissoluble minerals. Their linear stability analysis suggested that the dissolution front was most unstable to disturbances with wavelengths comparable to the thickness of the front.

More recently, Zhao *et al.* (2008) numerically modelled a three-dimensional dissolution front. For the numerical simulation of dissolution fronts it is common to perturb the initial planar front to generate a more complicated morphological shape during its evolution. However, Zhao *et al.* argue that the shape of the resulting dissolution front may be strongly dependent on its initial perturbation. To remove this possible dependency, they instead add a small randomly generated perturbation to the initial homogeneous porosity field, thus allowing the initial dissolution front to evolve freely. Their numerical model was verified against analytical solutions, and it was noted that the initial porosity perturbation did not affect the initial planar shape of the dissolution front during its propagation.

2.5.2 Convection with feedback

Despite the widespread occurrence of convective fluid circulation in geological formations, the possibility that it might also experience flow–reaction feedback does not seem to have received much attention from mathematical modellers. An exception is the work of Bolton *et al.* (1996, 1997, 1999), who constructed

a detailed mathematical model of buoyancy-driven flow in a quartz–silicic acid system. Their main interest was in how reaction–convection feedback modified rocks with pre-existing permeability structures, such as fracture zones and fault zones. They found extremely complicated patterns of coupled flow and transport, in which both thermosolutal effects and the finite timescale associated with reactions appeared to be important.

There are also some parallels to be drawn between reactive convection in geology and the behaviour of the mushy layers that form during the solidification of a multi-component fluid. These mushy layers separate the completely liquid phase from the completely solid phase and are, in essence, a reactive anisotropic porous medium through which the residual fluid can flow (Nield and Bejan 2006 §10.2.3; Worster 1997).

During solidification natural convection can occur as a result of two mechanisms: in order for the melt to solidify it must be cooled, and consequently the resulting thermal gradients lead to thermal convection; also, if the melt consists of different chemical components, then solutal convection can be driven by gradients in concentration if one or more component is preferentially incorporated into the solid (Worster 1997). In contrast with porous media convection models, however, within a mushy layer the temperature and concentration of the fluid are strongly coupled, and the buoyancy field is dominated by the concentration field, so there are no double-diffusive convection effects.

To simplify the analysis, some assumptions are made to create an ideal mushy layer: the fluid phase is isotropic and Boussinesq, the solid phase forms a stationary rigid matrix whose permeability is locally isotropic, and the solid and liquid phases are in local thermal equilibrium (Worster 1997).

In our model of reactive convection, which will be introduced in §2.6, we will make many of the same simplifying assumptions; however, there are some key differences between our model of reactive convection and that of convective flow in an ideal mushy layer that should be noted. The most obvious difference is the boundary conditions, as mushy layers are typically bounded between pure solid and liquid phases; other differences include the relative insignificance of latent heat when compared to the temperature difference across the porous layer, the

inclusion of solutal diffusion, and the dependence of reaction rate on porosity which arises because the reaction involves the direct exchange of solute with the solid matrix. Furthermore, our solid matrix is composed of solute as opposed to a difference phase of the fluid species. Thus, although we may expect loose analogies with mushy layer convection, we may also expect distinct behaviour.

2.5.3 Other contexts

Another flow–reaction process that has received attention from modellers is the propagation of gravity currents through a reactive medium in both unconfined permeable layers (Raw and Woods 2003) and layers of finite depth (Verdon and Woods 2007). The mechanisms involved are similar to those in the reaction-infiltration instability, although now the density of the injected fluid is different from that of the host fluid, owing to the different chemical composition of the fluids. Therefore, buoyancy forces induced by the difference in density of the two fluids, rather than an external pressure difference, drives the flow.

The dynamics and thermodynamics of magma chambers have been studied by Hallworth *et al.* (2005). Here, a homogeneous layer of saturated reactive porous media is heated from above. The heat flux causes the minerals on the rock matrix at the top of the layer to dissolve, which increases the density of the fluid and therefore drives convection in the lower layer. As this high concentration fluid mixes into the lower layer it precipitates onto the rock matrix, resulting in the release of latent heat, increasing the temperature of the lower layer. Eventually, the porous layer develops into a three-layer stratified system comprising pure fluid overlying a fluid-saturated nonreactive porous medium, in turn overlying the evolved saturated reactive porous medium.

A variation of dissolution-driven convection may be encountered during the geochemical sequestration of carbon dioxide. Here, the dissolution of buoyant carbon dioxide near the top of the layer into the pore fluid increases the density of the fluid; once the denser layer reaches a critical thickness it becomes unstable to convective overturning (Ennis-King *et al.* 2005; Riaz *et al.* 2006). This dissolved carbon dioxide can then react with minerals in the porous medium, altering its

porosity and permeability (Ennis-King and Paterson 2007).

2.6 Model equations

While models as complicated as Bolton *et al.*'s are undoubtedly required to describe real geological systems, there is also a case for studying more heavily idealised models to identify the key mechanisms and interactions involved in reactive convection. In this thesis we build upon the work of Pritchard and Richardson (2007) to include the effects of porosity evolution as a result of reactive convection. In this section we detail our model of buoyancy-driven flow and solute transport in a saturated horizontal porous medium, the porosity and permeability of which evolve through precipitation and dissolution as a mineral is lost or gained from the pore fluid.

2.6.1 Continuity equation

Consider the fluid flow across a unit cross-sectional area of a rock matrix perpendicular to the mean pore velocity $\hat{\mathbf{v}}$. Over the fraction ϕ of interconnected voids the mean flow velocity is $\hat{\mathbf{v}}$, while over the solid or inactive voids it will be zero. Therefore, averaged over the whole area, the flow per unit cross-sectional area is $\hat{\mathbf{u}} = \phi\hat{\mathbf{v}}$. This velocity $\hat{\mathbf{u}}$ is commonly known as the transport velocity, and can be interpreted as the velocity with which a fluid would be moving if it occupied the whole space and had the same volume flux (Phillips 1991, §2.5).

We assume that the mass density of the fluid is independent of the species concentration, which allows the flow and transport problems to be decoupled (Hassanizadeh and Leijnse 1988, Bear 2004, §5). This assumption is valid for real world fluid-rock interactions, for example, in a saturated layer of quartz rich sandstone or calcium carbonate. The density of quartz-saturated water can be up to 0.1% higher than that of pure water (Anderson and Burnham 1965), while the density of calcium carbonate saturated water can be up to 8% higher (Caciagli and Manning 2003). However, this assumption is a poor description for salt-water systems since the density of salt-saturated water is 35% higher than

that of pure water.

The conservation of fluid mass is derived by equating the rate of increase of fluid mass within an arbitrary volume of the porous medium to the net mass flux of fluid into this volume. The total mass of fluid in the volume can increase as a result of both advection and diffusion of fluid across the bounding surface, as well as a reaction within the volume which results in the transfer of chemical species from the solid to the fluid phase. Hence, under the assumption that the advective flux of fluid mass across the bounding surface of the volume is much greater than the diffusive flux, fluid mass conservation can be expressed as

$$\frac{\partial}{\partial \hat{t}}(\hat{\rho}_f \phi) + \hat{\nabla} \cdot (\hat{\rho}_f \hat{\mathbf{u}}) = \hat{Q}_C, \tag{2.2}$$

where $\hat{\rho}_f$ is the fluid density, $\hat{\mathbf{u}}$ is the transport velocity, and $\hat{Q}_C$ is the rate of addition of solute mass to the fluid per unit time per unit volume as a result of a reaction.

Similarly, the conservation of solid mass can be written as

$$\frac{\partial}{\partial \hat{t}}\left[(1-\phi)\hat{\rho}_s\right] = -\hat{Q}_C, \tag{2.3}$$

where $\hat{\rho}_s$ is the solid matrix density. From (2.3) we see that $\hat{Q}_C$ is the same size as the first term in (2.2). Therefore, under the assumption that the fluid flow is much faster than the rate of addition of species to the fluid and the rate of change of porosity, the fluid mass conservation (2.2) can be written as

$$\hat{\nabla} \cdot (\hat{\rho}_f \hat{\mathbf{u}}) = 0. \tag{2.4}$$

It is important to note that although this assumption is reasonable for buoyancy-driven convection, it is less reasonable for the reaction-diffusion instability which emerges at low Rayleigh numbers.

2.6.2 Darcy's law

In 1856 Henry Darcy published his famous report on the public fountains of Dijon (translated in Bobeck 2004), which included an equation relating the volumetric flow rate through a column of sand to the pressure difference along the column. In modern notation, neglecting body forces such as gravity, this is expressed as

$$\hat{u} = -\frac{\hat{K}}{\hat{\mu}} \frac{\partial \hat{p}}{\partial \hat{x}}, \tag{2.5}$$

where $\hat{\mu}$ is the dynamic viscosity of the fluid, $\partial \hat{p}/\partial \hat{x}$ is the pressure gradient in the flow direction, and $\hat{K}$ is the permeability of the medium which we will discuss in more detail in the next section. A three-dimensional tensorial form of this experimental result has been derived theoretically using volume averaging techniques by Whitaker (1986), who made no constitutive assumptions nor restricted his analysis to either spatially periodic or homogeneous porous media. However, we note that Whitaker does not actually derive the form of the permeability tensor $\hat{\mathbf{K}}$, leaving that task for experimental or numerical investigation.

Darcy's law is only valid if the transport velocity $\hat{\mathbf{u}}$ is sufficiently small, such that $\mathrm{Re} \sim 1$, where $\mathrm{Re} = \hat{\rho}_f \hat{u} \hat{\delta} / \hat{\mu}$ is the microscopic Reynolds number with length scale $\hat{\delta}$ given by the typical pore or particle diameter. Characteristic diameters are usually $1 - 10$ μm for sandstone and limestone, but could be as large as 10 cm for coarse gravel beds (Phillips 1991, §§2.6-2.7). Therefore, for Darcy's law to remain valid, the flow of water through sandstone requires flow velocities of $0.1 - 1$ ms^{-1}, while flow through very permeable material would require very slow flow velocities of 10^{-5} ms^{-1}.

Darcy's law becomes increasingly inaccurate as the flow velocity is increased so that $1 \lesssim \mathrm{Re} \lesssim 10$, as seen in very fast flows in permeable material. This transition is not one from linear to turbulent flow, but one where the form drag due to solid obstacles becomes comparable to the surface drag due to friction. This deviation from the linearity of Darcy's law is well described by the Forchheimer extension

$$\hat{\nabla} \hat{p} = -\frac{\hat{\mu}}{\hat{K}} \hat{\mathbf{u}} - c_F \hat{K}^{-\frac{1}{2}} \hat{\rho}_f |\hat{\mathbf{u}}| \hat{\mathbf{u}}, \tag{2.6}$$

where c_F is a dimensionless form-drag constant (Nield and Bejan 2006, §1.5.2).

For our study we use a two-dimensional form of (2.5) and include gravity so that

$$\hat{\mathbf{u}} = -\frac{\hat{K}}{\hat{\mu}}\hat{\nabla}\hat{p} - \frac{\hat{K}}{\hat{\mu}}\hat{\rho}_f\hat{g}\mathbf{e}_z, \tag{2.7}$$

where $\mathbf{e}_z$ is a unit vector in the z-direction.

2.6.3 Permeability

The permeability of a medium is a measure of the ability of that medium to allow fluids to pass through it. It can vary over many orders of magnitude in a single medium; for example, values range from $10^{-10} - 10^{-14}$ m^2 for sandstone, and $10^{-10} - 10^{-12}$ m^2 for limestone (Phillips 2009, Table 2.1). In general the permeability $\hat{\mathbf{K}}$ is a second-order tensor, but in the case of an isotropic medium it simplifies to a scalar.

For a porous medium that consists of particles of approximately spherical shape with a distribution of particle diameters $\hat{D}_p$, the Carmen-Kozeny relationship,

$$\hat{K} = \frac{\hat{D}_{p_2}^2\phi^3}{180(1-\phi)^2}, \tag{2.8}$$

provides a satisfactory expression for the permeability, where

$$\hat{D}_{p_2} = \frac{\int_0^\infty \hat{D}_p^3 h(\hat{D}_p)d\hat{D}_p}{\int_0^\infty \hat{D}_p^2 h(\hat{D}_p)d\hat{D}_p}, \tag{2.9}$$

and $h(\hat{D}_p)$ is the density function for the distribution of diameters $\hat{D}_p$, (Nield and Bejan 2006, §1.5). However, this relationship breaks down if the particles are not spherical or if there is a broad particle-size distribution.

For more general porous media, the relationship between the permeability $\hat{K}$ and porosity ϕ depends on the geometry of the fluid pathways. Generally, $\hat{K} \sim 10^{-2}\phi\hat{\delta}^2$, where $\hat{\delta}$ is the characteristic diameter of the fluid pathways. Typical values of $\hat{\delta}$ were given in §2.6.2. Following Phillips (1991, §4.7), in an evolving

porous medium, if the pathways are predominantly tubular then $\phi \sim n\hat{\delta}^2$, where n is the number of tubes per cross-sectional area, so as the pore diameter changes

$$\frac{\hat{K}}{\hat{K}_0} = \left(\frac{\phi}{\phi_0}\right)^2, \tag{2.10}$$

where the subscript 0 represents initial quantities before any evolution. However, if the fluid flows along a network of intersecting cracks or fissures, then $\phi \sim \hat{\lambda}\hat{\delta}$, where $\hat{\lambda}$ is the length of crack per unit area, and so

$$\frac{\hat{K}}{\hat{K}_0} = \left(\frac{\phi}{\phi_0}\right)^3. \tag{2.11}$$

More generally, the permeability can be modelled by

$$\hat{K}(\phi) = \hat{K}_0\left(\frac{\phi}{\phi_0}\right)^b, \tag{2.12}$$

where the exponent b typically lies between 2 and 3 inclusive. In this work we will take $b = 2$ throughout.

2.6.4 Heat equation

To derive an equation that expresses the first law of thermodynamics in a porous medium, we first assume that the diffusion of heat across a grain of porous material is rapid enough so that the solid and fluid phases are in local thermal equilibrium. Hence, we can write $\hat{T}_s = \hat{T}_f = \hat{T}$, where $\hat{T}_s$ and $\hat{T}_f$ are the temperatures of the solid and fluid phases, respectively. Furthermore, we assume that heat conduction in the solid and fluid phases occur in parallel so that there is no net heat transfer from one phase to the other, and that radiative effects, viscous dissipation, and the work done by pressure changes are negligible.

Therefore, the first law of thermodynamics in a porous medium may be written as (Nield and Bejan 2006, §2.1)

$$(\hat{\rho}\hat{c})_m \frac{\partial \hat{T}}{\partial \hat{t}} + (\hat{\rho}\hat{c})_f \hat{\mathbf{u}} \cdot \hat{\nabla}\hat{T} = \hat{\nabla} \cdot (\hat{k}_m \hat{\nabla}\hat{T}) + \hat{Q}_T, \tag{2.13}$$

where

$$(\hat{\rho}\hat{c})_m = \phi(\hat{\rho}\hat{c})_f + (1-\phi)(\hat{\rho}\hat{c})_s, \tag{2.14}$$

$$\hat{k}_m = \phi\hat{k}_f + (1-\phi)\hat{k}_s, \tag{2.15}$$

$$\hat{Q}_T = \phi\hat{Q}_f + (1-\phi)\hat{Q}_s, \tag{2.16}$$

are the volumetric heat capacity of the saturated medium, the overall thermal conductivity, and the overall heat production per unit volume of the medium, respectively, and the subscripts s and f refer to the solid and fluid phases, respectively. In this thesis we assume that there is no heat generation and consequently the $\hat{Q}_T$ term is neglected.

If we assume that the thermal conductivity of the fluid and solid phases are equal, then (2.13) can be rewritten as

$$(\hat{\rho}\hat{c})_m \frac{\partial \hat{T}}{\partial \hat{t}} + (\hat{\rho}\hat{c})_f \hat{\mathbf{u}} \cdot \hat{\nabla}\hat{T} = \hat{k}_m \hat{\nabla}^2 \hat{T}. \tag{2.17}$$

The effective thermal diffusivity of the medium $\hat{\kappa}_T$ can be calculated by dividing the thermal conductivity of the medium $\hat{k}_m$ by its volumetric heat capacity $(\hat{\rho}\hat{c})_m$ (Phillips 1991, §2.8). The thermal conductivity of a saturated quartz matrix lies in the range $2-6$ $\mathrm{Wm^{-1}K^{-1}}$, and the volumetric heat capacity of saturated quartz is approximately 10^6 $\mathrm{JK^{-1}m^{-3}}$ (Bolton *et al.* 1996). Therefore, the effective thermal diffusivity in saturated quartz is of the order of 10^{-6} $\mathrm{m^2s^{-1}}$.

2.6.5 Dissolved solute equation

The total mass of dissolved species in a unit averaging volume is $\phi\hat{C}$, where $\hat{C}$ represents the mass concentration of dissolved species per unit volume of fluid. The rate of change of the total mass of species is the net result of (i) the advection of solute into the volume by the movement of the interstitial fluid, (ii) diffusion and macroscopic dispersion, and (iii) addition of solute to the fluid by dissolution from, or removal of solute from the fluid by precipitation onto, the rock matrix

(Phillips 1991, §2.9). Therefore, the dissolved solute balance can be written as

$$\frac{\partial}{\partial \hat{t}}(\phi \hat{C}) + \hat{\nabla} \cdot (\hat{\mathbf{u}} \hat{C}) = \hat{\nabla} \cdot (\phi \hat{\kappa}_C \hat{\nabla} \hat{C}) + \hat{Q}_C, \tag{2.18}$$

where $\hat{\kappa}_C$ is the molecular diffusivity of the solute through the fluid, and $\hat{Q}_C$ is the rate of addition of solute to the fluid per unit volume.

As a typical value we will use the molecular diffusivity of dissolved silica: $\hat{\kappa}_C = 10^{-9}$ m^{2}s^{-1} (Bolton *et al.* 1996). Therefore, a typical Lewis number is $Le = \hat{\kappa}_T / \hat{\kappa}_C \approx 10^3$.

2.6.6 Equation of state and Oberbeck-Boussinesq approximation

For solutal convection we take the density to be given by the linear approximation

$$\hat{\rho}_f(\hat{C}) = \hat{\rho}_0[1 + \hat{\beta}_C(\hat{C} - \hat{C}_0)], \tag{2.19}$$

where $\hat{\rho}_0$ is the fluid density at some reference concentration $\hat{C}_0$. For thermosolutal convection the density is given by

$$\hat{\rho}_f(\hat{C}, \hat{T}) = \hat{\rho}_0[1 + \hat{\beta}_C(\hat{C} - \hat{C}_0) + \hat{\beta}_T(\hat{T} - \hat{T}_0)], \tag{2.20}$$

where $\hat{\rho}_0$ is the fluid density at some reference concentration $\hat{C}_0$ and reference temperature $\hat{T}_0$.

In order to simplify the analysis in this work, we assume that the Oberbeck-Boussinesq approximation is valid. Here, all properties of the saturated medium and of the fluid are set constant except for the density, but changes in the density may be ignored except in the buoyancy terms $\hat{\beta}_T \Delta \hat{T}$ and $\hat{\beta}_C \Delta \hat{C}$. This approximation remains valid as long as density changes $\Delta \hat{\rho}_f$ remain small when compared to the reference density $\hat{\rho}_0$ throughout the flow region and temperature and concentration variations are insufficient to cause the various fluid and solid properties of the medium to vary significantly from their mean values.

Under the Oberbeck-Boussinesq approximation, the continuity equation (2.4) becomes

$$\hat{\nabla} \cdot \hat{\mathbf{u}} = 0. \tag{2.21}$$

2.6.7 Reaction and porosity evolution

The source term $\hat{Q}_C$ in the solute transport equation (2.18) represents the increase or decrease in the amount of solute in the fluid as a result of the physical process of dissolution or precipitation of the solid phase, respectively. The detailed chemical kinetics of this process are not very well understood, however it is known that $\hat{Q}_C$ is proportional to the active surface area of rock exposed to the fluid within the pore network, the rate constant for the reaction, and a function of the precipitation and dissolution activities involved (Phillips 1991, §2.9). To overcome the lack of understanding, these factors, as well as the temperature dependence of the reaction, are lumped together in terms of an overall reaction rate. This lumped reaction rate can vary over many orders of magnitude: laboratory measurements on silicate minerals are relatively high ($0.6 - 6 \times 10^{-7}$ s^{-1}), whereas those inferred from deep ocean cores in siliceous sediments are five orders of magnitude smaller (Phillips 1991, §2.9).

Near equilibrium it can be expected that the reaction is first order, so the rate of production or disappearance of a dissolved substance is linearly proportional to the difference between the local concentration and the equilibrium concentration. Hence,

$$\hat{Q}_C = \hat{k}(\phi)(\hat{C}_{eq} - \hat{C}), \tag{2.22}$$

where $\hat{C}_{eq}$ is the equilibrium concentration of solute, which will in general depend on the local pressure, temperature and rock mineralogy.

Our lumped reaction rate $\hat{k}(\phi) \geq 0$ implicitly depends on the surface area of rock exposed to the fluid within the pore network. This should reduce to zero when either there is no rock or there are no pores. Therefore, for exploratory purposes we take

$$\hat{k}(\phi) = \hat{k}_{\text{ref}}\phi(1 - \phi), \tag{2.23}$$

where $\hat{k}_{\text{ref}}$ is some reference reaction rate which we define using the initial porosity ϕ_0 and initial reaction rate $\hat{k}_0$, so

$$\hat{k}_0 = \hat{k}_{\text{ref}}\phi_0(1-\phi_0). \tag{2.24}$$

With this definition of the reaction rate we assume there is no supply limitation of solute; that is, we assume that the porous medium consists entirely of soluble species. In realistic geological settings this assumption is unlikely to hold, however, it provides a reasonable starting point for exploring the effect of porosity evolution on reactive convection.

Alternative forms of the reaction rate were proposed by Chadam *et al.* (1986) and Zhao *et al.* (2008) when considering a dissolution front in reactive-infiltration instabilities. In both cases the reaction is limited by the supply of solute. Therefore, no reaction can occur once the porosity reaches a final value ϕ_{final}. Chadam *et al.* (1986) define their reaction rate as

$$\hat{k}(\phi) = \hat{k}(\phi_{\text{final}} - \phi)^{\frac{2}{3}}, \tag{2.25}$$

where they argue the 2/3 power is typical of a simplified surface dissolution and is included for specificity. Zhao *et al.* (2008) take a similar approach and define their reaction as

$$\hat{k}(\phi) = \hat{k}(\phi_{\text{final}} - \phi). \tag{2.26}$$

Here $\hat{k}$ is a constant reaction rate. It is important to note that both these expressions only consider the dissolution of solute from the rock matrix, however they could easily be extended to allow for precipitation.

Using mass conservation arguments, if $\hat{\rho}_s$ is the solid matrix density, which is typically about 2×10^3 kg m^{-3} for sandstone, then the source term $\hat{Q}_C$ can be expressed as

$$\hat{Q}_C = \hat{\rho}_s \frac{\partial \phi}{\partial \hat{t}}, \tag{2.27}$$

and thus the rate of change of porosity is proportional to the reaction rate,

$$\frac{\partial \phi}{\partial \hat{t}} = \frac{\hat{k}(\phi)}{\hat{\rho}_s}(\hat{C}_{eq} - \hat{C}). \tag{2.28}$$

Note that combining (2.18) and (2.28) gives the conservation equation for the total mass of the chemical species

$$\frac{\partial}{\partial \hat{t}}(\phi \hat{C} + (1-\phi)\hat{\rho}_s) + \hat{\nabla} \cdot (\hat{\mathbf{u}}\hat{C}) = \hat{\nabla} \cdot (\phi \hat{\kappa}_C \hat{\nabla} \hat{C}), \tag{2.29}$$

where, since we assume that the porous medium consists entirely of solute, $\hat{\rho}_s = \hat{C}_s$, the mass concentration of solute in the solid phase.

2.6.8 Summary of model equations

In summary, our model of buoyancy-driven flow and solute transport in a saturated horizontal porous medium is governed by:
Continuity equation

$$\hat{\nabla} \cdot \hat{\mathbf{u}} = 0, \tag{2.30}$$

Darcy's Law

$$\hat{\mathbf{u}} = -\frac{\hat{K}_0}{\hat{\mu}} \left(\frac{\phi}{\phi_0} \right)^2 \hat{\nabla} \hat{p} - \frac{\hat{K}_0}{\hat{\mu}} \left(\frac{\phi}{\phi_0} \right)^2 \hat{\rho_f}(\hat{C}, \hat{T}) \hat{g} \mathbf{e}_z, \tag{2.31}$$

Thermal energy balance

$$(\hat{\rho}\hat{c})_m \frac{\partial \hat{T}}{\partial \hat{t}} + (\hat{\rho}\hat{c})_f \hat{\mathbf{u}} \cdot \hat{\nabla} \hat{T} = (\hat{\rho}\hat{c})_m \hat{\kappa}_T \hat{\nabla}^2 \hat{T}, \tag{2.32}$$

Dissolved species balance

$$\frac{\partial}{\partial \hat{t}}(\phi \hat{C}) + \hat{\nabla} \cdot (\hat{\mathbf{u}}\hat{C}) = \hat{\nabla} \cdot (\phi \hat{\kappa}_C \hat{\nabla} \hat{C}) + \hat{k}_0 \frac{\phi(1-\phi)}{\phi_0(1-\phi_0)} (\hat{C}_{eq}(\hat{z}) - \hat{C}), \tag{2.33}$$

Porosity evolution (solid species balance)

$$\frac{\partial \phi}{\partial \hat{t}} = \frac{\hat{k}_0}{\hat{\rho}_s} \frac{\phi(1-\phi)}{\phi_0(1-\phi_0)} (\hat{C}_{eq}(\hat{z}) - \hat{C}), \tag{2.34}$$

Equation of state

$$\hat{\rho_f}(\hat{C}, \hat{T}) = \hat{\rho}_0 [1 + \hat{\beta}_C (\hat{C} - \hat{C}_0) + \hat{\beta}_T (\hat{T} - \hat{T}_0)]. \tag{2.35}$$

Chapter 3

Reactive solutal convection

In this chapter we consider the simplest model in which interactions between convective circulation and an evolving porous medium may occur: convection driven solely by solutally-induced density effects, in which the solute may be exchanged with the porous matrix by a first-order reaction which attempts to restore the local solute concentration to some local equilibrium value that varies with depth in the medium. This model can be thought of as a simple model of vertically varying rock geochemistry, or as representing thermally-controlled solubility in a system in which rapid thermal diffusion preserves a uniform geothermal temperature gradient.

In §3.1 we present a model of flow and transport in a porous medium with evolving porosity. We then, in §3.2, carry out a linear stability analysis of the onset of convection, paying particular attention to the permeability feedback effects which enter on a timescale generally slower than that of the flow. In §3.3, we validate the stability analysis using a numerical model, and carry out a sequence of numerical experiments to investigate the longer-term behaviour of the system. In particular, we seek to identify and interpret particular feedback mechanisms which control the evolution of the porous matrix. Finally, in §3.4 we summarise our results and draw some general conclusions.

This chapter has been published in the *Journal of Fluid Mechanics* (Ritchie and Pritchard 2011), in substantially the form in which it appears here.

3.1 Model description

We consider an initially homogeneous and isotropic porous layer of depth $\hat{h}$ with solutal mass concentrations $\hat{C}_0$ and $\hat{C}_1$ imposed at the bottom and top, respectively (figure 3.1). The bottom and top layers are presumed to be impermeable, and we impose chemical equilibrium at the boundaries.

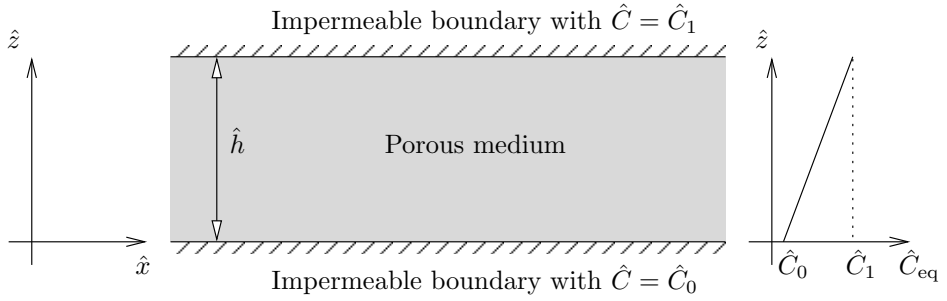

Figure 3.1: Schematic of the system under consideration.

We take $\hat{x}$ and $\hat{z}$ as the horizontal and vertical coordinates, respectively, with $\hat{z}$ increasing upwards. Making a Boussinesq approximation, the flow is governed by the equations of mass conservation and Darcy's law (§§2.6.1 and 2.6.2). The governing equations can be derived from the full thermosolutal system presented in chapter 2 in the limit $\hat{\kappa}_T \to \infty$, $\hat{\beta}_T = 0$. The appropriate equations are therefore

$$\hat{\nabla} \cdot \hat{\mathbf{u}} = 0, \tag{3.1}$$

$$\hat{\mathbf{u}} = -\frac{\hat{K}_0}{\hat{\mu}} \left(\frac{\phi}{\phi_0} \right)^2 \hat{\nabla} \hat{p} - \frac{\hat{K}_0}{\hat{\mu}} \left(\frac{\phi}{\phi_0} \right)^2 \hat{\rho}_f(\hat{C}) \hat{g} \mathbf{e}_z, \tag{3.2}$$

$$\frac{\partial (\phi \hat{C})}{\partial \hat{t}} + \hat{\nabla} \cdot (\hat{\mathbf{u}} \hat{C}) = \hat{\nabla} \cdot (\phi \hat{\kappa}_C \hat{\nabla} \hat{C}) + \hat{k}_0 \frac{\phi(1-\phi)}{\phi_0(1-\phi_0)} (\hat{C}_{eq}(\hat{z}) - \hat{C}), \tag{3.3}$$

$$\frac{\partial \phi}{\partial \hat{t}} = \frac{\hat{k}_0}{\hat{\rho}_s} \frac{\phi(1-\phi)}{\phi_0(1-\phi_0)} (\hat{C}_{eq}(\hat{z}) - \hat{C}), \tag{3.4}$$

$$\hat{\rho}_f(\hat{C}) = \hat{\rho}_0 [1 + \hat{\beta}_C (\hat{C} - \hat{C}_0)]. \tag{3.5}$$

Here $\hat{K}_0$ is the initial permeability, $\hat{\mu}$ is the fluid viscosity, $\hat{\rho}_f$ is the fluid density, $\hat{\mathbf{u}}$ is the two-dimensional fluid velocity, $\hat{\kappa}_C$ is the molecular diffusivity of the

solute through the fluid, and $\hat{k}_0$ is the initial reaction rate; $\hat{C}$ represents the mass concentration of solute in the fluid, and $\hat{C}_{eq}(\hat{z})$ is the equilibrium concentration of solute, which we assume varies linearly in $\hat{z}$. The choice of a linearly varying equilibrium concentration will permit us to define a non-evolving diffusive base state for the system. As before, a caret $\hat{}$ denotes a dimensional variable, while dimensionless variables are unadorned.

We seek an initial steady state solution where $\hat{\mathbf{u}} = 0$ and there is no lateral variation. We then find a linear distribution of solute concentration,

$$\hat{C}_s(\hat{z}) = \hat{C}_0 + (\hat{C}_1 - \hat{C}_0)\frac{\hat{z}}{\hat{h}} = \hat{C}_{eq}(\hat{z}). \tag{3.6}$$

3.1.1 Non-dimensionalisation

Equation (3.3) may be simplified by using (3.1) to obtain

$$\phi\frac{\partial\hat{C}}{\partial\hat{t}} + (\hat{\mathbf{u}}\cdot\hat{\nabla})\hat{C} = \hat{\kappa}_C\hat{\nabla}\cdot(\phi\hat{\nabla}\hat{C}) + \hat{k}_0\frac{\phi(1-\phi)}{\phi_0(1-\phi_0)}(\hat{C}_{eq}(\hat{z}) - \hat{C}). \tag{3.7}$$

We now define dimensionless variables as

$$\hat{\mathbf{x}} = \hat{h}\mathbf{x}, \quad \hat{\mathbf{u}} = \frac{\hat{\kappa}_C}{\hat{h}}\mathbf{u}, \quad \hat{t} = \frac{\phi_0\hat{h}^2}{\hat{\kappa}_C}t, \quad \hat{p} = \frac{\hat{\kappa}_C\hat{\mu}}{\hat{K}_0}p, \quad \hat{C} = \hat{C}_0 + (\hat{C}_1 - \hat{C}_0)C, \tag{3.8}$$

to obtain the dimensionless governing equations

$$\nabla\cdot\mathbf{u} = 0, \tag{3.9}$$

$$\nabla p = -\left(\frac{\phi}{\phi_0}\right)^{-2}\mathbf{u} - \mathcal{R}_C C\mathbf{e}_z - \frac{\mathcal{R}_C}{\hat{\beta}_C(\hat{C}_1 - \hat{C}_0)}\mathbf{e}_z, \tag{3.10}$$

$$\frac{\phi}{\phi_0}\frac{\partial C}{\partial t} + (\mathbf{u}\cdot\nabla)C = \nabla\cdot(\phi\nabla C) - k_0\frac{\phi(1-\phi)}{\phi_0(1-\phi_0)}(C - z), \tag{3.11}$$

$$\frac{\partial\phi}{\partial t} = -\delta k_0\frac{\phi(1-\phi)}{1-\phi_0}(C - z), \tag{3.12}$$

with the boundary conditions

$$w = 0 \quad \text{and} \quad C = z \quad \text{at} \quad z = 0 \quad \text{and at} \quad z = 1. \tag{3.13}$$

The dimensionless parameters k_0, δ and $\mathcal{R}_C$ are defined as

$$k_0 = \frac{\hat{h}^2 \hat{k}_0}{\hat{\kappa}_C}, \qquad \delta = \frac{(\hat{C}_1 - \hat{C}_0)}{\hat{\rho}_s}, \qquad \mathcal{R}_C = \frac{\hat{K}_0 \hat{g} \hat{h} \hat{\beta}_C (\hat{C}_1 - \hat{C}_0)}{\hat{\mu} \hat{\kappa}_C}. \tag{3.14}$$

The parameter $\mathcal{R}_C$ is a solutal Rayleigh number, positive values of which correspond to an unstable solutal density gradient. The parameter $k_0 > 0$ is a Damköhler number which provides the dimensionless reaction rate for the system: note that estimates for geochemical reaction rates may vary by many orders of magnitude (Phillips 2009, §2.8). Finally, δ is a matrix evolution parameter, which may be assumed to be much less than unity since mass concentrations of solute are typically much smaller than the density of the solid mineral (Phillips 2009, §2.8).

3.2 Linear stability analysis

We define infinitesimal perturbation variables, denoted by a dash, as

$$\mathbf{u}' = \mathbf{u}, \quad C' = C - z, \quad p' = p + \frac{1}{2}\mathcal{R}_C z^2 + \frac{\mathcal{R}_C}{\hat{\beta}_C(\hat{C}_1 - \hat{C}_0)} z, \quad \phi' = \phi - \phi_0, \tag{3.15}$$

and assume that the amplitude of the perturbations are much smaller than the matrix evolution parameter δ, in order to retain the δ term at linear order. The alternative assumption that δ is smaller than the amplitude of the perturbations is discussed in appendix A.1.

By neglecting second-order quantities, we may simplify (3.9)–(3.12) to obtain

$$\nabla \cdot \mathbf{u}' = 0, \tag{3.16}$$

$$\nabla p' = -\mathbf{u}' - \mathcal{R}_C C' \mathbf{e}_z, \tag{3.17}$$

$$\frac{\partial C'}{\partial t} + w' = \phi_0 \nabla^2 C' + \frac{\partial \phi'}{\partial z} - k_0 C', \tag{3.18}$$

$$\frac{\partial \phi'}{\partial t} = -\delta k_0 \phi_0 C', \tag{3.19}$$

with boundary conditions given by

$$w' = 0 \quad \text{and} \quad C' = 0 \quad \text{at} \quad z = 0 \quad \text{and at} \quad z = 1. \tag{3.20}$$

Note that at this linear order there is no effect of varying porosity and permeability in the velocity equation (3.17). Therefore only the solute fields feel the effect of porosity evolution.

We seek solutions of the form

$$\begin{aligned} &u' = U(z)e^{imx}e^{\sigma t}, \quad w' = W(z)e^{imx}e^{\sigma t}, \quad p' = P(z)e^{imx}e^{\sigma t} \\ &C' = \chi(z)e^{imx}e^{\sigma t}, \quad \phi' = \Phi(z)e^{imx}e^{\sigma t} \end{aligned} \tag{3.21}$$

where the real parts are assumed, the wave number m is a positive real number, and U, W, P, χ, Φ and σ are generally complex. Substituting these into (3.16)–(3.19) we obtain

$$imU(z) + \frac{\mathrm{d}}{\mathrm{d}z}W(z) = 0, \tag{3.22}$$

$$imP(z) = -U(z), \tag{3.23}$$

$$\frac{\mathrm{d}}{\mathrm{d}z}P(z) = -W(z) - \mathcal{R}_C \chi(z), \tag{3.24}$$

$$\left[\phi_0 \left(\frac{\mathrm{d}^2}{\mathrm{d}z^2} - m^2\right) - k_0 - \sigma\right] \chi(z) = W(z) - \frac{\mathrm{d}}{\mathrm{d}z}\Phi(z), \tag{3.25}$$

$$\sigma \Phi(z) = -\delta k_0 \phi_0 \chi(z). \tag{3.26}$$

Equations (3.22)–(3.26) can be combined and simplified to give

$$\left[\phi_0\left(\frac{\mathrm{d}^2}{\mathrm{d}z^2}-m^2\right)-\frac{\delta k_0\phi_0}{\sigma}\frac{\mathrm{d}}{\mathrm{d}z}-(k_0+\sigma)\right]\left[\frac{\mathrm{d}^2}{\mathrm{d}z^2}-m^2\right]W(z)=m^2\mathcal{R}_C W(z), \tag{3.27}$$

while $W(z)$ must satisfy the boundary conditions

$$W(z)=0 \quad \text{and} \quad \left(\frac{\mathrm{d}^2}{\mathrm{d}z^2}-m^2\right)W(z)=0 \quad \text{at} \quad z=0 \quad \text{and at} \quad z=1. \tag{3.28}$$

Adapting the approach of Chandrasekhar (1961, §15) for Rayleigh–Bénard convection, we seek solutions to (3.27) in the form $W(z)\propto\exp(qz)$, where q is a root of the auxiliary equation

$$\left[\phi_0(q^2-m^2)-\frac{\delta k_0\phi_0}{\sigma}q-(k_0+\sigma)\right][q^2-m^2]=m^2\mathcal{R}_C. \tag{3.29}$$

In general we may write

$$W(z)=A_1e^{q_1z}+A_2e^{q_2z}+A_3e^{q_3z}+A_4e^{q_4z}, \tag{3.30}$$

and the boundary conditions (3.28) may be written as

$$B\cdot\begin{bmatrix}A_1\\A_2\\A_3\\A_4\end{bmatrix}=\mathbf{0} \tag{3.31}$$

where

$$B=\begin{bmatrix}1 & 1 & 1 & 1\\ e^{q_1} & e^{q_2} & e^{q_3} & e^{q_4}\\ (q_1^2-m^2) & (q_2^2-m^2) & (q_3^2-m^2) & (q_4^2-m^2)\\ (q_1^2-m^2)e^{q_1} & (q_2^2-m^2)e^{q_2} & (q_3^2-m^2)e^{q_3} & (q_4^2-m^2)e^{q_4}\end{bmatrix}. \tag{3.32}$$

For nontrivial solutions, therefore, we require that

$$\det(B)=0. \tag{3.33}$$

3.2.1 Reaction but no matrix evolution

Before considering the full linear stability problem, it is helpful to examine the rather simpler case $\delta = 0$, so the reaction acts to eliminate solutal perturbations but does not modify the porosity.

If we take $\delta = 0$, then the terms in (3.29) that are linear in q disappear, and it has roots $q_1 = -q_2$ and $q_3 = -q_4 = -iq_0$, where

$$\begin{aligned} q_1 &= \left[\frac{1}{2\phi_0}(k_0 + \sigma + 2\phi_0 m^2 + \sqrt{(k_0+\sigma)^2 + 4\phi_0 m^2 \mathcal{R}_C})\right]^{1/2}, \\ q_0 &= \left[-\frac{1}{2\phi_0}(k_0 + \sigma + 2\phi_0 m^2 - \sqrt{(k_0+\sigma)^2 + 4\phi_0 m^2 \mathcal{R}_C})\right]^{1/2}. \end{aligned} \tag{3.34}$$

The condition (3.33) for nontrivial solutions therefore becomes

$$((k_0+\sigma)^2 + 4\phi_0 m^2 \mathcal{R}_C)\sinh(q_1)\sin(q_0) = 0. \tag{3.35}$$

For this reduced problem the principle of exchange of stabilities holds (see appendix A.2), so for marginal stability we set $\sigma = 0$. Equation (3.35) then has solutions given by

$$k_0^2 + 4\phi_0 m^2 \mathcal{R}_C = 0, \tag{3.36}$$

$$\text{or} \qquad q_1 = \left[\frac{1}{2\phi_0}(k_0 + 2\phi_0 m^2 + \sqrt{k_0^2 + 4\phi_0 m^2 \mathcal{R}_C})\right]^{1/2} = 0, \tag{3.37}$$

$$\text{or} \qquad q_0 = \left[-\frac{1}{2\phi_0}(k_0 + 2\phi_0 m^2 - \sqrt{k_0^2 + 4\phi_0 m^2 \mathcal{R}_C})\right]^{1/2} = n\pi, \tag{3.38}$$

where $n \in \mathbb{Z}$.

It is straightforward to show that solutions (3.36), (3.37) and (3.38) with $n = 0$ each give repeated roots in (3.29), and therefore cannot lead to a non-trivial solution of the linear problem. Solution (3.38) with $n \neq 0$ gives

$$\mathcal{R}_C = \mathcal{R}_{C,0}(m) = \frac{(\phi_0(n^2\pi^2 + m^2) + k_0)(n^2\pi^2 + m^2)}{m^2}, \quad \text{where} \quad n \in \mathbb{Z}, \tag{3.39}$$

and the four solutions to (3.29) remain linearly independent.

The quantity $\mathcal{R}_{C,0}(m)$ takes its minimum value, $\mathcal{R}_{C,0}^{\text{crit}}$, when

$$n = 1 \quad \text{and} \quad m = m_0^{\text{crit}} = \pi \left(1 + \frac{k_0}{\pi^2 \phi_0}\right)^{1/4}, \tag{3.40}$$

so

$$\mathcal{R}_{C,0}^{\text{crit}} = \phi_0 \pi^2 \left[1 + \left(1 + \frac{k_0}{\pi^2 \phi_0}\right)^{1/2}\right]^2 \tag{3.41}$$

If we set $k_0 = 0$ in (3.39) and (3.40), then we recover the marginal stability condition $\mathcal{R}_{C,0}^{\text{crit}} = 4\phi_0 \pi^2$ for single-diffusive solutal convection in a non-evolving porous medium. Figure 3.2 illustrates how $\mathcal{R}_{C,0}^{\text{crit}}$ increases with increasing k_0.

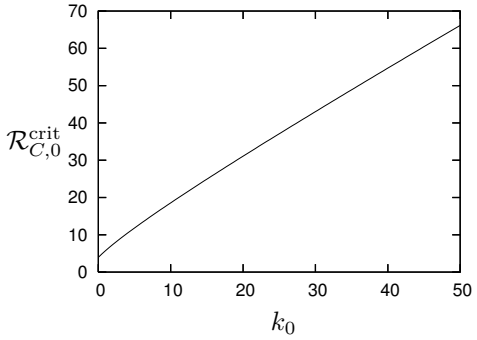

Figure 3.2: Stability boundary for $\mathcal{R}_{C,0}^{\text{crit}}$ with $\phi_0 = 0.1$ given by (3.41).

It can be seen from (3.40) that increasing the reaction rate k_0 both stabilises the system (by eliminating destabilising solutal perturbations) and favours the development of narrower convection cells. Pritchard and Richardson (2007) found the same qualitative behaviour in solutally destabilised double-diffusive convection with a reaction term, reflecting the strong similarity between these models. We will discuss below (§3.2.3) how the predictions with $\delta = 0$ relate to the onset of convection in the full system.

3.2.2 Linear stability analysis of the full problem

When $\delta \neq 0$, an analytical solution to (3.33) in terms of σ is not available. Therefore, the stability problem was investigated numerically by a continuation method, tracking σ as $\mathcal{R}_C$ changed, while keeping all other parameters fixed. A numerical solution to (3.35) for a large initial value of $\mathcal{R}_C$ was used as an initial guess. This method was implemented in Maple 12, using the built-in routine `fsolve`.

Unfortunately, the task of tracking the solution branch is numerically very laborious, largely because the analytical solutions for q_i are prohibitively complicated and so nested numerical solutions of (3.29) and (3.33) are required. Additionally, we found that to track a single branch it was necessary to reduce $\mathcal{R}_C$ in steps no larger than 10^{-2}, with smaller steps being required close to the bifurcation point discussed below (§3.2.3). On a desktop computer, the calculation of the results shown in figure 3.3 required around two hours to produce. This effectively precluded the thorough investigation of the full problem defined by (3.33): instead, a less formal Galerkin approach was employed both in order to search parameter space and to provide insight into the solution structure.

3.2.3 Galerkin approach to the linear stability problem

In the Galerkin approach, the vertical structure of the perturbations is approximated by a severely truncated Fourier series in z, producing a set of equations that may more readily be solved to provide rapid estimates of the stability behaviour.

3.2.3.1 Galerkin approach

We start with the system of equations (3.22)–(3.26), subject to the boundary conditions

$$\chi = 0 \quad \text{and} \quad W = 0 \quad \text{on} \quad z = 0 \quad \text{and on} \quad z = 1, \tag{3.42}$$

and to the usual non-triviality condition that the solution is not identically zero. Eliminating U, Φ and P we obtain the system

$$-\frac{1}{m^2}\frac{\mathrm{d}^2 W}{\mathrm{d}z^2} = -W - \mathcal{R}_C \chi, \tag{3.43}$$

$$\phi_0\left(\frac{\mathrm{d}^2\chi}{\mathrm{d}z^2} - m^2\chi\right) - (k_0+\sigma)\chi = W + \frac{\delta k_0 \phi_0}{\sigma}\frac{\mathrm{d}\chi}{\mathrm{d}z}, \tag{3.44}$$

subject to the same boundary conditions. It is possible to further eliminate either χ or W as in (3.27), but as this complicates the boundary conditions we retain both.

We will seek approximate solutions in the form

$$W(z) = \sin(\pi z) + W_2 \sin(2\pi z), \quad \chi(z) = \chi_1 \sin(\pi z) + \chi_2 \sin(2\pi z). \tag{3.45}$$

Note that the boundary conditions are automatically satisfied and that the non-triviality condition has been imposed by normalising the $\sin(\pi z)$ component of $W(z)$. We know that in the limit $\delta = 0$ this approximation will become exact, with $W_2 = 0 = \chi_2$; meanwhile we expect the second harmonics to be the first Fourier mode excited by interactions, as in the study of reactive convection by Gatica, Viljoen, and Hlavacek (1989) and in nonlinear convection problems close to the stability boundary (see e.g. Rudraiah, Srimani, and Friedrich 1982; Mamou and Vasseur 1999; Pritchard and Richardson 2007). Note that with this normalisation $W \neq 0$. The alternative scenario of normalising with respect to the concentration field χ to allow $W = 0$ is discussed in more detail in §3.2.3.5.

With four unknowns, we can choose to satisfy four integral conditions. The natural ones are obtained by extracting the first and second Fourier sine components of (3.43) and (3.44):

$$\int_0^1 \sin(\pi n z)\left[-\frac{1}{m^2}\frac{\mathrm{d}^2 W}{\mathrm{d}z^2}\right]\mathrm{d}z = \int_0^1 \sin(\pi n z)\left[-W - \mathcal{R}_C\chi\right]\mathrm{d}z, \tag{3.46}$$

$$\int_0^1 \sin(\pi n z)\left[\phi_0\left(\frac{\mathrm{d}^2\chi}{\mathrm{d}z^2} - m^2\chi\right) - (k_0+\sigma)\chi\right]\mathrm{d}z = \int_0^1 \sin(\pi n z)\left[W + \frac{\delta k_0\phi_0}{\sigma}\frac{\mathrm{d}\chi}{\mathrm{d}z}\right]\mathrm{d}z, \tag{3.47}$$

for $n = 1$ and for $n = 2$. This yields a system of four algebraic equations,

$$\frac{\pi^2}{2m^2} = -\frac{1}{2} - \frac{\mathcal{R}_C}{2}\chi_1, \tag{3.48}$$

$$-\frac{1}{2}\left(\phi_0\pi^2 + \phi_0 m^2 + k_0 + \sigma\right)\chi_1 = \frac{1}{2} - \frac{4\delta k_0\phi_0}{3\sigma}\chi_2, \tag{3.49}$$

$$\frac{2\pi^2 W_2}{m^2} = -\frac{1}{2}W_2 - \frac{\mathcal{R}_C}{2}\chi_2, \tag{3.50}$$

$$-\left(2\phi_0\pi^2 + \frac{\phi_0 m^2}{2} + \frac{k_0 + \sigma}{2}\right)\chi_2 = \frac{1}{2}W_2 + \frac{4\delta k_0\phi_0}{3\sigma}\chi_1. \tag{3.51}$$

The most productive approach to these equations is to eliminate W_2, χ_1 and χ_2 to obtain an equation for σ. Before doing so, it is helpful to express the Rayleigh number in terms of the critical condition for $\delta = 0$. We define $\mathcal{R}_C = \mathcal{R}_{C,0}(m) + \Delta$, where $\mathcal{R}_{C,0}(m)$ is given by (3.39). We can now write the growth rate for $\delta = 0$ as

$$\sigma = \sigma_0 = \frac{m^2\Delta}{\pi^2 + m^2}. \tag{3.52}$$

With this notation, we find that $\sigma \neq 0$ satisfies the quartic

$$a_4\sigma^4 + a_3\sigma^3 + a_2\sigma^2 + a_1\sigma + a_0 = 0, \tag{3.53}$$

where

$$a_4 = 9m^4 + 36\pi^4 + 45\pi^2 m^2, \tag{3.54}$$

$$\begin{aligned} a_3 = {} & 27\pi^2 k_0(m^2 + \pi^2) + 54\pi^2\phi_0 m^4 + 189\pi^4\phi_0 m^2 + 135\pi^6\phi_0 \\ & - \left(18m^4 + 45\pi^2 m^2\right)\Delta, \end{aligned} \tag{3.55}$$

$$a_2 = -(135\pi^4\phi_0 m^2 + 54\pi^2\phi_0 m^4 + 27\pi^2 k_0 m^2)\Delta + 9m^4\Delta^2, \tag{3.56}$$

$$a_1 = 0, \tag{3.57}$$

$$a_0 = \left(256\pi^4 + 320\pi^2 m^2 + 64m^4\right)\phi_0^2 k_0^2\delta^2. \tag{3.58}$$

Because (3.53) is a polynomial, it is straightforward to locate all the complex roots numerically (for example, using the `fsolve` command in Maple), and thus to track all the solutions through parameter space.

3.2.3.2 The behaviour of roots $\sigma(\mathcal{R}_C; m)$

Figure 3.3 shows representative results of the unstable roots of σ when the wavenumber m and all the parameters except Δ are fixed, while Δ is varied about zero. Note that we have not shown the stable roots in figure 3.3. For this, and all subsequent figures in this section, the default parameter values were $\phi_0 = 0.1$, $k_0 = 10$, $m = 3$ and $\delta = 0.1$: this rather large value of δ was chosen to make deviations from the case $\delta = 0$ as apparent as possible.

When Δ is large and positive, so $\mathcal{R}_C$ is somewhat larger than $\mathcal{R}_{C,0}$, the branch of σ with largest real part closely tracks σ_0. It deviates weakly from this as Δ is reduced, until this branch and the one below merge. This occurs at about $\Delta \approx 0.7$ in figures 3.3(a) and (b); more generally (see the asymptotic analysis in §3.2.3.3.1) the point at which this occurs scales as $\Delta \sim \delta^{2/3}$ and $\sigma \sim \delta^{2/3}$. At this bifurcation point the values of σ become complex. As Δ is further reduced, $\Re(\sigma)$ continues to fall, but never reaches zero, asymptoting toward it as $\Delta \to -\infty$ (see §3.2.3.3.3); meanwhile $\Im(\sigma)$ first increases rapidly in magnitude and then decays. This behaviour appears to be generic for all values of m, although the position of the bifurcation point changes with m.

This behaviour may be interpreted physically. It is straightforward to show from (3.22)–(3.26) that the principle of the exchange of stabilities does not hold for the base state, since when $\sigma = 0$ and $\delta \neq 0$, (3.26) requires $\chi = 0$, and the system may be reduced to $\mathrm{d}^2W/\mathrm{d}z^2 = m^2W$ with $W(0) = 0 = W(1)$ and no non-trivial solutions. Thus, although the system with $\delta \neq 0$ can mimic the system with $\delta = 0$ closely (to within $\mathcal{O}(\delta^2)$: see §3.2.3.3.2), as $\mathcal{R}_C \to \mathcal{R}_{C,0}$ something must break down. What emerges is a weakly growing travelling mode, which will be discussed further in the next section. It is interesting and unexpected that the system is unstable for all values of $\mathcal{R}_C$, even when $\mathcal{R}_C$ is reduced well below $\mathcal{R}_{C,0}$.

Figure 3.3 also compares the predictions of the Galerkin analysis with those from the full numerical solution of (3.33), again taking a relatively large value of δ. Good agreement can be seen for values of Δ as low as the bifurcation point; even thereafter, the real part of the growth rate is tracked very accurately, while errors in the imaginary part are of the order of 10%. Further comparisons were carried

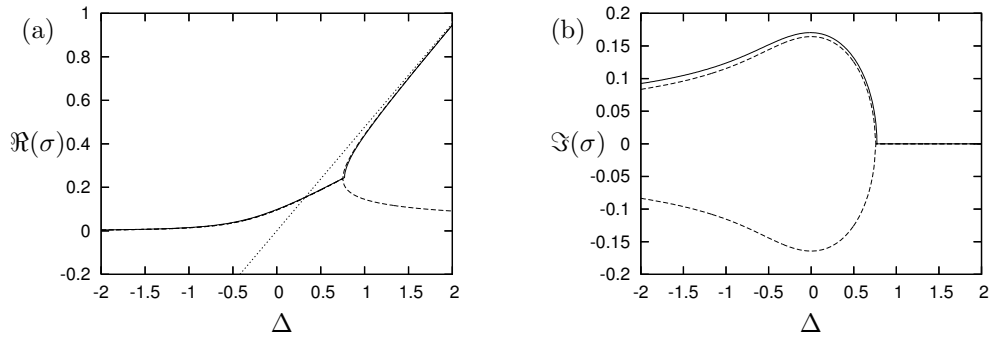

Figure 3.3: Behaviour of σ close to $\Delta = 0$, for $k_0 = 10$, $\delta = 0.1$, $\phi_0 = 0.1$ $m = 3$. Figure (a) shows $\Re(\sigma)$, while figure (b) shows $\Im(\sigma)$. Solid lines are full numerical solutions to the linear problem; dashed lines are Galerkin solutions for the upper two roots; dotted line in (a) shows the results for $\delta = 0$.

out for smaller values of δ, with correspondingly still better agreement. Note that the numerical solution tracks only one branch below the bifurcation point, and it appears to be arbitrary whether it selects the positive or the negative solution for $\Im(\sigma)$.

3.2.3.3 Asymptotic analysis of the quartic in the Galerkin approach

To analyse the asymptotic behaviour of σ, it is helpful to rewrite the quartic (3.53) as

$$a_4\sigma^4 + (b_3 - c_3\Delta)\sigma^3 + (d_2\Delta^2 - c_2\Delta)\sigma^2 + b_0\delta^2 = 0, \tag{3.59}$$

where

$$a_4 = 9m^4 + 36\pi^4 + 45\pi^2m^2, \tag{3.60}$$
$$b_3 = 27\pi^2k_0(m^2 + \pi^2) + 54\pi^2\phi_0m^4 + 189\pi^4\phi_0m^2 + 135\pi^6\phi_0, \tag{3.61}$$
$$c_3 = 18m^4 + 45\pi^2m^2, \tag{3.62}$$
$$d_2 = 9m^4, \tag{3.63}$$
$$c_2 = 135\pi^4\phi_0m^2 + 54\pi^2\phi_0m^4 + 27\pi^2k_0m^2, \tag{3.64}$$
$$b_0 = \left(256\pi^4 + 320\pi^2m^2 + 64m^4\right)\phi_0^2k_0^2. \tag{3.65}$$

We will always take $\delta \ll 1$, and seek asymptotic scalings for σ and Δ in terms of δ.

3.2.3.3.1 Small Δ: location of the bifurcation point

We start by looking at the asymptotics for $\Delta \ll 1$. We first eliminate all terms in (3.59) which must be sub-dominant, obtaining

$$a_4\sigma^4 + b_3\sigma^3 - c_2\Delta\sigma^2 + b_0\delta^2 \approx 0. \tag{3.66}$$

There will always be a negative, order-unity solution $\sigma \sim -b_3/a_4$; all other roots of the quartic must be small in magnitude. Taking $\sigma \ll 1$ and retaining only possible dominant terms, we can reduce the equation further to the cubic

$$b_3\sigma^3 - c_2\Delta\sigma^2 + b_0\delta^2 \approx 0. \tag{3.67}$$

The bifurcation can occur if all three of these terms are of the same order. This requires $\sigma \sim \delta^{2/3}$ and $\Delta \sim \delta^{2/3}$, so we set $\sigma = \delta^{2/3}\Sigma$ and $\Delta = \delta^{2/3}D$, with Σ and D of order unity, to obtain

$$f(\Sigma) \equiv b_3\Sigma^3 - c_2D\Sigma^2 + b_0 \approx 0. \tag{3.68}$$

The discriminant of (3.68) is given by

$$\Lambda = 4c_2^3b_0D - 27b_3^2b_0^2 \tag{3.69}$$

and it is apparent that for sufficiently large D, Λ will be strictly positive and (3.68) will have three real roots, while for smaller values of D, Λ will be negative and (3.68) will have only one real root and two complex ones. We locate the bifurcation point by requiring $\Lambda = 0$, giving

$$D = \left(\frac{27b_3^2b_0}{4c_2^3}\right)^{1/3}, \quad \text{and hence} \quad \Sigma = \left(\frac{2b_0}{b_3}\right)^{1/3}. \tag{3.70}$$

$(\delta,\, m)$	Numerical $(\Delta,\, \sigma)$	Asymptotic $(\Delta,\, \sigma)$
(0.1, 3)	(0.7540, 0.2393)	(0.7564, 0.2405)
(0.01, 3)	(0.1629, 0.0510)	(0.1630, 0.0518)
(0.001, 3)	(0.0352, 0.0110)	(0.0351, 0.0112)
(0.0001, 3)	(0.0076, 0.0022)	(0.0076, 0.0024)
(0.1, 10)	(0.4421, 0.2683)	(0.4411, 0.2677)
(0.01, 10)	(0.0951, 0.0570)	(0.0950, 0.0577)
(0.001, 10)	(0.0205, 0.0120)	(0.0205, 0.0124)

Table 3.1: Comparisons of (3.70) with numerical solutions of (3.53). Parameter values: $k_0 = 10$, $\phi_0 = 0.1$.

Comparisons of (3.70) with numerical solutions of (3.53) in Table 3.1 suggest that these asymptotics capture the behaviour of the solutions well.

3.2.3.3.2 Regular perturbation to σ_0

When $\Delta = \mathcal{O}(1)$, we expect that there will be a solution branch with $\sigma \approx \sigma_0$. To locate this branch, we set $\sigma = \sigma_0 + \sigma_1$ in (3.59), obtaining an equation of the form

$$A_4\sigma_1^4 + A_3\sigma_1^3 + A_2\sigma_1^2 + A_1\sigma_1 + A_0 + B_0\delta^2 = 0, \tag{3.71}$$

where all constants except δ and σ_1 are implicitly of order 1, though not necessarily positive. Seeking a regular perturbation so $\sigma_1 \ll 1$, this reduces to

$$A_1\sigma_1 + B_0\delta^2 \approx 0, \quad \text{i.e.} \quad \sigma_1 \sim -\frac{B_0}{A_1}\delta^2. \tag{3.72}$$

Thus the effect of matrix evolution on the growth rate of instabilities is negligibly small, $\mathcal{O}(\delta^2)$, as long as we are away from the $\delta = 0$ stability boundary.

3.2.3.3.3 Behaviour as $\Delta \to -\infty$

Finally, we investigate the behaviour of the dominant solution branch as $\Delta \to -\infty$. Taking $\sigma \sim \Delta^\alpha$ for some α, we find two possibilities. If $\alpha = 1$ then we have a balance between the σ^4, σ^3 and σ^2 terms, and it is easy to show that both

resulting solutions have negative real part. More interestingly, for any negative value of α we find that the leading order balance must be between the σ^2 term and the σ^0 term, eventually giving solutions of the form

$$\sigma \sim \delta\sigma_0 = \pm\frac{\delta}{\Delta}k_0\phi_0\left(-\frac{256\pi^4+320\pi^2m^2+64m^4}{9m^4}\right)^{1/2}, \tag{3.73}$$

regardless of the value of α chosen. These leading order terms are imaginary, which means that these solution branches must then have real part smaller than $\mathcal{O}(\delta/\Delta)$.

To find the leading order real part, we set $\sigma = \delta\sigma_0 + \delta^2\sigma_1$ in (3.59), and obtain

$$\sigma_1 = -\frac{32}{9}\frac{k_0^2\phi_0^2(33\pi^4m^2+15\pi^2m^4+2m^6+20\pi^6)}{m^6\Delta^3}, \tag{3.74}$$

which is strictly real, and tends to zero from above as $\Delta \to -\infty$. This is consistent with figure 3.3, and reinforces the fact that the system is always unstable, no matter the value of $\mathcal{R}_C$.

3.2.3.4 Eigenfunction structure and instability mechanism

The Galerkin stability analysis provides not just the complex growth rate σ but also the quantities W_2, χ_1 and χ_2 that define the corresponding vertical eigenfunction. To elucidate the mechanism involved in the instability, it is useful to examine these quantities.

We first identify how the second harmonic alters the shapes and relative phases of the various perturbations. We may write

$$\begin{aligned} w(x,z,t) &= \Re\left(e^{imx}e^{(\sigma_R+i\sigma_I)t}\left(\sin(\pi z)+W_2\sin(2\pi z)\right)\right) \\ &= e^{\sigma_R t}\left[\sin(\pi z)\cos(mx+\sigma_I t)+|W_2|\sin(2\pi z)\cos(mx+\sigma_I t+\theta)\right], \end{aligned} \tag{3.75}$$

where $\theta = \arg(W_2)$. It is clear that $|W_2|$ controls the relative strength of the second harmonic. The relative phase θ then controls the way in which the second harmonic distorts the first. If $\theta = 0$, then the second harmonic accentuates the

perturbation in $0 < z < \frac{1}{2}$ and reduces it in $\frac{1}{2} < z < 1$: the net effect is to distort the convection cells by squashing them downwards towards the base of the layer. Similarly, if $\theta = \pm\pi$, the second harmonic squashes the convection cells upwards. If $0 < \theta < \pi$, the enhancement in the lower region and the reduction in the upper region are both displaced leftward: the effect is that the vertical axis of the convective cell is tilted slightly to the right, with an additional downward ($0 < \theta < \frac{\pi}{2}$) or upward ($\frac{\pi}{2} < \theta < \pi$) squashing. Conversely, if $-\pi < \theta < 0$, the cells are tilted slightly to the left.

Similar interpretations can be given for other quantities. For example, $|\chi_1|$ and $|\chi_2|$ measure the importance of the first and second harmonics in the concentration perturbation; $\arg(\chi_1)$ describes the horizontal offset between C' and w', while $\arg(\chi_2/\chi_1)$ describes the relative phase of the second harmonic to the first in C', and thus describes the manner in which the concentration perturbations are distorted by the second harmonic. In what follows, we will also consider the porosity perturbation ϕ', defining Φ_1 and Φ_2 in the obvious manner and obtaining them via (3.26).

Figures 3.4 and 3.5 show how the amplitudes and phases of the perturbations to vertical velocity, concentration and porosity vary as Δ changes. They should be read in conjunction with figure 3.6, which illustrates how the corresponding spatial structure of the fastest-growing eigenfunction behaves as Δ is reduced. All the cases plotted in figure 3.6 lie in the regime where σ is fully complex: the bifurcation point for these parameter values occurs at approximately $\Delta = 0.7$.

For values of Δ to the right of the bifurcation point ($\Delta \approx 0.7$), the perturbations to concentration and porosity are both small (figure 3.4(a)) and are in phase such that maxima of the first harmonic of ϕ' correspond to minima of the first harmonic of χ (figure 3.4(b)). A change in trend is immediately noticeable at the bifurcation point: although the first harmonic of concentration continues to vary smoothly, and it remains almost perfectly in phase with the velocity ($\arg(\chi_1) \approx -\pi$, as can be seen in figure 3.4(b)), the trend in the amplitude of the porosity perturbation alters, and it is no longer perfectly in phase with the concentration perturbation: as $\arg(\Phi_1)$ decreases (figure 3.4(b)), the extrema of ϕ' move rightwards relative to those of w' and C'.

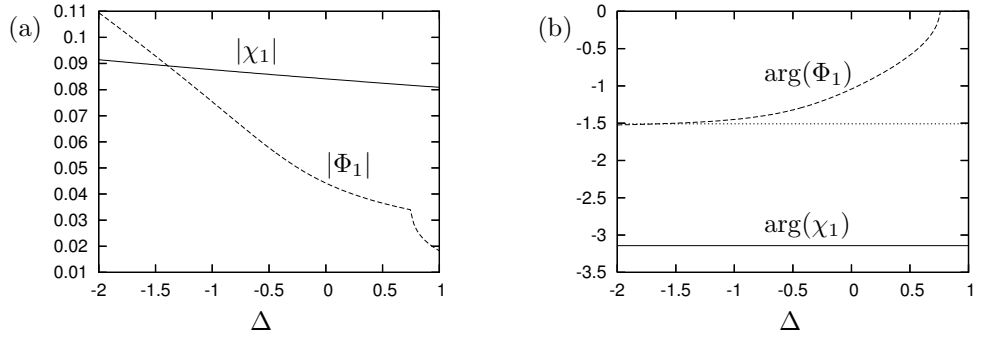

Figure 3.4: (a) Amplitudes and (b) relative phases of the first harmonics as functions of Δ. In (a), solid line is $|\chi_1|$ and dashed line is $|\Phi_1|$. In (b), solid line is $\arg(\chi_1)$ and dashed line is $\arg(\Phi_1)$; the dotted line is $-\frac{\pi}{2}$. Parameter values: $\phi_0 = 0.1$, $k_0 = 10$, $\delta = 0.1$, $m = 3$.

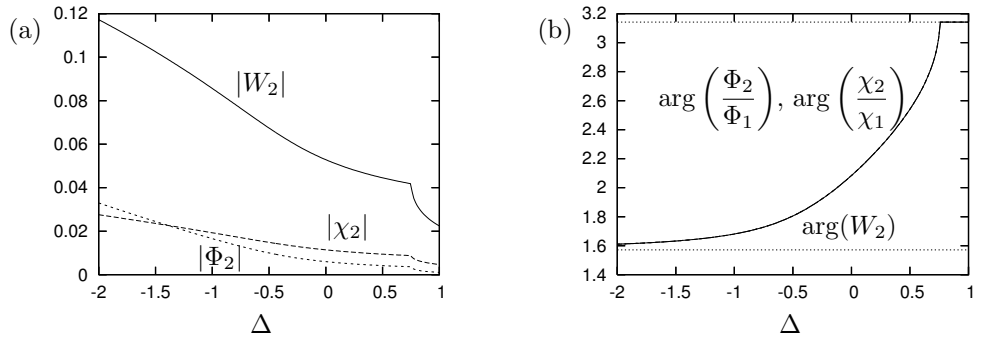

Figure 3.5: (a) Amplitudes and (b) relative phases of the second harmonics as functions of Δ. In (a), solid line is $|W_2|$, heavy dashed line is $|\chi_2|$ and light dashed line is $|\Phi_2|$. In (b), solid line is $\arg(W_2)$, heavy dashed line is $\arg(\chi_2/\chi_1)$ and light dashed line is $\arg(\Phi_2/\Phi_1)$; the three lines are practically indistinguishable. The dotted lines are π and $\frac{\pi}{2}$. Parameter values: $\phi_0 = 0.1$, $k_0 = 10$, $\delta = 0.1$, $m = 3$.

This is the situation that is beginning to emerge in figures 3.6(a) and (b), where $\Delta = 0.5$. The pattern of flow, concentration and porosity is very similar to that for simple convection. Downflow draws down higher concentrations from the upper boundary while upflow draws up lower concentrations from the lower boundary. Upflow occurs in high-permeability regions and downflow in low-permeability regions: since the concentration and porosity perturbations are still approximately 'in phase', the reaction will tend to amplify the porosity perturbation. The small

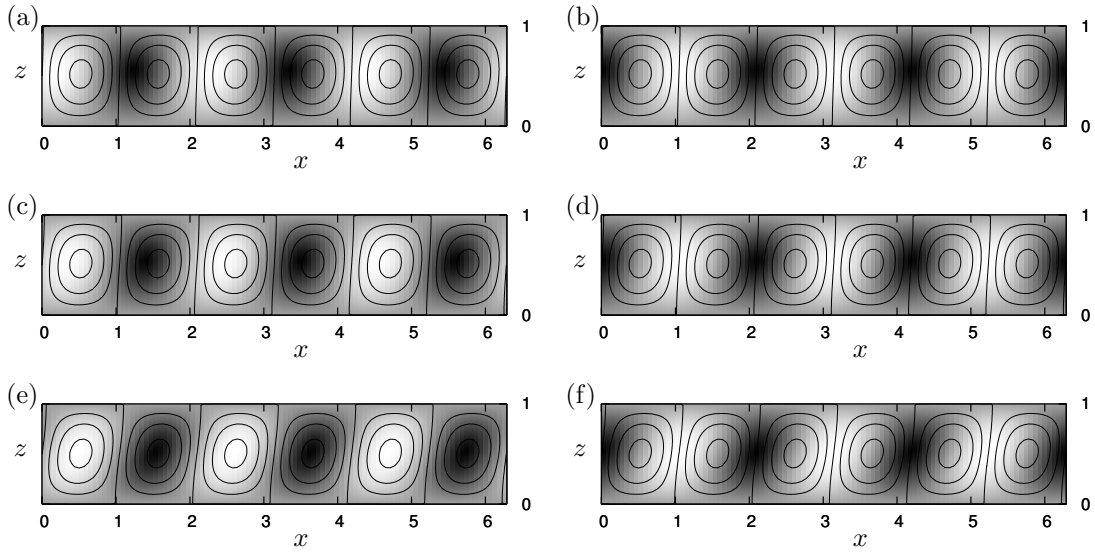

Figure 3.6: Eigenfunctions from the Galerkin analysis, with the leftward-propagating mode taken in each case. Left-hand column: streamlines superimposed on ϕ perturbation. Right-hand column: streamlines superimposed on C perturbation. Parameters were $\phi_0 = 0.1$, $k_0 = 10$, $m = 3$. In (a) and (b), $\Delta = 0.5$; in (c) and (d), $\Delta = 0$; in (e) and (f), $\Delta = -1$. In each case the values of ψ on the streamlines are evenly spaced, and in each plot darker shading corresponds to lower values; scales are arbitrary.

phase difference between C' and ϕ' is just apparent, but the distortion caused by the second harmonics is almost imperceptible at this stage.

As Δ is reduced a little further, the concentration and porosity continue to move further out of phase (figure 3.4(b)), the porosity perturbation grows in importance (figure 3.4(a)), and the second harmonics start to become apparent. The relative phases of all the second harmonics are in the range $(\frac{\pi}{2}, \pi)$ (figure 3.5(b)), so they tilt the convection pattern rightward. This can be seen in figures 3.6(c) and (d) for $\Delta = 0$: the velocity and concentration perturbations are still closely in phase, but the leftward offset of the porosity perturbation is greater and the rightward tilting of the cells is more evident. Note that it is at roughly this value of Δ that the migration rate of the pattern is greatest (see figure 3.3(b)).

As Δ is reduced still further, the phase difference between the porosity and con-

centration perturbations approaches $\frac{\pi}{2}$ (figure 3.4(b)), so they are almost exactly a quarter of a period out of phase: this is visible in figures 3.6(e) and (f) ($\Delta = -1$). The importance of the second harmonics increases (figure 3.5(a)) and their phase difference from the first harmonic approaches $\frac{\pi}{2}$ (figure 3.5(b)), so they tend to tilt the cells rightward without squashing them upward or downward. The tilting is now clearly evident.

We are now in a position to discuss the mechanisms that maintain this amplifying travelling-wave mode. Recall that the concentration perturbation equation (3.18) contains two source terms which must balance the dissipative effects of the reaction and diffusion terms. The first of these sources is the convective term $-w'$; the second is the term $\partial\phi'/\partial z$ which represents net diffusive transport due to gradients in porosity superimposed on the background vertical gradient of concentration. When the porosity perturbation is weak and the system is dominated by convection, the convective source term dominates. When the porosity perturbation is stronger and convective flow is weak, the importance of the porosity-gradient mechanism increases. Because the porosity perturbation is offset from the concentration perturbation, the effect of this term is felt differently by different parts of the concentration field. Given a 'cell' of high C', it can be seen by comparing figures 3.6(e) and (f) that the porosity gradient will be negative both to the top left and to the bottom right of this 'cell', and positive to the top right and the bottom left of it. Since the cell is already tilted to the right, this mechanism acts to maintain the tilting against buoyant effects that would tend to restore it to an upright convective cell, and diffusive effects that would tend to eliminate the perturbation altogether. Meanwhile, the offset between C' and ϕ' has the additional effect of causing the porosity perturbations to migrate leftward. Essentially, then, this mode of behaviour can be characterised as a kind of reaction–diffusion instability which is parasitic on the background vertical concentration gradient. This reaction–diffusion instability is discussed in more detail in the next section.

The modes described here, comprising travelling-wave patterns of tilted cells, are reminiscent of similar patterns seen in mushy layers (Anderson and Worster 1996) and in nonlinear simulations of double-diffusive convection (Mamou and Vasseur 1999; Mamou, Vasseur, and Hasnaoui 2001). The mechanisms, however, are

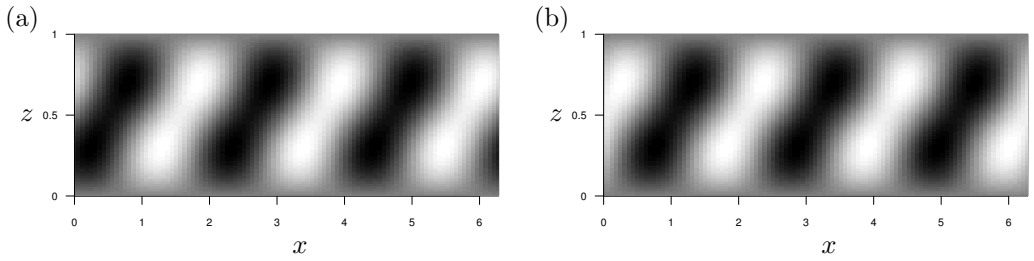

Figure 3.7: Eigenfunctions from the Galerkin analysis for $\mathcal{R}_C = 0$; (a) shows the ϕ perturbation, while (b) shows the C perturbation. Parameters were $\phi_0 = 0.1$, $k_0 = 10$, $m = 3$. In each plot darker shading corresponds to lower values; scales are arbitrary.

distinct: the mushy-layer process depends crucially on the release of latent heat and on the timescale of solidification (Anderson and Worster 1996, §5), while the process in non-reactive convection depends on the double-diffusive effects which permit overstable oscillations.

3.2.3.5 Reaction–diffusion instability

In order to further elucidate the mechanisms involved in the reaction-diffusion instability we return to the system of equations given by (3.43) and (3.44) subject to the boundary conditions (3.42). We will seek approximate solutions in the form

$$W(z) = W_1 \sin(\pi z) + W_2 \sin(2\pi z), \quad \chi(z) = \sin(\pi z) + \chi_2 \sin(2\pi z). \tag{3.76}$$

Note that the boundary conditions are automatically satisfied but, in contrast to §3.2.3.1, we have imposed the non-triviality condition by normalising the $\sin(\pi z)$ component of $\chi(z)$ rather than the $\sin(\pi z)$ component of $W(z)$. This normalisation now allows us to study the reaction-diffusion unencumbered by any distractions from the velocity field since it allows the solution $W = 0$.

Figure 3.7 illustrates the spatial structure of the fastest-growing eigenfunction when $\mathcal{R}_C = 0$ and $W = 0$. The porosity and concentration perturbations are both tilted rightwards and are a quarter period out of phase. As above, this

offset between the ϕ' and C' perturbations causes the porosity gradient to be felt differently by different parts of the concentration field; this in turn maintains the tilting of the cells, while causing the porosity perturbations to migrate leftwards. Note that the tilting in this case is more pronounced than when $\mathcal{R}_C \neq 0$ since there are now no convective terms trying to hold cells upright. This mechanism was discussed in detail in the previous section.

3.2.3.6 Predictions of stability behaviour

It is easy to scan systematically across $(\mathcal{R}_C, m)$-space and thus locate the fastest-growing perturbation for each value of $\mathcal{R}_C$: for all values of the parameters considered, there was a single unambiguous maximum over m. We confine the discussion in this section to the branch with the highest value of $\Re(\sigma)$, noting that when $\Im(\sigma) \neq 0$ the complex conjugate of the branch plotted will also be a solution (see figure 3.3).

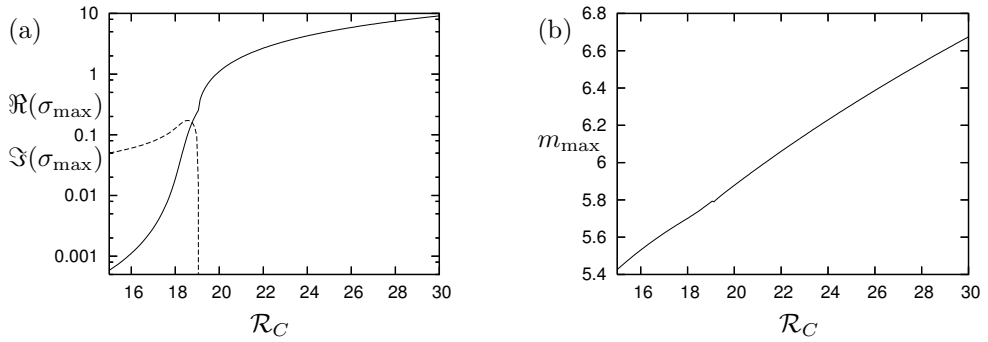

Figure 3.8: (a) The real and imaginary parts of the maximum growth rate; and (b) the corresponding wavenumber. Parameters were $\phi_0 = 0.1$, $k_0 = 10$ and $\delta = 0.1$. In (a), the solid line denotes $\Re(\sigma_{\max})$ and the dashed line denotes $\Im(\sigma_{\max})$; note the logarithmic scale.

Figure 3.8 illustrates how the wavenumber and growth rate of the fastest-growing perturbation vary with $\mathcal{R}_C$, for a specific value of k_0. In figure 3.8(a) it is clear that the emergence of oscillatory modes at $\mathcal{R}_C \approx 19$ coincides with a rapid, but not catastrophic, decrease in growth rates. There is a small, but noticeable, rapid change in the favoured wavenumber at this point, which appears to be genuine

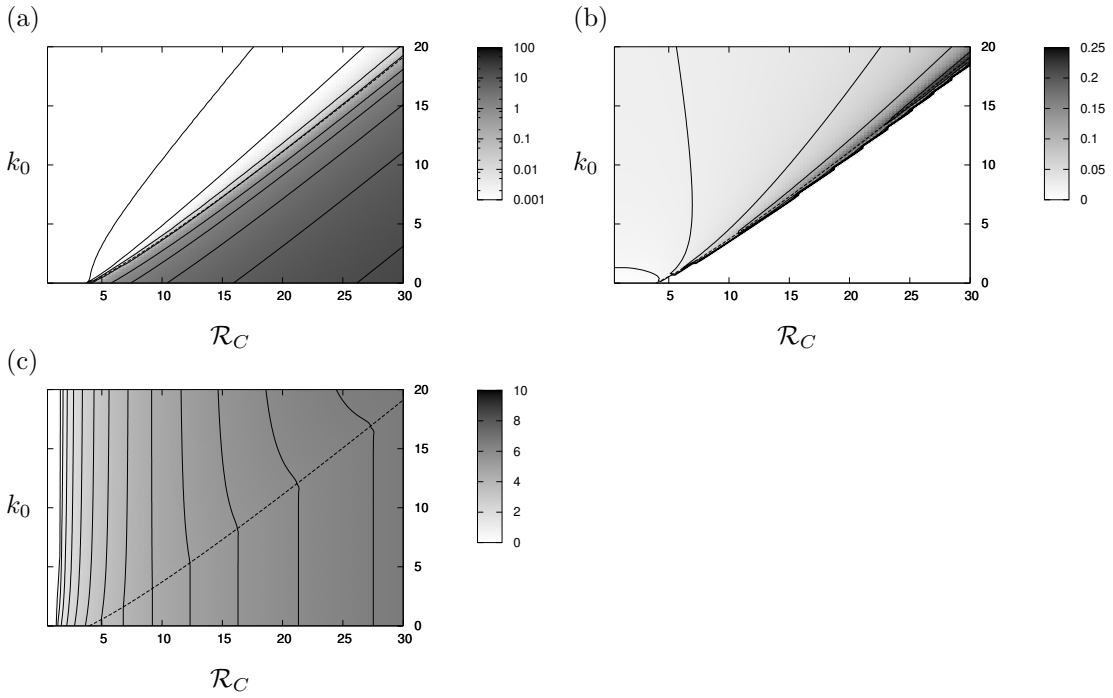

Figure 3.9: Results from the Galerkin analysis with $\phi_0 = 0.1$ and $\delta = 0.1$. (a) $\Re(\sigma_{\max})$: contours are at $\Re(\sigma_{\max}) = 0.0001$, 0.001, 0.01, 0.1, 1, 2, 4, 8 and 16. (Note the logarithmic scale.) (b) $\Im(\sigma_{\max})$: contours are at $\Im(\sigma) = 0.01$, 0.025, 0.05, 0.1 and 0.2. (c) The corresponding wavenumber $m_{\max}$: contours are at intervals of 0.5 starting at $m_{\max} = 0.5$. The dashed line in each plot represents $\mathcal{R}_{C,0}^{\text{crit}}(k_0)$.

rather than a plotting artefact.

Figure 3.9 extends figure 3.8 to demonstrate how the stability of the system varies with $\mathcal{R}_C$ and k_0, again taking $\delta = 0.1$ to emphasise the effect of the matrix evolution. It is evident from this figure that the stability boundary $\mathcal{R}_{C,0}^{\text{crit}}$ from the case $\delta = 0$ provides a good estimate of the boundary between two regimes of behaviour. For $\mathcal{R}_C \gtrsim \mathcal{R}_{C,0}^{\text{crit}}$, matrix evolution is insignificant: $\Im(\sigma_{\max})$ is zero, and the favoured wavenumber $m_{\max}$ increases along the stability boundary but is otherwise independent of k_0 in this regime. For $\mathcal{R}_C \lesssim \mathcal{R}_{C,0}^{\text{crit}}$, the travelling-wave mode dominates, with $\Re(\sigma_{\max})$ very close to zero and $\Im(\sigma_{\max})$ decaying gradually away from the boundary. In this regime, $m_{\max}$ does vary somewhat with k_0, and for sufficiently small values of $\mathcal{R}_C$ the favoured wavenumber becomes very small.

This indicates that when buoyancy effects are very small the instability favours extremely long-wave perturbations: in practice these may not be realised within a finite or a periodic domain.

3.3 Numerical results

A full numerical integration of the system was carried out in order both to test the predictions of the linear stability analysis and to examine the nonlinear behaviour and flow–permeability feedback over longer timescales.

The dimensionless system (3.9)–(3.12) was written in streamfunction form as

$$\nabla \cdot \left[\left(1 + \frac{\phi'}{\phi_0} \right)^{-2} \nabla \psi' \right] = -\mathcal{R}_C \frac{\partial C'}{\partial x}, \tag{3.77}$$

$$\begin{aligned} &\left(1 + \frac{\phi'}{\phi_0} \right) \frac{\partial C'}{\partial t} + \frac{\partial \psi'}{\partial x} + \left(\frac{\partial \psi'}{\partial x} \frac{\partial C'}{\partial z} - \frac{\partial \psi'}{\partial z} \frac{\partial C'}{\partial x} \right) = (\phi_0 + \phi') \nabla^2 C' \\ &+ \frac{\partial \phi'}{\partial z} + \left(\frac{\partial \phi'}{\partial x} \frac{\partial C'}{\partial x} + \frac{\partial \phi'}{\partial z} \frac{\partial C'}{\partial z} \right) - k_0 \left(1 + \frac{\phi'}{\phi_0} \right) \frac{(1 - (\phi_0 + \phi'))}{(1 - \phi_0)} C', \end{aligned} \tag{3.78}$$

$$\frac{\partial \phi'}{\partial t} = -\delta k_0 (\phi_0 + \phi') \frac{(1 - (\phi_0 + \phi'))}{(1 - \phi_0)} C', \tag{3.79}$$

where $u' = -\partial \psi' / \partial z$ and $w' = \partial \psi' / \partial x$. This formulation eliminates the need to include pressure and impose continuity, and makes the numerical integration significantly easier. The corresponding form of the boundary conditions (3.20) is

$$\frac{\partial \psi'}{\partial x} = 0 \quad \text{and} \quad C' = 0 \quad \text{at} \quad z = 0 \quad \text{and} \quad z = 1. \tag{3.80}$$

This system was integrated using the finite element package Comsol Multiphysics v3.5a in a rectangular domain, $0 < x < 10$, $0 < z < 1$, with the boundary conditions (3.80) applied on the horizontal boundaries, and periodicity imposed on the vertical boundaries. Numerical experiments were conducted both with zero initial conditions and with initial conditions into which a small periodic

perturbation had been introduced,

$$C'(x,z,0) = z(1-z)\epsilon\sin(\pi x), \quad \phi(x,z,0) = \phi_0 + 0.01z(1-z)\sin(\pi x), \quad (3.81)$$

where $\epsilon = 10^{-3}$. There was no perceptible difference between the results for the two cases.

To verify that our numerical model converged a number of simulations were conducted over 5000 time units using various values for the relative and absolute tolerances. For simulations with no reaction ($k_0 = 0$) and with a slower reaction ($k_0 = 10$) we found that our solution had converged with a relative tolerance of 10^{-3} and an absolute tolerance of 10^{-4}.

The robustness of our numerical model was checked by conducting simulations using 1120, 4480, 17920, and 71680 triangular mesh elements. Model results were mesh independent when we used at least 4480 elements, however, the time to conduct each simulation increased dramatically. Therefore, for all the tests conducted we used 4480 mesh elements. This ensured our results were mesh independent to two significant figures (see Tables B.3 and B.4), yet the time to complete each simulation was reasonable (of the order of 10 mins on a desktop PC). Further details of the tolerance and mesh independence testing can be found in appendix B.1.

3.3.1 Stability boundary and the onset of convection

Recall that figure 3.2 shows the critical stability curve when $\delta = 0$ given by (3.41). This curve gives the values of $\mathcal{R}_{C,0}^{\text{crit}}$ used in our simulations.

Figure 3.10 summarises a large number of numerical experiments carried out to validate the linear stability analysis against the numerics. In each simulation we took $\phi_0 = 0.1$ and $\delta = 0.001$; each simulation was 1500 time units long and was started from the initial conditions (3.81). This length of simulation ensured that the system had enough time for convection to develop, even in the marginal cases. The criterion used to distinguish between non-convective and convective cases was whether by the end of the simulation the maximum value of $|\mathbf{u}|$ was

greater or less than 10^{-1}.

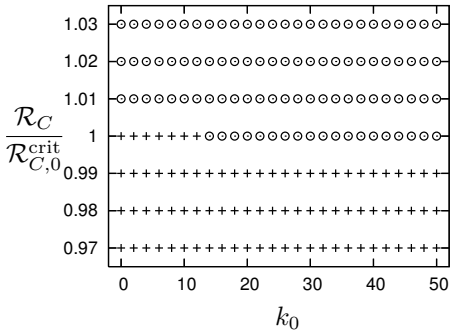

Figure 3.10: $\mathcal{R}_C/\mathcal{R}_{C,0}^{\text{crit}}$ from numerical tests with $\phi_0 = 0.1$ and $\delta = 0.001$. The points represent non-convective (+) or convective ($\odot$) behaviour.

Figure 3.11 shows the maximum absolute velocity for $\mathcal{R}_C/\mathcal{R}_{C,0}^{\text{crit}} = 0.99$, 1.00, and 1.01. When $\mathcal{R}_C/\mathcal{R}_{C,0}^{\text{crit}} = 0.99$ (figure 3.11(a)) the maximum velocity was always well below the cut-off point for convective behaviour, and when $\mathcal{R}_C/\mathcal{R}_{C,0}^{\text{crit}} = 1.01$ (figure 3.11(b)) the maximum velocity was always well above the cut-off point. When $\mathcal{R}_C/\mathcal{R}_{C,0}^{\text{crit}} = 1.00$ (figure 3.11(c)), however, we can see the transition from non-convective to convective behaviour at $k_0 \approx 14$.

As can be seen from figure 3.10(b) the linear stability result for $\delta = 0$, (3.39), agrees well with the numerical results. This suggests, in agreement with §3.2.3, that the effects of porosity evolution on the onset of convection are rather subtle.

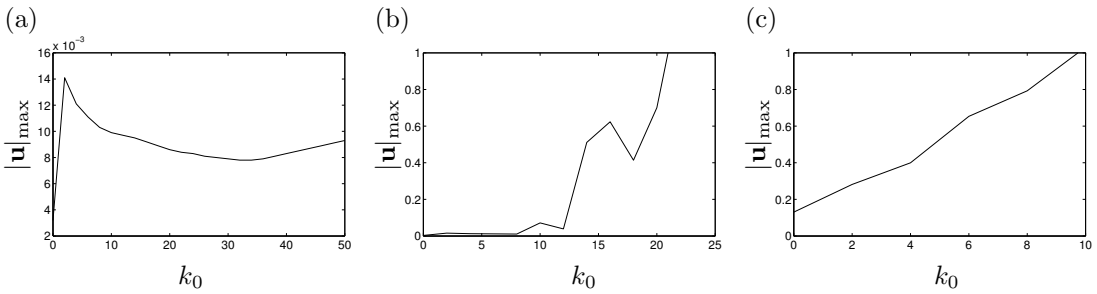

Figure 3.11: Maximum absolute velocity at each reaction rate for (a) $\mathcal{R}_C/\mathcal{R}_{C,0}^{\text{crit}} = 0.99$, (b) $\mathcal{R}_C/\mathcal{R}_{C,0}^{\text{crit}} = 1.00$, and (c) $\mathcal{R}_C/\mathcal{R}_{C,0}^{\text{crit}} = 1.01$.

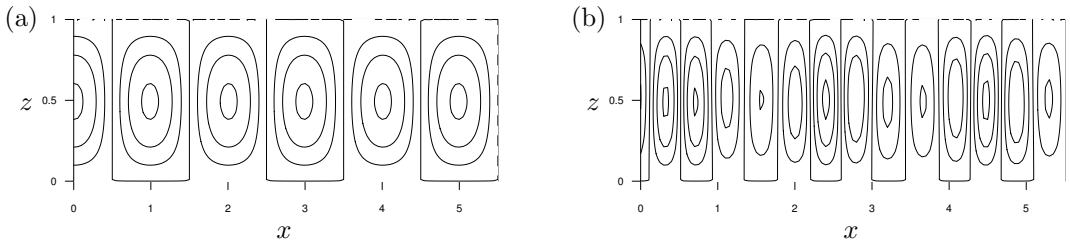

Figure 3.12: Streamlines for simulations with (a) $k_0 = 0$, and (b) $k_0 = 40$. In both cases there was no porosity evolution ($\delta = 0$) and the Rayleigh number was 1% above the critical Rayleigh number given by (3.41).

A key qualitative prediction of the linear stability analysis is that along the line $\mathcal{R}_C = \mathcal{R}_{C,0}^{\text{crit}}$ the wave number of the fastest-growing perturbations should increase with the reaction rate. Figure 3.12 shows the streamlines for two simulations: one with no reaction ($k_0 = 0$) and one with a higher reaction rate ($k_0 = 40$). In each case the Rayleigh number was 1% above the critical Rayleigh number given by (3.39). For no reaction, both (3.40) and the numerics give a wavenumber of π, corresponding to a wavelength of 2. For $k_0 = 40$, (3.40) predicts the wavenumber to be $m_0^{\text{crit}} \approx 7.98$, and the numerical results show the wavenumber to be $m \approx 7.54$. The discrepancy can be attributed to the horizontal periodicity of the numerical domain: the numerical value of m corresponds to 12 pairs of counter-rotating cells in $0 \leq x \leq 10$, while the theoretically predicted value would require between 12 and 13 such pairs. Similar discretisation errors were noted by Pritchard and Richardson (2007).

3.3.2 Long-term behaviour

In order to examine the long-term behaviour of the system we pay particular attention to two cases: one with a 'slower' reaction ($k_0 = 10$) and one with a 'faster' reaction ($k_0 = 40$). Each simulation was 5000 time units long, and we took $\phi_0 = 0.1$ and $\delta = 0.001$. In each case we used four values of the Rayleigh number: the critical Rayleigh number given by (3.39), and 10%, 20%, and 50% above this value.

3.3.2.1 Reference case: $k_0 = 10$ and $\mathcal{R}_C = 1.1\mathcal{R}_{C,0}^{\text{crit}}$

We first consider the slow reaction with $k_0 = 10$. As a reference case for the long-term behaviour we begin by focusing on the simulation with a Rayleigh number 10% above the critical value, $\mathcal{R}_C = 20.42$ (compared with $\mathcal{R}_{C,0}^{\text{crit}} \approx 18.56$). Figure 3.11 shows the evolution of the concentration perturbation C', the porosity ϕ, and the absolute velocity $|\mathbf{u}|$ for the left half of the domain as well as the horizontally averaged porosity $\overline{\phi}$ for the whole domain. The solid lines on the concentration and porosity plots are the streamlines, and the arrows on the absolute velocity plot are the velocity field.

By $t = 100$ steady convection has been established (figure 3.11(a)). At this time the concentration and porosity fields are in phase: that is, regions of $C' > 0$ coincide with regions of lower porosity ($\phi < \phi_0$) and regions of $C' < 0$ coincide with regions of higher porosity ($\phi > \phi_0$). From (3.19) we expect porosity to decrease where $C' > 0$, and to increase where $C' < 0$. As the flow is buoyancy driven, downward flow is favoured where $C' > 0$, drawing down higher concentrations from the top boundary, and upward flow is favoured where $C' < 0$, drawing up lower concentrations from the bottom boundary: this is the essential mechanism that sustains convection. Furthermore, flow is faster in areas of higher porosity, shown by the closer packed streamlines in regions of $\phi > \phi_0$ which coincide with the darker areas of the absolute velocity field. Hence, upward flow is faster than downward flow.

Once steady convection has been established, the porosity field continues to evolve until it triggers a secondary instability in the form of a phase shift. Figure 3.11(b) shows the fields at $t = 200$, just before the phase shift. Comparing with figure 3.11(a), we can see that although the concentration field is the same, the porosity field has evolved further and now has more pronounced areas of high and low porosity. The horizontally averaged porosity field $\overline{\phi}$ indicates that the lower half of the domain is dominated by lower porosity as a result of the precipitation in downwelling regions, while the upper half is dominated by higher porosity as a result of the dissolution in upwelling regions. As a result of this evolution the absolute velocity field now has more pronounced areas of upwards flow coinciding with areas of higher porosity. Also, the centres of the circulation cells have moved

upwards slightly.

Part-way through the shift ($t = 215$, figure 3.11(c)), the concentration field has moved approximately an eighth of a cell (0.25 x-units) to the right, but the porosity field remains the same as before the shift. Also, in the absolute velocity field we see that the upwards flow has remained in approximately the same position, but the downwards flow has shifted towards the right, while there is a slight tilting of the cells to the left (most apparent in the concentration field). By the end of the shift at $t = 250$ (figure 3.11(d)) the concentration field and streamlines have moved a half cell (one x-unit) to the right, and the centre of the circulation cells has moved slightly downward, but the porosity field is still effectively unchanged. There is still downward flow where $C' > 0$, but this now coincides with high porosity regions. Therefore, downward flow is now faster than upward flow.

Further evidence of this phase shift can be seen in figures 3.12(a) and (b), which show the maximum absolute velocity throughout the whole domain. From these figures we see that convection develops and is maintained for approximately 200 time steps, but there is a dip in the velocity around the time of the phase shift as the circulation slows and then re-establishes itself. After this shift, the system settles back into a quasi-equilibrium state of almost steady convection.

The secondary instability occurs as a result of the positive feedback between the concentration and porosity fields which causes clogging in the downflow regions. This clogging eventually reaches some critical state and displaces the downflow sideways resulting in narrower convection cells. These are overcome by diffusion, and the circulation begins to shut down before it is replaced by a reversed circulation. Bolton, Lasaga, and Rye (1999) identified a similar mechanism which acted to displace the 'stalk' of rising thermal plumes in their simulations. The sideways migration of these fully developed, nonlinear convection cells is also reminiscent of the migration of small-amplitude cells seen in the linear analysis close to $\mathcal{R}_C = \mathcal{R}_{C,0}^{\text{crit}}$ (§3.2.3.4). Unlike the phenomenon seen in the linear case, the tilting and sideways movement here is readily halted by the tendency of buoyancy-driven convection to favour stationary, upright cells.

At $t = 250$ (figure 3.11(d)) the concentration and porosity fields are out of phase: areas of large positive concentration perturbations now coincide with areas of high

porosity, and vice versa. In these high concentration ($C' > 0$) areas porosity will decrease, and in low concentration $C' < 0$ areas porosity will increase. Therefore, the porosity evolution strives to get the concentration and porosity fields back into phase.

The porosity evolution is shown in figures 3.12(a) and (b), plotted with the maximum absolute velocity to display the correlation with the phase shifts. At the time of the phase shift (denoted by the vertical dotted line) the porosity contrast has reached a local maximum, with a peak in the maximum porosity and a trough in the minimum porosity. After the shift, the maximum porosity decreases and the minimum porosity increases, because the concentration and porosity fields are now out of phase. By $t \approx 500$, the concentration and porosity fields are back in phase and so now the porosity contrast begins to increase again at a similar rate to before the phase shift.

By $t = 710$ (figure 3.11(e)), the porosity is now back in phase with the concentration field. There is faster upwards flow in regions of higher porosity, and slower downflow in low porosity regions, as before the first phase shift. Note that there is now a distinct vertical asymmetry in the circulation and porosity field: there is more dissolution towards the top of the domain and the circulation has correspondingly moved upwards to this higher porosity region. Further evidence of this asymmetry can be seen in the horizontally averaged porosity as the region of lower porosity now extends over more than half the domain. After this, the system goes through another phase shift, again moving one half cell to the right, displaying the same behaviour as with the first shift. This shift can be seen in figures 3.12(a) and (b) as the sharp dip in $|\mathbf{u}|_{\max}$ at $t \approx 750$. These figures also show similar porosity behaviour to the first phase shift, with the porosity contrast peaking around the time of the shift.

From figures 3.12(a) and (b) we can see that the system only undergoes two rapid phase shifts, and subsequent changes take place over a much longer timescale. By $t = 1500$ (figure 3.11(f)) the system is back in phase, but with the circulation field shifted a further quarter cell to the right. There is now a more distinct vertical asymmetry in the circulation and porosity fields, with higher porosity regions and the centres of the circulation cells now even closer to the top of the domain. Also,

the magnitude of the concentration perturbations and the absolute velocity are reduced.

By $t = 3000$, (figure 3.11(g)), the circulation has shifted a further quarter cell to the right but the system is still in phase, with upflow concentrated in more highly permeable vertical channels. Alternate high-permeability channels are more pronounced: this can be explained as the result of an instability whereby a slightly more permeable channel 'steals' flux from its neighbours and thus experiences more rapid dissolution. This is akin to the 'screening' effect that causes dissolution patterns to be dominated by a few large fingers (Daccord 1987; Hoefner and Fogler 1988). This screening effect competes with the convective circulation to set the favoured wavenumber of the system, leading to the alternation that is observed. There is a superficial similarity between the high permeability channels here and the chimneys observed in mushy layers (Worster 1997), although the channels here are merely regions of enhanced porosity rather than regions where the porous matrix has been entirely dissolved. The layering of high porosity over lower porosity regions is also more pronounced at this stage than at earlier times.

The slow evolution continues and by $t = 4000$ (figure 3.11(h)) the fields have changed considerably. The concentration perturbations are now very small and there is distinct layering in the porosity field, with a low porosity barrier in the middle of the domain and regions of higher porosity at the top and bottom of the domain, as seen in the $\overline{\phi}$ plot. This low porosity barrier is pierced by occasional high porosity channels, but it cannot extend to the lower boundary since the boundary conditions there fix the concentration at its equilibrium value C_{eq}, and hence fix the porosity at $\phi = \phi_0$. There is still evidence of the period-doubling seen at earlier times, with alternate high porosity channels more pronounced. From the streamlines and the absolute velocity field we see that because of this barrier, two-layered convection has developed. In the top layer the concentration and porosity fields are in phase, but in the bottom layer they are out of phase.

By the end of the simulation at $t = 5000$ (figure 3.11(i)) only the lower layer where the concentration and porosity fields are out of phase has survived and it now penetrates the upper layer. The period-doubling has survived, but there is now more pronounced alternate downflow in the high porosity channels. Note

that even after more than 1000 time units the lower layer has not yet reversed phase.

3.3.2.2 Effect of varying the Rayleigh number

Figure 3.12 shows the porosity evolution and maximum absolute velocity for each of the convective Rayleigh numbers with $k_0 = 10$. Initial adjustment to steady convection happens very rapidly, within roughly the first ten time units. The system then evolves gradually until the first phase shift, the signature of which is a sharp drop in the maximum absolute velocity. The higher the Rayleigh number, the longer it is before the phase shift occurs. The porosity contrast is at its greatest when a phase shift occurs, and the higher the Rayleigh number the greater the porosity change when the system shifts. This behaviour is expected since as we increase the Rayleigh number, we are increasing the concentration difference between the top and bottom of the domain. Therefore, we expect to see bigger absolute velocities and to require bigger porosity differences to trigger a phase shift.

When $\mathcal{R}_C = \mathcal{R}_{C,0}^{\text{crit}}$ the system appears for around a thousand timesteps to be non-convective (figure 3.10(b)), but after this time a weak circulation does develop. This reflects the fact that even at or below the 'threshold' $\mathcal{R}_C = \mathcal{R}_{C,0}^{\text{crit}}$ the system remains weakly unstable, as shown in §3.2.3. Meanwhile, when $\mathcal{R}_C = 1.2\mathcal{R}_{C,0}^{\text{crit}}$ and $\mathcal{R}_C = 1.5\mathcal{R}_{C,0}^{\text{crit}}$ we see similar behaviour to that with $\mathcal{R}_C = 1.1\mathcal{R}_{C,0}^{\text{crit}}$.

3.3.2.3 Effect of varying the reaction rate

We now consider the faster reaction with $k_0 = 30$. To allow direct comparison with the long-term behaviour in the slow reaction case we focus on a simulation with a Rayleigh number 10% above the critical value, $\mathcal{R}_C = 47.34$ compared with $\mathcal{R}_{C,0}^{\text{crit}} \approx 43.03$. Figure 3.13 shows the evolution of the concentration perturbation C', the porosity ϕ, and the absolute velocity $|\mathbf{u}|$ for the left half of the domain as well as the horizontally averaged porosity $\overline{\phi}$ for the whole domain, while figure 3.14 shows the corresponding evolution of the maximum velocity and the porosity contrast. The most prominent difference between figure 3.14 and figure 3.12 is

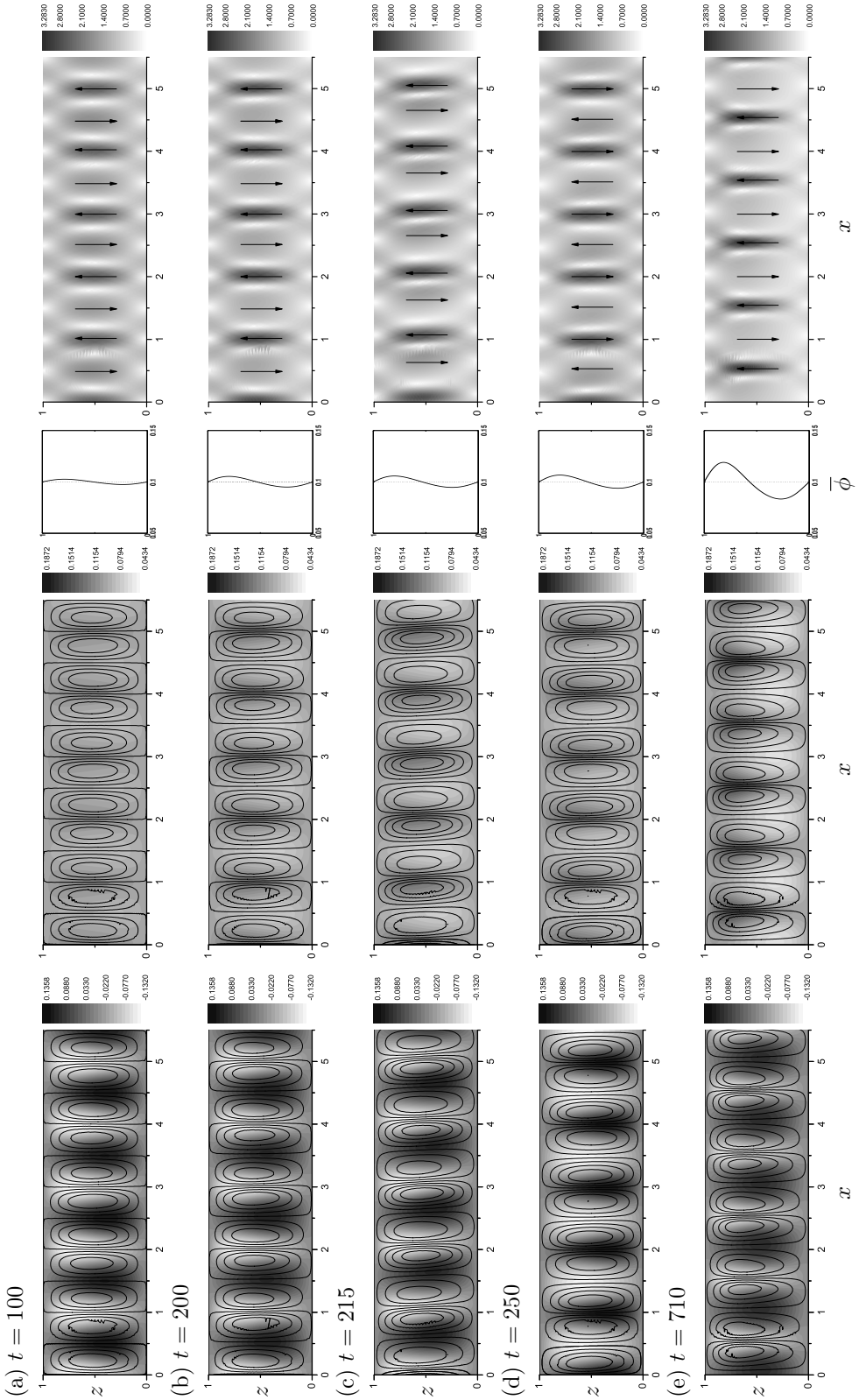
(a) $t = 100$
(b) $t = 200$
(c) $t = 215$
(d) $t = 250$
(e) $t = 710$
z
x
$\overline{\phi}$

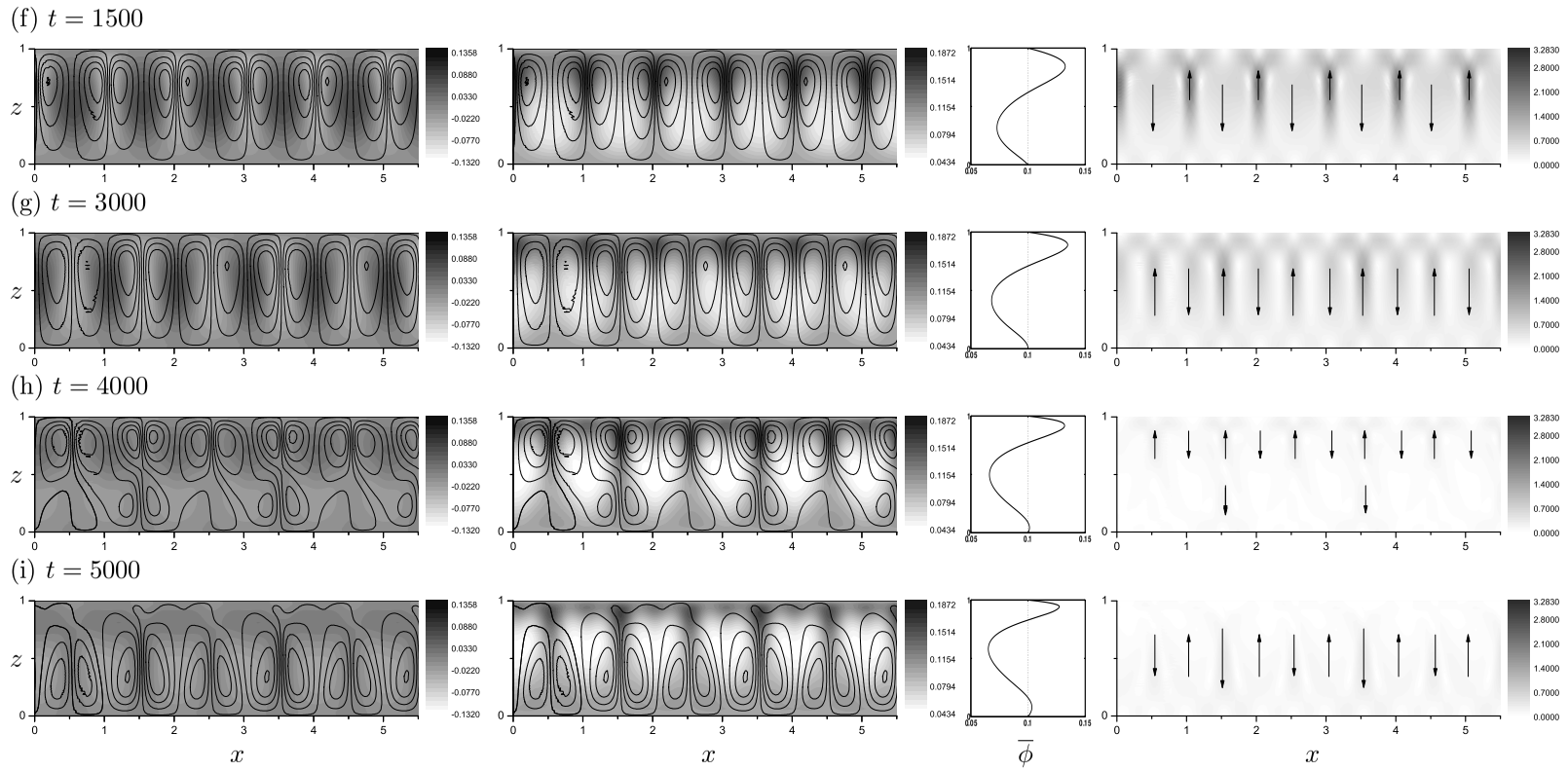

Figure 3.11: Evolution with $k_0 = 10$. Shading indicates solutal concentration perturbation C' (left), porosity ϕ with its horizontal average $\overline{\phi}$ (centre), and absolute velocity $|\mathbf{u}|$ (right). Solid lines are streamlines and arrows indicate the velocity field but are not drawn to scale. The irregularities in the streamlines around $x = 0.75$ are artefacts of the plotting software, caused by the irregular mesh triangulation in this region.

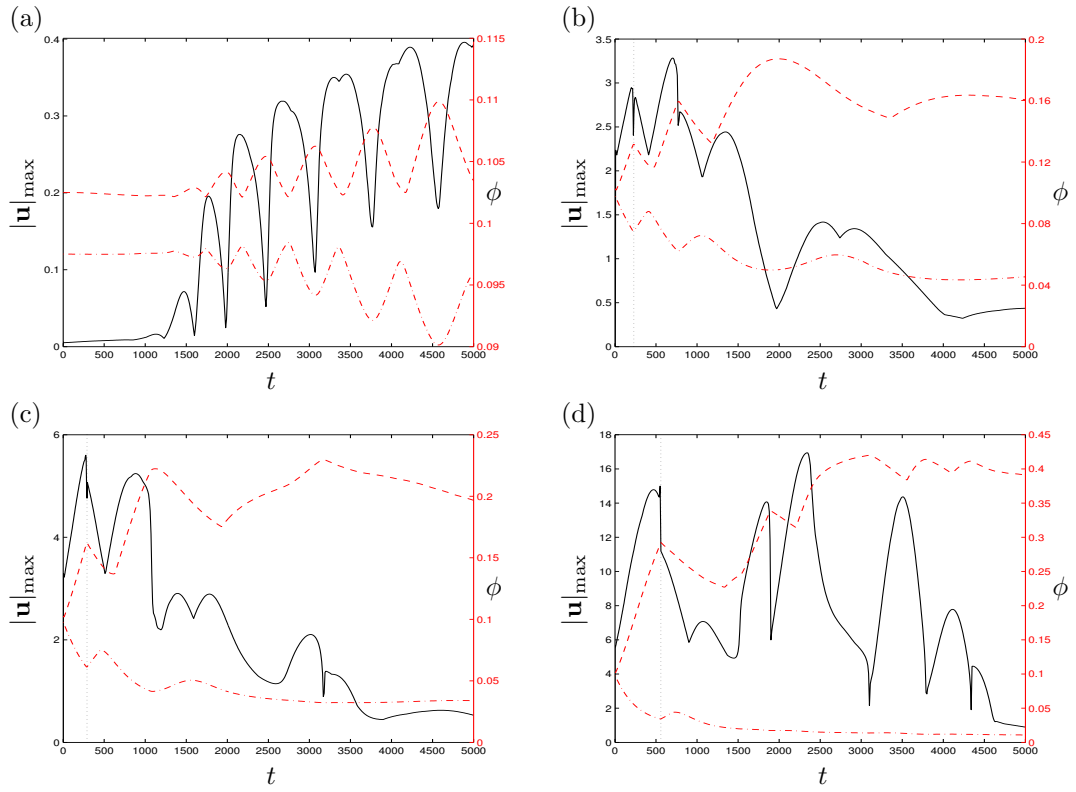

Figure 3.12: Maximum absolute velocity $|\mathbf{u}|$ and maximum and minimum porosity ϕ throughout the whole domain when $k_0 = 10$. Here the solid line represents the maximum velocity, the dashed line represents the maximum porosity and the dashed-dotted line represents the minimum porosity. In (a) $\mathcal{R}_C = \mathcal{R}_{C,0}^{\text{crit}}$, (b) $\mathcal{R}_C = 1.1\mathcal{R}_{C,0}^{\text{crit}}$, (c) $\mathcal{R}_C = 1.2\mathcal{R}_{C,0}^{\text{crit}}$, and (d) $\mathcal{R}_C = 1.5\mathcal{R}_{C,0}^{\text{crit}}$.

that the higher reaction rate and higher Rayleigh number lead to faster evolution of the system. What is of more interest is whether the qualitative development also changes.

Buoyancy-driven convection has been established by $t \approx 10$ (not shown): at this time the convection pattern closely resembles figure 3.11(a), and there are ten pairs of counter-rotating cells in the full domain, corresponding to a wave number of $m \approx 6.28$. However, (3.40) predicts a rather higher critical wave number $m_0^{\text{crit}} \approx 7.44$, and by $t = 50$ (figure 3.13(a)) additional convection cells have appeared at $x \approx 3.5$ and $x \approx 9.5$. These subsequently expand so that there are twelve pairs of counter-rotating cells in the domain, corresponding to

a wavenumber of $m \approx 7.54$. The emergence of the two pairs of counter-rotating cells, on top of an existing although weakly defined porosity structure, results in a less uniform cell pattern, with some cells now tilting and slightly more pronounced upflow in some channels than others (figure 3.13(b)). Note from figure 3.14 that the emergence of the extra cells does not affect the maximum absolute velocity.

Once convection has been established with an appropriate wave number, the porosity field evolves until it triggers a secondary instability, as with the slower reaction rate (§3.3.2.1). Figure 3.13(b) shows the fields at $t = 180$, just before the phase shift (compare figure 3.11(b) for the case $k_0 = 10$). As before, the concentration perturbation and porosity fields are initially in phase before the shift, while after the phase shift ($t = 210$, figure 3.13(c)) the concentration perturbation field and streamlines have moved a half cell (≈ 1 x-unit) to the right, and now the cells are more upright. Furthermore, the concentration perturbation and porosity fields are now out of phase. The overall pattern is similar to figure 3.11(d), although the strengths of the cells are less uniform: this may be because the faster reaction promotes the 'screening' effect in which cells compete with their neighbours for flux (§3.3.2.1).

The phase shift can also be seen in the maximum absolute velocity and porosity contrast (figure 3.14). Convection develops and is maintained for almost 200 time steps, but there is a dip in the velocity around the time of the phase shift (marked by the vertical dotted line) as the circulation slows and then re-establishes itself. After this shift, the system settles back into a quasi-equilibrium state of steady convection, with the maximum velocity and porosity contrast first declining and then gradually increasing again as the porosity comes back into phase with the concentration. (Precisely analogous behaviour can be seen in figure 3.12.)

By $t = 380$ (figure 3.13(d)), the concentration and porosity fields are back in phase, although the porosity perturbations are small and the centres of the circulation cells have moved upwards. No further rapid phase shifts occur, but the slow evolution continues. At first the porosity contrast becomes more pronounced, with 'eyes' of high porosity developing at the top of the layer and regions of lower porosity in the middle of the domain; meanwhile the circulation pattern becomes more irregular than §3.3.2.1, with a weak lower layer of counter-rotating

cells forming in places and flow in the middle of the layer focussed into a few narrow channels (figure 3.13(e)): the picture is reminiscent of figure 3.11(h), but the flow pattern is more irregular and the overall porosity contrast more strongly dominated by the 'eyes' near the upper boundary. As the simulation continues, the qualitative picture is unaltered (figure 3.13(f)), but the maximum velocity gradually declines (figure 3.14) and the low porosity barrier becomes more pronounced, now extending over three quarters of the domain. This suggests that the very long-term attractor of the system may be a non-convective state with a considerably decreased porosity throughout the layer.

3.4 Discussion and conclusions

We have investigated the behaviour of an idealised mathematical model of geochemical convection in a reactive porous medium. The model can be obtained from the full thermosolutal model described in chapter 2, in the limit of very high thermal diffusivity and finite solutal diffusivity with negligible thermal expansion.

Although the porosity evolution is slow on the timescale of convection and reaction, it exerts an unexpected influence on the stability properties of the system. When the system is strongly buoyantly unstable, the reaction acts to remove destabilising solute and thus to stabilise the system. However, when the system is close to the threshold of instability (as calculated without porosity evolution), a new unstable mode becomes available, and persists even when the Rayleigh number is reduced below the critical value for buoyant instability. This new mode is essentially a reaction–diffusion instability which is driven by solute fluxes caused by the interaction between the porosity perturbation and the background vertical concentration gradient.

Over longer timescales, the porosity evolution introduces further new behaviour: although quasi-steady convective circulation becomes established as in non-reactive convection, it cannot persist indefinitely. Instead, the porosity changes associated with the circulation become steadily more pronounced, and ultimately trigger a relatively rapid reorganisation of the flow in which the entire pattern of convective cells shifts sideways by half a wavelength.

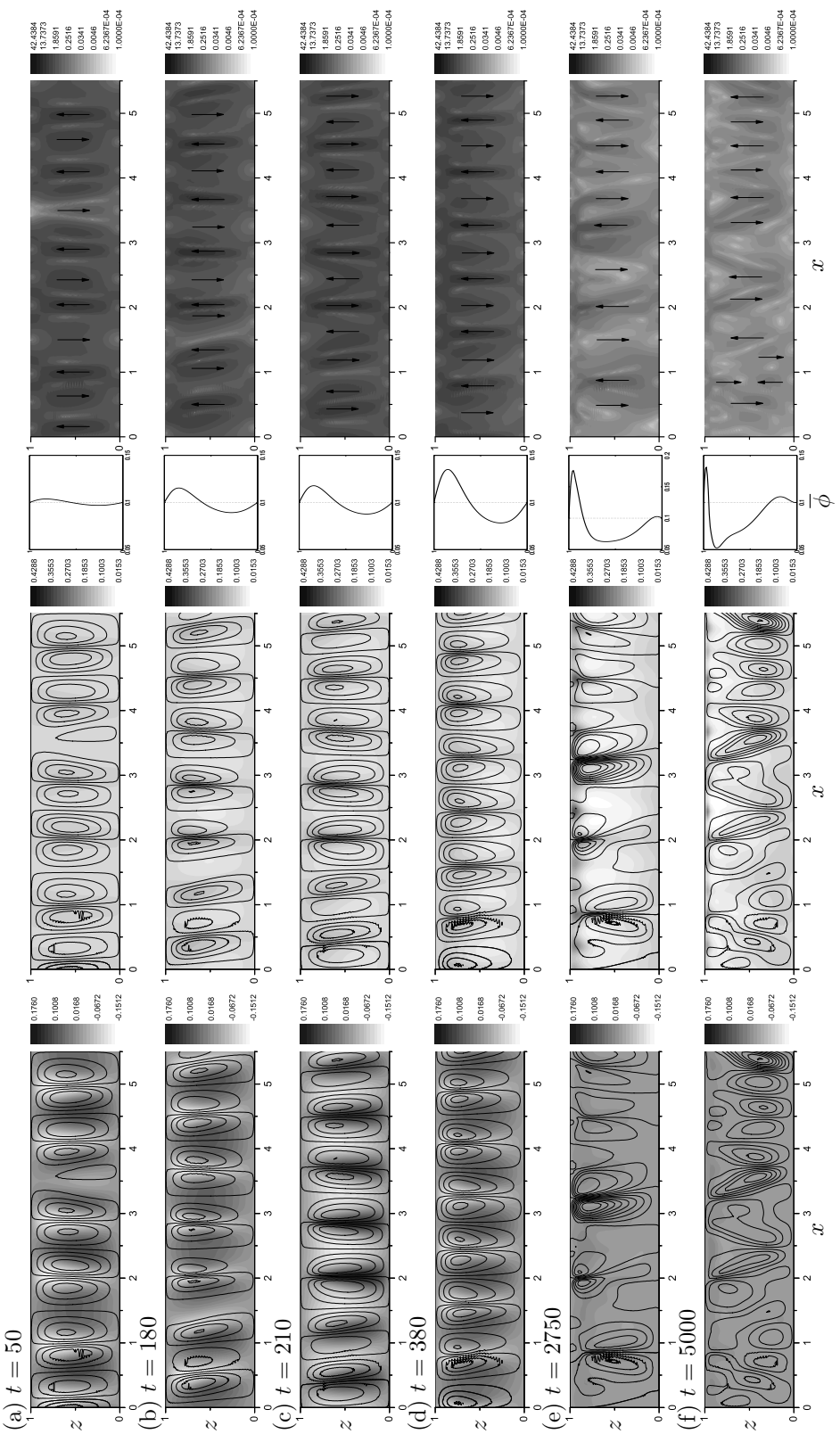

Figure 3.13: Evolution with $k_0 = 30$. Shading indicates solutal concentration perturbation C' (left), porosity ϕ with its horizontal average $\overline{\phi}$ (centre), and absolute velocity $|\mathbf{u}|$ (right). Solid lines are streamlines and arrows indicate the velocity field but are not drawn to scale. The irregularities in the streamlines around $x = 0.75$ are artefacts of the plotting software, caused by the irregular mesh triangulation in this region.

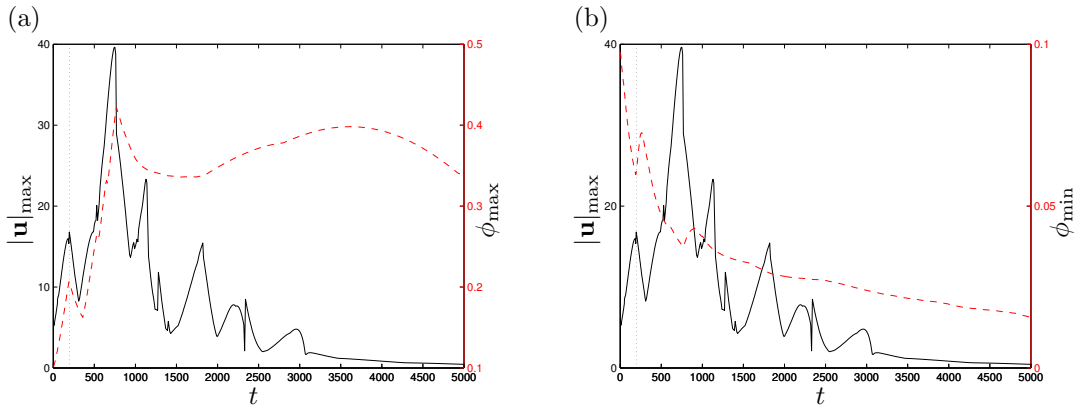

Figure 3.14: Maximum absolute velocity $|\mathbf{u}|$ and (a) maximum and (b) minimum porosity ϕ throughout the whole domain when $\phi_0 = 0.1$, $\delta = 0.001$, $k_0 = 30$ and $\mathcal{R}_C = 1.1\mathcal{R}_{C,0}^{\text{crit}}$. Here the solid line represents the maximum velocity and the dashed line represents the maximum or minimum porosity.

The repeated interplay between episodes of quasi-steady convection and the rapid reorganisations that punctuate them eventually develops a layered porosity structure, with the centre of the layer being dominated by a low-porosity band broken by occasional higher-permeability vertical channels, and pockets of enhanced porosity occurring nearer the top and the bottom of the layer. There appears to be no long-term steady convective state towards which the system asymptotes, although once layering has become established there is a tendency for the strength of convection to decrease.

These findings complement the numerical experiments of Bolton *et al.* (1996; 1997; 1999) by demonstrating that geochemical convection can spontaneously give rise to heterogeneous porosity fields, and not merely enhance heterogeneities that already exist. Their wider implication is that in situations where long-term convective transport is simulated in order to determine patterns of mineralisation, such as ore deposition (e.g. Raffensperger and Garven 1995a,b), it may be essential to incorporate flow–reaction–permeability coupling in order to capture even the outline of the mineralisation patterns. Another implication is that, because of the development of instabilities which scale in a nonlinear manner with the matrix evolution rate δ, simulations which accelerate the rock evolution to reduce runtime may thereby distort their results in unexpected ways. This implication was supported by further numerical simulations (omitted here for brevity) which

found that increasing δ by a factor of ten resulted in more pronounced tilting of the circulation cells, as well as triggering earlier and more frequent episodes of rapid flow reorganisation and a more strongly layered porosity structure.

The most natural extension of the work described in this chapter is to the full thermosolutal system. Firstly, however, we will briefly consider the effect of Neumann boundary conditions at the top and bottom of the layer.

Chapter 4

Reactive solutal convection with Neumann boundary conditions

It is well known that in non-reactive single-diffusive porous medium convection changing from constant solutal concentration (Dirichlet) to no-flux (Neumann) boundary conditions reduces the critical Rayleigh number from $\mathcal{R}_C^{\text{crit}} = 4\pi^2$ to $\mathcal{R}_C^{\text{crit}} = 12$ (see table 2.1), as well as changing the vertical structure of the perturbations (Nield and Bejan 2006). The most realistic boundary conditions are mixed boundary conditions which are a linear combination of Dirichlet and Neumann boundary conditions. However, in this thesis we focus our attention on the extremal cases of either Dirichlet or Neumann boundary conditions.

In this chapter we examine the effect that Neumann boundary conditions at the top and bottom of the layer have on both the onset of convection and the long-term behaviour of reactive convection in an evolving porous layer. As well as changing the vertical structure of the perturbations, this change in boundary conditions also means that the porosity ϕ can now evolve at the top and bottom boundary. Furthermore, in contrast to Dirichlet conditions, Neumann conditions ensure that the total amount of solute within the layer is conserved. We use the same model as in the previous chapter, so the dimensionless governing equations are given by (3.9)–(3.12).

In §4.1 we carry out a linear stability analysis of the onset of convection. We

then, in §4.2, validate this stability analysis using a numerical model, and carry out a sequence of numerical experiments to investigate the longer-term behaviour of the system. Finally, in §4.3 we summarise our results and draw some general conclusions.

4.1 Linear stability analysis

The non-dimensional linearised governing equations are given by (3.16)–(3.19), but these are now subject to the boundary conditions

$$w' = 0 \quad \text{and} \quad \frac{\partial C'}{\partial z} = 0 \quad \text{at} \quad z = 0 \quad \text{and at} \quad z = 1. \tag{4.1}$$

We seek Fourier mode solutions of the form

$$\begin{aligned} &u' = U(z)e^{imx}e^{\sigma t}, \quad w' = W(z)e^{imx}e^{\sigma t}, \quad p' = P(z)e^{imx}e^{\sigma t}, \\ &C' = \chi(z)e^{imx}e^{\sigma t}, \quad \phi' = \Phi(z)e^{imx}e^{\sigma t}, \end{aligned} \tag{4.2}$$

where the real parts are assumed, the wave number m is a positive real number, and U, W, P, χ, Φ and σ are generally complex. Substituting these into (3.16)–(3.19), and combining and simplifying gives (3.27), which we repeat here

$$\left[\phi_0\left(\frac{\mathrm{d}^2}{\mathrm{d}z^2} - m^2\right) - \frac{\delta k_0 \phi_0}{\sigma}\frac{\mathrm{d}}{\mathrm{d}z} - (k_0 + \sigma)\right]\left[\frac{\mathrm{d}^2}{\mathrm{d}z^2} - m^2\right] W(z) = m^2 \mathcal{R}_C W(z). \tag{4.3}$$

In contrast to problem in chapter 3, $W(z)$ must now satisfy the boundary conditions

$$W(z) = 0 \quad \text{and} \quad \frac{\mathrm{d}}{\mathrm{d}z}\left(\frac{\mathrm{d}^2}{\mathrm{d}z^2} - m^2\right) W(z) = 0 \quad \text{at} \quad z = 0 \quad \text{and at} \quad z = 1. \tag{4.4}$$

Using the same approach as in §3.3, we seek solutions to (4.3) in the form $W(z) \propto \exp(qz)$, where q is a root of the auxiliary equation (3.29), i.e.

$$\left[\phi_0(q^2 - m^2) - \frac{\delta k_0 \phi_0}{\sigma} q - (k_0 + \sigma)\right][q^2 - m^2] = m^2 \mathcal{R}_C. \tag{4.5}$$

In general we may write

$$W(z) = A_1 e^{q_1 z} + A_2 e^{q_2 z} + A_3 e^{q_3 z} + A_4 e^{q_4 z}, \tag{4.6}$$

and the boundary conditions (4.4) may be written as

$$B \cdot \begin{bmatrix} A_1 \\ A_2 \\ A_3 \\ A_4 \end{bmatrix} = \mathbf{0}, \tag{4.7}$$

where

$$B = \begin{bmatrix} 1 & 1 & 1 & 1 \\ e^{q_1} & e^{q_2} & e^{q_3} & e^{q_4} \\ q_1(q_1^2 - m^2) & q_2(q_2^2 - m^2) & q_3(q_3^2 - m^2) & q_4(q_4^2 - m^2) \\ q_1(q_1^2 - m^2)e^{q_1} & q_2(q_2^2 - m^2)e^{q_2} & q_3(q_3^2 - m^2)e^{q_3} & q_4(q_4^2 - m^2)e^{q_4} \end{bmatrix}. \tag{4.8}$$

Note that rows 3 and 4 differ from those of the matrix B defined in (3.32). For nontrivial solutions, therefore, we require that

$$\det(B) = 0. \tag{4.9}$$

4.1.1 Reaction but no matrix evolution

It is helpful, as before, to examine the rather simpler case with $\delta = 0$ before we consider the full linear stability problem. As with Dirichlet boundary conditions (cf. §3.3.1), (4.5) has roots $q_1 = -q_2$ and $q_3 = -q_4 = -iq_0$, where

$$\begin{aligned} q_1 &= \left[\frac{1}{2\phi_0}(k_0 + \sigma + 2\phi_0 m^2 + \sqrt{(k_0+\sigma)^2 + 4\phi_0 m^2 \mathcal{R}_C}) \right]^{1/2}, \\ q_0 &= \left[-\frac{1}{2\phi_0}(k_0 + \sigma + 2\phi_0 m^2 - \sqrt{(k_0+\sigma)^2 + 4\phi_0 m^2 \mathcal{R}_C}) \right]^{1/2}. \end{aligned} \tag{4.10}$$

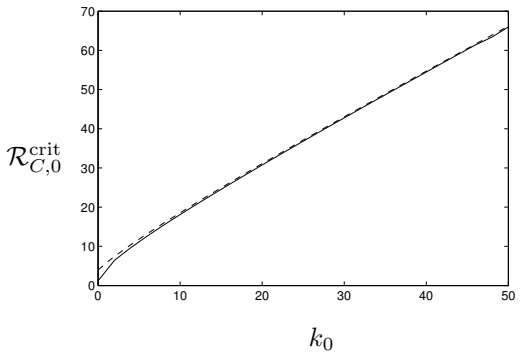

Figure 4.1: Stability boundary for $\mathcal{R}_{C,0}^{\text{crit}}$ with $\delta = 0$ and $\phi_0 = 0.1$; the dashed line represents the stability boundary for constant solutal boundary conditions with $\delta = 0$.

The condition (4.9) for nontrivial solutions therefore becomes

$$\begin{aligned} 2(q_1 q_0 m^4 - q_1^3 q_0^3 + q_1 q_0^3 m^2 - q_1^3 q_0 m^2)(\cosh q_1 \cos q_0 - 1) + \\ (2q_0^4 m^2 + 2q_1^4 m^2 - q_1^6 + q_0^6 - q_1^2 m^4 + q_0^2 m^4) \sinh q_1 \sin q_0 = 0 \end{aligned} \tag{4.11}$$

As before, for this reduced problem the principle of exchange of stabilities holds (see Appendix A.2), so for marginal stability we set $\sigma = 0$.

We solve (4.11) numerically using Maple 12 and the built-in routine `fsolve`. We specify the parameters ϕ_0 and k_0 and solve (4.11) for $\mathcal{R}_{C,0}(m)$. For each m the value of $\mathcal{R}_C$ given by $q_0 = \pi$ was used as an initial guess.

When $k_0 = 0$ we recover the marginal stability condition $\mathcal{R}_{C,0}^{\text{crit}} = 12\phi_0$ and $m_0^{\text{crit}} = 0$ for single-diffusive convection with no-flux boundary conditions in a non-evolving porous medium. Figure 4.1 illustrates how $\mathcal{R}_{C,0}^{\text{crit}}$ increases with increasing k_0. It is apparent that $\mathcal{R}_{C,0}^{\text{crit}}$ for Neumann boundary conditions asymptotes to the critical Rayleigh number for Dirichlet boundary conditions as the reaction rate is increased, suggesting that the reaction negates any effect that Neumann conditions may have on the onset of convection.

	$\delta = 0.1$		$\delta = 0.001$	
m	Dirichlet BCs (Δ, σ)	Neumann BCs (Δ, σ)	Dirichlet BCs (Δ, σ)	Neumann BCs (Δ, σ)
3	(0.7721, 0.2464)	(0.7598, 0.2400)	(0.03612, 0.01166)	(0.03553, 0.01123)
4	(0.6057, 0.2527)	(0.5969, 0.2432)	(0.02832, 0.01186)	(0.02790, 0.01148)
5	(0.5317, 0.2567)	(0.5249, 0.2477)	(0.02485, 0.01208)	(0.02453, 0.01169)
6	(0.4939, 0.2612)	(0.4884, 0.2541)	(0.02307, 0.01226)	(0.02281, 0.01199)
7	(0.4728, 0.2637)	(0.4688, 0.2591)	(0.02207, 0.01232)	(0.02186, 0.01215)
8	(0.4603, 0.2679)	(0.4565, 0.2619)	(0.02148, 0.01250)	(0.02130, 0.01223)

Table 4.1: Comparisons of bifurcation point with constant and no-flux boundary conditions for $\delta = 0.1$ and $\delta = 0.001$. Parameter values: $k_0 = 10$, $\phi_0 = 0.1$.

4.1.2 Linear stability analysis of the full problem

When $\delta \neq 0$, an analytical solution to (4.9) in terms of σ is not available. Therefore, as in §3.2.2, the stability problem was investigated numerically by a continuation method, tracking σ as $\mathcal{R}_C$ changed, while keeping all other parameters fixed. A numerical solution to (4.11) for a large initial value of $\mathcal{R}_C$ was used as an initial guess. This method was implemented in Maple 12, using the built-in routine `fsolve`.

Figure 4.2 shows representative results when the wavenumber m and all the parameters except $\Delta = \mathcal{R}_C - \mathcal{R}_{C,0}(m)$ are fixed, while Δ is varied about zero. The default parameters were $k_0 = 10$, $\phi_0 = 0.1$, and $\delta = 0.1$. Comparing this to figure 3.3 for Dirichlet boundary conditions with the same parameter values, we see that the behaviour is very similar. When Δ is large and positive the branch of σ with largest real part closely tracks σ_0. It deviates weakly from this as Δ is reduced, and at $\Delta \approx 0.7$ the values of σ become complex. As Δ is further reduced, $\Re(\sigma)$ continues to fall, but never reaches zero, asymptoting toward it as $\Delta \to -\infty$. Meanwhile, $\Im(\sigma)$ first increases rapidly in magnitude and then decays.

Table 4.1 compares the location Δ of the bifurcation point and the value of σ at this point for Dirichlet and Neumann boundary conditions for two values of δ: $\delta = 0.1$ and $\delta = 0.001$. We can see that for both sets of boundary conditions the bifurcation occurs at approximately the same value of Δ, and the growth rate σ is approximately the same, too. This agrees with our observations when $\delta = 0$ (§4.1.1) that the reaction negates any effect the Neumann boundary conditions may have on the onset of convection.

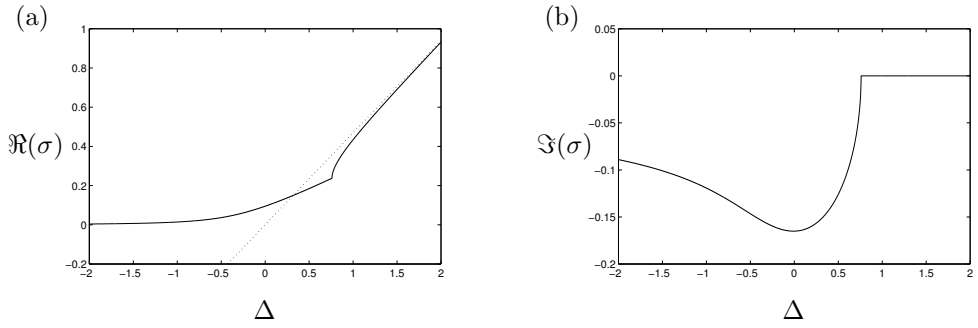

Figure 4.2: Behaviour of σ close to $\mathcal{R}_{C,0}^{\text{crit}}$ for $k_0 = 10$, $\delta = 0.1$, $\phi_0 = 0.1$, $m = 3$. Figure (a) shows $\Re(\sigma)$, while (b) shows $\Im(\sigma)$. The dotted line shows the result for $\delta = 0$.

4.2 Numerical results

A full numerical integration of the system was carried out in order both to test the predictions of the linear stability analysis and to examine whether the change of boundary conditions affects the nonlinear behaviour and flow-permeability feedback over longer timescales.

The dimensionless system of equations was written in streamfunction form (3.77)–(3.79), with corresponding boundary conditions

$$\frac{\partial \psi'}{\partial x} = 0 \quad \text{and} \quad \frac{\partial C'}{\partial z} = 0 \quad \text{at} \quad z = 0 \quad \text{and} \quad z = 1. \tag{4.12}$$

This system was integrated using the finite element package Comsol Multiphysics v3.5a in a rectangular domain, $0 < x < 10$, $0 < z < 1$, with the boundary conditions (4.12) applied on the horizontal boundaries, and periodicity imposed on the vertical boundaries. Numerical experiments were conducted both with zero initial conditions and with initial conditions into which a small periodic perturbation had been introduced,

$$C'(x, z, 0) = z(1 - z)\epsilon \sin(\pi x), \quad \phi(x, z, 0) = \phi_0 + 0.01z(1 - z)\sin(\pi x), \tag{4.13}$$

where $\epsilon = 10^{-3}$. There was no perceptible difference between the results for the

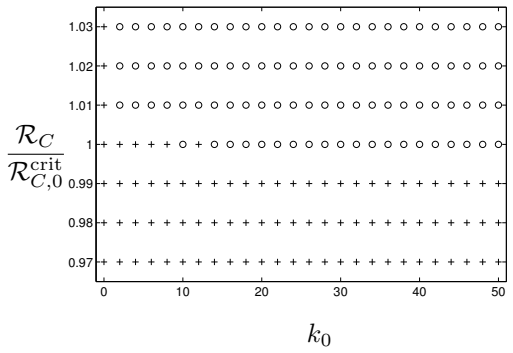

Figure 4.3: $\mathcal{R}_C/\mathcal{R}_{C,0}^{\text{crit}}$ from numerical tests with $\phi_0 = 0.1$ and $\delta = 0.001$. The points represent non-convective (+) or convective (∘) behaviour.

two cases.

4.2.1 Stability boundary and the onset of convection

Recall that figure 4.1 shows the critical stability curve when $\delta = 0$. This curve gives the values of $\mathcal{R}_{C,0}^{\text{crit}}$ used in our simulations.

Figure 4.3 summarises a large number of numerical experiments carried out to validate the linear stability analysis. In each simulation we took $\phi_0 = 0.1$ and $\delta = 0.001$; each simulation was 1500 time units long and was started from the initial conditions (4.13). This length of simulation ensured that the system had enough time for convection to develop, even in the marginal cases. The criterion used to distinguish between non-convective and convective cases was whether by the end of the simulation the maximum value of $|\mathbf{u}|$ was greater or less than 10^{-1}. Note that when $k_0 = 0$ the model does not become unstable around $\mathcal{R}_{C,0}^{\text{crit}}$; in fact, convection only occurs within the first 1500 time units when $\mathcal{R}_C \approx 1.25\mathcal{R}_{C,0}^{\text{crit}}$.

A key qualitative prediction of the linear stability analysis with Dirichlet boundary conditions is that along the line $\mathcal{R}_C = \mathcal{R}_{C,0}^{\text{crit}}$ the wavenumber of the fastest-growing perturbations should increase with the reaction rate. We would expect similar behaviour with Neumann boundary conditions since the stability boundary is similar to that with Dirichlet boundary conditions. Figure 4.4 shows the streamlines for two simulations: one with no reaction ($k_0 = 0$) and one with a

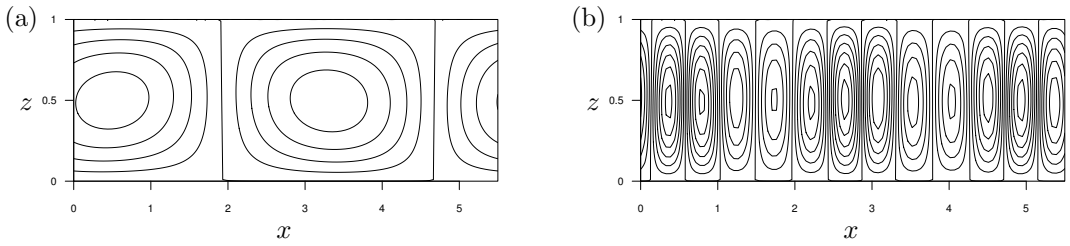

Figure 4.4: Streamlines for simulations with (a) $k_0 = 0$ and $\mathcal{R}_C = 1.25\mathcal{R}_{C,0}^{\text{crit}}$, and (b) $k_0 = 40$ and $\mathcal{R}_C = 1.01\mathcal{R}_{C,0}^{\text{crit}}$. In both cases there was no porosity evolution ($\delta = 0$).

higher reaction rate ($k_0 = 40$). For $k_0 = 0$ the Rayleigh number was 25% above the critical Rayleigh number, and for $k_0 = 40$ the Rayleigh number was 1% above the critical Rayleigh number. The values of Rayleigh number used guaranteed the model was unstable. When there is no reaction the linear stability analysis predicts a wavenumber $m_0^{\text{crit}} = 0$, while the numerical results produce convection with a wavenumber $m \approx 1.26$. However, if we increase the length of the simulation to 8000 time units, the wavelength increases until it is the size of the domain, corresponding to a wavenumber $m = \pi/5$. Furthermore, with this longer length of simulation convection can occur with a Rayleigh number 1% above the critical value.

For $k_0 = 40$, the linear stability analysis predicts the wavenumber to be $m_0^{\text{crit}} \approx 7.97$, and the numerical results show the wavenumber to be $m \approx 7.54$. The discrepancy can be attributed to the horizontal periodicity of the numerical domain: the numerical value of m corresponds to 12 pairs of counter-rotating cells in $0 \leq x \leq 10$, while the theoretically predicted value would require between 12 and 13 such pairs. Similar discretisation errors were noted in §3.3.1 with Dirichlet boundary conditions and by Pritchard and Richardson (2007).

4.2.2 Long-term behaviour

When examining the long-term behaviour of the system we will pay particular attention to two cases: one with a slower reaction $k_0 = 10$ and one with a faster reaction, $k_0 = 30$. Each simulation we describe lasted for 5000 time units and

employed the parameters $\phi_0 = 0.1$ and $\delta = 0.001$. We will present results for four values of the Rayleigh number: the critical Rayleigh number, and 10%, 20%, and 50% above this value.

4.2.2.1 Reference case: $k_0 = 10$ and $\mathcal{R}_C = 1.1\mathcal{R}_{C,0}^{\mathbf{crit}}$

We first consider the slow reaction with $k_0 = 10$. As a reference case for the long-term behaviour we begin by focusing on the simulation with a Rayleigh number 10% above the critical value, $\mathcal{R}_C = 19.90$ (compared with $\mathcal{R}_{C,0}^{\text{crit}} \approx 18.10$). Figure 4.5 shows the evolution of the concentration perturbation C', the porosity ϕ, and the absolute velocity $|\mathbf{u}|$, for the left half of the domain. The solid lines on the concentration and porosity plots are the streamlines, and the arrows on the absolute velocity plot indicate the velocity field.

Comparing figure 4.5 with figure 3.11 for the Dirichlet boundary condition case, we see that the long-term evolution of this system has many similarities with the Dirichlet model. By $t = 100$ steady convection has been established (figure 4.5(a)). At this time the concentration and porosity fields are in phase: that is, regions of $C' > 0$ coincide with regions of lower porosity ($\phi < \phi_0$) and regions of $C' < 0$ coincide with regions of higher porosity ($\phi > \phi_0$).

Once convection has been established, the porosity field evolves until it triggers a secondary instability, as with the Dirichlet boundary condition case (cf §3.3.2.1). Figure 4.5(b) shows the fields at $t = 215$ just before the phase shift. Although the concentration field is the same as in figure 4.5(a), the porosity field has evolved further and now has more pronounced areas of high and low porosity. As a result of this evolution the absolute velocity field now has more pronounced areas of upwards flow coinciding with areas of higher porosity. The centres of the circulation cells have also moved upwards slightly.

Part-way through the shift ($t = 230$, figure 4.5(c)), the concentration field has moved approximately a quarter of a cell (0.25 x-units) to the right, but the porosity field remains the same as before the shift. Also, in the absolute velocity field we see that the upwards flow has remained in approximately the same position, but the downwards flow has shifted towards the right, while there is a tilting of

the cells to the left (most apparent in the concentration field). By the end of the shift at $t = 255$ (figure 4.5(d)) the concentration field and streamlines have moved a half cell (0.5 x-units) to the right, and the centre of the circulation cells has moved slightly downward, but the porosity field is still effectively unchanged. There is still downward flow where $C' > 0$, but this now coincides with high porosity regions. Therefore, downward flow is now faster than upward flow.

Further evidence of this phase shift can be seen in figure 4.6(b), which shows the maximum absolute velocity and porosity contrast throughout the whole domain. Convection develops and is maintained for approximately 200 time steps, but there is a dip in the velocity around the time of the phase shift as the circulation slows and then re-establishes itself. After this shift, the system settles back into a quasi-equilibrium state of almost steady convection, with the maximum velocity and porosity contrast first declining and then gradually increasing again as the porosity comes back into phase with the concentration. The same behaviour can be seen in figure 3.12 which shows the maximum absolute velocity and porosity contrast throughout the whole domain with constant boundary conditions.

By $t = 700$ the concentration and porosity fields are back in phase, with faster upwards flow in regions of higher porosity and slower downflow in regions of lower porosity, as before the first phase shift. As with constant solutal boundary conditions, the system only undergoes two rapid phase shifts, and subsequent changes take place over much longer timescales.

The long-term behaviour of the system is qualitatively the same as for Dirichlet boundary conditions, but the porosity evolution is marginally slower. By $t = 4000$ (figure 4.5(h)) the concentration perturbations are very small and there is distinct layering in the porosity field, with a low porosity barrier in the middle of the domain which is pierced by occasional high porosity channels. There is evidence of period-doubling with alternate high porosity channels more pronounced. From the streamlines and the absolute velocity field we see that because of this barrier, two-layered convection is beginning to develop. By the end of the simulation at $t = 5000$ (figure 4.5(i)) the lower layer has moved upwards, penetrating the upper layer. The period-doubling has survived but there is now more pronounced downflow in alternate high porosity channels.

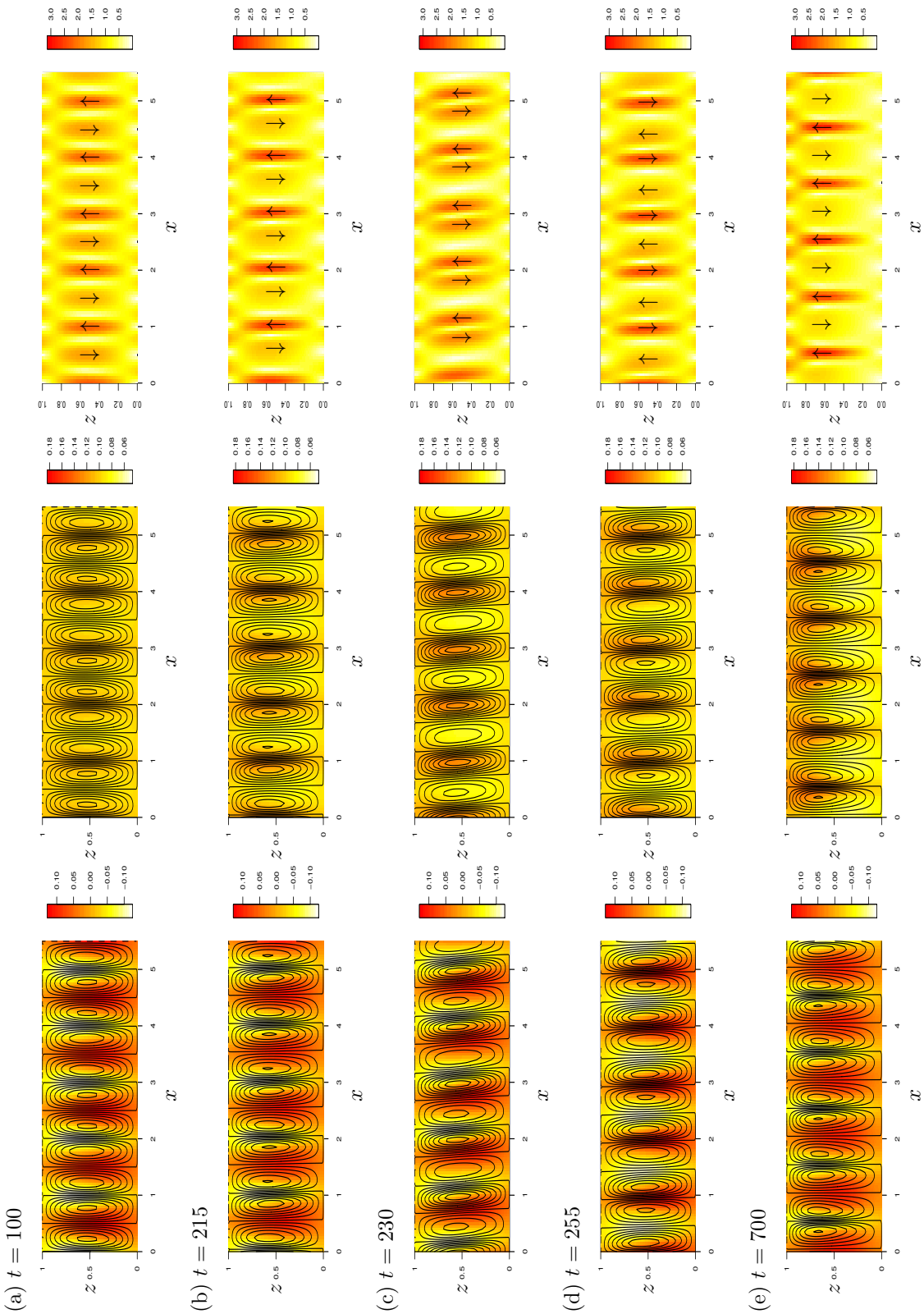
(a) $t = 100$
(b) $t = 215$
(c) $t = 230$
(d) $t = 255$
(e) $t = 700$
x
z

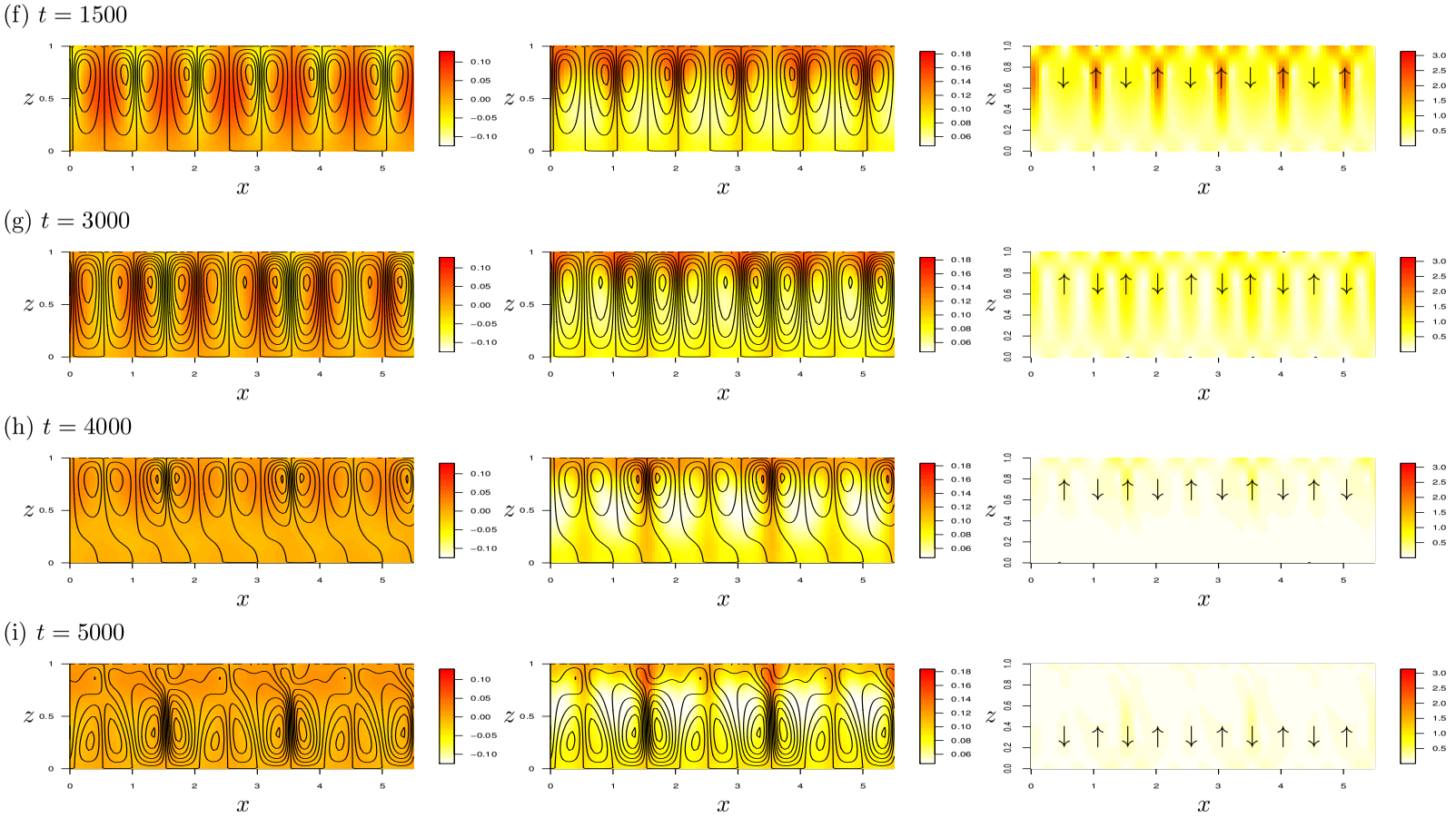

Figure 4.5: Evolution with $k_0 = 10$. Shading indicates solutal concentration perturbation C' (left), porosity ϕ (centre), and absolute velocity $|\mathbf{u}|$ (right). Solid lines are streamlines and arrows indicate the velocity field but are not drawn to scale.

4.2.2.2 Effect of varying the Rayleigh number

Figure 4.6 shows the porosity evolution and maximum absolute velocity for each of the convective Rayleigh numbers with $k_0 = 10$. Comparing with figure 3.12 for Dirichlet boundary conditions, we see that the model exhibits almost the same behaviour with both sets of boundary conditions. However, with Neumann boundary conditions the system settles down to the slow timescale evolution sooner, and therefore the final state of the system is slightly different.

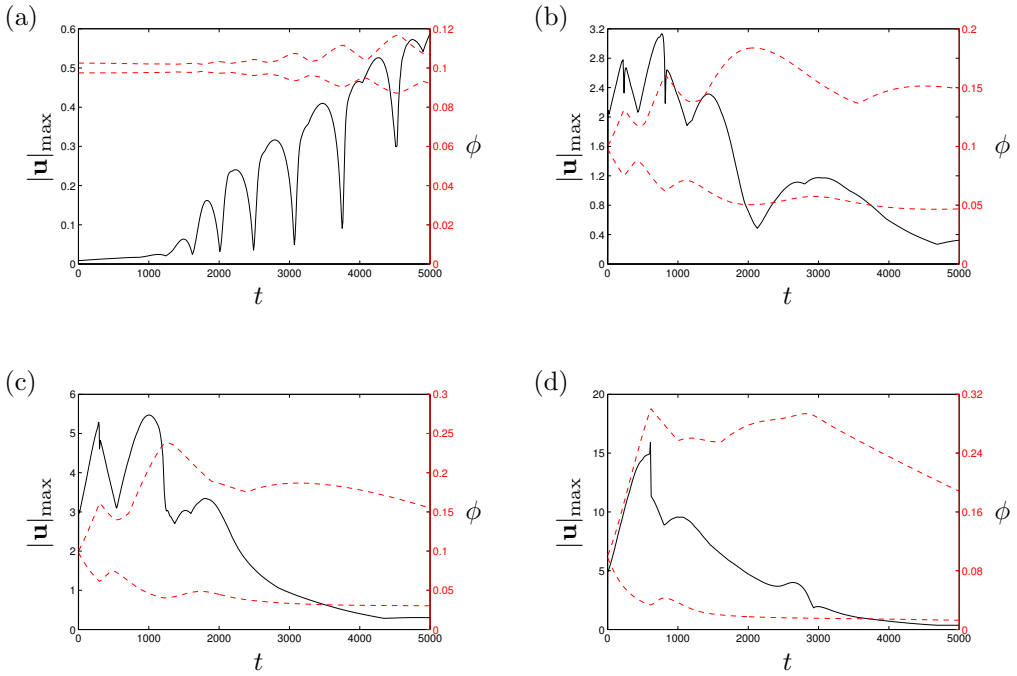

Figure 4.6: Maximum absolute velocity $|\mathbf{u}|$ and maximum and minimum porosity ϕ throughout the whole domain when $k_0 = 10$. Here the solid line represents the maximum velocity, the dashed line represents the porosity. In (a) $\mathcal{R}_C = \mathcal{R}_{C,0}^{\text{crit}}$, (b) $\mathcal{R}_C = 1.1\mathcal{R}_{C,0}^{\text{crit}}$, (c) $\mathcal{R}_C = 1.2\mathcal{R}_{C,0}^{\text{crit}}$, and (d) $\mathcal{R}_C = 1.5\mathcal{R}_{C,0}^{\text{crit}}$.

4.2.2.3 Effect of varying the reaction rate

We now consider the faster reaction with $k_0 = 30$. To allow direct comparison with the long-term behaviour in the slow reaction case we focus on a simulation

with a Rayleigh number 10% above the critical value ($\mathcal{R}_C = 47.0524$ compared with $\mathcal{R}_{C,0}^{\text{crit}} \approx 42.7749$). Figure 4.7 shows the evolution of the concentration perturbation C', the porosity ϕ, and the absolute velocity $|\mathbf{u}|$, for the left half of the domain, while figure 4.8 shows the corresponding evolution of the maximum velocity and the porosity contrast. The most prominent difference between figure 4.8 and figure 3.14 for Dirichlet boundary conditions is that the system settles down to the slow timescale evolution much sooner with the Neumann boundary conditions (at $t \approx 1500$ compared with $t \approx 3100$). This effect was also seen with a slower reaction rate and higher Rayleigh numbers (§4.2.2.2). This suggests that Neumann boundary conditions stabilise the system to rapid readjustments over time.

Buoyancy-driven convection has been established by $t \approx 10$ (not shown): at this time the convection pattern closely resembles figure 4.5(a), and there are ten pairs of counter-rotating cells in the full domain, corresponding to a wave number of $m \approx 6.28$, compared to the critical wavenumber $m_0^{\text{crit}} \approx 7.42$. In contrast to the situation with Dirichlet boundary conditions, however, additional cells do not appear and the simulation continues with a lower wavenumber than predicted by the linear stability analysis.

As with the slower reaction, once convection has been established the porosity field evolves until it triggers a secondary instability. Figure 4.7(a) shows the fields at $t = 250$, just before the phase shift. As before, the concentration perturbation and porosity fields are initially in phase before the shift, while after the phase shift ($t = 290$, figure 4.7(b)) the concentration perturbation field and streamlines have moved a half cell (≈ 1 x-unit) to the right, and now the cells are more upright. Furthermore, the concentration perturbation and porosity fields are now out of phase. As before, the phase shift can also be seen in the maximum absolute velocity and porosity contrast (figure 4.8).

By $t = 700$ (figure 4.7(c)), the concentration and porosity fields are back in phase, although the porosity perturbations are small and the centres of the circulation cells have moved upwards. After this time, as with the Dirichlet boundary condition case with increased reaction rate (§3.3.2.3), the porosity contrast becomes more pronounced, with 'eyes' of high porosity developing at the top of the layer

and regions of lower porosity in the middle of the domain; meanwhile the circulation pattern becomes more irregular (figure 4.7(d)). By the end of the simulation, the circulation is now marginally stronger in the lower half of the domain (figure 4.7(e)), but the maximum velocity and porosity has continued to decline (figure 4.8).

4.3 Summary and conclusions

In this chapter we have investigated the effect of changing the top and bottom boundary conditions from Dirichlet to Neumann conditions on both the onset of convection and the long-term behaviour in a reactive and evolving porous layer.

Although this change of boundary conditions has a strong effect on the onset of convection in a non-reactive and non-evolving layer, reducing the critical Rayleigh number from $\mathcal{R}_C = 4\pi^2$ to $\mathcal{R}_C = 12$, the introduction of a reaction between the saturating fluid and the rock matrix negates this difference. The reaction stabilises the system and, as the reaction rate is increased, the critical Rayleigh number with Neumann boundary conditions asymptotes to that with Dirichlet boundary conditions. Furthermore, when the porosity is allowed to evolve, the systems with Dirichlet and Neumann boundary conditions exhibit very similar behaviour.

Over longer timescales with Neumann boundary conditions, the system undergoes fewer phase shifts and therefore settles into a phase of slow evolution at an earlier point in the simulation. This suggests that these boundary conditions stabilise the system to these rapid reorganisations.

A variety of other boundary conditions could of course be investigated (Lapwood 1948, Nield and Bejan 2006). However, the results of this chapter suggest that these are unlikely to lead to qualitatively new behaviour. Therefore, in the next chapter we extend this simple model to consider the full thermosolutal system.

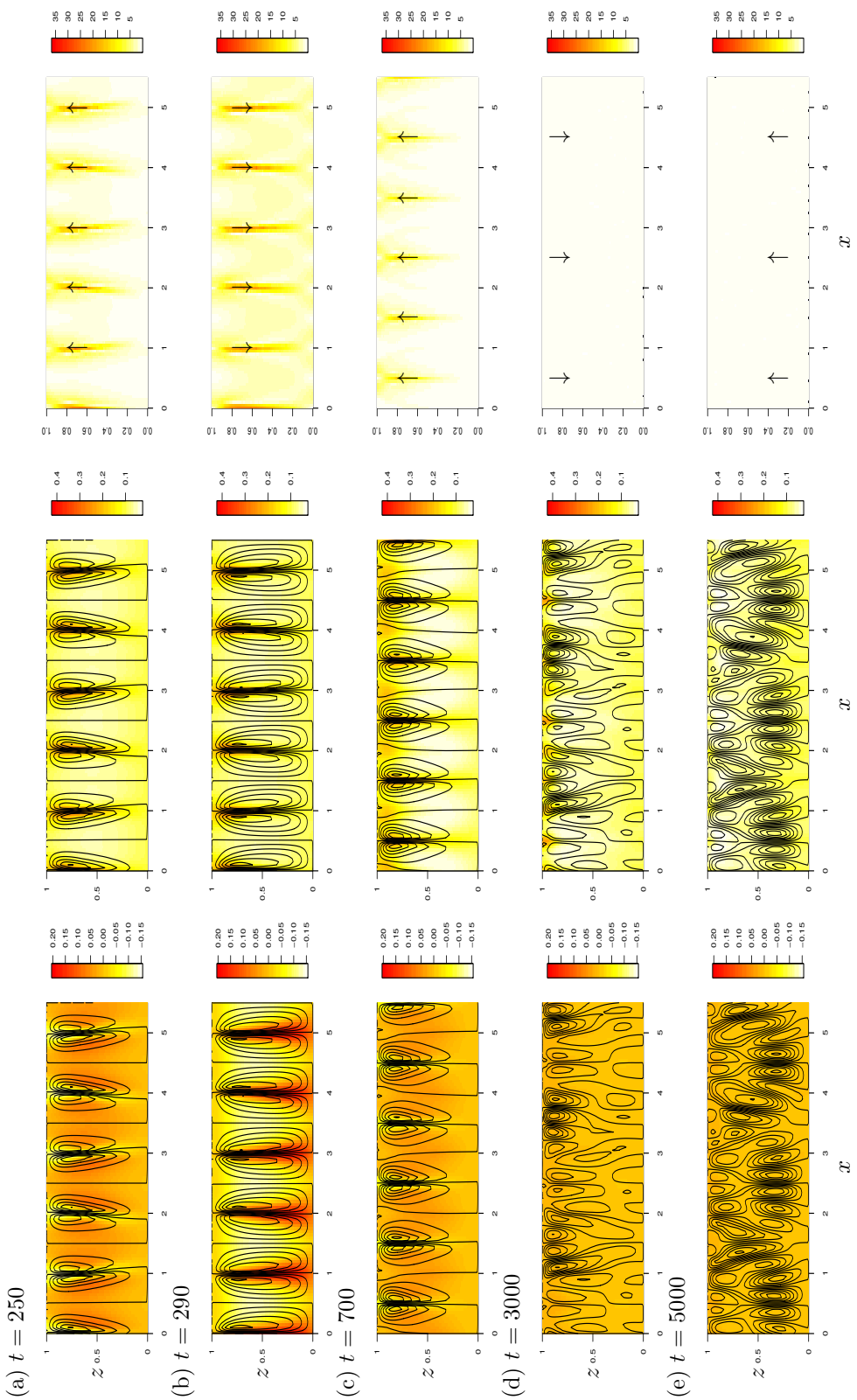

Figure 4.7: Evolution with $k_0 = 30$. Shading indicates solutal concentration perturbation C' (left), porosity ϕ (centre), and absolute velocity $|\mathbf{u}|$ (right). Solid lines are streamlines and arrows indicate the velocity field but are not drawn to scale.

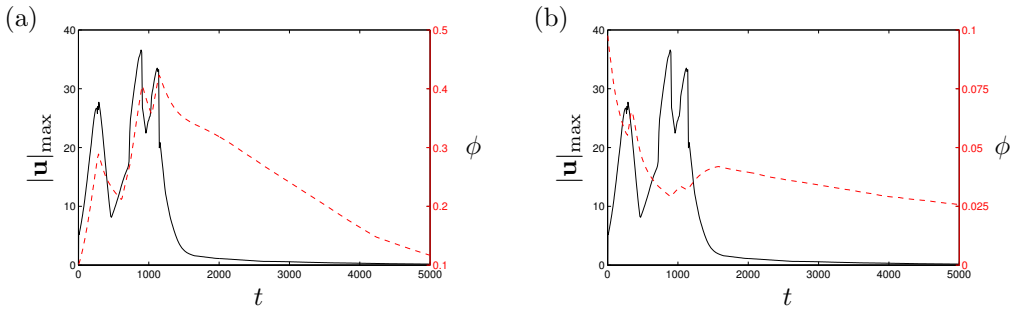

Figure 4.8: Maximum absolute velocity $|\mathbf{u}|$ and (a) maximum and (b) minimum porosity ϕ throughout the whole domain when $k_0 = 30$ and $\mathcal{R}_C = 1.1\mathcal{R}_{C,0}^{\text{crit}}$. Here the solid line represents the maximum velocity and the dashed line represents the porosity.

Chapter 5

Thermosolutal convection: linear stability analysis

In this chapter and the next we build upon the work of chapter 3, and consider reactive double-diffusive convection in an evolving porous layer, bounded above and below by impermeable layers held at constant concentration and temperature. This model is an extension of the fixed porosity model of Pritchard and Richardson (2007). Following Pritchard and Richardson (2007), we will neglect the thermal contribution of the reaction, and focus on the effect on convection of the solute exchange between the fluid and the porous matrix as the temperature varies.

In §5.1 we recapitulate our model of flow and transport in a porous medium with evolving porosity. We then, in §5.2, carry out a linear stability analysis of the onset of convection, paying particular attention to the permeability feedback effects which enter on a timescale generally slower than that of the flow.

In chapter 6 we will investigate the longer-term behaviour numerically.

5.1 Model Description

We consider an initially homogeneous and isotropic porous layer of depth $\hat{h}$ with solutal mass concentrations $\hat{C}_0$ and $\hat{C}_1$ and temperatures $\hat{T}_0$ and $\hat{T}_1$ imposed at the bottom and top, respectively. The bottom and top layers are presumed to be impermeable, and we impose chemical equilibrium at the boundaries.

We take $\hat{x}$ and $\hat{z}$ as the horizontal and vertical coordinates, respectively, with $\hat{z}$ increasing upwards. The appropriate governing equations, which were discussed in detail in chapter 2, are

$$\hat{\nabla}\cdot\hat{\mathbf{u}} = 0, \tag{5.1}$$

$$\hat{\mathbf{u}} = -\frac{\hat{K}}{\hat{\mu}}\left(\frac{\phi}{\phi_0}\right)^2\hat{\nabla}\hat{p} - \frac{\hat{K}}{\hat{\mu}}\left(\frac{\phi}{\phi_0}\right)^2\hat{\rho}_f\hat{g}\mathbf{e}_z, \tag{5.2}$$

$$(\hat{\rho}\hat{c})_m\frac{\partial\hat{T}}{\partial\hat{t}} + (\hat{\rho}\hat{c})_f(\hat{\mathbf{u}}\cdot\hat{\nabla})\hat{T} = (\hat{\rho}\hat{c})_m\hat{\kappa}_T\hat{\nabla}^2\hat{T}, \tag{5.3}$$

$$\frac{\partial(\phi\hat{C})}{\partial\hat{t}} + \hat{\nabla}\cdot(\hat{\mathbf{u}}\hat{C}) = \hat{\nabla}\cdot(\phi\hat{\kappa}_C\hat{\nabla}\hat{C}) + \hat{k}_0\frac{\phi(1-\phi)}{\phi_0(1-\phi_0)}(\hat{C}_{eq}(\hat{T}) - \hat{C}), \tag{5.4}$$

$$\frac{\partial\phi}{\partial\hat{t}} = \frac{\hat{k}_0}{\hat{\rho}_s}\frac{\phi(1-\phi)}{\phi_0(1-\phi_0)}(\hat{C}_{eq}(\hat{T}) - \hat{C}), \tag{5.5}$$

$$\hat{\rho}_f(\hat{C},\hat{T}) = \hat{\rho}_0[1 + \hat{\beta}_C(\hat{C}-\hat{C}_0) + \hat{\beta}_T(\hat{T}-\hat{T}_0)]. \tag{5.6}$$

Here $\hat{K}_0$ is the initial permeability, $\hat{\mu}$ is the fluid viscosity, $\hat{\rho}_f$ is the fluid density, and $\hat{\mathbf{u}}$ is the two-dimensional fluid velocity; $\hat{T}$ represents the temperature and we assume local thermal equilibrium between the fluid and the rock matrix; $\hat{C}$ is the mass concentration of solute in the fluid, and $\hat{C}_{eq}(\hat{T})$ is the equilibrium concentration of solute at a given temperature; $\hat{\kappa}_T$ is the effective diffusivity of heat through the saturated medium, and $\hat{\kappa}_C$ is the molecular diffusivity of the solute through the fluid. The volumetric heat capacity of the fluid is given by $(\hat{\rho}\hat{c})_f$ and that of the saturated medium is given by $(\hat{\rho}\hat{c})_m = \phi(\hat{\rho}\hat{c})_f + (1-\phi)(\hat{\rho}\hat{c})_s$, where the subscript s denotes properties of the solid rock matrix. As before, a caret $\hat{}$ denotes a dimensional variable, while dimensionless variables are unadorned.

Following Jupp and Woods (2003) and Pritchard and Richardson (2007), we take

the equilibrium concentration to vary linearly in $\hat{T}$. We write

$$\hat{C}_{eq}(\hat{T}) = \hat{C}_0 + \hat{\gamma}(\hat{T} - \hat{T}_0) \tag{5.7}$$

and assuming chemical equilibrium on the boundaries gives

$$\hat{\gamma} = \frac{\hat{C}_1 - \hat{C}_0}{\hat{T}_1 - \hat{T}_0}. \tag{5.8}$$

The coefficient $\hat{\gamma}$ may be positive or negative; if $\hat{\gamma} > 0$ then the solubility increases with temperature (as with a prograde mineral, such as silica), while if $\hat{\gamma} < 0$ then the solubility decreases with temperature (as with a retrograde mineral, such as anhydrite, see Jupp and Woods (2003) and references therein). In the majority of solutions the solubility increases with temperature; however, natural gypsum is a notable exception with the solubility decreasing from 2.4×10^{-5} kg m^{-3} at 293 K to 2.2×10^{-6} kg m^{-3} at 353 K (Phillips 2009, §2.9). It therefore follows that, with a prograde mineral, the gradients of concentration and temperature must be the same sign, and so they contribute in opposing senses to the stability; with a retrograde mineral, the gradients of concentration and temperature must be of opposite sign and so be either both stabilising or destabilising. As a result of our assumption of chemical equilibrium at the boundaries, we cannot choose the stability properties independently of the pro- or retrograde nature of the mineral.

We seek an initial steady state solution where $\hat{\mathbf{u}} = \mathbf{0}$ and there is no lateral variation. We then find a linear distribution of temperature and thus of solute concentration,

$$\hat{T}_b(\hat{z}) = \hat{T}_0 + (\hat{T}_1 - \hat{T}_0)\frac{\hat{z}}{\hat{h}}, \quad \hat{C}_b(\hat{z}) = \hat{C}_0 + (\hat{C}_1 - \hat{C}_0)\frac{\hat{z}}{\hat{h}}. \tag{5.9}$$

The initial distribution of solute corresponds to $\hat{C}_b = \hat{C}_{eq}(\hat{T}_b)$.

5.1.1 Streamfunction formulation and non-dimensionalisation

Equation (5.4) may be simplified using (5.1) to obtain

$$\phi\frac{\partial\hat{C}}{\partial\hat{t}} + (\hat{\mathbf{u}}\cdot\hat{\nabla})\hat{C} = \hat{\kappa}_C\hat{\nabla}\cdot(\phi\hat{\nabla}\hat{C}) + \hat{k}(\phi)(\hat{C}_{\rm eq}(\hat{T}) - \hat{C}). \tag{5.10}$$

We write $\hat{\mathbf{u}}(\hat{x},\hat{z},\hat{t})$ in terms of a streamfunction $\hat{\psi}(\hat{x},\hat{z},\hat{t})$ so that $u' = -\partial\psi'/\partial z$ and $w' = \partial\psi'/\partial x$. We then define dimensionless variables as

$$\begin{gathered}\hat{\mathbf{x}} = \hat{h}\mathbf{x}, \quad \hat{\psi} = \phi_0\hat{\kappa}_T\psi, \quad \hat{t} = \frac{\hat{h}^2}{\hat{\kappa}_T}t, \\ \hat{C} = \hat{C}_b(\hat{z}) + (\hat{C}_1 - \hat{C}_0)C', \quad \hat{T} = \hat{T}_b(\hat{z}) + (\hat{T}_1 - \hat{T}_0)T',\end{gathered} \tag{5.11}$$

where T' and C' are perturbations to the base state temperature and concentration fields, respectively. We can then eliminate $\hat{p}$ to obtain the dimensionless governing equations

$$\nabla\cdot\left[\left(\frac{\phi}{\phi_0}\right)^{-2}\nabla\psi\right] = -\mathcal{R}_C\frac{\partial C'}{\partial x} - \mathcal{R}_T\frac{\partial T'}{\partial x}, \tag{5.12}$$

$$\frac{\partial T'}{\partial t} - \lambda\left[\frac{\partial\psi}{\partial z}\frac{\partial T'}{\partial x} - \frac{\partial\psi}{\partial x}\left(1 + \frac{\partial T'}{\partial z}\right)\right] = \nabla^2 T', \tag{5.13}$$

$$\begin{gathered}\phi\frac{\partial C'}{\partial t} - \phi_0\left[\frac{\partial\psi}{\partial z}\frac{\partial C'}{\partial x} - \frac{\partial\psi}{\partial x}\left(1 + \frac{\partial C'}{\partial z}\right)\right] = \\ \frac{1}{Le}\left[\phi\,\nabla^2 C' + \frac{\partial\phi}{\partial x}\frac{\partial C'}{\partial x} + \frac{\partial\phi}{\partial z}\left(1 + \frac{\partial C'}{\partial z}\right)\right] + k_0\frac{\phi(1-\phi)}{1-\phi_0}(T' - C'),\end{gathered} \tag{5.14}$$

$$\frac{\partial\phi}{\partial t} = \delta k_0\frac{\phi(1-\phi)}{1-\phi_0}(T' - C'), \tag{5.15}$$

subject to the boundary conditions

$$\frac{\partial\psi}{\partial x} = 0, \quad T' = 0, \quad \text{and} \quad C' = 0 \quad \text{at} \quad z = 0 \quad \text{and at} \quad z = 1. \tag{5.16}$$

The dimensionless parameters k_0, δ, λ, Le, $\mathcal{R}_T$ and $\mathcal{R}_C$ are defined as

$$\begin{gathered} k_0 = \frac{\hat{h}^2\hat{k}_0}{\phi_0\hat{\kappa}_T}, \qquad \delta = \frac{(\hat{C}_1 - \hat{C}_0)}{\hat{\rho}_s}, \qquad \lambda = \frac{\phi_0(\hat{\rho}\hat{c})_f}{(\hat{\rho}\hat{c})_m}, \qquad Le = \frac{\hat{\kappa}_T}{\hat{\kappa}_C}, \\ \mathcal{R}_T = \frac{\hat{K}_0\hat{\rho}_0\hat{g}\hat{h}\hat{\beta}_T(\hat{T}_1 - \hat{T}_0)}{\phi_0\hat{\mu}\hat{\kappa}_T}, \qquad \mathcal{R}_C = \frac{\hat{K}_0\hat{\rho}_0\hat{g}\hat{h}\hat{\beta}_C(\hat{C}_1 - \hat{C}_0)}{\phi_0\hat{\mu}\hat{\kappa}_T}. \end{gathered} \tag{5.17}$$

The parameters $\mathcal{R}_T$ and $\mathcal{R}_C$ can be either positive or negative, with positive values encouraging instability. We can define

$$\begin{aligned} \mathcal{R}_C^{\text{solute}} &= \frac{\hat{K}_0\hat{\rho}_0\hat{g}\hat{h}\hat{\beta}_C(\hat{C}_1 - \hat{C}_0)}{\hat{\mu}\hat{\kappa}_C} = \phi_0 Le\mathcal{R}_C, \\ \mathcal{R}_T^{\text{temp}} &= \frac{\hat{K}_0\hat{\rho}_0\hat{g}\hat{h}\hat{\beta}_T(\hat{\rho}\hat{c})_f(\hat{T}_1 - \hat{T}_0)}{\hat{\mu}(\hat{\rho}\hat{c})_m\hat{\kappa}_T} = \lambda\mathcal{R}_T, \end{aligned} \tag{5.18}$$

where $\mathcal{R}_C^{\text{solute}}$ and $\mathcal{R}_T^{\text{temp}}$ are the Rayleigh numbers which emerge naturally from the pure solutal and pure thermal problems, respectively. The Lewis number Le is known to be greater than unity (§2.6.5), and the dimensionless reaction rate (Damköhler number) $k_0 > 0$: recall that estimates for geochemical reaction rates may vary by many orders of magnitude (§2.6.7). The differential heat transport rate λ clearly satisfies $0 < \lambda \leq 1$, and for the purposes of this study we will take it to be constant. Finally, δ is a matrix evolution rate, the magnitude of which may be assumed to be much less than unity since mass concentrations of solute are typically much smaller than the density of the solid mineral (Phillips 2009, §2.8). In contrast to chapter 3, this parameter is not necessarily positive since we may take $\hat{C}_1 \lessgtr \hat{C}_0$.

5.2 Linear stability analysis: general problem

By defining the porosity perturbation as $\phi' = \phi - \phi_0$ and assumming that the magnitudes of perturbations to the base state are small, we may simplify (5.12)–(5.15) to obtain

$$\nabla^2\psi = -\mathcal{R}_T\frac{\partial T'}{\partial x} - \mathcal{R}_C\frac{\partial C'}{\partial x}, \tag{5.19}$$

$$\frac{\partial T'}{\partial t} + \lambda \frac{\partial \psi}{\partial x} = \nabla^2 T', \tag{5.20}$$

$$\frac{\partial C'}{\partial t} + \frac{\partial \psi}{\partial x} = \frac{1}{Le}\left[\nabla^2 C' + \frac{1}{\phi_0}\frac{\partial \phi'}{\partial z}\right] + k_0(T' - C'), \tag{5.21}$$

$$\frac{\partial \phi'}{\partial t} = \delta k_0 \phi_0 (T' - C'), \tag{5.22}$$

subject to the boundary conditions

$$\frac{\partial \psi}{\partial x} = 0, \quad T' = 0, \quad \text{and} \quad C' = 0 \quad \text{at} \quad z = 0 \quad \text{and at} \quad z = 1. \tag{5.23}$$

We seek Fourier-mode solutions of the form

$$\begin{aligned} \psi &= \Psi(z) e^{imx} e^{\sigma t}, \quad T' = \Theta(z) e^{imx} e^{\sigma t}, \\ C' &= \chi(z) e^{imx} e^{\sigma t}, \quad \phi' = \Phi(z) e^{imx} e^{\sigma t}, \end{aligned} \tag{5.24}$$

where the real parts are assumed, the wave number m is a positive real number, and Ψ, Θ, χ, Φ and σ are generally complex. Substituting these into equations (5.19)–(5.22) we obtain

$$\left(\frac{\mathrm{d}^2}{\mathrm{d}z^2} - m^2\right)\Psi(z) = -im\left(\mathcal{R}_T \Theta(z) + \mathcal{R}_C \chi(z)\right), \tag{5.25}$$

$$\left(\frac{\mathrm{d}^2}{\mathrm{d}z^2} - m^2 - \sigma\right)\Theta(z) = im\lambda\Psi(z), \tag{5.26}$$

$$\left(\frac{1}{Le}\left(\frac{\mathrm{d}^2}{\mathrm{d}z^2} - m^2\right) - k_0 - \sigma\right)\chi(z) = im\Psi(z) - \frac{1}{Le\phi_0}\frac{\mathrm{d}}{\mathrm{d}z}\Phi(z) - k_0\Theta(z), \tag{5.27}$$

$$\sigma\Phi(z) = \delta k_0 \phi_0 \left(\Theta(z) - \chi(z)\right). \tag{5.28}$$

Equations (5.25)–(5.28) can be combined and simplified to give

$$\begin{aligned}\left[\frac{1}{Le}\left(\frac{\mathrm{d}^2}{\mathrm{d}z^2}-\frac{\delta k_0}{\sigma}\frac{\mathrm{d}}{\mathrm{d}z}-m^2\right)-k_0-\sigma\right]\times\\ \left[\left(\frac{\mathrm{d}^2}{\mathrm{d}z^2}-m^2-\sigma\right)\left(\frac{\mathrm{d}^2}{\mathrm{d}z^2}-m^2\right)-\lambda m^2\mathcal{R}_T\right]\Theta(z)\\ =\lambda m^2\mathcal{R}_C\left[\frac{1}{\lambda}\left(\frac{\mathrm{d}^2}{\mathrm{d}z^2}-m^2-\sigma\right)-\frac{1}{Le}\frac{\delta k_0}{\sigma}\frac{\mathrm{d}}{\mathrm{d}z}-k_0\right]\Theta(z),\end{aligned} \tag{5.29}$$

while $\Theta(z)$ must satisfy the boundary conditions

$$\begin{aligned}\Theta(z)=0,\quad \left(\frac{\mathrm{d}^2}{\mathrm{d}z^2}-m^2-\sigma\right)\Theta(z)=0,\\ \text{and}\quad \left(\frac{\mathrm{d}^2}{\mathrm{d}z^2}-m^2-\sigma\right)\left(\frac{\mathrm{d}^2}{\mathrm{d}z^2}-m^2\right)\Theta(z)=0,\end{aligned} \tag{5.30}$$

at $z=0$ and $z=1$.

Again adapting the approach of Chandrasekhar (1961, §15) for Rayleigh–Bénard convection, as in §3.2, we seek solutions to (5.29) in the form $\Theta(z)\propto\exp(qz)$, where q is a root of the auxiliary equation

$$\begin{aligned}\frac{1}{\lambda m^2\mathcal{R}_C}\left[\frac{1}{Le}\left(q^2-\frac{\delta k_0}{\sigma}q-m^2\right)-k_0-\sigma\right]\left[\left(q^2-m^2-\sigma\right)\left(q^2-m^2\right)-\lambda m^2\mathcal{R}_T\right]\\ =\left[\frac{1}{\lambda}\left(q^2-m^2-\sigma\right)-\frac{1}{Le}\frac{\delta k_0}{\sigma}q-k_0\right].\end{aligned} \tag{5.31}$$

In general we may write

$$\Theta(z)=A_1e^{q_1z}+A_2e^{q_2z}+A_3e^{q_3z}+A_4e^{q_4z}+A_5e^{q_5z}+A_6e^{q_6z}, \tag{5.32}$$

and the boundary conditions (5.30) may be written as

$$\mathrm{B}\cdot[A_1,A_2,A_3,A_4,A_5,A_6]^T=\mathbf{0}, \tag{5.33}$$

where the elements of the matrix B are given by

$$\begin{aligned} b_{1j} = 1, \quad b_{2j} = e^{q_j}, \quad b_{3j} = (q_j^2 - m^2 - \sigma), \quad b_{4j} = (q_j^2 - m^2 - \sigma)e^{q_j}, \\ b_{5j} = (q_j^2 - m^2)(q_j^2 - m^2 - \sigma), \quad b_{6j} = (q_j^2 - m^2)(q_j^2 - m^2 - \sigma)e^{q_j}, \end{aligned} \tag{5.34}$$

for $j = 1 \ldots 6$. For nontrivial solutions we require that

$$\det(\mathrm{B}) = 0. \tag{5.35}$$

Using column operations the determinant can be simplified to

$$(e^{q_2} - e^{q_1})(e^{q_4} - e^{q_3})(e^{q_6} - e^{q_5})(e^{q_3} - e^{q_1})(e^{q_5} - e^{q_1}) \det(\mathrm{C}) = 0. \tag{5.36}$$

The details of the column operations and the form of the matrix C are given in Appendix A.3.

5.3 Linear stability analysis: special cases

Before considering the full linear stability problem, it is helpful to recover some results for the rather simpler case with $\delta = 0$ presented in Pritchard and Richardson (2007).

With $\delta = 0$ the terms in (5.31) that are linear in q disappear, and it becomes a cubic in q^2. Therefore, it has roots $q_1 = -q_2$, $q_3 = -q_4$, and $q_5 = -q_6$, and the determinant condition (5.35) becomes

$$\begin{aligned} &\sinh(q_1)\sinh(q_3)\sinh(q_5)\times \\ &\qquad \left[(q_1 - q_3)^2(q_1 + q_3)^2(q_1 - q_5)^2(q_1 + q_5)^2(q_3 - q_5)^2(q_3 + q_5)^2\right] = 0. \end{aligned} \tag{5.37}$$

Hence, for linearly independent roots we require either

$$q_1 = in\pi, \quad q_3 = in\pi, \quad \text{or} \quad q_5 = in\pi \quad \text{where} \quad n \in \mathbb{Z}. \tag{5.38}$$

Now, setting $q = in\pi$ in (5.31) results in the solvability condition

$$a\sigma_0^2 + b\sigma_0 + c = 0 \tag{5.39}$$

where we define $\sigma = \sigma_0$ as the growth rate for $\delta = 0$ and, defining $M = m^2$ for convenience,

$$\begin{aligned} a &= (M + n^2\pi^2), \\ b &= \left(1 + \frac{1}{Le}\right)(M + n^2\pi^2)^2 + k_0(M + n^2\pi^2) - M(\mathcal{R}_C + \lambda\mathcal{R}_T), \\ c &= \frac{1}{Le}(M + n^2\pi^2)^3 + k_0(M + n^2\pi^2)^2 - M(M + n^2\pi^2)\left(\mathcal{R}_C + \frac{\lambda\mathcal{R}_T}{Le}\right) \\ &\quad - k_0 M\lambda(\mathcal{R}_C + \mathcal{R}_T). \end{aligned} \tag{5.40}$$

This is identical to the solvability condition given by equations (3.7) and (3.8) of Pritchard and Richardson (2007). The stability boundaries of the system correspond to the condition $\mathrm{Re}(\sigma_{0+}) = 0$ where $\sigma = \sigma_{0\pm}$ are the two roots of (5.39).

5.3.1 No reaction: $k_0 = 0$

When there is no reaction ($k_0 = 0$) we recover classic double-diffusive convection (see e.g. Nield and Bejan 2006 §9, Phillips 1991 §5.3), and the growth rate σ_{0+} is determined by (5.39) and (5.40) with $k_0 = 0$. Instability will occur whenever $\mathrm{Re}(\sigma_{0+}) > 0$ with $n \in \mathbb{N}$, i.e. whenever (i) $b < 0$, or (ii) $b > 0$ and $c < 0$ (so that $\sqrt{b^2 - 4ac} > b$).

(i) If $b < 0$ then

$$\mathcal{R}_T > \left(1 + \frac{1}{Le}\right)\frac{(M + n^2\pi^2)^2}{M\lambda} - \frac{\mathcal{R}_C}{\lambda}. \tag{5.41}$$

The lowest value of $\mathcal{R}_T$ for which $b < 0$ occurs is when $n = 1$, $M = \pi^2$, so

$$\mathcal{R}_T > \mathcal{R}_T^b(\mathcal{R}_C) = \left(1 + \frac{1}{Le}\right)\frac{4\pi^2}{\lambda} - \frac{\mathcal{R}_C}{\lambda}. \tag{5.42}$$

When crossing this boundary $b^2 - 4ac < 0$, so the instability is oscillatory.

(ii) If $c < 0$, then

$$\mathcal{R}_T > \frac{(M + n^2\pi^2)^2}{M\lambda} - \frac{Le}{\lambda}\mathcal{R}_C. \tag{5.43}$$

The lowest value of $\mathcal{R}_T$ for which $c < 0$ occurs is when $n = 1$, $M = \pi^2$, so

$$\mathcal{R}_T > \mathcal{R}_T^c(\mathcal{R}_C) = \frac{4\pi^2}{\lambda} - \frac{Le}{\lambda}\mathcal{R}_C, \tag{5.44}$$

with the additional requirement that condition (5.42) is not satisfied, i.e. that $b > 0$. When crossing this boundary $\sigma_{0+} = 0$ (i.e. the principle of exchange of stabilities holds), so the loss of stability is through an exponentially growing perturbation.

Hence, instability will occur if either (5.42) or (5.44) is satisfied, and the system will be stable if neither is satisfied. An illustration of the stability boundaries is given in figure 5.1(a).

The intersection of $\mathcal{R}_T^c$ with the $\mathcal{R}_T-$axis occurs when $\mathcal{R}_T = 4\pi^2/\lambda < \mathcal{R}_T^b(0)$. Therefore, $\mathcal{R}_T^c$ determines the stability criterion $\mathcal{R}_T^{\text{temp}} < 4\pi^2$ for pure thermal convection (Nield and Bejan 2006 §6; Lapwood 1948). Similarly, the stability criterion for pure solutal convection is given by $\mathcal{R}_C^{\text{solute}} < 4\phi_0\pi^2$ (as in chapter 3). The lines $\mathcal{R}_T = \mathcal{R}_T^b$ and $\mathcal{R}_T = \mathcal{R}_T^c$ intersect at the critical value

$$\mathcal{R}_C^{\text{crit}} = -\frac{4\pi^2}{Le(Le-1)}. \tag{5.45}$$

When $\mathcal{R}_C < \mathcal{R}_C^{\text{crit}}$, the criterion $\mathcal{R}_T < \mathcal{R}_T^b$ gives stability, while when $\mathcal{R}_C > \mathcal{R}_C^{\text{crit}}$, the criterion $\mathcal{R}_T < \mathcal{R}_T^c$ gives stability.

5.3.2 Reactive case: $k_0 > 0$

We now consider the case of reactive double-diffusive convection with a non-evolving rock matrix. The results in §§5.3.2–5.3.2.2 are presented in detail in Pritchard and Richardson (2007), but it is useful for this study to recap some general features of the stability diagram in the $(\mathcal{R}_C, \mathcal{R}_T)$ plane.

We will determine two boundaries: (i) the boundary $\mathcal{R}_T = \mathcal{R}_{T,0}^b(\mathcal{R}_C)$ above which

there exist (M, n) such that $b < 0$, and (ii) the boundary $\mathcal{R}_T = \mathcal{R}^c_{T,0}(\mathcal{R}_C)$ above which there exist (M, n) such that $c < 0$. The unstable region is then the union of the regions $\mathcal{R}_T > \mathcal{R}^b_{T,0}$ and $\mathcal{R}_T > \mathcal{R}^c_{T,0}$. Furthermore, we will also determine the axis intercepts and examine how increasing the reaction rate k_0 affects the stability diagram.

(i) If $b < 0$ then

$$\mathcal{R}_T > f(M, n) = \frac{1}{\lambda}\left(\left(1 + \frac{1}{Le}\right)\frac{(M + n^2\pi^2)^2}{M} + k_0\frac{(M + n^2\pi^2)}{M} - \mathcal{R}_C\right). \quad (5.46)$$

Clearly $f(M, n)$ is least restrictive when n takes its minimum value, $n = 1$. Hence, $f(M, 1)$ will be least restrictive when we choose M such that $f(M, 1)$ is minimised over M. Now,

$$\frac{\partial f}{\partial M} = 0 \quad \Longrightarrow \quad M = M_b = \pi\left[\frac{k_0 Le + \pi^2(1 + Le)}{1 + Le}\right]^{1/2} \quad (5.47)$$

where M_b is the unique solution for real, positive M. Note that (5.47) corrects equation (3.15) of Pritchard and Richardson (2007). Therefore, the instability condition is given by

$$\mathcal{R}_T > \mathcal{R}^b_{T,0}(\mathcal{R}_C) = \frac{\pi^2}{\lambda}\left(1 + \frac{1}{Le}\right)\left(1 + \sqrt{1 + \frac{k_0 Le}{\pi^2(1 + Le)}}\right)^2 - \frac{\mathcal{R}_C}{\lambda}. \quad (5.48)$$

Note that both M_b and $\mathcal{R}^b_{T,0}(\mathcal{R}_C)$ are increasing functions of k_0, and so the effect of the reaction rate is to increase the threshold of instability and increase the wavenumber at the threshold of instability, resulting in narrower convection cells.

(ii) If $c < 0$ then

$$\mathcal{R}_T > \mathcal{R}^c_{T,0}(\mathcal{R}_C) = \min_{M,n} g(M, n), \quad (5.49)$$

where

$$g(M,n) = \frac{k_0 Le}{k_0 Le + M + n^2\pi^2} \times \left[\frac{(M+n^2\pi^2)^2}{M} - \mathcal{R}_C\left(1 + \frac{(M+n^2\pi^2)}{k_0\lambda}\right) + \frac{1}{Le}\frac{(M+n^2\pi^2)^3}{Mk_0\lambda}\right]. \quad (5.50)$$

We will write $\mathcal{R}^c_{T,0} = g(M,n)$ to indicate the boundary $c = 0$ for given values of (M,n), while $\mathcal{R}^c_{T,0}(\mathcal{R}_C)$ will represent the minimum over (M,n) of g, i.e. the stability boundary if M, n are not imposed.

The global minimum of $g(M,n)$ over M and n always occurs on the boundary $n = 1$ and corresponds to a local minimum over M (see appendix A.4, which corrects Pritchard and Richardson 2007). Denoting this minimum by $M = M_c$ and taking $n = 1$, the condition $\partial g/\partial M = 0$ leads to a quartic equation for M_c,

$$\frac{M_c^4}{Le^2} + \left(\frac{2k_0}{Le} + \frac{2\pi^2}{Le^2}\right)M_c^3 + \left(\frac{2k_0\pi^2 + k_0\lambda\mathcal{R}_C}{Le} - \mathcal{R}_C k_0 + k_0^2\right)M_c^2 + \left(-\frac{2k_0\pi^4}{Le} - \frac{2\pi^6}{Le^2}\right)M_c - k_0^2\pi^4 - \frac{2k_0\pi^6}{Le} - \frac{\pi^8}{Le^2} = 0, \quad (5.51)$$

and we have $\mathcal{R}^c_{T,0}(\mathcal{R}_C) = g(M_c, 1)$.

5.3.2.1 Axis intercepts

We first consider the intercepts when $\mathcal{R}_C = 0$. Here there is no solutal contribution to buoyancy, and so we have pure thermal convection. When $\mathcal{R}_C = 0$, the axis intercept of $\mathcal{R}^b_{T,0}$ is given by

$$\mathcal{R}^b_{T,0}(0) = \frac{\pi^2}{\lambda}\left(1 + \frac{1}{Le}\right)\left(1 + \sqrt{1 + \frac{k_0 Le}{\pi^2(1+Le)}}\right)^2. \quad (5.52)$$

For the axis intercept of $\mathcal{R}^c_{T,0}$ we first note that (5.51) has the unique positive solution $M_c = \pi^2$ for $\mathcal{R}_C = 0$. Therefore, the axis intercept is given by

$$\mathcal{R}^c_{T,0}(0) = g(\pi^2, 1) = \frac{4\pi^2}{\lambda} < \mathcal{R}^b_{T,0}(0), \quad (5.53)$$

and so $\mathcal{R}^c_{T,0}(0)$ will always lie below $\mathcal{R}^b_{T,0}(0)$. Hence, instability will occur when $\mathcal{R}_T > \mathcal{R}^c_{T,0}(0)$.

The other case to consider occurs when there is no direct thermal contribution to buoyancy, i.e. when $\mathcal{R}_T = 0$, but there is still a solutal contribution. As before, instability will occur if there exists some $M > 0$ such that either (i) $b < 0$, or (ii) $c < 0$ and $b > 0$.

(i) We already have the full solution (5.48) for the boundary $\mathcal{R}_T = \mathcal{R}^b_T$, therefore requiring $\mathcal{R}^b_{T,0} = 0$ gives the boundary

$$\mathcal{R}_C = \mathcal{R}^b_{C,0} = \pi^2 \left(1 + \frac{1}{Le}\right) \left(1 + \sqrt{1 + \frac{k_0 Le}{\pi^2(1 + Le)}}\right)^2 . \tag{5.54}$$

(ii) When $c < 0$, with $n = 1$ and general M,

$$\mathcal{R}^c_{C,0} = S(M) = \frac{k_0 Le(M + \pi^2)^2 + (M + \pi^2)^3}{LeM(k_0\lambda + M + \pi^2)}. \tag{5.55}$$

There is not a simple expression for the positive real root of $\mathrm{d}S/\mathrm{d}M = 0$, but we note that

$$\begin{aligned} S(M) &\leq \frac{k_0(M + \pi^2)}{M} + \frac{1}{Le}\frac{(M + \pi^2)^2}{M} \\ &< S_1(M) = \frac{k_0(M + \pi^2)}{M} + \left(1 + \frac{1}{Le}\right)\frac{(M + \pi^2)^2}{M}, \end{aligned} \tag{5.56}$$

where $S_1(M)$ is the value of $\mathcal{R}_C$ from (5.46) for which $b = 0$ when $\mathcal{R}_T = 0$ and $n = 1$. This means that $\min_M S(M) < \min_M S_1(M)$, so the curve $\mathcal{R}_T = \mathcal{R}^c_{T,0}$ always intercepts the $\mathcal{R}_C$ axis to the left of the curve $\mathcal{R}_T = \mathcal{R}^b_{T,0}$. This suggests, together with the result that $\mathcal{R}^c_{T,0}(0) < \mathcal{R}^b_{T,0}(0)$, that for $\mathcal{R}_C > 0$ the stability boundary for $k_0 > 0$ is given by the criterion $c = 0$ rather than by $b = 0$.

5.3.2.2 Critical reaction rate

We have seen that for pure double-diffusive convection when $\mathcal{R}_C < \mathcal{R}^{\mathrm{crit}}_C$, the stability boundary is given by $\mathcal{R}_T = \mathcal{R}^b_{T,0}$, while when $\mathcal{R}_C > \mathcal{R}^{\mathrm{crit}}_C$, the stability

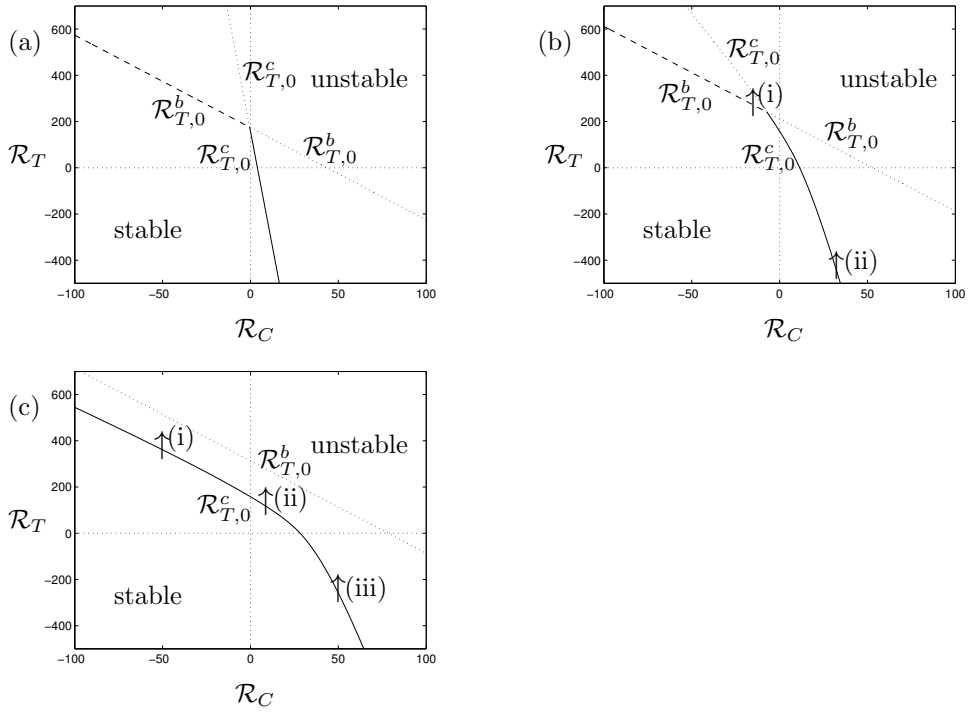

Figure 5.1: Linear stability boundaries for $\lambda = 0.25$, $Le = 10$, and (a) $k_0 = 0$, (b) $k_0 = 5$, (c) $k_0 = 20$. The solid lines represent stability boundaries on which $\sigma_{0+} = 0$, the dashed lines represent stability boundaries on which $\mathrm{Re}(\sigma_{0+}) = 0$ but $\mathrm{Im}(\sigma_{0+}) \neq 0$, and the dotted lines represent the continuation of $\mathcal{R}^b_{T,0}$ and $\mathcal{R}^c_{T,0}$ above the boundary. The numbered arrows on (b) and (c) represent the transects taken when examining the stability of the full problem (§5.4.1.1).

boundary is given by $\mathcal{R}_T = \mathcal{R}^c_{T,0}$ (§5.3.1) . By examining the limits $\mathcal{R}_C \to \pm\infty$ we can investigate how this changes as the reaction rate k_0 increases.

Following Pritchard and Richardson (2007), we see that as $\mathcal{R}_C \to \infty$, $\mathcal{R}^c_{T,0} < \mathcal{R}^b_{T,0}$, and so the curve $\mathcal{R}_T = \mathcal{R}^c_{T,0}$ always provides the stability boundary. In the other limit, $\mathcal{R}_C \to -\infty$, $\mathcal{R}^c_{T,0} < \mathcal{R}^b_{T,0}$ if and only if

$$k_0 > k_0^{\mathrm{crit}} = \frac{\pi^2}{1-\lambda}\left(1 - \frac{1}{Le}\right). \tag{5.57}$$

Therefore, the stability boundary is given by $\mathcal{R}_T = \mathcal{R}^b_{T,0}$ for sufficiently small k_0. As k_0 is increased, the curve $\mathcal{R}_T = \mathcal{R}^c_{T,0}$ drops below $\mathcal{R}_T = \mathcal{R}^b_{T,0}$ and so becomes

the stability boundary.

It is important to note that the condition $k_0 > k_0^{\text{crit}}$ does not itself guarantee that $\mathcal{R}_{T,0}^c$ lies below $\mathcal{R}_{T,0}^b$ for all $\mathcal{R}_C$. However, numerical investigation suggests that $\mathcal{R}_{T,0}^c < \mathcal{R}_{T,0}^b$ for all $\mathcal{R}_C$ once k_0 is even very slightly above this boundary. Therefore, we may take $k_0 \approx k_0^{\text{crit}}$ as marking the reaction rate above which $\mathcal{R}_{T,0}^b$ becomes irrelevant.

5.3.2.3 Description of stability boundaries

Figure 5.1 illustrates the evolution of the stability boundaries $\mathcal{R}_{T,0}^b$ and $\mathcal{R}_{T,0}^c$ in the $(\mathcal{R}_C, \mathcal{R}_T)$-plane as k_0 is increased from 0. When $k_0 = 0$ (figure 5.1(a)), the stability boundary is given by $\mathcal{R}_{T,0}^b$ in the solutally stable (SS) regime $\mathcal{R}_C < 0$ and by $\mathcal{R}_{T,0}^c$ in the solutally unstable (SU) regime $\mathcal{R}_C > 0$. In the SS regime the transition to instability is through a growing oscillatory mode as $\text{Im}(\sigma_{0+}) \neq 0$, whereas in the SU regime $\text{Im}(\sigma_{0+}) = 0$ and the transition to instability is by direct onset of steady-state convection with finite amplitude. Furthermore, in the SS regime as $\mathcal{R}_C$ decreases, $\mathcal{R}_{T,0}^b$ increases. Hence, a greater destabilising temperature gradient is required to overcome the stabilising concentration gradient and allow the system to become unstable.

Increasing the reaction rate to $k_0 = 5 < k_0^{\text{crit}}$ (figure 5.1(b)) decreases the size of the unstable region with $\mathcal{R}_{T,0}^b$ moving up everywhere, and $\mathcal{R}_{T,0}^c$ moving upwards and rightwards in the SU regime and downwards in the SS regime. Physically, in the SU regime the reaction tends to eliminate destabilising solutal perturbations and so stabilises the system, so a greater value of $\mathcal{R}_C$ is required to allow the system to become unstable.

As the reaction rate is increased further to $k_0 = 20 > k_0^{\text{crit}}$ (figure 5.1(c)) the $\mathcal{R}_{T,0}^c$ stability boundary moves even further rightwards in the SU regime, stabilising the system. The boundary $\mathcal{R}_{T,0}^c$ has now passed entirely below the boundary $\mathcal{R}_{T,0}^b$ and so the transition to instability is always by direct rather than oscillatory onset. In the SS regime, the $\mathcal{R}_T^c$ stability boundary has moved further downwards since a supercritical reaction rate destabilises the system by weakening the stabilising solutal perturbations. Hence, a lower value of $\mathcal{R}_T$ is required for instability in

this regime than when $k_0 = 0$.

5.4 Linear stability analysis: full problem

Now that we have recovered some stability results from the reduced problem with $\delta = 0$, we consider the stability of the full problem. When $\delta \neq 0$, an analytical solution of (5.36) in terms of σ is not available. Therefore, we follow the approach of chapters 3 and 4 for reactive solutal convection and investigate the stability problem numerically using a continuation method, tracking σ as $\mathcal{R}_T$ is changed, while keeping $\mathcal{R}_C$ and all other parameters fixed. A numerical solution to (5.37) for a large value of $\mathcal{R}_T$ was used as an initial guess.

The task of tracking each solution branch is numerically very laborious, largely because the analytical solutions for q_i are prohibitively complicated and so nested numerical solutions of (5.31) and (5.36) are required. As with the solutal convection problem (§3.2.2) we found that to track a single branch it was necessary to reduce $\mathcal{R}_T$ in steps no larger than 10^{-2}, with smaller steps required around the bifurcation points discussed below (§5.4.1). Additionally, to track the bifurcation point accurately we needed to further simplify the determinant (5.36). When $\delta \neq 0$,

$$(e^{q_2} - e^{q_1})(e^{q_4} - e^{q_3})(e^{q_6} - e^{q_5})(e^{q_3} - e^{q_1})(e^{q_5} - e^{q_1}) \neq 0. \tag{5.58}$$

Therefore, to track each solution branch, we are only required to solve $\det(\mathrm{C}) = 0$. Nevertheless, each set of plots within figures 5.2 and 5.3 each took around twelve hours to produce on a desktop computer. This effectively precluded the thorough investigation of the full problem defined by (5.36): instead, as before, we employed a less formal Galerkin approach in order to both search parameter space and provide insight into the solution structure.

5.4.1 Galerkin approach to the linear stability problem

We start with the system of equations (5.25)–(5.28), subject to the boundary conditions

$$\Psi = 0, \quad \Theta = 0 \quad \text{and} \quad \chi = 0 \quad \text{on} \quad z = 0 \quad \text{and} \quad z = 1, \tag{5.59}$$

and to the usual non-triviality condition that the solution is not identically zero. Rearranging (5.28) we see that

$$\Phi(z) = \frac{\delta k_0 \phi_0 (\Theta(z) - \chi(z))}{\sigma}, \tag{5.60}$$

and then we can eliminate $\Phi(z)$ from (5.27) to obtain the system

$$\left(\frac{\mathrm{d}^2}{\mathrm{d}z^2} - m^2\right)\Psi(z) = -im\left(\mathcal{R}_T\Theta(z) + \mathcal{R}_C\chi(z)\right), \tag{5.61}$$

$$\left(\frac{\mathrm{d}^2}{\mathrm{d}z^2} - m^2 - \sigma\right)\Theta(z) = im\lambda\Psi(z), \tag{5.62}$$

$$\left(\frac{1}{Le}\left(\frac{\mathrm{d}^2}{\mathrm{d}z^2} - m^2\right) - k_0 - \sigma\right)\chi(z) = im\Psi(z) - \frac{1}{Le}\frac{\delta k_0}{\sigma}\left(\frac{\mathrm{d}}{\mathrm{d}z}\Theta(z) - \frac{\mathrm{d}}{\mathrm{d}z}\chi(z)\right) - k_0\Theta(z), \tag{5.63}$$

subject to the same boundary conditions.

We seek approximate solutions of the form

$$\Psi(z) = \sin(\pi z) + \Psi_2 \sin(2\pi z), \tag{5.64}$$

$$\Theta(z) = \Theta_1 \sin(\pi z) + \Theta_2 \sin(2\pi z), \tag{5.65}$$

$$\chi(z) = \chi_1 \sin(\pi z) + \chi_2 \sin(2\pi z). \tag{5.66}$$

Note that the boundary conditions are automatically satisfied and that the non-triviality condition has been imposed by normalising the $\sin(\pi z)$ component of $\psi(z)$. We know that in the limit $\delta = 0$ this approximation will become exact with

$\Psi_2 = \Theta_2 = \chi_2 = 0.$

With six unknowns we can choose to satisfy six integral conditions. The natural ones are obtained by extracting the first and second Fourier sine components of (5.61)–(5.63):

$$\int_0^1 \sin(\pi n z)\left[\frac{\mathrm{d}^2\Psi}{\mathrm{d}z^2} - m^2\Psi\right]\mathrm{d}z = \int_0^1 \sin(\pi n z)\left[-im\mathcal{R}_T\Theta - im\mathcal{R}_C\chi\right]\mathrm{d}z, \quad (5.67)$$

$$\int_0^1 \sin(\pi n z)\left[\frac{\mathrm{d}^2\Theta}{\mathrm{d}z^2} - m^2\Theta - \sigma\Theta\right]\mathrm{d}z = \int_0^1 \sin(\pi n z)[im\lambda\Psi]\mathrm{d}z, \quad (5.68)$$

$$\begin{aligned}\int_0^1 \sin(\pi n z)\left[\frac{1}{Le}\left(\frac{\mathrm{d}^2\chi}{\mathrm{d}z^2} - m^2\chi\right) - (k_0+\sigma)\chi\right]\mathrm{d}z = \\ \int_0^1 \sin(\pi n z)\left[im\Psi - \frac{1}{Le}\frac{\delta k_0}{\sigma}\left(\frac{\mathrm{d}\Theta}{\mathrm{d}z} - \frac{\mathrm{d}\chi}{\mathrm{d}z}\right) - k_0\Theta\right]\mathrm{d}z,\end{aligned} \quad (5.69)$$

for $n = 1$ and for $n = 2$. This yields a system of six algebraic equations,

$$-\frac{1}{2}\left(\pi^2 + m^2\right) = -\frac{im}{2}\left(\mathcal{R}_T\Theta_1 + \mathcal{R}_C\chi_1\right), \quad (5.70)$$

$$-\frac{1}{2}\left(4\pi^2 + m^2\right)\Psi_2 = -\frac{im}{2}\left(\mathcal{R}_T\Theta_2 + \mathcal{R}_C\chi_2\right), \quad (5.71)$$

$$-\frac{1}{2}\left(\pi^2 + m^2 + \sigma\right)\Theta_1 = \frac{1}{2}im\lambda, \quad (5.72)$$

$$-\frac{1}{2}\left(4\pi^2 + m^2 + \sigma\right)\Theta_2 = \frac{1}{2}im\lambda\Psi_2, \quad (5.73)$$

$$-\frac{1}{2}\frac{1}{Le}\left(\pi^2 + m^2 + Le(k_0+\sigma)\right)\chi_1 = \frac{1}{2}(im - k_0\Theta_1) + \frac{4}{3}\frac{1}{Le}\frac{\delta k_0}{\sigma}(\Theta_2 - \chi_2), \quad (5.74)$$

$$-\frac{1}{2}\frac{1}{Le}\left(4\pi^2 + m^2 + Le(k_0+\sigma)\right)\chi_2 = \frac{1}{2}(im\Psi_2 - k_0\Theta_2) + \frac{4}{3}\frac{1}{Le}\frac{\delta k_0}{\sigma}(\chi_1 - \Theta_1). \quad (5.75)$$

We can then eliminate Ψ_2, Θ_1, Θ_2, χ_1, and χ_2 and find that σ satisfies the sextic

$$a_6\sigma^6 + a_5\sigma^5 + a_4\sigma^4 + a_3\sigma^3 + a_2\sigma^2 + a_1\sigma + a_0 = 0, \quad (5.76)$$

where the coefficients a_i are omitted here for brevity. These may readily be

obtained by using the commands

```
sigeq:=subs(solve(eqset,psi2,Theta1,Theta2,chi1,chi2,sigma),sigma):
                    a_i:=coeff(lhs(sigeq),sigma,i);
```

in Maple for $0 \leq$ `i` ≤ 6. Here `eqset` refers to the algebraic system (5.70)–(5.75).

It is straightforward to locate all the complex roots of (5.76) numerically, for example using the `fsolve` command in Maple, and thus to track all the solutions through parameter space.

5.4.1.1 Behaviour of roots σ

To examine the behaviour of σ it is helpful to express the thermal Rayleigh number in terms of the critical conditions for $\delta = 0$. We define $\mathcal{R}_T = \mathcal{R}^b_{T,0}(\mathcal{R}_C, m) + \Delta^b$, where $\mathcal{R}^b_{T,0}(\mathcal{R}_C, m)$ is given by (5.46) with $n = 1$ and $M = m^2$, and $\mathcal{R}_T = \mathcal{R}^c_{T,0}(\mathcal{R}_C, m) + \Delta^c$ where $\mathcal{R}^c_{T,0}(\mathcal{R}_C, m)$ is given by (5.50) with $n = 1$ and $M = m^2$. In this and future sections we will focus on two reaction rates: a subcritical reaction rate $k_0 = 5$ and a supercritical reaction rate $k_0 = 20$. When $k_0 = 5$ the stability boundary is given by $\mathcal{R}^b_{T,0}$ for $\mathcal{R}_C \lesssim -10$ and by $\mathcal{R}^c_{T,0}$ for $\mathcal{R}_C \gtrsim -10$ (figure 5.1(b)). When $k_0 = 20$, the stability boundary is given solely by $\mathcal{R}^c_{T,0}$ (figure 5.1(c)).

Figures 5.2 and 5.3 show the behaviour of σ as $\mathcal{R}_C$ is increased for $k_0 = 5$ and $k_0 = 20$, respectively, where the wavenumber m and all other parameters except Δ^c are fixed. For this, and all subsequent figures in this section, the default parameters were $\phi_0 = 0.1$, $Le = 10$, $\lambda = 0.25$, and $\delta = 0.1$ for $\mathcal{R}_C > 0$, $\delta = -0.1$ for $\mathcal{R}_C < 0$. We note that the value of the Lewis number used is smaller than the predicted value $Le \approx 1000$ given in §2.6.5, however, the value $Le = 10$ is still bigger than unity and allows for the faster diffusion of heat than solute. The large value of $|\delta|$ was chosen to make deviations from the $\delta = 0$ case as apparent as possible.

For $k_0 = 5$ we consider two different values of $\mathcal{R}_C$ (indicated by the numbered arrows on figure 5.1(b)) in order to cross both stability boundaries:

(i) when $\mathcal{R}_C = -15$, $\mathcal{R}^c_{T,0} > 0$ and we have a stabilising solutal gradient and a destabilising temperature gradient;
(ii) when $\mathcal{R}_C = 30$, $\mathcal{R}^c_{T,0} < 0$ and we have a destabilising solutal gradient and a stabilising temperature gradient.

We first consider $\mathcal{R}_C = -15$ (figure 5.2(a, b)). When $\delta = 0$ the stability boundary is given by $\mathcal{R}_T = \mathcal{R}^b_{T,0}$ (figure 5.1(b)) and the transition to instability is through a growing oscillatory mode where $\mathrm{Im}(\sigma) \neq 0$. When Δ^b is large and positive the dominant σ branch very closely follows that of σ_{0+}. However, below $\Delta^b \approx 0.3$, the dominant branch switches to one which appears to asymptote to zero as $\Delta^b \to -\infty$, with $\mathrm{Im}(\sigma) = 0$.

When $\mathcal{R}_C = 30$ (figure 5.2(c, d)) the branch of σ with the largest real part closely tracks the σ_{0+} branch when Δ^c is large and positive. It deviates weakly from this as Δ^c is reduced, until this branch and the one below merge. This occurs at $\Delta^c \approx 11.8$, and at this bifurcation point the values of σ become complex. As Δ^c is further reduced, $\mathrm{Re}(\sigma)$ continues to fall and asymptotes to zero as $\Delta^c \to -\infty$. The behaviour of the stability branches is very similar to that seen in reactive solutal convection (cf. figure 3.3).

For $k_0 = 20$ we consider three different values of $\mathcal{R}_C$, as indicated by the numbered arrows on figure 5.1(c), in order to cover the three regimes of interest in double-diffusive convection:
(i) when $\mathcal{R}_C = -50$, $\mathcal{R}^c_{T,0} > 0$ and we have a stabilising solutal gradient and a destabilising temperature gradient;
(ii) when $\mathcal{R}_C = 10$, $\mathcal{R}^c_{T,0} > 0$ and we have destabilising solutal and temperature gradients;
(iii) when $\mathcal{R}_C = 50$, $\mathcal{R}^c_{T,0} < 0$ and we have a destabilising solutal gradient and a stabilising temperature gradient.

We first consider $\mathcal{R}_C = -50$ (figure 5.3(a, b)). When Δ^c is large and positive, the branch of σ with the largest real part closely tracks the σ_{0+} branch. As Δ^c is reduced σ deviates from the σ_{0+} branch and asymptotes to zero from above as $\Delta^c \to -\infty$. Along this branch $\mathrm{Im}(\sigma) = 0$. The sub-dominant σ branch also displays some interesting behaviour. As $\Delta^c \to \infty$, $\mathrm{Re}(\sigma)$ tends to zero from below, with $\mathrm{Im}(\sigma) \neq 0$. As Δ^c is reduced $\mathrm{Re}(\sigma)$ decreases until $\Delta^c \approx -2.9$ where

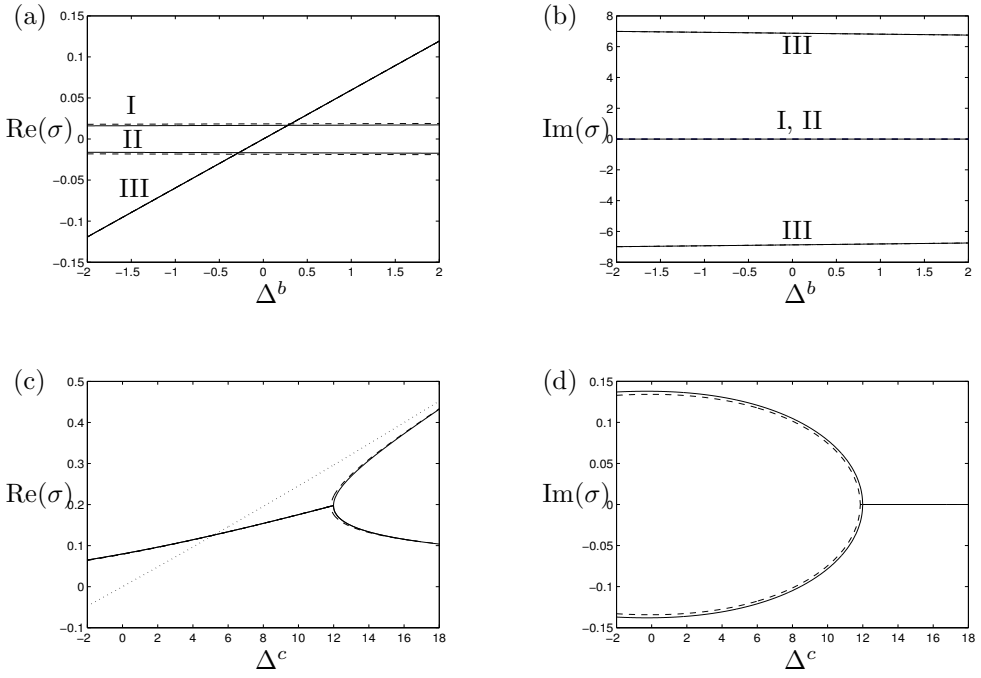

Figure 5.2: Behaviour of σ for $k_0 = 5$, $\phi_0 = 0.1$, $Le = 10$, $\lambda = 0.25$, $m = 3$, and (a, b) $\mathcal{R}_C = -15$, $\delta = -0.1$ close to $\Delta^b = 0$, (c, d) $\mathcal{R}_C = 30$, $\delta = 0.1$ close to $\Delta^c = 0$. The left-hand column shows $\mathrm{Re}(\sigma)$, while the right-hand column shows $\mathrm{Im}(\sigma)$. Solid lines are full numerical solutions to the linear problem; dashed lines are Galerkin solutions; dotted lines in the left-hand column show the results for $\delta = 0$. Roman numerals on (a, b) are to aid in identifying the corresponding real and imaginary parts of each σ branch.

this branch bifurcates with the upper branch tending to zero from below, and the lower branch tending to σ_{0+} as $\Delta^c \to -\infty$. At the bifurcation point the values of σ become strictly real.

We next consider $\mathcal{R}_C = 10$ (figure 5.3(c, d)) and $\mathcal{R}_C = 50$ (figure 5.3(e, f)). In both these cases we have a destabilising solutal gradient and the behaviour of the σ branches is very similar to that seen with $k_0 = 5$ (figure 5.2(e, f)), as well as to that seen in reactive solutal convection (figure 3.3). In each case the position of the bifurcation point changes. When $\mathcal{R}_C = 10$ (figure 5.3(c, d)) the bifurcation occurs at $\Delta^c \approx 2.2$, and when $\mathcal{R}_C = 50$ (figure 5.3(e, f)), it occurs at $\Delta^c \approx 4.3$.

It can be shown that the bifurcation point scales as $\Delta^c \sim |\delta|^{2/3}$ and $\sigma \sim |\delta|^{2/3}$ (see §5.4.2.1).

Figures 5.2 and 5.3 also compare the predictions of the Galerkin analysis with those from the full numerical solution of (5.36). In each case, good agreement can be seen, with errors in the imaginary part of the order of 10% or smaller. Note that full solutions for the subdominant branches were obtained by using the Galerkin solution as an initial guess.

It is clear that there are three different scenarios of interest, which depend on the signs of the underlying thermal and solutal gradients. The first scenario occurs when the solutal gradient is destabilising and, regardless of the thermal gradient, the behaviour of σ closely resembles that seen in chapter 3 for reactive solutal convection. This similarity in behaviour is unsurprising since faster thermal diffusion means that the thermal gradient is secondary in solute-driven convection. In the second and third scenarios the solutal gradient is stabilising and the thermal gradient is destabilising. If the reaction rate is subcritical then the dominant branch switches from being strictly real to complex as Δ^b increases (figures 5.2(a, b)), whereas if the reaction rate is supercritical then the dominant branch remains strictly real as Δ^c increases (figures 5.3(a, b)).

5.4.2 Asymptotic analysis of the sextic in the Galerkin approach

To analyse the behaviour of σ close to critical values of $\mathcal{R}_T$ we assume $\mathcal{R}_C = \mathcal{O}(1)$ and rewrite the sextic (5.76) as

$$\begin{aligned} &a_6\sigma^6 + (b_5 - c_5\mathcal{R}_T)\sigma^5 + (b_4 - c_4\mathcal{R}_T + d_4\mathcal{R}_T^2)\sigma^4 + (b_3 - c_3\mathcal{R}_T + d_3\mathcal{R}_T^2)\sigma^3 \\ &+ (b_2 - c_2\mathcal{R}_T + d_2\mathcal{R}_T^2 + e_2\delta^2)\sigma^2 + (e_1 - f_1\mathcal{R}_T)\delta^2\sigma + (e_0 - f_0\mathcal{R}_T + g_0\mathcal{R}_T^2)\delta^2 = 0. \end{aligned} \tag{5.77}$$

Here the coefficients a_i, b_i, c_i, d_i, e_i, f_i, and g_i are of order unity, but not necessarily positive since they may depend on $\mathcal{R}_C$. We will always take $|\delta| \ll 1$, and seek asymptotic scalings for σ in terms of δ.

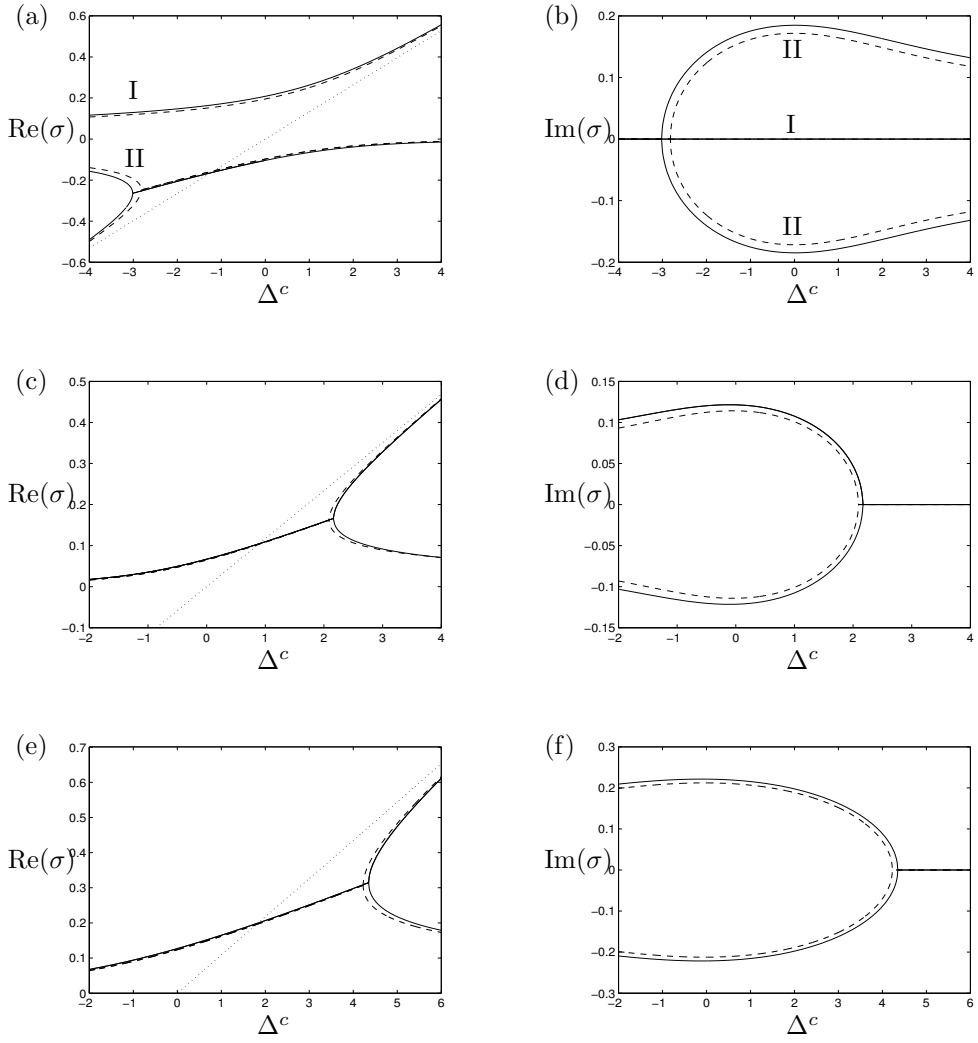

Figure 5.3: Behaviour of σ close to $\Delta^c = 0$, for $k_0 = 20$, $\phi_0 = 0.1$, $Le = 10$, $\lambda = 0.25$, $m = 3$, and (a, b) $\mathcal{R}_C = -50$, $\delta = -0.1$, (c, d) $\mathcal{R}_C = 10$, $\delta = 0.1$, (e, f) $\mathcal{R}_C = 50$, $\delta = 0.1$. The left-hand column shows $\mathrm{Re}(\sigma)$, while the right-hand column shows $\mathrm{Im}(\sigma)$. Solid lines are full numerical solutions to the linear problem; dashed lines are Galerkin solutions; dotted lines in the left-hand column show the results for $\delta = 0$. Roman numerals on (a, b) are to aid in identifying the corresponding real and imaginary parts of each σ branch.

5.4.2.1 Small Δ^c: location of the bifurcation point

To analyse the asymptotic behaviour of σ around Δ^c, it is helpful to rewrite (5.77) with $\mathcal{R}_T = \mathcal{R}^c_{T,0}(\mathcal{R}_C, m) + \Delta^c$ as

$$a_6\sigma^6 + (b_5 - c_5\Delta^c)\sigma^5 + (b_4 - c_4\Delta^c + d_4(\Delta^c)^2)\sigma^4 + (b_3 - c_3\Delta^c + d_3(\Delta^c)^2)\sigma^3 + (e_2\delta^2 - c_2\Delta^c + d_2(\Delta^c)^2)\sigma^2 + (e_1 - f_1\Delta^c)\delta^2\sigma + (e_0 - f_0\Delta^c + g_0(\Delta^c)^2)\delta^2 = 0, \tag{5.78}$$

where all the coefficients a_i–g_i are different from those in (5.77) but are still of order unity and not necessarily positive.

To locate the bifurcation point we consider $\Delta^c \ll 1$ and eliminate all terms in (5.78) which must be sub-dominant, obtaining

$$a_6\sigma^6 + b_5\sigma^5 + b_4\sigma^4 + b_3\sigma^3 + (e_2\delta^2 - c_2\Delta^c)\sigma^2 + e_1\delta^2\sigma + e_0\delta^2 \approx 0. \tag{5.79}$$

If σ is of order unity then $\sigma \sim -b_5/a_6$; all other roots of the sextic must be small in magnitude. Taking $\sigma \ll 1$ we can eliminate further sub-dominant terms and reduce the equation to the cubic

$$b_3\sigma^3 + (e_2\delta^2 - c_2\Delta^c)\sigma^2 + e_1\delta^2\sigma + e_0\delta^2 \approx 0. \tag{5.80}$$

The bifurcation can only occur if the σ^3, σ^2, and σ^0 terms are all of the same order. This requires $\delta^2 < \Delta^c$, and $\sigma \sim |\delta|^{2/3}$ and $\Delta \sim |\delta|^{2/3}$. Therefore, setting $\sigma = |\delta|^{2/3}\Sigma$ and $\Delta = |\delta|^{2/3}D$, with Σ and D of order unity, we obtain

$$f(\Sigma) \equiv b_3\Sigma^3 - c_2D\Sigma^2 + e_0 \approx 0. \tag{5.81}$$

The discriminant of (5.81) is given by

$$\Lambda = 4c_2^3e_0D - 27b_3^2e_0^2. \tag{5.82}$$

It is apparent that if both c_2 and e_0 have the same sign, then for sufficiently large D, Λ will be strictly positive and (5.81) will have three real roots, while for smaller values of D, Λ will be negative and (5.81) will have only one real root and two complex ones. Alternatively, when either c_2 or e_0 are negative, then for sufficiently small D, Λ will be strictly positive and (5.81) will have three real

roots, while for larger values of D, Λ will be negative and (5.81) will have only one real root and two complex ones.

We can rewrite c_2 and e_0 as

$$c_2 = c_{20} - c_{21}\mathcal{R}_C, \quad \text{where} \quad c_{20}, c_{21} > 0, \tag{5.83}$$

$$e_0 = \mathcal{R}_C(e_{01} + e_{02}\mathcal{R}_C), \quad \text{where} \quad e_{01}, e_{02} > 0. \tag{5.84}$$

Hence, $c_2 > 0$ for $\mathcal{R}_C < c_{20}/c_{21}$, and $e_0 >$ for $\mathcal{R}_C > 0$ or $\mathcal{R}_C < -e_{01}/e_{02}$.

We locate the bifurcation point by requiring $\Lambda = 0$, giving

$$D = \frac{3}{2}\frac{(2b_3^2 e_0)}{c_2}^{1/3}, \quad \text{and hence} \quad \Sigma = \frac{(2b_3^2 e_0)}{b_3}^{1/3} \quad \text{for} \quad e_0 > 0, \tag{5.85}$$

and

$$D = -\frac{3}{2}\frac{(2b_3^2|e_0|)}{c_2}^{1/3}, \quad \text{and hence} \quad \Sigma = -\frac{(2b_3^2|e_0|)}{b_3}^{1/3} \quad \text{for} \quad e_0 < 0. \tag{5.86}$$

Comparisons of (5.85) and (5.86) with numerical solutions of (5.76) are shown in table 5.1. We take $Le = 10$, $\lambda = 0.25$, and $\phi_0 = 0.1$ throughout, and in table 5.1(a) $\mathcal{R}_C = 50$, $k_0 = 20$, so that $e_0 > 0$, and in (b) $\mathcal{R}_C = -10$, $k_0 = 20$, so that $e_0 < 0$. The results suggest that these asymptotics capture the behaviour of the solutions well.

5.4.2.2 Regular perturbation to σ_0

When $\mathcal{R}_T = \mathcal{O}(1)$, we expect that there will be a solution branch with $\sigma \approx \sigma_{0+}$. To locate this branch, we set $\sigma = \sigma_{0+} + \sigma_1$ in (5.77), obtaining an equation of the form

$$A_6\sigma_1^6 + A_5\sigma_1^5 + A_4\sigma_1^4 + A_3\sigma_1^3 + (B_2\delta^2 + C_2)\sigma_1^2 + (B_1\delta^2 + C_1)\sigma_1 + B_0\delta^2 = 0, \tag{5.87}$$

(a)

(δ, m)	Numerical (Δ^c, σ)	Asymptotic (Δ^c, σ)
(0.1, 3)	(4.2256, 0.3083)	(4.2879, 0.3102)
(0.01, 3)	(0.9209, 0.0672)	(0.9238, 0.0668)
(0.001, 3)	(0.1989, 0.0145)	(0.1990, 0.0144)
(0.1, 10)	(14.4471, 0.4539)	(14.7499, 0.4497)
(0.01, 10)	(3.1636, 0.0973)	(3.1778, 0.0969)
(0.001, 10)	(0.6840, 0.0210)	(0.6846, 0.0209)

(b)

(δ, m)	Numerical (Δ^c, σ)	Asymptotic (Δ^c, σ)
(-0.1, 3)	(-1.9418, -0.1551)	(-1.9456, -0.1578)
(-0.01, 3)	(-0.4191, -0.0334)	(-0.4192, -0.0340)
(-0.001, 3)	(-0.0904, -0.0071)	(-0.0903, -0.0073)
(-0.1, 10)	(-0.4552, -0.3539)	(-0.4661, -0.3451)
(-0.01, 10)	(-0.1000, -0.0730)	(-0.1004, -0.0744)
(-0.001, 10)	(-0.0217, -0.0151)	(-0.0216, -0.0160)

Table 5.1: Comparisons of (5.85) and (5.86) with the bifurcation point obtained from numerical solutions of (5.76). Parameter values: $Le = 10$, $\lambda = 0.25$, and $\phi_0 = 0.1$, and (a) $k_0 = 20$, $\mathcal{R}_C = 50$, (b) $k_0 = 20$, $\mathcal{R}_C = -10$.

where all coefficients except δ and σ_1 are implicitly of order 1, though not necessarily positive. Seeking a regular perturbation so $\sigma_1 \ll 1$, this reduces to

$$C_1\sigma_1 + B_0\delta^2 \approx 0, \quad \text{i.e.} \quad \sigma_1 \sim -\frac{B_0}{A_1}\delta^2. \tag{5.88}$$

Thus the effect of matrix evolution on the growth rate of instabilities is negligibly small, $\mathcal{O}(\delta^2)$, as long as we are away from the $\delta = 0$ stability boundary. This result is similar to that found in chapter 3.

5.4.3 Eigenfunction structure and instability mechanism

As well as providing the complex growth rate σ, the Galerkin stability analysis also provides the quantities W_2, Θ_1, Θ_2, χ_1, and χ_2 that define the corresponding vertical eigenfunction. To elucidate the mechanism involved in the instability, it is useful to examine these quantities.

As in chapter 3 we may write

$$\begin{aligned}\psi(x,z,t) &= \Re\left(e^{imx}e^{(\sigma_R+i\sigma_I)t}\left(\sin(\pi z)+\Psi_2\sin(2\pi z)\right)\right)\\ &= e^{\sigma_R t}\left[\sin(\pi z)\cos(mx+\sigma_I t)+|\Psi_2|\sin(2\pi z)\cos(mx+\sigma_I t+\theta)\right],\end{aligned} \tag{5.89}$$

where $\theta = \arg(\Psi_2)$. The reader is referred to §3.2.3.4 for discussion of the effect of the second harmonic on the shapes and relative phases of the various perturbations.

We will consider three different scenarios as described in §5.4.1.1: firstly the combination of a destabilising solutal gradient with either a stabilising or destabilising thermal gradient; secondly a destabilising thermal gradient with a stabilising solutal gradient and a subcritical reaction rate so the onset of instability is oscillatory; and thirdly a destabilising thermal gradient with a stabilising solutal gradient and a supercritical reaction rate.

In our formulation, when the thermal gradient is destabilising $\hat{T}_1 - \hat{T}_0 < 0$, so $T' < 0$ in regions which become warmer than the base state, and $T' > 0$ in regions which become cooler. Similarly, when the solutal gradient is stabilising $\hat{C}_1 - \hat{C}_0 < 0$, so $C' < 0$ in regions of higher concentration, and $C' > 0$ in regions of lower concentration. Therefore, in order to avoid confusion when considering the spatial structure of the fastest-growing eigenfunction we define $\tilde{T} = -\mathrm{sgn}(\mathcal{R}_T)T'$ and $\tilde{C} = \mathrm{sgn}(\mathcal{R}_C)C'$. With this reformulation, $\tilde{T} > 0$ and $\tilde{C} > 0$ will always correspond to regions of higher temperatures and concentrations, respectively, while $\tilde{T} < 0$ and $\tilde{C} < 0$ will correspond to regions of lower temperatures and concentrations, respectively. We also define $\tilde{\phi}$ via (5.60), so that $\tilde{\phi} > 0$ will always correspond to regions of higher porosity, while $\tilde{\phi} < 0$ will correspond to regions of lower porosity.

5.4.3.1 Scenario one: destabilising solutal gradient

In this section we consider the combination of a destabilising solutal gradient with either a stabilising or a destabilising thermal gradient. Recall from (5.22) that the porosity evolution is driven by the difference $\tilde{T} - \tilde{C}$. Regardless of the direction

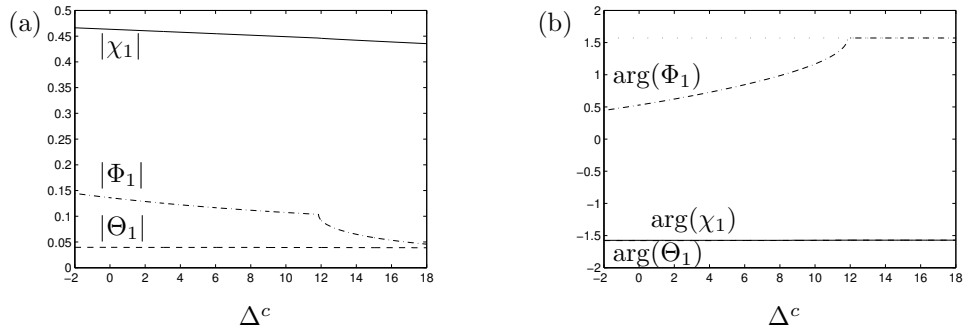

Figure 5.4: (a) Amplitudes and (b) relative phases of the first harmonics as functions of Δ^c. In (a), solid line is $|\chi_1|$, dashed line is $|\Theta_1|$, and dashed-dotted line is $|\Phi_1|$. In (b), solid line is $\arg(\chi_1)$, dashed line is $\arg(\Theta_1)$, and dashed-dotted line is $\arg(\Phi_1)$; the light dotted lines are $-\frac{\pi}{2}$ and $\frac{\pi}{2}$. Parameter values: $\phi_0 = 0.1$, $k_0 = 5$, $\delta = 0.1$, $m = 3$, $Le = 10$, $\lambda = 0.25$, $\mathcal{R}_C = 30$.

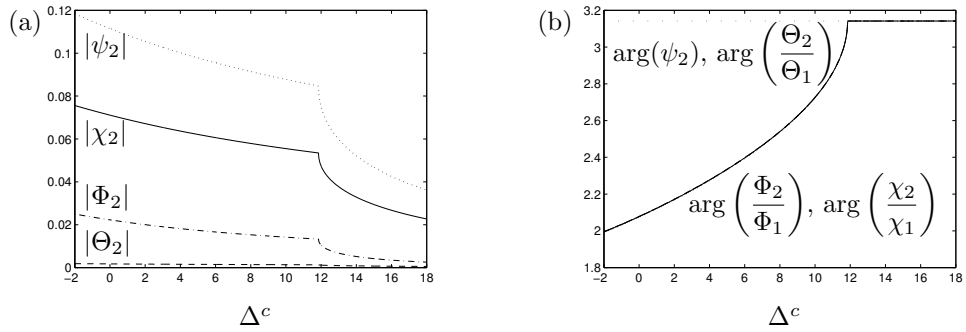

Figure 5.5: (a) Amplitudes and (b) relative phases of the second harmonics as functions of Δ^c. In (a), solid line is $|\chi_2|$, dashed line is $|\Theta_2|$, dashed-dotted line is $|\Phi_2|$, and dotted line is $|\psi_2|$. In (b), solid line is $\arg(\chi_2/\chi_1)$, dashed line is $\arg(\Theta_2/\Theta_1)$, dashed-dotted line is $\arg(\Phi_2/\Phi_1)$, and the dotted line is $\arg(\psi_2)$; the light dotted line is π. The four lines are practically indistinguishable. Parameter values: $\phi_0 = 0.1$, $k_0 = 5$, $\delta = 0.1$, $m = 3$, $Le = 10$, $\lambda = 0.25$, $\mathcal{R}_C = 30$.

of the thermal gradient, the amplitude of the concentration perturbation $\tilde{C}$ will always dominate the amplitude of the thermal perturbation $\tilde{T}$ since the diffusion of heat is much faster than the diffusion of solute through the fluid. Therefore, these situations are analogous to those found in chapter 3 for reactive solutal convection, where the porosity evolution is driven solely by the concentration perturbation.

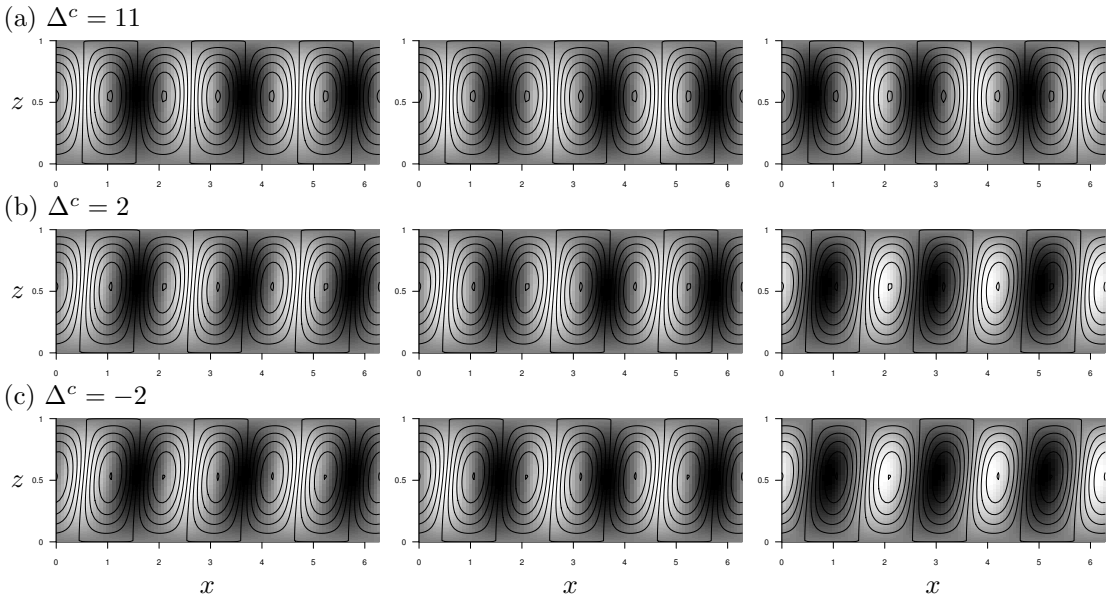

Figure 5.6: Eigenfunctions from the Galerkin analysis. Left-hand column: streamlines superimposed on concentration perturbation $\tilde{C}$. Centre column: streamlines superimposed on temperature perturbation $\tilde{T}$. Right-hand column: streamlines superimposed on porosity perturbation $\tilde{\phi}$. Parameters were $\phi_0 = 0.1$, $k_0 = 5$, $\delta = 0.1$, $m = 3$, $Le = 10$, $\lambda = 0.25$, $\mathcal{R}_C = 30$. In each case the values of ψ on the streamlines are evenly spaced, and in each plot darker shading corresponds to lower values; scales are arbitrary.

We first consider the combination of a destabilising solutal gradient and a stabilising thermal gradient (arrow (ii), figure 5.1(b)). Figures 5.4 and 5.5 show how the amplitudes and phases of the perturbations to the streamfunction, temperature, concentration and porosity vary as Δ^c changes for $k_0 = 5$, $\mathcal{R}_C = 30$. They should be read in conjunction with figures 5.2(c, d) which illustrate the behaviour of σ with Δ^c, and figure 5.6 which illustrates how the corresponding spatial structure of the fastest-growing eigenfunction behaves as Δ^c is reduced. All the cases plotted in figure 5.6 lie in the regime where σ is fully complex; the bifurcation for these parameter values occurs at $\Delta^c \approx 12$.

For values to the right of the bifurcation point ($\Delta^c \approx 12$), the perturbations to

concentration, temperature, and porosity are all small (figure 5.4(a)) and are in phase (figure 5.4(b)) such that maxima of the first harmonic of $\tilde{\phi}$ correspond to minima of the first harmonics of $\tilde{C}$ and $\tilde{T}$. A change in trend is immediately noticeable at the bifurcation point: although the first harmonics of concentration and temperature continue to vary smoothly, and they remain almost perfectly in phase with the streamfunction ($\arg(\chi_1)$, $\arg(\Theta_1) \approx -\pi/2$, as can be seen in figure 5.4(b)), the trend in the amplitude of the porosity perturbation alters. As $\arg(\Phi_1)$ decreases (figure 5.4(b)), $\tilde{\phi}$ is no longer perfectly in phase with the concentration and temperature perturbations, with its extrema moving rightwards relative to those of ψ, $\tilde{C}$, and $\tilde{T}$.

This is the situation that is beginning to emerge in figure 5.6(a), where $\Delta^c = 11$. The pattern of flow, concentration, temperature, and porosity is very similar to that of simple convection; downflow draws down higher concentrations and temperatures from the upper boundary while upflow draws up lower concentrations and temperatures from the lower boundary. Upflow occurs in high-permeability regions and downflow in low-permeability regions: since the concentration and temperature perturbations are still approximately 'in phase' with the porosity perturbations, the reaction will tend to amplify the porosity perturbation. The small phase difference between the porosity perturbation and the concentration and temperature perturbations is just apparent.

As Δ^c is reduced a little further, the concentration and temperature perturbations continue to move further out of phase with the porosity perturbations (figure 5.4(b)), the porosity perturbation grows in importance (figure 5.4(a)), and the second harmonics start to become apparent. The relative phases of all the second harmonics are in the range $(\frac{\pi}{2}, \pi)$ (figure 5.5(b)), so they tilt the convection pattern rightward. This can be seen in figure 5.6(b) for $\Delta^c = 2$; the streamfunction, concentration, and temperature perturbations are still closely in phase, but the rightward tilting of the streamfunction, concentration and porosity cells is more evident. The tilting in the temperature cells, however, is harder to discern since $|\Theta_2| \ll |\Theta_1|$ (figures 5.4(a), 5.5(a)).

As Δ^c is reduced still further, the phase difference between the porosity and concentration and temperature perturbations approaches $\frac{\pi}{2}$ (figure 5.4(b)), so

they are almost a quarter of a period out of phase; this is visible in figure 5.6(c) ($\Delta^c = -2$). The importance of the second harmonics increases (figure 5.5(a)) and their phase difference from the first harmonic approaches $\frac{\pi}{2}$ (figure 5.5(b)), so they tend to tilt the cells rightward without squashing them upward or downward. The tilting in the streamfunction, concentration and porosity fields is now clearly evident.

Similar behaviour can also be seen when the thermal gradient is destabilising and the reaction rate is increased (arrow (ii), figure 5.1(c)). Figures 5.7 and 5.8 show how the amplitudes and phases of the perturbations to the streamfunction, temperature, concentration and porosity vary as Δ^c changes for $k_0 = 20$, $\mathcal{R}_C = 10$. They should be read in conjunction with figure 5.3(c, d) which illustrate the behaviour of σ with Δ^c, and figure 5.9 which illustrates how the corresponding spatial structure of the fastest-growing eigenfunction behaves as Δ^c is reduced. All the cases plotted in figure 5.9 lie in the regime where σ is fully complex; the bifurcation for these parameter values occurs at $\Delta^c \approx 2.2$.

Again, we see that just to the left of the bifurcation point at $\Delta^c = 2$ (figure 5.9(a)), the pattern of flow, concentration, temperature, and porosity is very similar to that of simple convection. In this case downflow draws down higher concentrations and lower temperatures from the upper boundary while upflow draws up lower concentrations and higher temperatures from the lower boundary. Upflow occurs in high-permeability regions and downflow in low-permeability regions.

As Δ^c is reduced the phase difference between the porosity and concentration and temperature perturbations approaches $\frac{\pi}{2}$ (figure 5.7(b)), so they are almost a quarter of a period out of phase; this is visible in figure 5.9(c) ($\Delta^c = -1$). Furthermore, the importance of the second harmonics increases (figure 5.8(a)) and their phase difference from the first harmonic approaches $\frac{\pi}{2}$ (figure 5.8(b)), so they tend to tilt the cells rightward without squashing them upward or downward. The tilting of the porosity and concentration fields is clearly evident (figure 5.9(c)), but the tilting of the streamfunction is harder to discern since $|\psi_2|$ is much smaller than in the previous stabilising thermal gradient case.

The mechanisms that maintain this amplifying travelling-wave mode are very

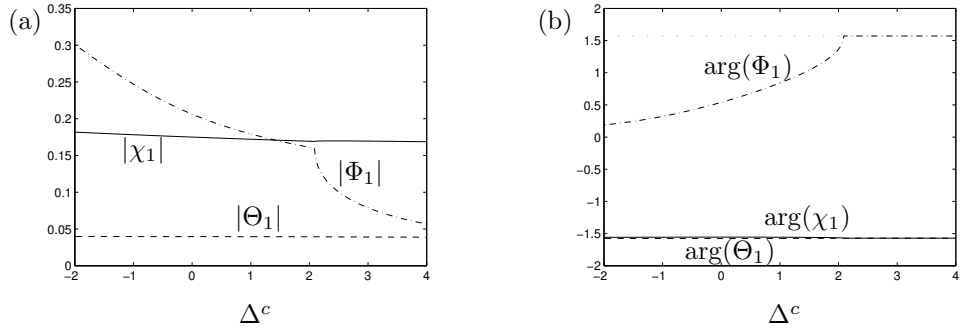

Figure 5.7: (a) Amplitudes and (b) relative phases of the first harmonics as functions of Δ^c. In (a), solid line is $|\chi_1|$, dashed line is $|\Theta_1|$, and dashed-dotted line is $|\Phi_1|$. In (b), solid line is $\arg(\chi_1)$, dashed line is $\arg(\Theta_1)$, and dashed-dotted line is $\arg(\Phi_1)$; the light dotted lines are $-\frac{\pi}{2}$ and $\frac{\pi}{2}$. Parameter values: $\phi_0 = 0.1$, $k_0 = 20$, $\delta = 0.1$, $m = 3$, $Le = 10$, $\lambda = 0.25$, $\mathcal{R}_C = 10$.

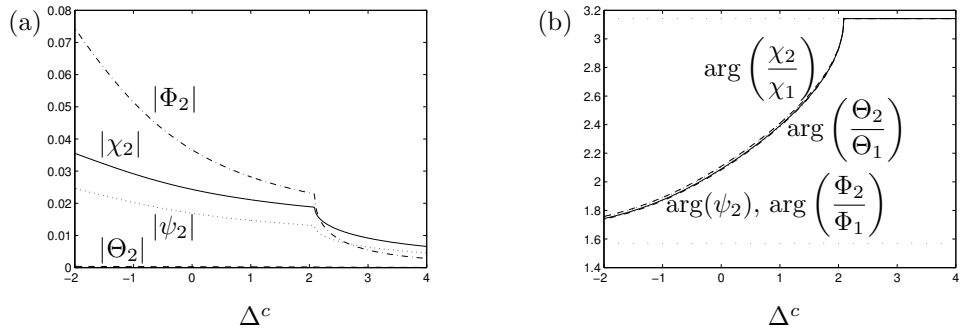

Figure 5.8: (a) Amplitudes and (b) relative phases of the second harmonics as functions of Δ^c. In (a), solid line is $|\chi_2|$, dashed line is $|\Theta_2|$, dashed-dotted line is $|\Phi_2|$, and dotted line is $|\psi_2|$. In (b), solid line is $\arg(\chi_2/\chi_1)$, dashed line is $\arg(\Theta_2/\Theta_1)$, dashed-dotted line is $\arg(\Phi_2/\Phi_1)$, and the dotted line is $\arg(\psi_2)$; the four lines are practically indistinguishable. The light dotted lines are π and $\frac{\pi}{2}$. Parameter values: $\phi_0 = 0.1$, $k_0 = 20$, $\delta = 0.1$, $m = 3$, $Le = 10$, $\lambda = 0.25$, $\mathcal{R}_C = 10$.

similar to those noted in §3.2.3.4 for reactive solutal convection. Recall that the temperature perturbation equation (5.20) contains one source term, the convective term $\partial\psi/\partial x$, which must balance the dissipative effect of the diffusion term. The concentration perturbation equation (5.21), however, contains two source terms which must balance the dissipative effects of the reaction and dif-

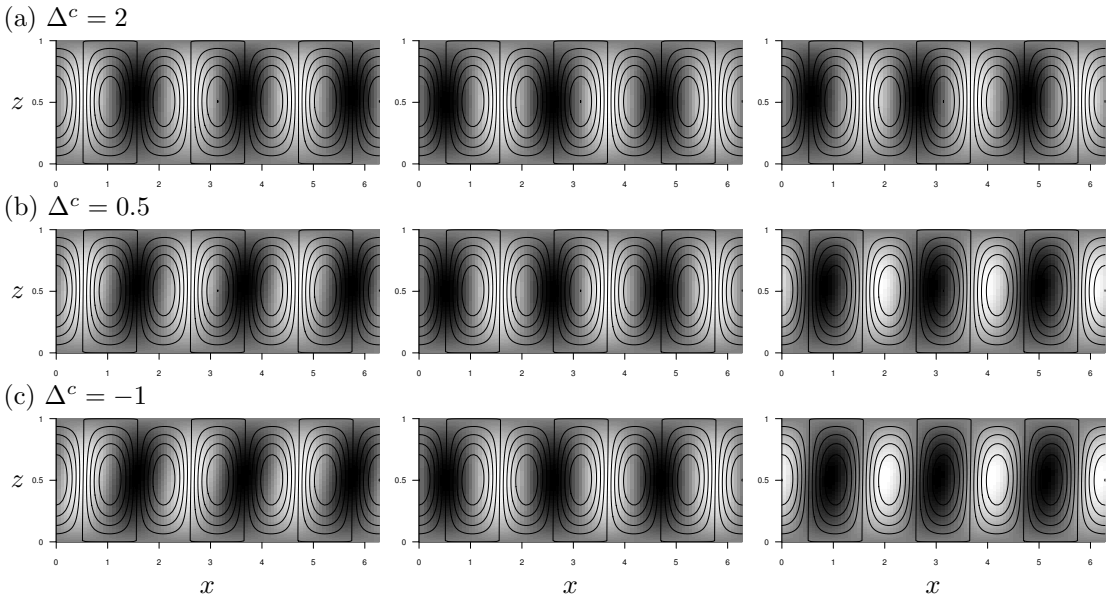

Figure 5.9: Eigenfunctions from the Galerkin analysis. Left-hand column: streamlines superimposed on concentration perturbation $\tilde{C}$. Centre column: streamlines superimposed on temperature perturbation $\tilde{T}$. Right-hand column: streamlines superimposed on porosity perturbation $\tilde{\phi}$. Parameters were $\phi_0 = 0.1$, $k_0 = 20$, $\delta = 0.1$, $m = 3$, $Le = 10$, $\lambda = 0.25$, $\mathcal{R}_C = 10$. In each case the values of ψ on the streamlines are evenly spaced, and in each plot darker shading corresponds to lower values; scales are arbitrary.

fusion terms: the convective term, and the term $\partial\phi'/\partial z$, which represents net diffusive transport due to gradients in porosity superimposed on the background vertical gradient of concentration. When the porosity perturbation is weak and the system is dominated by convection, the convective source term dominates in both the temperature and concentration equations. When convective flow is weak, however, diffusion dominates the temperature perturbation equation and the importance of the porosity gradient mechanism in the concentration perturbation equation increases. This mechanism acts to maintain the tilting against buoyant effects that would tend to restore cells to upright convective cells, and diffusive effects that would tend to eliminate the perturbation altogether. Meanwhile, the offset between $\tilde{C}$ and $\tilde{\phi}$ has the additional effect of causing the porosity

perturbations to migrate leftward.

5.4.3.2 Scenario two: stabilising solutal gradient, destabilising thermal gradient, subcritical reaction rate

In this and the subsequent section we consider the combination of a stabilising solutal gradient with a destabilising thermal gradient. Here, we consider this combination along with a subcritical reaction rate, so the transition to instability is through a growing oscillatory mode.

Figures 5.10 and 5.11 show how the amplitudes and phases of the perturbations to the streamfunction, temperature, concentration and porosity vary as Δ^b changes for $k_0 = 5$ and $\mathcal{R}_C = -15$. They should be read in conjunction with figures 5.2(a, b) which illustrate the behaviour of σ with Δ^c, and figure 5.12, which illustrates how the corresponding spatial structure of the fastest-growing eigenfunction behaves as Δ^b is reduced. We recall that at $\Delta^b \approx 0.4$ we abruptly switch stability branches in order to remain on the dominant branch (figure 5.2(a, b)). For values of $\Delta^b \gtrsim 0.4$ the dominant values of σ are complex, but for $\Delta^b \lesssim 0.4$ the dominant values are strictly real.

For $\Delta^b > 0.4$, the perturbations to concentration, temperature, and porosity are all small (figure 5.10(a)) and are approximately in phase (figure 5.10(b)) such that the maxima of the first harmonics of $\tilde{C}$ and $\tilde{T}$ roughly coincide with the minima of the first harmonic of $\tilde{\phi}$. The slight offset between extrema of $\tilde{C}$, $\tilde{T}$, and $\tilde{\phi}$ can be seen more clearly in figure 5.12(a), but the pattern of flow, concentration, temperature, and porosity is still very similar to that of simple convection; downflow draws down lower concentrations and temperatures from the upper boundary, while upflow draws up higher concentrations and temperatures. Upflow occurs in low-permeability regions and downflow in high-permeability regions.

A change is immediately noticeable when the dominant branch abruptly switches at $\Delta^b \approx 0.4$: the first harmonic of $\tilde{\phi}$ increases (figure 5.10(a)), and the perturbations are now out of phase (figure 5.10(b)) with the extrema of $\tilde{C}$ and $\tilde{T}$ moving leftwards, and the extrema of $\tilde{\phi}$ moving rightwards relative to those of ψ. The second harmonics are now all non-zero (figure 5.11(a)), with the relative phases

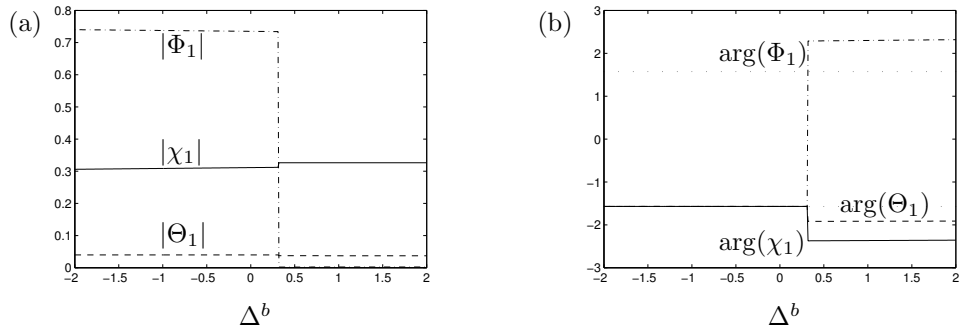

Figure 5.10: (a) Amplitudes and (b) relative phases of the first harmonics as functions of Δ^b. In (a), solid line is $|\chi_1|$, dashed line is $|\Theta_1|$, and dashed-dotted line is $|\Phi_1|$. In (b), solid line is $\arg(\chi_1)$, dashed line is $\arg(\Theta_1)$, and dashed-dotted line is $\arg(\Phi_1)$. The light dotted lines are $-\frac{\pi}{2}$ and $\frac{\pi}{2}$. Parameter values: $\phi_0 = 0.1$, $k_0 = 5$, $\delta = -0.1$, $m = 3$, $Le = 10$, $\lambda = 0.25$, $\mathcal{R}_C = -15$. The jump at $\Delta^b \approx 0.4$ is a result of the change of dominant branch.

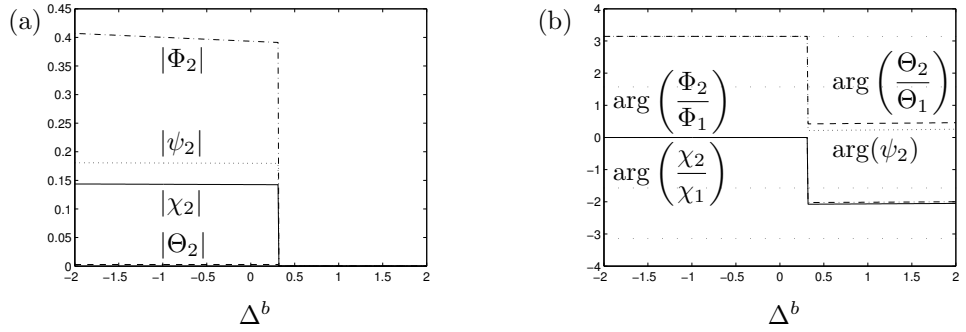

Figure 5.11: (a) Amplitudes and (b) relative phases of the second harmonics as functions of Δ^b. In (a), solid line is $|\chi_2|$, dashed line is $|\Theta_2|$, dashed-dotted line is $|\Phi_2|$, and dotted line is $|\psi_2|$. In (b), solid line is $\arg(\chi_2/\chi_1)$, dashed line is $\arg(\Theta_2/\Theta_1)$, dashed-dotted line is $\arg(\Phi_2/\Phi_1)$, and the dotted line is $\arg(\psi_2)$. The light dotted lines are π, $\frac{\pi}{2}$, $-\frac{\pi}{2}$, and $-\pi$. Parameter values: $\phi_0 = 0.1$, $k_0 = 5$, $\delta = -0.1$, $m = 3$, $Le = 10$, $\lambda = 0.25$, $\mathcal{R}_C = -15$. The jump at $\Delta^b \approx 0.4$ is a result of the change of dominant branch.

of the second harmonics of ψ and $\tilde{T}$ equal to π, and those of $\tilde{C}$ and $\tilde{\phi}$ equal to 0 (figure 5.11(b)). Therefore, the temperature and streamfunction fields are squashed upwards, whereas the concentration and porosity fields are squashed downwards. This can be seen in figure 5.12(b) for $\Delta^b = 0$; downflow is now oc-

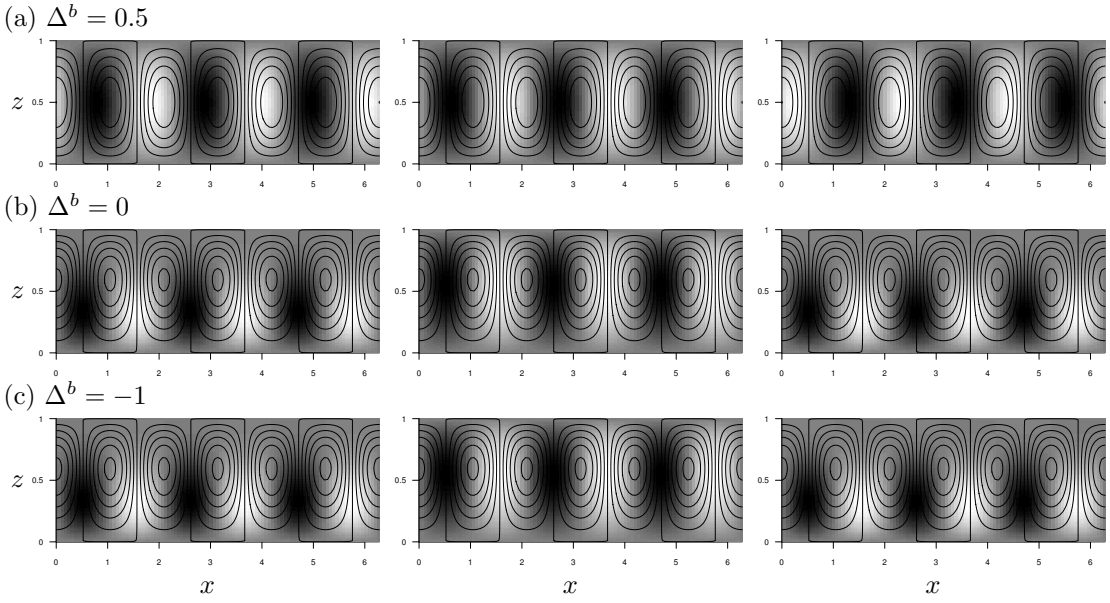

Figure 5.12: Eigenfunctions from the Galerkin analysis. Left-hand column: streamlines superimposed on concentration perturbation $\tilde{C}$. Centre column: streamlines superimposed on temperature perturbation $\tilde{T}$. Right-hand column: streamlines superimposed on porosity perturbation $\tilde{\phi}$. Parameters were $\phi_0 = 0.1$, $k_0 = 5$, $\delta = -0.1$, $m = 3$, $Le = 10$, $\lambda = 0.25$, $\mathcal{R}_C = -15$. In each case the values of ψ on the streamlines are evenly spaced, and in each plot darker shading corresponds to lower values; scales are arbitrary.

curring in low-permeability regions and upflow in high-permeability regions, and it is evident that the circulation and temperature cells have moved upwards, but the porosity and concentration cells have moved towards the bottom of the layer.

By comparing the magnitudes of the individual terms in (5.20) and (5.21) as Δ^b is reduced we can elucidate the mechanisms that cause the upwards squashing of the circulation and temperature cells, and the downward squashing of the porosity and concentration cells. For $\Delta^b > 0.4$, before the branch switch, the porosity perturbation is weak and the system is dominated by convection. After the branch switch, although vertical convection still balances with diffusion in the temperature perturbation equation (5.20), it now balances with the $\partial\phi'/\partial z$

term in the concentration perturbation equation (5.21). This results in an offset between the porosity and circulation cells as faster vertical velocities must correspond to higher vertical porosity gradients. Therefore, the porosity cells move towards the bottom of the layer and the circulation cells move upwards. This offset then results in the temperature cells moving upwards, and the concentration cells moving downwards.

5.4.3.3 Scenario three: stabilising solutal gradient, destabilising thermal gradient, supercritical reaction rate

We now consider the combination of a stabilising solutal gradient with a destabilising thermal gradient along with a supercritical reaction rate, so the onset of convection is through a monotonic instability.

Figures 5.13 and 5.14 show how the amplitudes and phases of the perturbations to the streamfunction, temperature, concentration and porosity vary as Δ^c changes for $k_0 = 20$, $\mathcal{R}_C = -50$. They should be read in conjunction with figures 5.3(a, b) which illustrate the behaviour of σ with Δ^c, and figure 5.15, which illustrates how the corresponding spatial structure of the fastest-growing eigenfunction behaves as Δ^c is reduced. Recall in this case there is no bifurcation point and for all values of Δ^c, σ is strictly real.

At $\Delta^c = 3$, the perturbations to concentration, temperature, and porosity are all small (figure 5.13(a)), and are out of phase (figure 5.13(b)) such that the maxima of $\tilde{C}$, $\tilde{T}$, and $\tilde{\phi}$ all coincide. This is the situation in figure 5.15(a); downflow draws down lower concentrations and temperatures from the upper boundary, while upflow draws up higher concentrations and temperatures from the lower boundary. Downflow occurs in low-permeability regions and upflow in high-permeability regions.

As Δ^c is reduced the first harmonic of $\tilde{\phi}$ grows in importance, while those of $\tilde{C}$ and $\tilde{T}$ remain small (figure 5.13(a)), and the second harmonics become more apparent (figure 5.14(a)). Furthermore, the temperature and streamfunction cells are squashed upwards ($\arg(\psi_2) = \arg(\Theta_2/\Theta_1) = \pi$, figure 5.14(b)), and the concentration and porosity cells are squashed downwards ($\arg(\chi_2/\chi_1) = \arg(\Phi_2/\Phi_1) =$

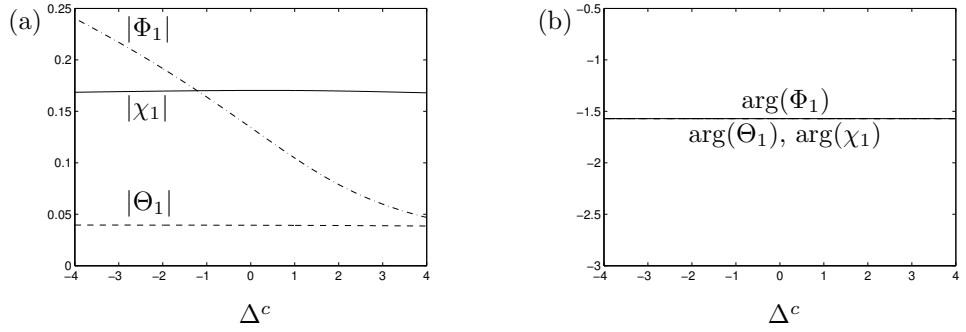

Figure 5.13: (a) Amplitudes and (b) relative phases of the first harmonics as functions of Δ^c. In (a), solid line is $|\chi_1|$, dashed line is $|\Theta_1|$, and dashed-dotted line is $|\Phi_1|$. In (b), solid line is $\arg(\chi_1)$, dashed line is $\arg(\Theta_1)$, and dashed-dotted line is $\arg(\Phi_1)$; the three lines are indistinguishable. Parameter values: $\phi_0 = 0.1$, $k_0 = 20$, $\delta = -0.1$, $m = 3$, $Le = 10$, $\lambda = 0.25$, $\mathcal{R}_C = -50$.

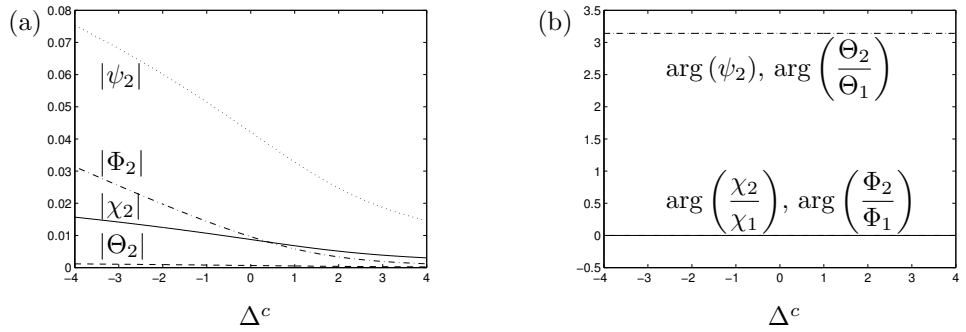

Figure 5.14: (a) Amplitudes and (b) relative phases of the second harmonics as functions of Δ^c. In (a), solid line is $|\chi_2|$, dashed line is $|\Theta_2|$, dashed-dotted line is $|\Phi_2|$, and dotted line is $|\psi_2|$. In (b), solid line is $\arg(\chi_2/\chi_1)$, dashed line is $\arg(\Theta_2/\Theta_1)$, dashed-dotted line is $\arg(\Phi_2/\Phi_1)$, and the dotted line is $\arg(\psi_2)$; each set of lines are practically indistinguishable. Parameter values: $\phi_0 = 0.1$, $k_0 = 20$, $\delta = -0.1$, $m = 3$, $Le = 10$, $\lambda = 0.25$, $\mathcal{R}_C = -50$.

0, figure 5.14(b)). This squashing of cells can be seen in figures 5.15(b) and (c) for $\Delta^c = 0$ and $\Delta^c = -3$, respectively. Note that the amplitudes of the first and second harmonics are much smaller here than in the subcritical reaction case, and hence the squashing of cells is not as evident as in figures 5.12(b) and (c).

The behaviour here is identical to that seen in the subcritical reaction case after the abrupt branch switching ($\Delta^b < 0.4$). As in that case, vertical convection

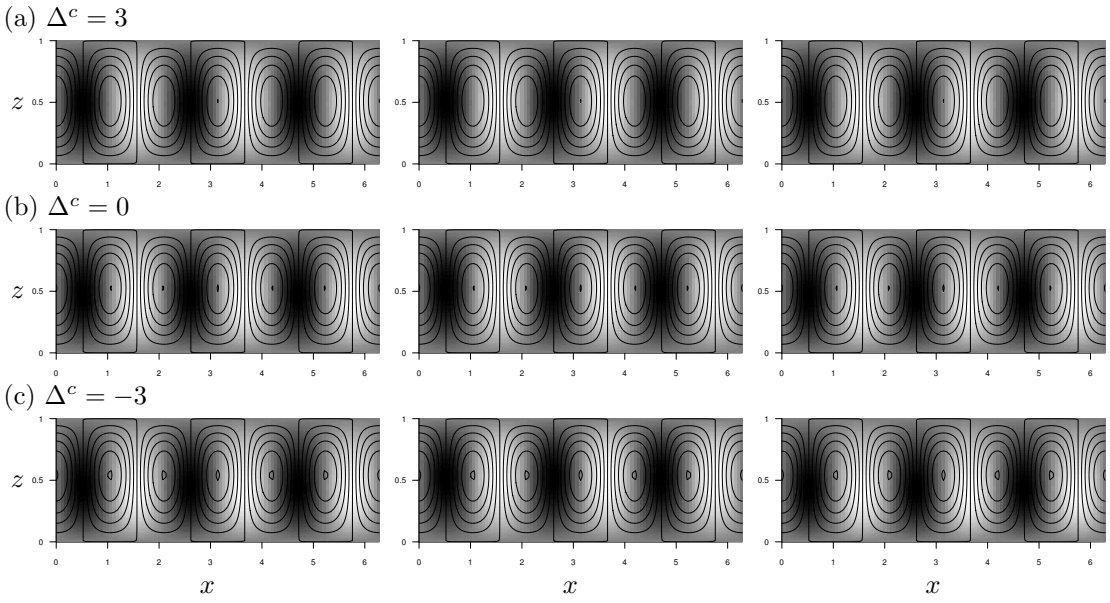

Figure 5.15: Eigenfunctions from the Galerkin analysis. Left-hand column: streamlines superimposed on concentration perturbation $\tilde{C}$. Centre column: streamlines superimposed on temperature perturbation $\tilde{T}$. Right-hand column: streamlines superimposed on porosity perturbation $\tilde{\phi}$. Parameters were $\phi_0 = 0.1$, $k_0 = 20$, $\delta = -0.1$, $m = 3$, $Le = 10$, $\lambda = 0.25$, $\mathcal{R}_C = -50$. In each case the values of ψ on the streamlines are evenly spaced, and in each plot darker shading corresponds to lower values; scales are arbitrary.

balances with diffusion in the temperature perturbation equation (5.20), and it balances with the $\partial\phi'/\partial z$ term in the concentration perturbation equation (5.21), for all values of Δ^c. This results in an offset between the porosity and circulation cells, which in turn causes the upwards movement of circulation and temperature cells, and downwards movement of the porosity and concentration cells.

5.5 Summary of linear stability analysis

We have performed a linear stability analysis to investigate how the evolution of a reactive porous medium affects the onset of thermosolutal convection.

We have revisited the linear stability analysis of non-evolving reactive thermosolutal convection, as presented in Pritchard and Richardson (2007), and noted that precipitation and dissolution change the positions of the stability boundaries from those in pure thermosolutal convection. Increasing the reaction rate stabilises the system in the solutally unstable regime as the reaction eliminates destabilising solutal perturbations. A strong reaction rate ($k_0 > k_0^{\text{crit}}$) destabilises the system in the solutally stable regime as it weakens the stabilising solutal perturbations.

As with solutal convection, the porosity evolution influenced the stability boundary, even though it occurs over a longer timescale than convection and reaction. Regardless of the reaction rate and the exact destabilising nature of the thermal and solutal gradients, when the system is close to the threshold of instability (as calculated without porosity evolution), a new unstable reaction-diffusion mode becomes available, and this mode persists when the thermal Rayleigh number is reduced below the critical value required for buoyant instability. This unstable reaction-diffusion mode was also seen in chapter 3 for subcritical values of the solutal Rayleigh number.

In the solutally unstable regime, regardless of whether the system was thermally stable or unstable, the behaviour of the growth rate σ and the perturbation structures revealed by the Galerkin analysis are qualitatively identical to those obtained in chapter 3 for reactive evolving solutal convection. Recall that the model of reactive solutal convection is derived from the full thermsolutal model in the limit $\hat{\kappa}_T \to \infty$ and $\hat{\beta}_T = 0$, and therefore can be thought of as thermosolutal convection with an infinite Lewis number. Although we use a lower value of the Lewis number, $Le = 10$, for thermosolutal convection, this similarity in behaviour is unsurprising since we still have faster thermal diffusion than solutal diffusion, and so the thermal gradient is secondary in solute-driven convection.

Different behaviour was seen in the solutally stable regime, however. Here, the reaction rate plays an important role at the onset of convection, with a 'slow'

subcritical reaction leading to an oscillatory instability, but a 'faster' supercritical reaction leading to a monotonic instability. Instead of the tilted cells and lateral movement seen in the solutally unstable case, the Galerkin analysis shows a vertical displacement of the cells, with the porosity and concentration cells being squashed towards the bottom of the layer, while circulation and temperature cells are squashed towards the top of the layer.

In the next chapter we will use numerical techniques to verify the linear stability analysis and investigate the long-term evolution in both the solutally stable and unstable regimes.

Chapter 6

Thermosolutal convection: numerical results

In this chapter we validate the stability analysis of chapter 5 using a numerical model, and carry out a sequence of numerical experiments to investigate the longer-term behaviour of the system. In particular, we seek to identify and interpret particular feedback mechanisms which control the evolution of the porous matrix. Finally, we summarise our results and draw some general conclusions.

6.1 Numerical simulations

A full numerical integration of the system was carried out in order both to test the predictions of the linear stability analysis and to examine the nonlinear behaviour and flow-permeability feedback over longer time scales.

Since preliminary numerical simulations encountered problems with negative porosities which developed at isolated grid points, we define $\Phi = \ln(\phi)$ to ensure values of ϕ remain positive. Furthermore, we define $\tilde{T} = -\mathrm{sgn}(\mathcal{R}_T)T'$ and

$\tilde{C} = \mathrm{sgn}(\mathcal{R}_C)C'$ as in §5.4.3, and rewrite (5.12)–(5.15) as

$$\nabla \cdot \left[\left(\frac{\exp(\Phi)}{\phi_0} \right)^{-2} \nabla \psi \right] = -\mathcal{R}_C \mathrm{sgn}(\mathcal{R}_C) \frac{\partial \tilde{C}}{\partial x} + \mathcal{R}_T \mathrm{sgn}(\mathcal{R}_T) \frac{\partial \tilde{T}}{\partial x}, \tag{6.1}$$

$$\frac{\partial \tilde{T}}{\partial t} - \lambda \left[\frac{\partial \psi}{\partial z} \frac{\partial \tilde{T}}{\partial x} - \frac{\partial \psi}{\partial x} \left(-\mathrm{sgn}(\mathcal{R}_T) + \frac{\partial \tilde{T}}{\partial z} \right) \right] = \nabla^2 \tilde{T}, \tag{6.2}$$

$$\begin{aligned} \exp(\Phi) \frac{\partial \tilde{C}}{\partial t} - \phi_0 \left[\frac{\partial \psi}{\partial z} \frac{\partial \tilde{C}}{\partial x} - \frac{\partial \psi}{\partial x} \left(\mathrm{sgn}(\mathcal{R}_C) + \frac{\partial \tilde{C}}{\partial z} \right) \right] = \\ \frac{1}{Le} \nabla \cdot \left(\exp(\Phi) \frac{\partial \tilde{C}}{\partial x}, \exp(\Phi) \left(\mathrm{sgn}(\mathcal{R}_C) + \frac{\partial \tilde{C}}{\partial z} \right) \right) \\ -k_0 \frac{\exp(\Phi)(1 - \exp(\Phi))}{1 - \phi_0} (\mathrm{sgn}(\mathcal{R}_C \mathcal{R}_T) \tilde{T} + \tilde{C}), \end{aligned} \tag{6.3}$$

$$\frac{\partial \Phi}{\partial t} = -\delta k_0 \frac{(1 - \exp(\Phi))}{1 - \phi_0} (\mathrm{sgn}(\mathcal{R}_T) \tilde{T} + \mathrm{sgn}(\mathcal{R}_C) \tilde{C}), \tag{6.4}$$

This redefinition guarantees that $\tilde{T} > 0$ and $\tilde{C} > 0$ will correspond to regions of higher temperatures and concentrations, respectively, while $\tilde{T} < 0$ and $\tilde{C} < 0$ will correspond to regions of lower temperatures and concentrations, respectively.

The system (6.1)–(6.4) was numerically integrated using the finite element package Comsol Multiphysics v3.5a. The equations were solved in a rectangular domain, $0 < x < 10$, $0 < z < 1$, and the boundary conditions (5.16) were applied on the horizontal boundaries, while periodicity was imposed on the vertical boundaries. For all numerical simulations described here, the initial conditions were taken to be

$$\begin{aligned} \tilde{T}(x, z, 0) = \tilde{C}(x, z, 0) = z(1 - z)\epsilon \sin(\pi x), \\ \Phi(x, z, 0) = \ln(\phi_0 + 0.01 z(1 - z) \sin(\pi x)), \end{aligned} \tag{6.5}$$

where $\epsilon = 10^{-3}$.

To verify that our numerical model converged a number of simulations were conducted over 5000 time units using various values for the relative and absolute tolerances. We used two reaction rates, $k_0 = 5$ and $k_0 = 20$, and three values of the solutal Rayleigh number, $\mathcal{R}_C = -15$, $\mathcal{R}_C = 10$ and $\mathcal{R}_C = 30$, to cover each

convective quadrant of the stability diagram (see figure 5.1). We found that our solution had converged with a relative tolerance of 10^{-3} and an absolute tolerance of 10^{-4}.

The robustness of our numerical model was checked by conducting simulations using 1120, 4480, 17920, and 71680 triangular mesh elements. Model results were mesh independent when we used at least 4480 elements, however, the time to conduct each simulation increased dramatically. Therefore, for all the tests conducted we used 4480 mesh elements. Further details of the tolerance and mesh independence testing can be found in appendix B.2.

6.1.1 Stability boundary and the onset of convection

Figure 6.1 summarises a large number of numerical simulations carried out to validate the linear stability analysis against the numerics. Each simulation was 1500 time units long and was started from the initial conditions (6.5). This length of simulation ensured that there was enough time for convection to develop, even in the marginal cases. Convection was said to have developed if the maximum value of $|\mathbf{u}|$ was greater than 10^{-1} by the end of the simulation.

Figure 6.1(a) shows the results for $k_0 = 5$, while (b) shows the results for $k_0 = 20$. In both cases the linear stability results for $\delta = 0$ (see §5.3.2) agree very well with the numerical results. This suggests that the effects of porosity evolution on the onset of convection are rather subtle, as also seen for single-diffusive convection (see §3.3.1).

6.1.2 Long-term behaviour

When examining the long-term behaviour of the system, we will consider three different scenarios as in §5.4.3: firstly the combination of a destabilising solutal gradient with either a stabilising or destabilising thermal gradient; secondly a destabilising thermal gradient with a stabilising solutal gradient and a subcritical reaction rate so the onset of instability is oscillatory; and thirdly a destabilising thermal gradient with a stabilising solutal gradient and a supercritical reaction

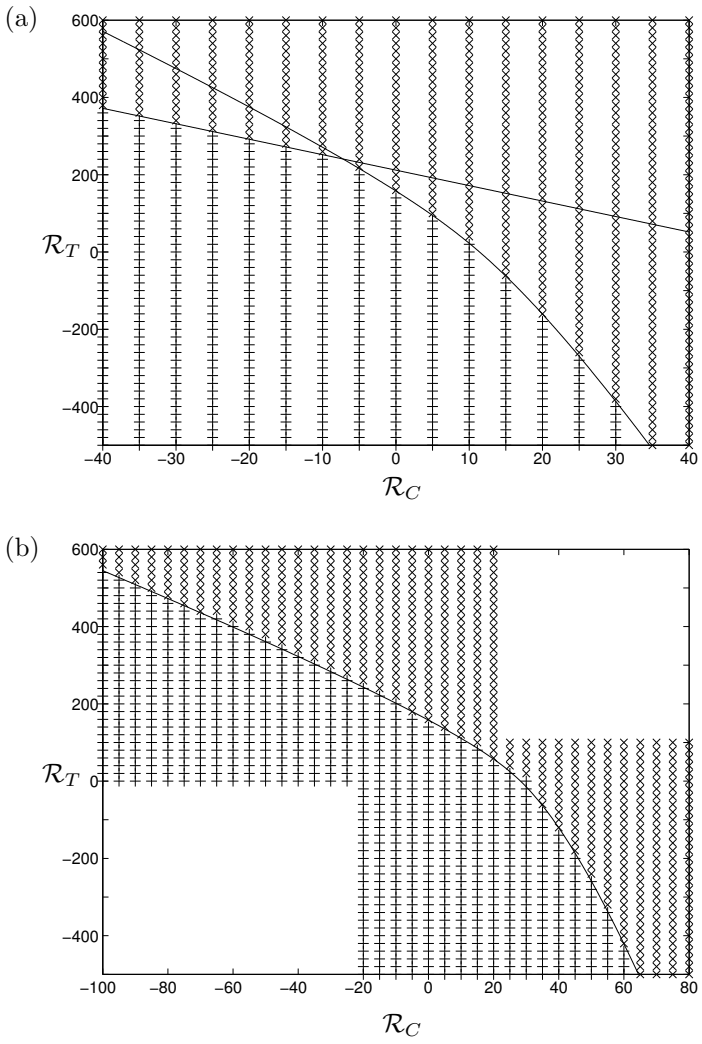

Figure 6.1: Numerical tests of the stability boundaries for $\lambda = 0.25$, $Le = 10$, $\phi_0 = 0.1$, $|\delta| = 0.001$, and (a) $k_0 = 5$, (b) $k_0 = 20$. The solid lines represent $\mathcal{R}_T = \mathcal{R}_T^b$ and $\mathcal{R}_T = \mathcal{R}_T^c$ (cf. figures 5.1(b, c); the points represent either the non-convective (+) or convective (×) case.

rate so the onset of instability is direct. Each simulation we describe lasted for 10^4 time units and used the parameters $\phi_0 = 0.1$, $|\delta| = 0.001$, $Le = 10$, and $\lambda = 0.25$. For each value of the solutal Rayleigh number $\mathcal{R}_C$ used we take the corresponding thermal Rayleigh number to be 10% above its critical value as defined in §5.3.2.

6.1.2.1 Scenario one: destabilising solutal gradient

In this section we consider the combination of a destabilising solutal gradient with either a stabilising or destabilising thermal gradient. Recall from §5.4.3.1 that these situations are analogous to those found in reactive solutal convection where the porosity evolution is driven solely by the concentration perturbation. Therefore, we expect the long-term behaviour to be similar to that presented in §3.3.2. However, will we discover that there are some subtle differences that result from the relative strength of the thermal gradient when compared with the solutal gradient. When the solutal gradient dominates the thermal gradient a slow lateral migration of the convection pattern occurs and, when the thermal gradient dominates the solutal gradient, we see the complete suppression and re-emergence of convection over long time scales.

Stabilising thermal gradient

We first consider the combination of a destabilising solutal gradient with a stabilising thermal gradient. Figure 6.2 shows the evolution of the concentration perturbation $\tilde{C}$, temperature perturbation $\tilde{T}$ and the porosity ϕ for the left half of the domain for $\mathcal{R}_C = 30$, $\mathcal{R}_T = -348$ and $k_0 = 5$. The solid lines on each plot are the streamlines, which are evenly spaced with the same contours used at each time.

By $t = 70$, steady convection has been established (figure 6.2(a)). At this time all the fields are in phase; that is, regions of $\tilde{C} > 0$ and $\tilde{T} > 0$ coincide with regions of lower porosity ($\phi < \phi_0$), and regions of $\tilde{C} < 0$ and $\tilde{T} < 0$ coincide with regions of higher porosity ($\phi > \phi_0$). From (6.4), we expect porosity to decrease where $\tilde{C} > 0$ and $\tilde{T} > 0$ and to increase where $\tilde{C} < 0$ and $\tilde{T} < 0$, since the concentration perturbations are larger than the temperature perturbations throughout the domain because thermal diffusion is faster than solutal diffusion. As the flow is buoyancy-driven, downward flow is favoured where $\tilde{C} > 0$ and $\tilde{T} > 0$, drawing down higher concentrations and temperatures from the top boundary, and upward flow is favoured where $\tilde{C} < 0$ and $\tilde{T} < 0$, drawing up lower concentrations and temperatures from the bottom boundary: this is the essential mechanism

that sustains convection.

Once steady convection has been established, the porosity field continues to evolve with porosity increasing in regions which coincide with $\tilde{C} < 0$ and $\tilde{T} < 0$, and decreasing in regions which coincide with $\tilde{C} > 0$ and $\tilde{T} > 0$. This evolution continues until it triggers a secondary instability in the form of a phase shift. Figure 6.2(b) shows the fields at $t = 300$, part-way through the shift. We can see that both the concentration and temperature fields have moved approximately an eighth of a cell (0.25 x-units) to the right, but the porosity field remains the same as before the shift. Furthermore, there is a slight tilting of the concentration, temperature and circulation cells to the left. This tilting is most apparent in the streamlines.

By the end of the shift at $t = 500$ (figure 6.2(c)), the concentration and temperature fields along with the streamlines have moved a half cell (approximately a half x-unit) to the right, but the porosity field is still effectively unchanged. Downward flow still occurs in regions where $\tilde{C} > 0$ and $\tilde{T} > 0$, but this now coincides with high-porosity regions.

Further evidence of the phase shift can be seen in figure 6.6(a), which shows the maximum absolute velocity. We can see that convection develops and is maintained for approximately 350 time steps before the velocity dips slightly around the time of the phase shift as the circulation slows and then re-establishes itself.

As in reactive solutal convection (see §3.3.2), the secondary instability occurs as a result of the positive feedback between the porosity field and the concentration and temperature fields, which results in clogging in the downflow regions. This clogging eventually reaches some critical state and displaces the downflow sideways resulting in tilted convection cells. These are overcome by diffusion and the circulation begins to shut down, before being replaced by a reversed circulation. The sideways migration of these of these fully developed, nonlinear convection cells is reminiscent of the migration of small amplitude cells seen in the linear analysis close to $\mathcal{R}_T = \mathcal{R}^c_{T,0}$ (§5.4.3.1). However, unlike the phenomenon seen in the linear case, the tilting and sideways movement here is readily halted by the tendency of buoyancy-driven convection to favour stationary, upright cells.

At $t = 500$ the concentration and temperature fields are out of phase with the porosity field: regions of large positive concentration and temperature perturbations now coincide with regions of high porosity and vice versa. In these $\tilde{C} > 0$ and $\tilde{T} > 0$ regions porosity will decrease, and in $\tilde{C} < 0$ and $\tilde{T} < 0$ regions porosity will increase. Therefore, the porosity evolution strives to get the concentration and temperature fields back into phase with the porosity field.

Figure 6.6(a) also shows the porosity evolution, plotted with the maximum absolute velocity to illustrate the correlation with the phase shifts. At the time of the phase shift, the porosity contrast has reached a local maximum, with a peak in the maximum porosity and a trough in the minimum porosity. After the shift the maximum porosity decreases and the minimum porosity increases as now the porosity field is out of phase with the concentration and temperature fields. By $t \approx 600$, the porosity field is back in phase with the concentration and temperature field and the porosity contrast begins to increase again at a similar rate to that before the phase shift. This behaviour of the maximum velocity and porosity contrast is the same signature of a phase shift as seen in chapter 3 for solutal convection (cf. figure 3.12).

At $t = 800$ (figure 6.2(d)), the porosity is approximately back in phase with the concentration and temperature fields. There is now a vertical asymmetry in the porosity field with more dissolution towards the top of the domain, and correspondingly the centres of the circulation cells have moved slightly upwards towards these high porosity regions.

From figure 6.6(a) we can see that the system undergoes many phase shifts, but each subsequent shift occurs over a longer time scale. By $t = 1500$ (figure 6.2(e)) the system has undergone another phase shift and the concentration, temperature and circulation cells have shifted a further half cell to the right. There is still subtle evidence of a vertical asymmetry in the porosity and circulation fields, with higher porosity regions and the centres of the circulation cells appearing in the top of the domain.

By $t = 3000$ (figure 6.2(f)), the vertical asymmetry in the porosity and circulation cells is more distinct. There is clear evidence of layering in the porosity field with low porosity dominating the lower half of the domain. The system is still

undergoing slow phase shifts, and the concentration, temperature and circulation fields have shifted a further half cell to the right.

This slow rightwards movement and porosity layering continues through to the end of the simulation. At $t = 5000$ (figure 6.2(g)) the concentration, temperature and circulation fields have shifted a further half cell to the right and the leftward tilting is still obvious. Here the dashed contours represent additional streamlines to aid with the flow visualisation. The layer of low porosity has moved upwards slightly and, correspondingly, the centres of the circulation cells have moved upwards, too.

By $t = 7500$ (figure 6.2(h)), the temperature, concentration and circulation cells have shifted further to the right. The low porosity barrier in the centre of the domain is now pierced by higher porosity channels, but the centres of the circulation cells remain near the top of the domain, so very little flow reaches the bottom of the domain. By $t = 10000$ (figure 6.2(i)) the high porosity channels have evolved sufficiently to allow the circulation to span the full height of the domain. Note that in these channels the flow is much faster, as seen by the tighter packed streamlines.

Similar behaviour can be seen when the reaction rate is increased to $k_0 = 20$. Figure 6.3 shows the evolution of the concentration perturbation $\tilde{C}$, temperature perturbation $\tilde{T}$ and the porosity ϕ for the left half of the domain for $\mathcal{R}_C = 30$, $\mathcal{R}_T = -13$ and $k_0 = 20$, while figure 6.6(b) shows the corresponding evolution of the maximum absolute velocity and the porosity contrast. The most prominent difference between figure 6.6(a) and (b) is that the higher reaction rate leads to faster evolution of the system.

Buoyancy-driven convection has been established by $t \approx 30$ (not shown); at this time the convection pattern closely resembles figure 6.2(a), with 10 pairs of counter-rotating cells in the full domain. Once steady convection has been established, the porosity field continues to evolve until it triggers a secondary instability, as with the slower reaction rate. Figure 6.3(a) shows the fields at $t = 200$, just before the first phase shift. As before, the concentration and temperature fields are in phase with the porosity field. Note that the streamlines are tighter packed in the higher porosity regions, indicating that upward flow is

faster than downward flow.

By the end of the shift at $t = 300$ (figure 6.3(b)), the concentration and temperature fields along with the streamlines have moved a half cell (approximately one half x-unit) to the left, but the porosity field is still effectively unchanged. Furthermore, the concentration and temperature fields are now out of phase with the porosity. The overall pattern is similar to figure 6.2(c).

The phase shift can also be seen in the maximum absolute velocity and porosity contrast (figure 6.6(b)). Convection develops and is maintained for approximately 200 time units, but there is a dip in the velocity around the time of the phase shift as the circulation slows and re-establishes itself. After this shift, the system settles back into a quasi-equilibrium state of steady convection with the maximum velocity and porosity contrast first declining then gradually increasing again as the porosity comes back into phase with the concentration and temperature fields. Analogous behaviour can be seen in figure 6.6(a), although with a faster reaction rate we note that the dip in the maximum velocity is much sharper, and the change in the porosity contrast occurs over a shorter period of time. The sharper dip of the maximum velocity and faster change of the porosity contrast was also seen for reactive solutal convection when the reaction rate was increased (§3.3.2.3).

By $t = 500$ (figure 6.3(c)), the porosity field is back in phase with the concentration and temperature fields, and, as with the slower reaction rate, there is a vertical asymmetry in the porosity field with more dissolution towards the top of the domain. However, in this case alternate high porosity channels are more pronounced, as seen by the tighter packed streamlines in alternate downflow regions.

The system undergoes two more rapid phase shifts; figure 6.3(d) shows the fields at $t = 1500$ after the last rapid shift. The porosity field is again out of phase with the concentration and temperature fields, but now the circulation is much slower. The system now settles into a regime of slow evolution and, although there are no more rapid phase shifts, a slow movement to the left continues, similar to the constant movement seen in the slower reaction rate case. However, note that in this case the symmetry has been broken in the opposite sense, with both the direction of the tilt and the migration reversed from the slower reaction case. This

movement can be seen as the small peaks in the maximum velocity and changes in the porosity contrast in figure 6.6(b), which are analogous to the signature of the faster phase shifts.

As this slow evolution continues, first the porosity contrast becomes more pronounced (figure 6.3(e)), with 'eyes' of high porosity developing near the top of the layer and regions of lower porosity in the centre of the domain. Alternate high porosity channels remain more pronounced. Precisely analogous behaviour was seen in §3.3.2.3 for reactive solutal convection. However, here the slow evolution of the porosity field is hampered by the almost continual slow leftward migration of the circulation, concentration and temperature fields. While reactive solutal convection can be thought of as thermsolutal convection in the limit of infinite Lewis number (cf. §5.5), in the thermosolutal case $Le = 10$, and so thermal diffusion is much slower. Although thermal diffusion is faster than solutal diffusion in both cases, with thermosolutal convection it is not fast enough to restore the tilted cells to their upright position and hence cease the lateral migration of the cells.

At $t = 4500$ (figure 6.3(f)), the 'eyes' of high porosity have developed into higher porosity channels, but since the porosity field is out of phase with the concentration and temperature fields, by $t = 6000$ (figure 6.3(g)) these channels have been blocked, and the layer is dominated by lower porosity, with regions of higher porosity towards the bottom. Once the fields are back in phase, these high porosity regions begin to move back upwards from the bottom of the layer(figure 6.3(h)), until eventually they span the height of the domain (figure 6.3(i)). This layering behaviour is analogous to that seen with a slower reaction rate (figures 6.2(g)-(i)), but the faster reaction rate causes it to occur over a faster timescale.

Destabilising thermal gradient

We now consider the combination of a destabilising solutal gradient with a destabilising thermal gradient. Figure 6.4 shows the evolution of the concentration perturbation $\tilde{C}$, the temperature perturbation $\tilde{T}$ and the porosity ϕ for the left half of the domain for $\mathcal{R}_C = 10$, $\mathcal{R}_T = 25$ and $k_0 = 5$, while the corresponding evolution of the maximum absolute velocity and the porosity contrast is shown in

figure 6.6(c). Although the behaviour in this case is very similar to that seen with a slow reaction rate and a stabilising thermal gradient (figures 6.2 and 6.6(a)), there are some subtle differences.

In this case steady convection is established by $t \approx 130$ (not shown). At this time all the fields are in phase; that is, regions of $\tilde{C} > 0$ and $\tilde{T} < 0$ coincide with regions of lower porosity ($\phi < \phi_0$), and regions of of $\tilde{C} < 0$ and $\tilde{T} > 0$ coincide with regions of higher porosity ($\phi > \phi_0$).

As in the stabilising thermal gradient case, the porosity field evolves until it triggers a secondary instability. Just before the phase shift (figure 6.4(a)), the porosity field is in phase with the concentration and temperature fields, while afterwards the concentration and temperature fields and the streamlines have moved a half cell to the right, resulting in the porosity field now being out of phase with the concentration and temperature fields (figure 6.4(b)). This is the same shifting mechanism as seen in the stabilising thermal gradient case, and the overall pattern after the shift is similar to that seen in figure 6.2(c).

Comparing figures 6.6(a) and (c) we can see that the phase shifts take longer with a destabilising thermal gradient, since the porosity contrast signature of increasing then decreasing occurs over more time units. However, this difference could be a result of the lower solutal Rayleigh number $\mathcal{R}_C$ as opposed to an effect caused by the destabilising thermal gradient. Furthermore, while the maximum velocity remains at a similar level throughout the simulation for $\mathcal{R}_T < 0$ and $k_0 = 5$, it reduces to about half its initial value after $t \approx 5000$ with the destabilising thermal gradient.

Despite these very subtle differences, the long-term behaviour is very similar with both cases undergoing a continuous rightwards migration throughout the simulation, with the porosity field tending towards a layered structure as in figure 6.2(i).

Finally, figure 6.5 shows the evolution of the concentration perturbation $\tilde{C}$, temperature perturbation $\tilde{T}$ and the porosity ϕ for the left half of the domain for $\mathcal{R}_C = 10$, $\mathcal{R}_T = 122$ and $k_0 = 20$, while the corresponding evolution of the maximum absolute velocity and the porosity contrast is shown in figure 6.6(d). As seen before, the higher reaction rate leads to faster phase shifts, and a faster

evolution of the system.

Buoyancy-driven convection has been established by $t \approx 10$ (not shown), with 5 pairs of counter-rotating cells in the full domain. At this time all the fields are in phase, and the porosity field continues to evolve until it triggers a secondary instability, as with all previous cases. Figure 6.5(a) shows the fields just before the first phase shift at $t = 50$. Note that the streamlines are tighter packed in higher porosity regions, so upward flow is faster than downward flow. During the phase shift, the concentration, temperature and circulation fields tilt to the left and begin moving rightwards (figure 6.5(b)) until, after the shift, the fields have moved a half cell (≈ 1 x-unit) to the right, and the concentration and temperature fields are now out of phase with the porosity field (figure 6.5(c)). Now, from the streamlines we see that downward flow is faster than upward flow.

Again, the phase shift can be seen in the maximum absolute velocity and porosity contrast (figure 6.6(d)), with the dip in the maximum velocity at the time of the phase shift as the circulation slows then re-establishes itself. After the shift the system settles back into a quasi-equilibrium state of steady convection with the maximum velocity and porosity contrast first declining then gradually increasing again as the porosity comes back into phase with the concentration and temperature fields. Analogous behaviour can be seen in all subplots of figure 6.6, although with a faster reaction rate we note that the dip in the maximum velocity is much sharper, and the change in the porosity contrast occurs over a shorter period of time.

By $t = 180$ (figure 6.5(d)), the porosity field is back in phase with the concentration and temperature fields. As with previous cases, there is a distinct vertical asymmetry in the porosity field with more dissolution towards the top of the domain, and the centres of the circulation cells have moved upwards.

The system undergoes two more rapid phase shifts; figure 6.5(e) shows the fields just after the last rapid shift at $t = 530$. The porosity field is now out of phase with the concentration and temperature fields, and the circulation is beginning to slow. The system now settles into a regime of slow evolution where the circulation is almost non-existent.

By $t = 3000$ (figure 6.5(f)), the concentration and temperature perturbations

are now much smaller and the vertical asymmetry is now very distinct, with a region of lower porosity dominating the centre of the domain, with a region of much higher porosity at the top boundary and a region of slightly higher porosity at the bottom boundary. Here the dashed contours represent additional streamline contours to aid in the visualisation of the flow. The lower region of higher porosity begins to push its way upwards (figure 6.5(g)) with new circulation cells, squashing the original circulation cells upwards. This reversal of flow brings all the fields back into phase with each other ($t = 6000$, figure 6.5(h)). The upwards migration of the high porosity layer continues ($t = 8000$, figure 6.5(i)), until convection is suddenly re-established at $t \approx 9500$.

Figure 6.5(i) shows the fields at the end of the simulation. The concentration and temperature perturbations are slightly bigger than before the re-establishment of convection, and there is evidence of further rightwards movement. Note that there are now 6 pairs of counter-rotating cells in the full domain, corresponding to a wavenumber of $m \approx 3.77$, whereas previously there were 5 pairs corresponding to a wavenumber of $m \approx 3.14$. Allowing for the quantisation of m which is imposed by the horizontal periodicity of the computational domain, both of these values compare well with the critical wavenumber $m_{C,0}^{\text{crit}} \approx 3.56$ predicted by (5.51).

6.1.2.2 Scenario two: stabilising solutal gradient, destabilising thermal gradient, subcritical reaction rate

In this and the subsequent section we consider the combination of a stabilising solutal gradient with a destabilising thermal gradient. Here, we consider this combination with a subcritical reaction rate and we recall that in this case the transition to instability is through a growing oscillatory mode.

Figure 6.7 shows the evolution of the concentration perturbation $\tilde{C}$, the temperature perturbation $\tilde{T}$ and the porosity ϕ for the left half of the domain for $\mathcal{R}_C = -15$, $\mathcal{R}_T = 299$ and $k_0 = 5$ at the onset of convection. The solid lines on each plot are the streamlines, which are evenly spaced. Note the different magnitudes on each subset of plots.

At $t = 2$ (figure 6.7(a)) all the fields are in phase; that is, regions of $\tilde{C} > 0$

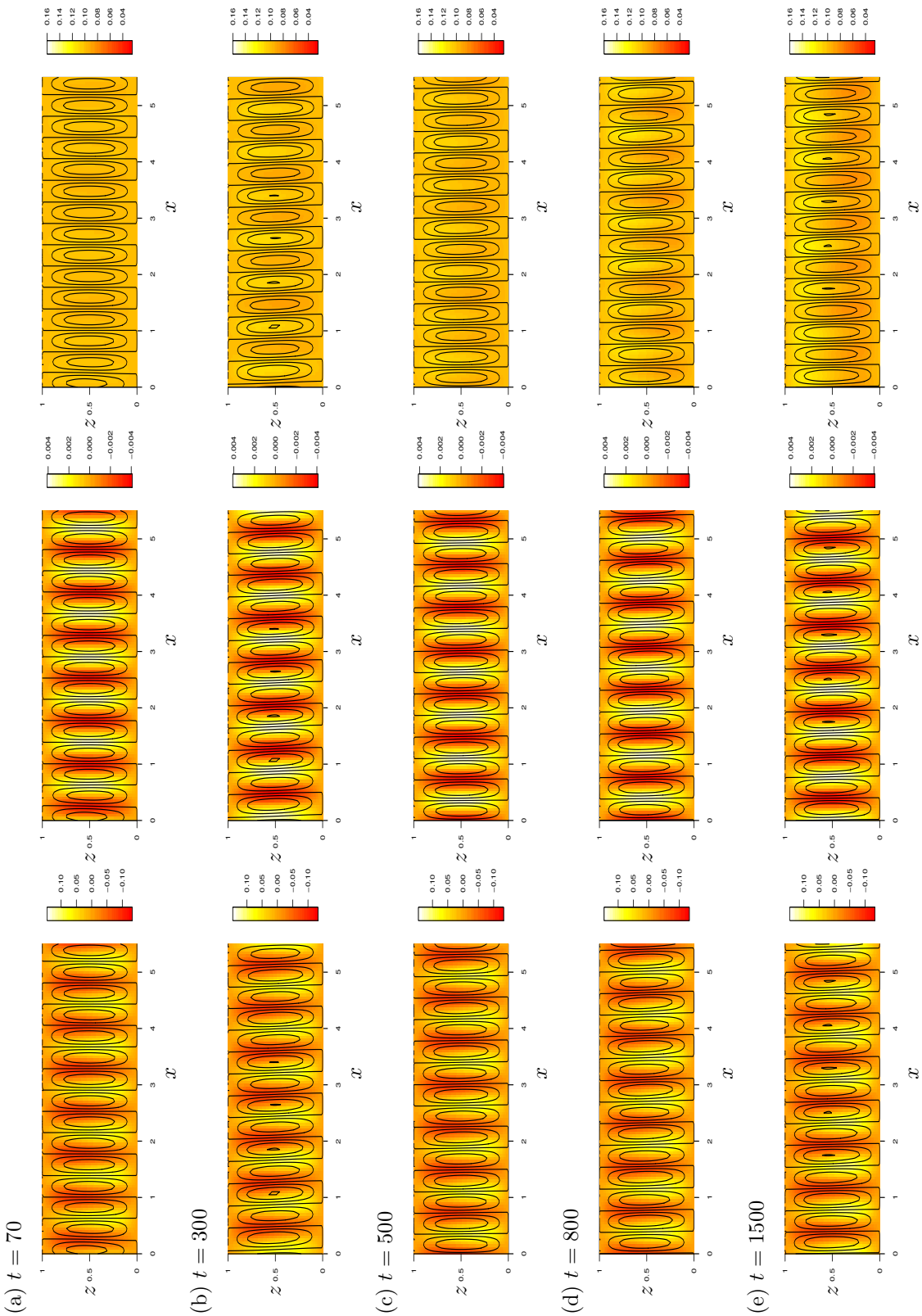
(a) $t = 70$
(b) $t = 300$
(c) $t = 500$
(d) $t = 800$
(e) $t = 1500$
z
x

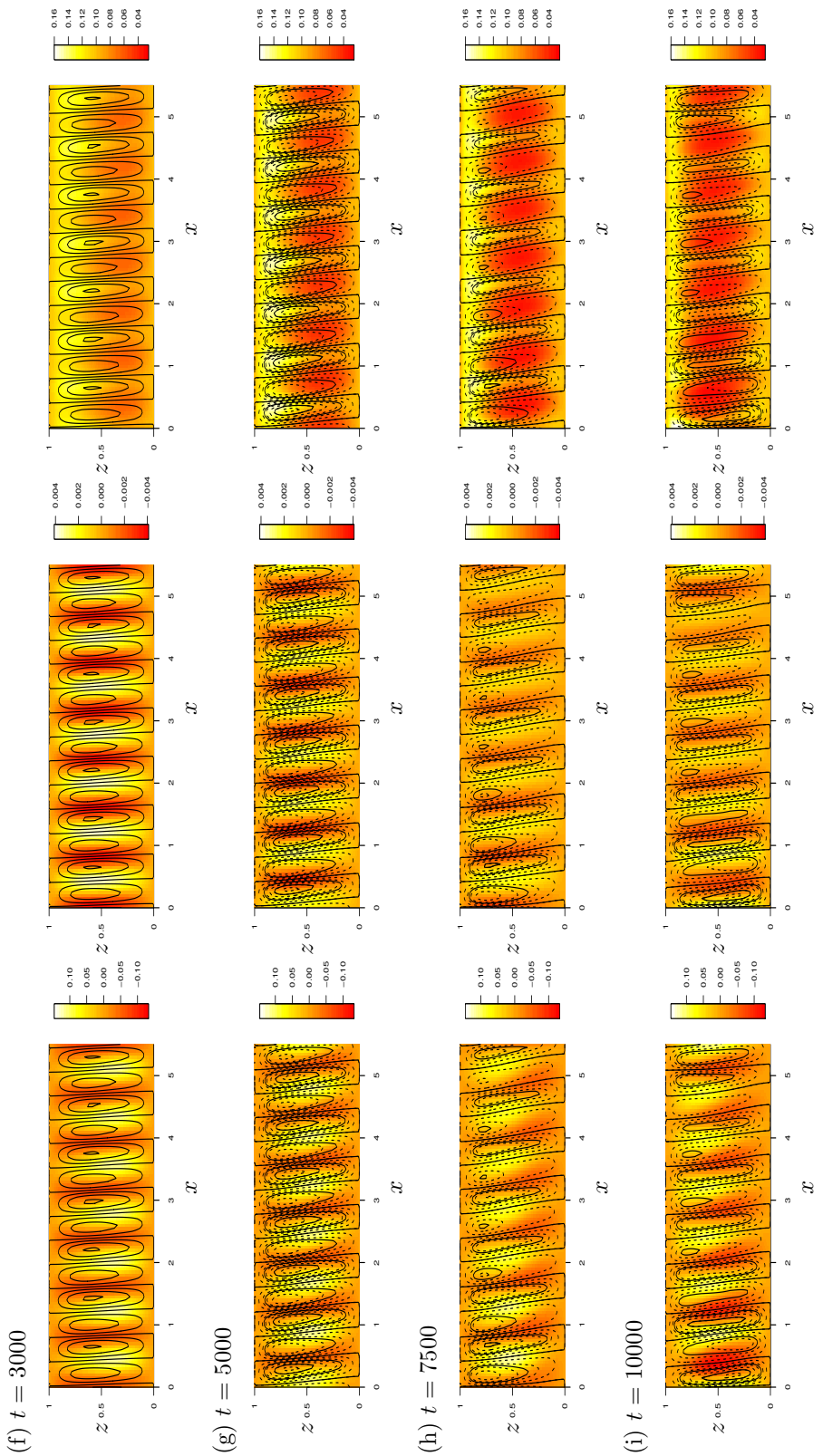

Figure 6.2: Evolution for $\mathcal{R}_C = 30$, $\mathcal{R}_T = -348$, and $k_0 = 5$. Shading indicates solutal concentration perturbation $\tilde{C}$ (left), temperature perturbation $\tilde{T}$ (centre), and porosity ϕ (right). Solid and dashed lines are streamlines.

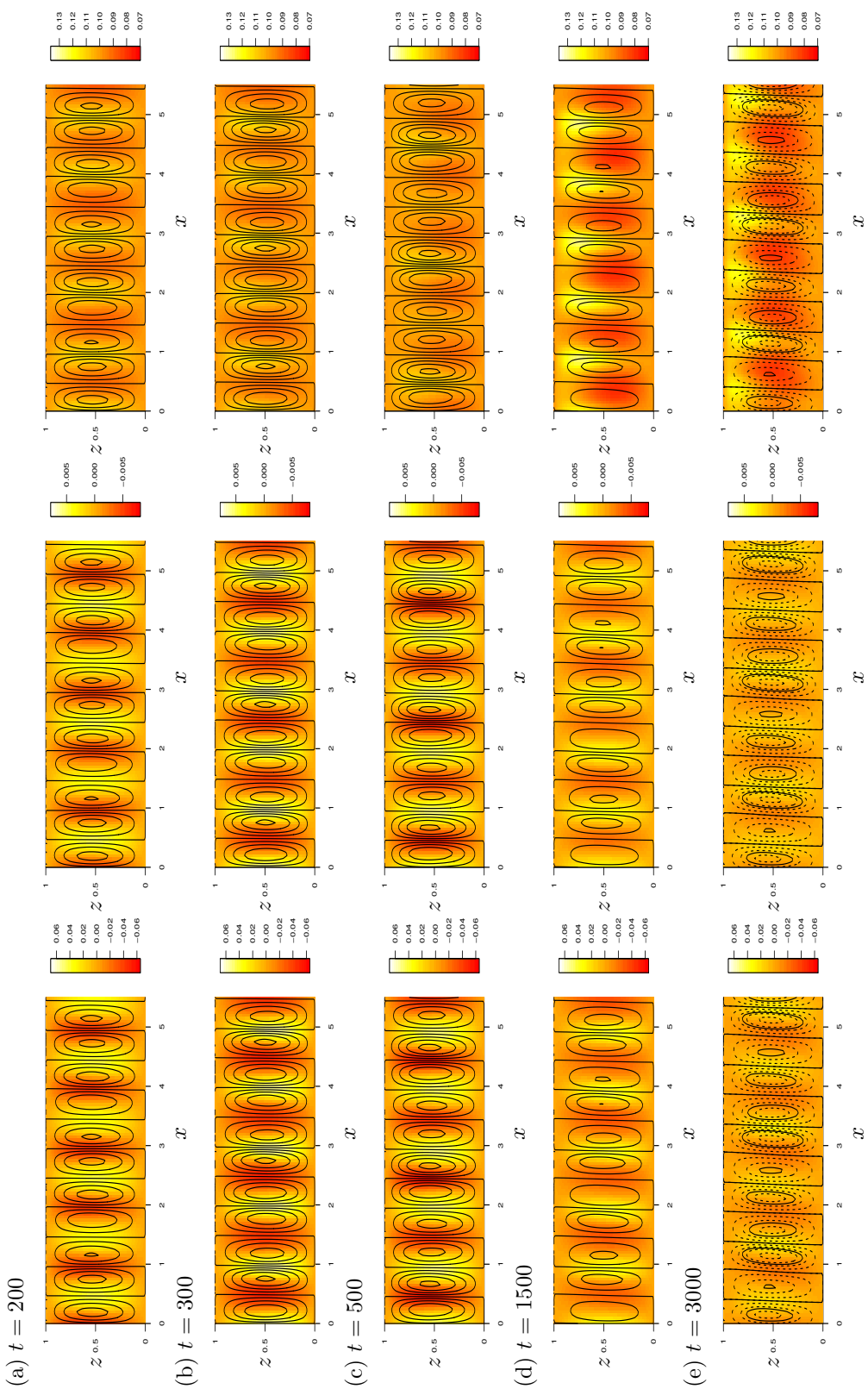
(a) $t = 200$
(b) $t = 300$
(c) $t = 500$
(d) $t = 1500$
(e) $t = 3000$
x
z

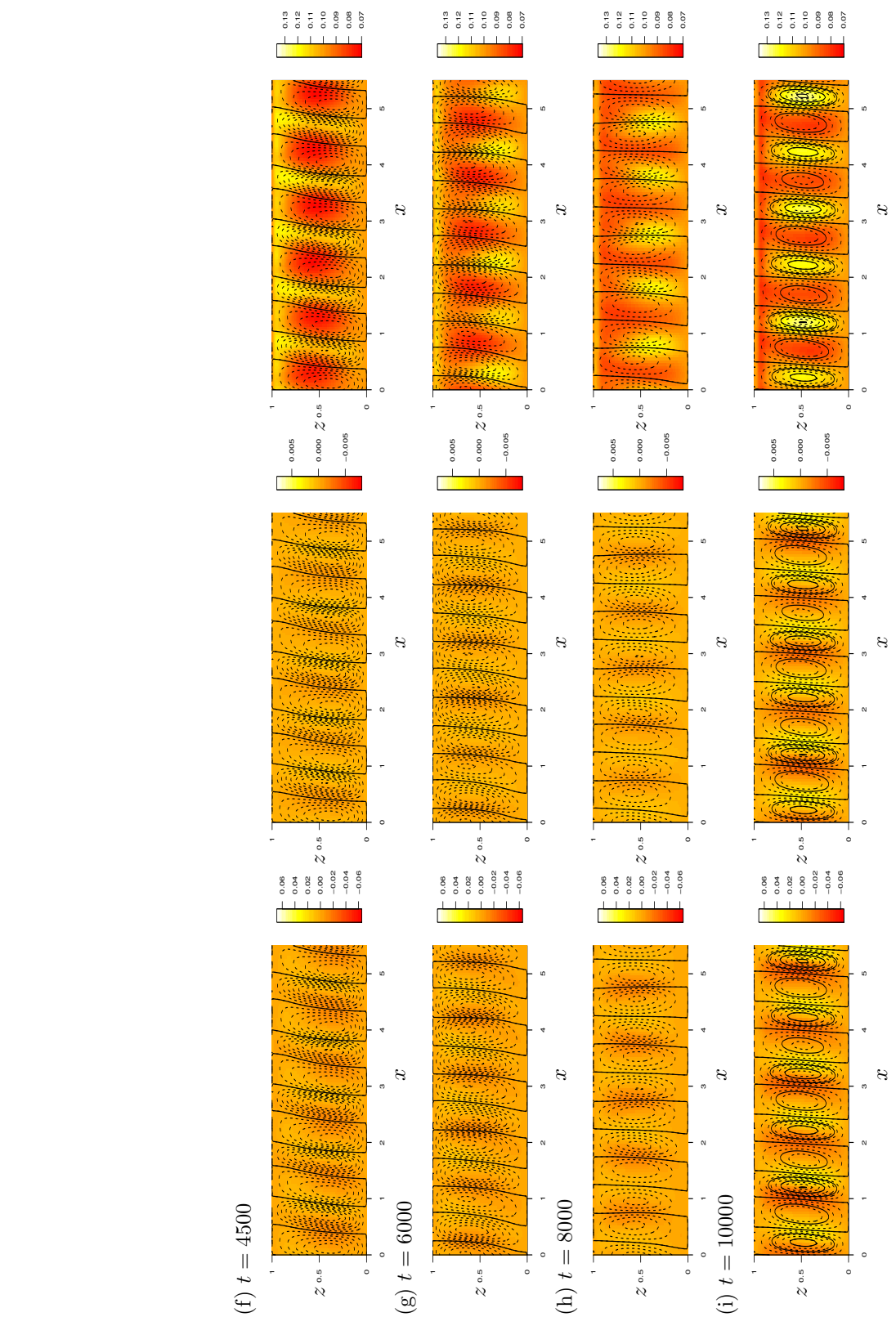

Figure 6.3: Evolution for $\mathcal{R}_C = 30$, $\mathcal{R}_T = -13$, and $k_0 = 20$. Shading indicates solutal concentration perturbation $\tilde{C}$ (left), temperature perturbation $\tilde{T}$ (centre), and porosity ϕ (right). Solid and dashed lines are streamlines.

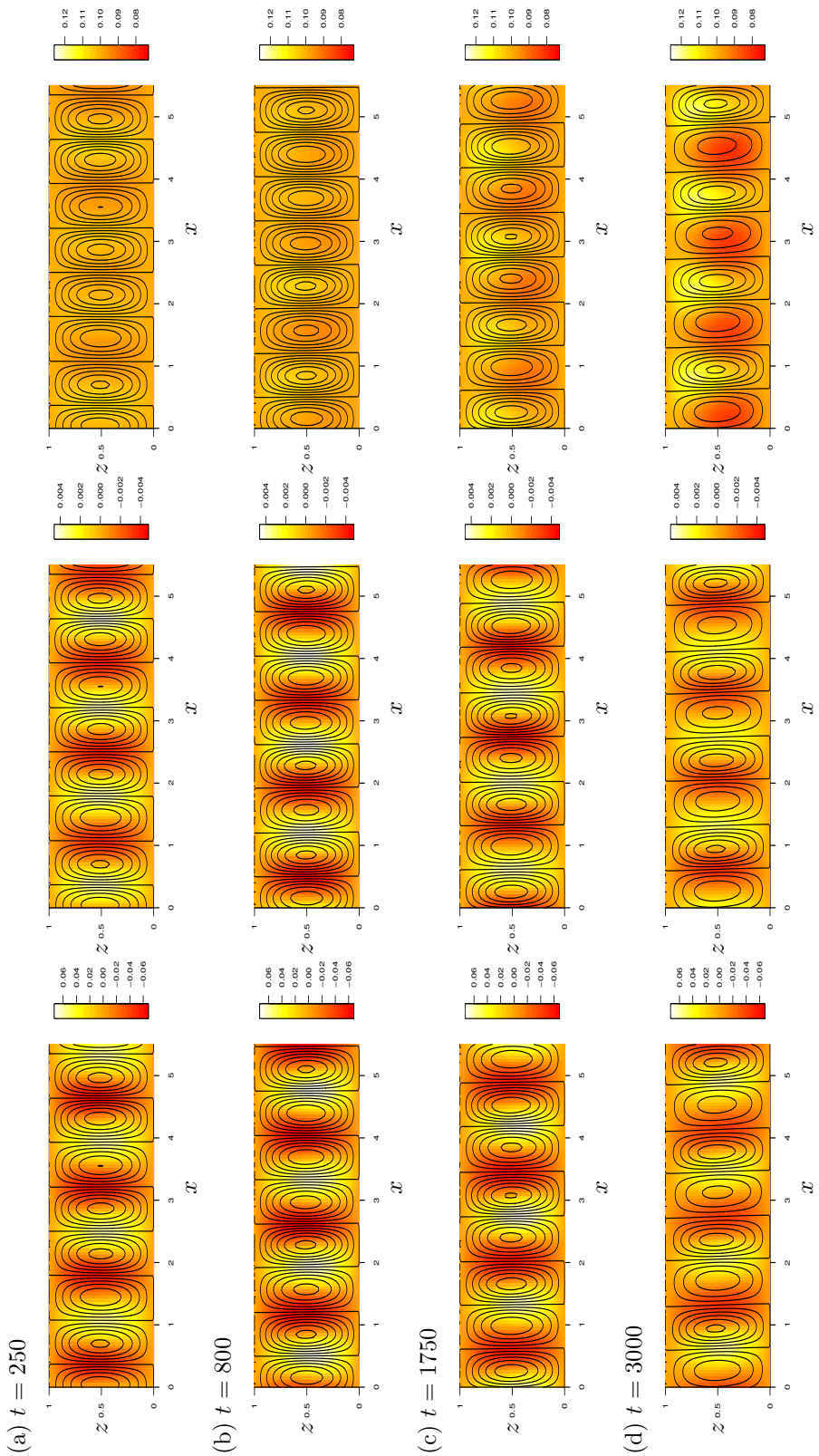
(a) $t = 250$
(b) $t = 800$
(c) $t = 1750$
(d) $t = 3000$
x
z

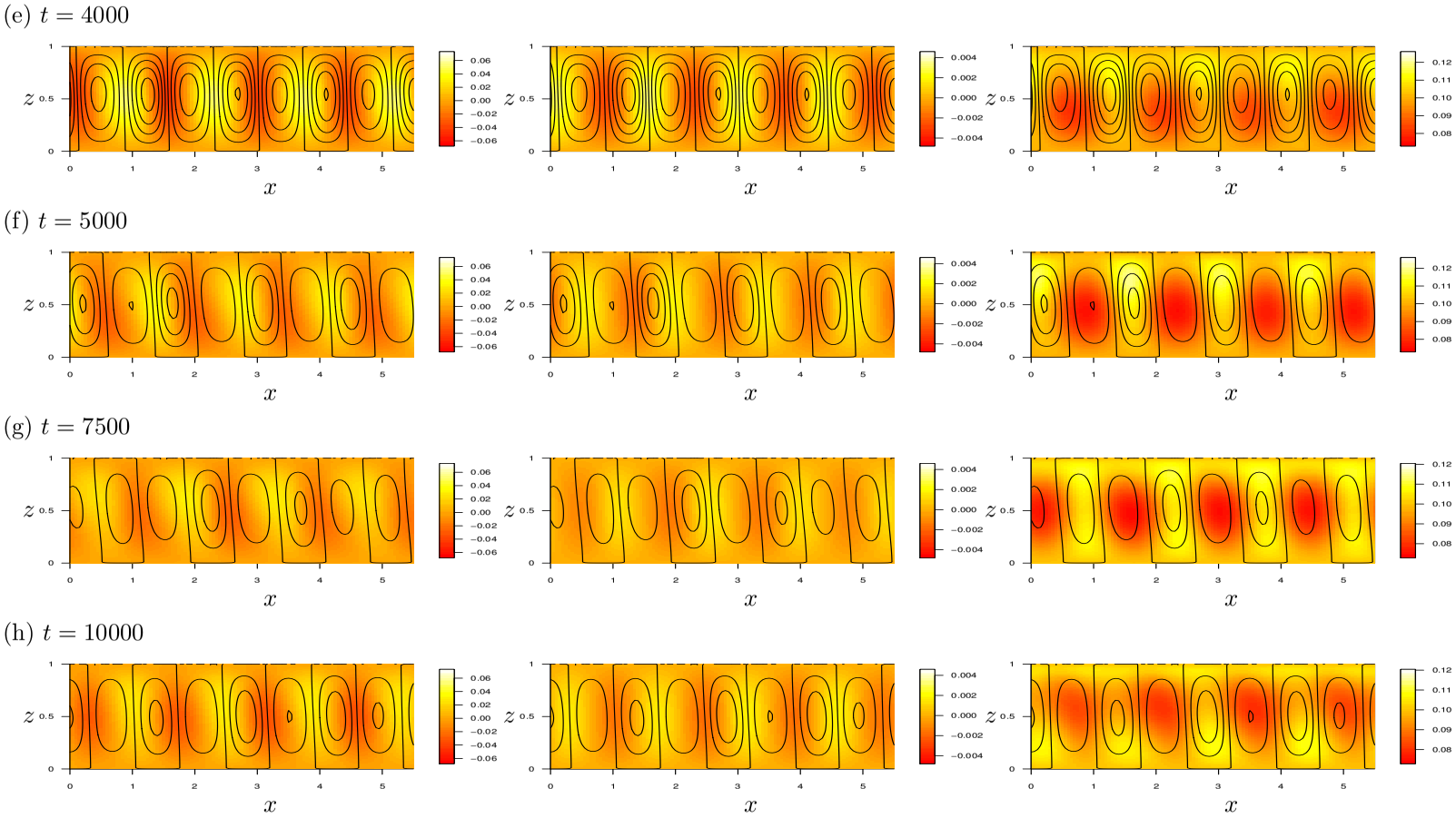

Figure 6.4: Evolution for $\mathcal{R}_C = 10$, $\mathcal{R}_T = 25$, and $k_0 = 5$. Shading indicates solutal concentration perturbation $\tilde{C}$ (left), temperature perturbation $\tilde{T}$ (centre), and porosity ϕ (right). Solid lines are streamlines.

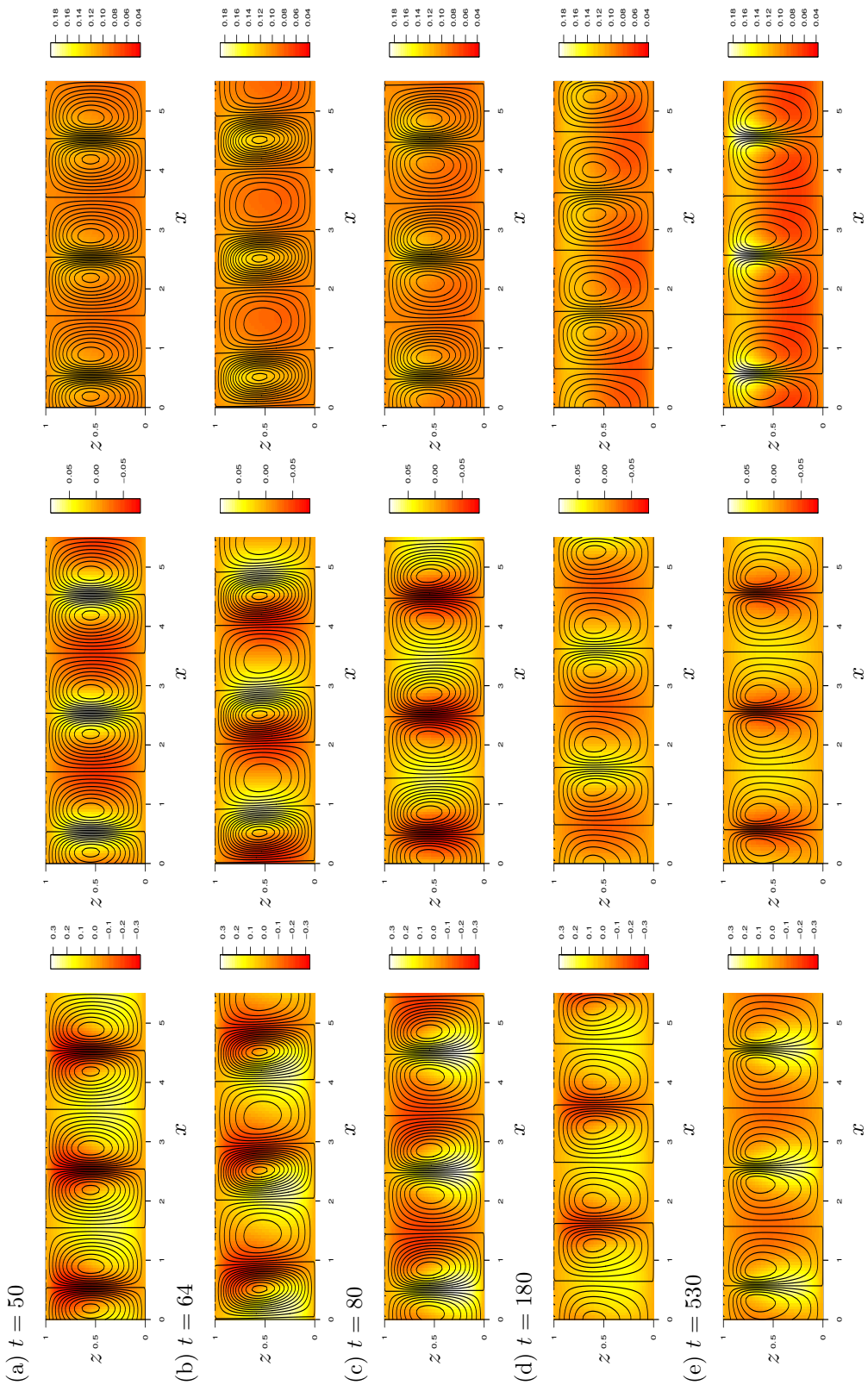
(a) $t = 50$
(b) $t = 64$
(c) $t = 80$
(d) $t = 180$
(e) $t = 530$
z
x

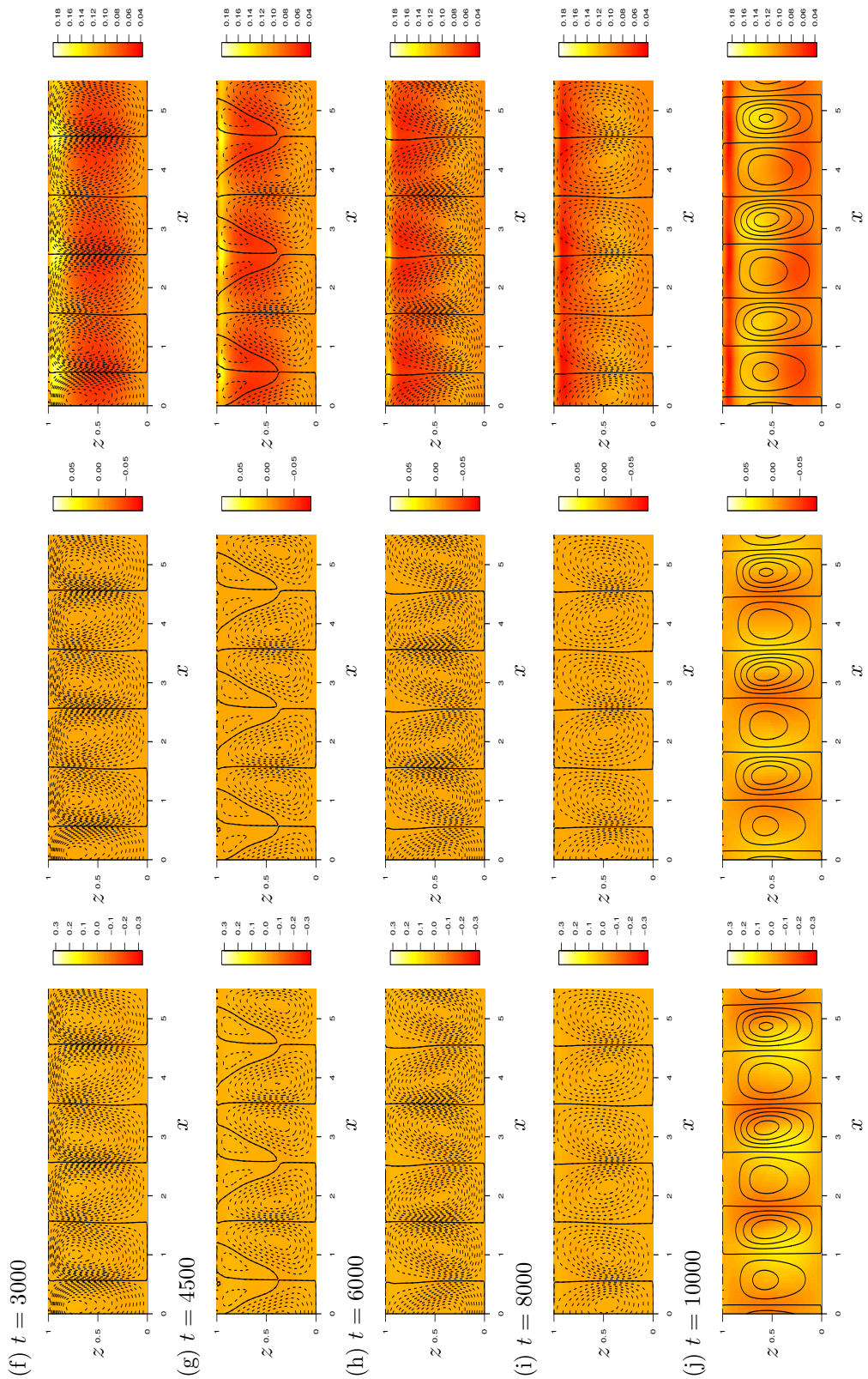

Figure 6.5: Evolution for $\mathcal{R}_C = 10$, $\mathcal{R}_T = 122$, and $k_0 = 20$. Shading indicates solutal concentration perturbation $\tilde{C}$ (left), temperature perturbation $\tilde{T}$ (centre), and porosity ϕ (right). Solid and dashed lines are streamlines.

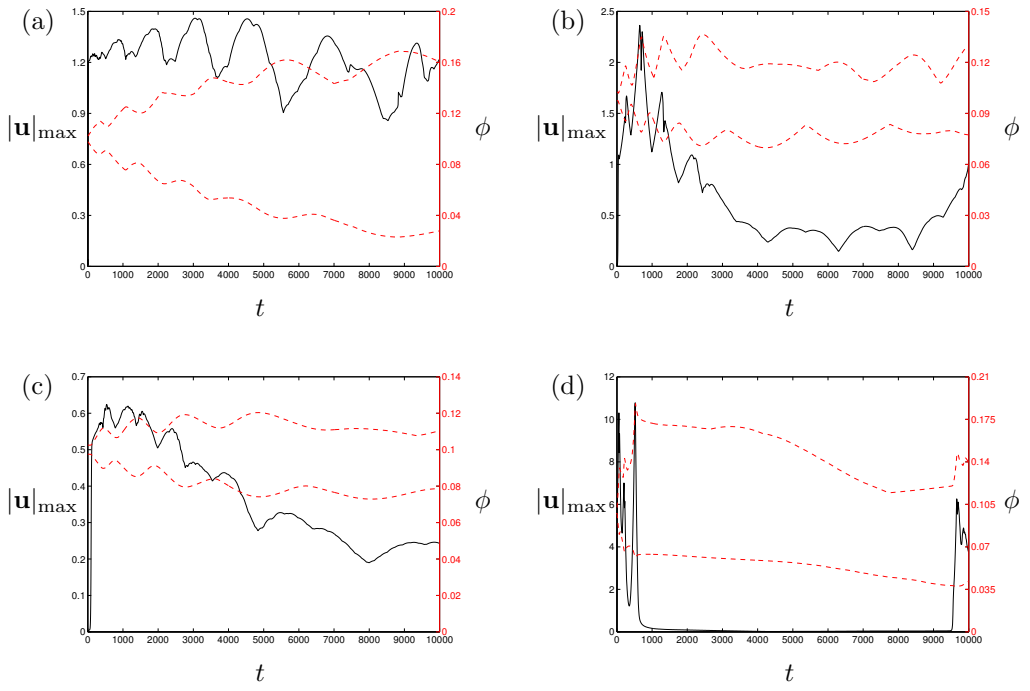

Figure 6.6: Maximum absolute velocity $|\mathbf{u}|$ (solid) and maximum and minimum porosity ϕ (dashed) throughout the whole domain for (a) $k_0 = 5$, $\mathcal{R}_C = 30$, $\mathcal{R}_T = -348$; (b) $k_0 = 20$, $\mathcal{R}_C = 30$, $\mathcal{R}_T = -13$; (c) $k_0 = 5$, $\mathcal{R}_C = 10$, $\mathcal{R}_T = 25$; (d) $k_0 = 20$, $\mathcal{R}_C = 10$, $\mathcal{R}_T = 122$.

and $\tilde{T} > 0$ coincide with regions of lower porosity ($\phi < \phi_0$), and regions of $\tilde{C} < 0$ and $\tilde{T} < 0$ coincide with regions of higher porosity ($\phi > \phi_0$). At this time we have upwards flow in $\tilde{C} > 0$ and $\tilde{T} > 0$ regions, and downwards flow in $\tilde{C} < 0$ and $\tilde{T} < 0$ regions. However, by $t = 2.2$ (figure 6.7(b)), the flow direction has switched, but the concentration, temperature and porosity fields have remained in phase. The concentration and temperature fields move a half cell by $t = 2.3$ (figure 6.7(c)), so again we have upwards flow in $\tilde{C} > 0$ and $\tilde{T} > 0$ regions, but now the concentration and temperature fields are out of phase with the porosity field. The fields remain out of phase, and by $t = 3$ (figure 6.7(d)) nonlinear effects have become significant as seen by the plumes of high and low concentration perturbations.

The oscillatory onset can also be seen in the inset of figure 6.10(a), which shows the maximum absolute velocity. We can see that the maximum velocity grows as convection tries to establish but then drops as the flow direction changes. This occurs twice before the phase shift at $t = 2.3$, after which the velocity grows rapidly as convection is established.

Since nonlinear effects enter the system so rapidly, there is not a chance to see the upward movement of the circulation and temperature fields and downwards movement of the concentration and porosity fields predicted by the Galerkin analysis of §5.4.3.2. However, the concentration and temperature fields are out of phase with the porosity field, as predicted.

Figure 6.8 shows the long-term evolution of the concentration perturbation $\tilde{C}$, temperature perturbation $\tilde{T}$ and porosity ϕ for the left half of the domain. The solid lines on each plot are the streamlines, which are evenly spaced with the same contours used at each time. These should be read in conjunction with figure 6.10(a) which shows the evolution of the maximum absolute velocity, and the maximum and minimum porosity.

At $t = 100$ (figure 6.8(a)) the concentration and temperature fields are very similar to those at the onset of convection ($t = 3$, figure 6.7(d)), but the porosity field has begun to evolve with porosity increasing where $\tilde{C} < 0$ and $\tilde{T} < 0$ and decreasing where $\tilde{C} > 0$ and $\tilde{T} > 0$, in agreement with (6.4). Therefore, the porosity is reduced slightly near the top of the layer, and correspondingly the

centres of the circulation cells have moved down towards the bottom of the layer. This region of reduced porosity is pierced by higher porosity channels which correspond with the downflow regions of the circulation. Here, downflow is faster than upflow as seen by the tighter packed streamlines.

The porosity continues to evolve and by $t = 500$ (figure 6.8(b)) the region of lower porosity at the top of the domain has extended downwards, squashing the circulation cells even more. High porosity channels still pierce the low porosity region in areas of downwards flow, but now upflow under the low porosity barrier is faster than downflow.

Figure 6.10(a) shows the evolution of the maximum absolute velocity, and we can see that convection is established and maintained until $t \approx 750$ when the porosity evolution has forced the circulation into too small a region to be maintained (figure 6.8(c)). We then enter a regime of slow porosity evolution which strives to reach a state where convection can be maintained again.

At $t = 1000$ (figure 6.8(d)) the circulation is still contained in the lower half of the domain, but additional counter-rotating cells have formed in the high porosity region at the bottom of the channels. Again, the dashed contours are additional streamlines to aid with the flow visualisation. By $t = 5000$ (figure 6.8(e)) these new circulation cells have pushed upwards and now extend the full height of the domain, squashing the original circulation cells even further at the bottom of the domain. Note that further pairs of counter-rotating circulation cells have formed at the top of the domain at the top of the high porosity channel, and by $t = 10000$ (figure 6.8(f)) these circulation cells have started to dominate the domain.

From the maximum porosity curve in figure 6.10(a), we can split the slow evolution regime into two regions: one where the maximum porosity decreases ($t \approx 750 - 10000$), and one where it increases ($t \approx 10000 - 180000$). These regions correspond to periods where the system is dominated by faster upflow, and faster downflow, respectively.

By $t = 15000$ (figure 6.8(g)), the new circulation cells have extended to cover most of the domain, and the high porosity channel is now more evident. This channel continues to be eroded ($t = 17500$, figure 6.8(h)) until vigorous convection can be reestablished ($t = 17600$, figure 6.8(i)). The downwards movement of the

circulation cells continues, however, and by the end of the simulation ($t = 20000$, figure 6.8(j)) the very vigorous convection is localised in high porosity regions near the bottom of the domain (note the different scale on the porosity plot).

The maximum porosities of $\phi = 0.8$ observed at the end of this simulation may not be physically realistic in the context of naturally occurring porous media, where ϕ rarely exceeds 0.6 (see §2.1). This high porosity is a result of our assumption that there is no supply limitation of solute in the porous medium (cf. §2.6.7). We would expect a more complete model to predict lower maximum porosities; however, our results strongly suggest that even in such a model the complete depletion of the reactive mineral from parts of the rock matrix may be expected.

6.1.2.3 Scenario three: stabilising solutal gradient, destabilising thermal gradient, supercritical reaction rate

We finally consider the combination of a stabilising solutal gradient with a destabilising thermal gradient along with a supercritical reaction rate, so the transition to instability is by direct onset of finite amplitude convection. Figure 6.9 shows the long-term evolution of the concentration perturbation $\tilde{C}$, temperature perturbation $\tilde{T}$ and porosity ϕ for the left-half of the domain. The solid lines on each plot are the streamlines, which are evenly spaced with the same contours used at each time. These should be read in conjunction with figure 6.10(b) which shows the evolution of the maximum absolute velocity, and the maximum and minimum porosity.

Convection is established by $t \approx 2$ (not shown). At this time the fields are out of phase with regions of $\tilde{C} > 0$ and $\tilde{T} > 0$ coinciding with regions of higher porosity ($\phi > \phi_0$), and regions of $\tilde{C} < 0$ and $\tilde{T} < 0$ coinciding with regions of lower porosity ($\phi < \phi_0$). From (6.4), we expect porosity to increase where $\tilde{C} < 0$ and $\tilde{T} < 0$ and to decrease where $\tilde{C} > 0$ and $\tilde{T} > 0$. As the flow is buoyancy driven, downward flow is favoured where $\tilde{C} < 0$ and $\tilde{T} < 0$, drawing down lower concentrations and temperatures from the top boundary, and upward flow is favoured where $\tilde{C} > 0$ and $\tilde{T} > 0$, drawing up higher concentrations and temperatures from the bottom boundary: this is the essential mechanism that sustains convection.

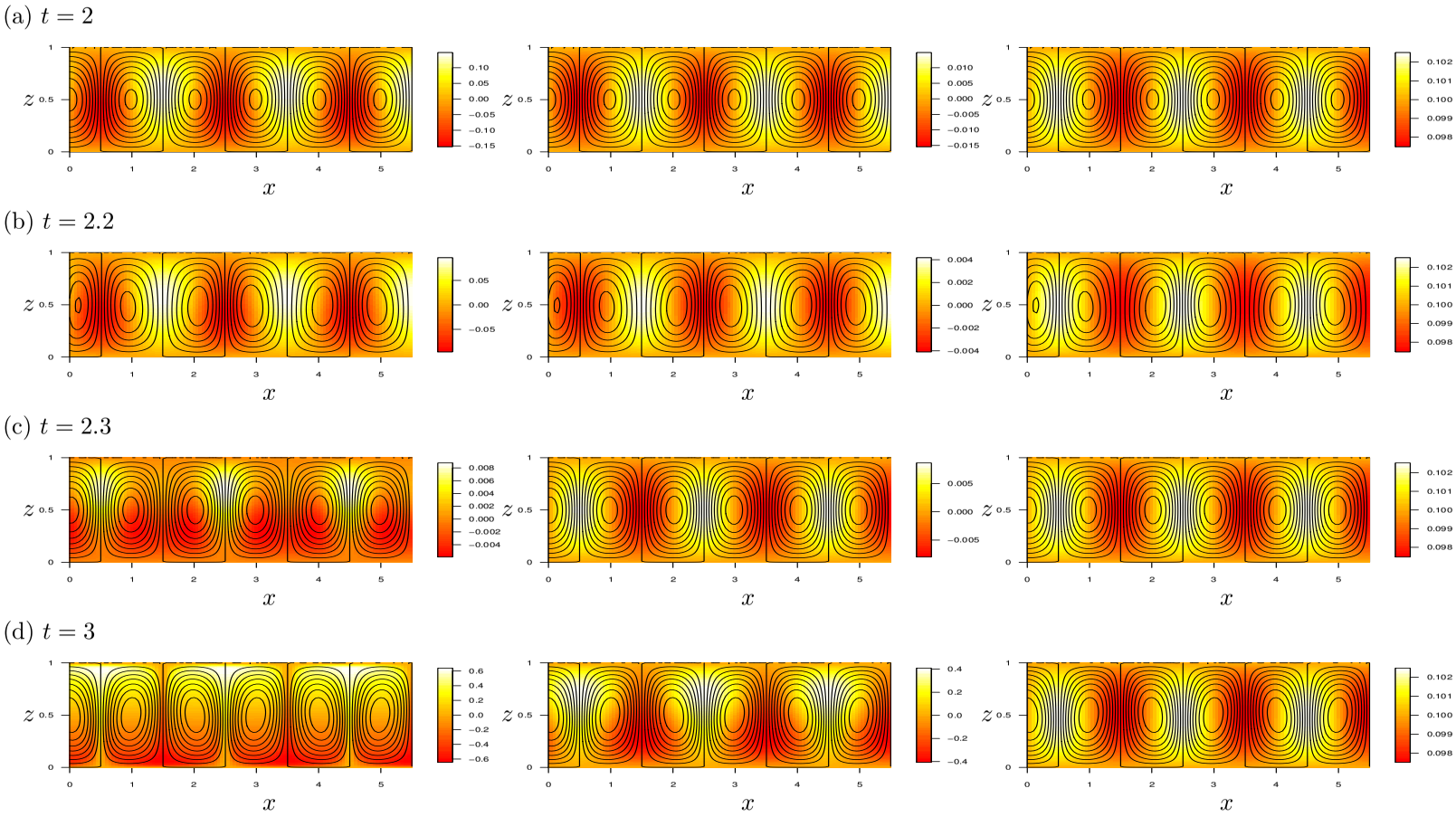

Figure 6.7: Onset of convection for $\mathcal{R}_C = -15$, $\mathcal{R}_T = 299$, and $k_0 = 5$. Shading indicates solutal concentration perturbation $\tilde{C}$ (left), temperature perturbation $\tilde{T}$ (centre), and porosity ϕ (right). Solid lines are streamlines.

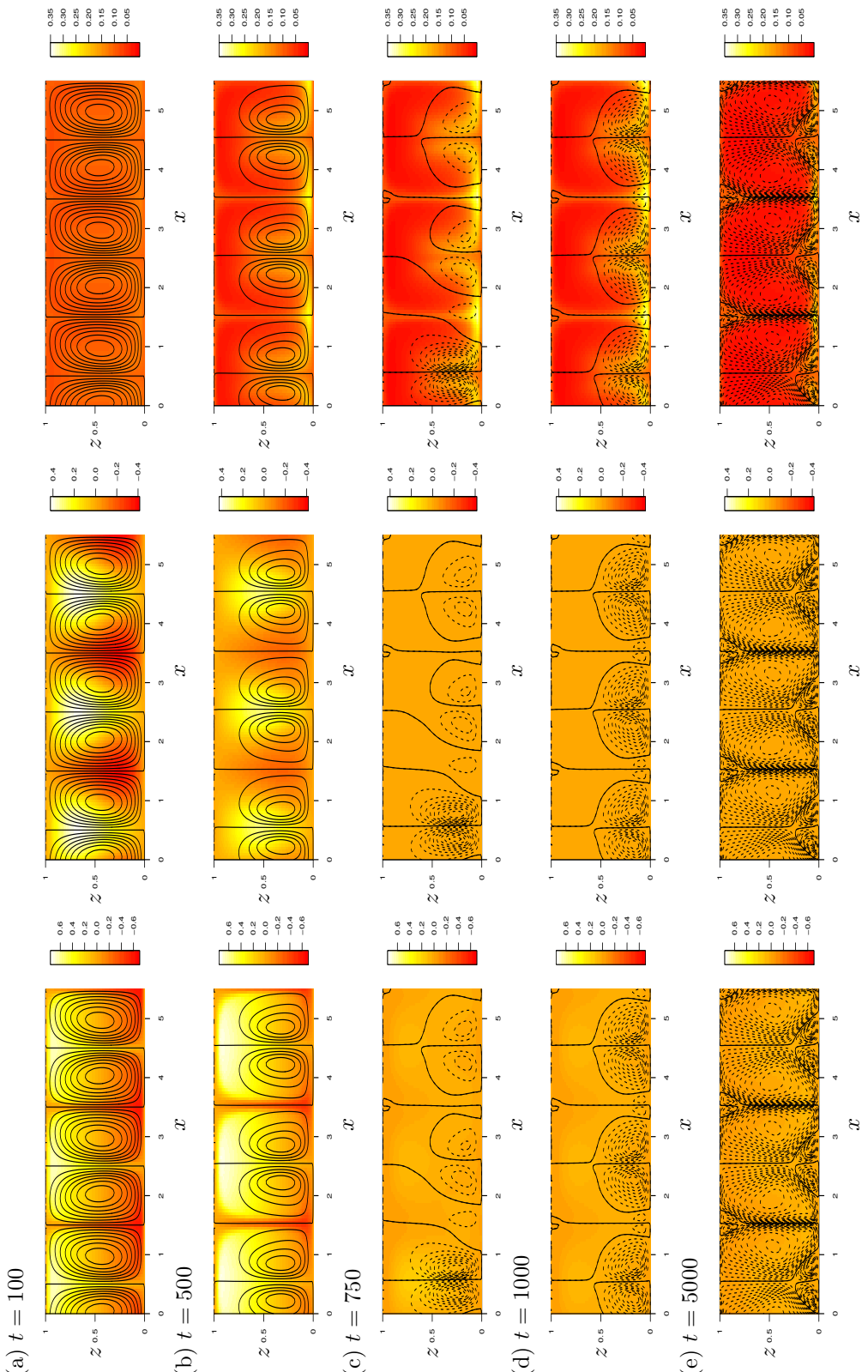
(a) $t = 100$
(b) $t = 500$
(c) $t = 750$
(d) $t = 1000$
(e) $t = 5000$
x
z

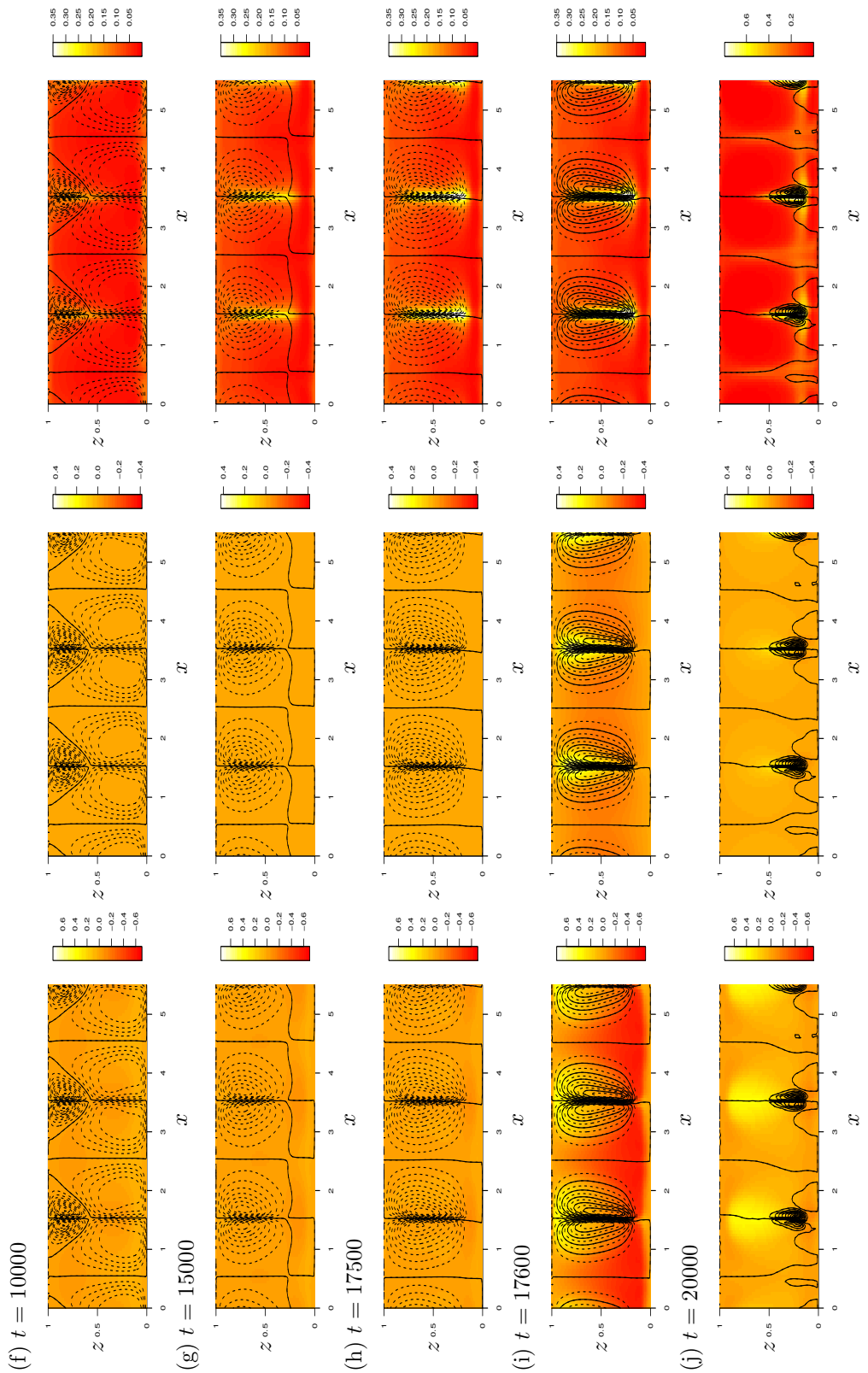

Figure 6.8: Evolution for $\mathcal{R}_C = -15$, $\mathcal{R}_T = 299$, and $k_0 = 5$. Shading indicates solutal concentration perturbation $\tilde{C}$ (left), temperature perturbation $\tilde{T}$ (centre), and porosity ϕ (right). Solid and dashed lines are streamlines.

Once convection has been established, the flow very quickly becomes dominated by nonlinear effects. Therefore, there is not a chance to see the upward movement of the circulation and temperature fields and downwards movement of the concentration and porosity fields predicted by the Galerkin analysis of §5.4.3.3. However, the concentration and temperature fields are out of phase with the porosity field, as predicted.

Since the diffusion of solute is much slower than the diffusion of heat, the concentration perturbations are carried around by the flow; this is the picture that has emerged by $t = 100$ (figure 6.9(a)) where we have plumes of low concentration being pulled towards the bottom of the domain, and those of high concentration being pulled towards the top of the domain by the circulation. The porosity field continues to evolve with porosity increasing in regions which coincide with $\tilde{C} < 0$ and $\tilde{T} < 0$, and decreasing in regions which coincide with $\tilde{C} > 0$ and $\tilde{T} > 0$. Therefore, the porosity is reduced near the top of the layer, and correspondingly the centres of the circulation cells have moved downwards. However, this region of low porosity is pierced by higher porosity channels in which fluid is carried towards the bottom of the layer. Furthermore, we have faster downflow than upflow, as can be seen by the tighter packed streamlines in these regions.

From figure 6.10(b) we can see that the maximum velocity increases as convection is established, and then suddenly convection is halted at $t \approx 130$. During this time, the porosity contrast has increased dramatically, but once convection is halted we enter a regime of slow porosity evolution. This is identical behaviour to that seen in the previous section with a lower reaction rate, although in this case the period of vigorous convection is much shorter.

Figure 6.9(b) shows the fields at $t = 130$ just as the convection is halted. The dashed contours represent additional streamlines which are plotted to aid with the visualisation of the flow. By this time, both the concentration and temperature perturbations are greatly reduced, and, although the porosity field looks similar to that at $t = 100$, the porosity contrast between the regions of high and low porosity has increased. As a result of the region of low porosity extending across the top half of the domain, the circulation has been squashed further towards the bottom of the layer, and hence, the vigorous convection cannot continue resulting

in this much slower circulation.

By $t = 500$ (figure 6.9(c)), the circulation has been squashed even further towards the bottom of the domain, and there is now no circulation in the top half of the domain. Small additional circulation cells have appeared at the bottom of the domain in the high porosity regions, and these grow in size ($t = 1000$, figure 6.9(d)), until by $t = 2000$ (figure 6.9(e)) they extend the full height of the domain. Note that throughout this evolution, the region of high porosity at the bottom of the layer has become thinner, so now most of the layer is dominated by lower porosity. However, channels of slightly higher porosity still pierce the domain, but these now contain fluid moving upwards towards the top of the domain. Furthermore, the top of these channels now contain a pair of counter-rotating circulation cells.

By $t = 5000$ (figure 6.9(f)), the circulation cells that appeared at the top of the higher porosity channels have increased in size, and, in the region of downflow the porosity has increased. These circulation cells continue to push downwards, until by $t = 7000$ (figure 6.9(g)) they almost dominate the domain.

From the maximum porosity curve in figure 6.10(b) we can see that the slow evolution can be split into three regions: from $t \approx 130 - 2000$ the maximum porosity remains constant, then from $t \approx 2000 - 6000$ it decreases, before increasing again from $t \approx 6000$. These regions correspond to periods where the system is dominated by faster downflow in high porosity regions, then faster upflow, and finally faster downflow, respectively. A similar pattern was seen in the previous section for a subcritical reaction rate.

By $t = 9000$ (figure 6.9(h)) the centres of the circulation have moved downwards, and the porosity has increased further in the downflow channel. The porosity continues to increase until, by $t = 10000$ (figure 6.9(i)) vigorous convection is able to return.

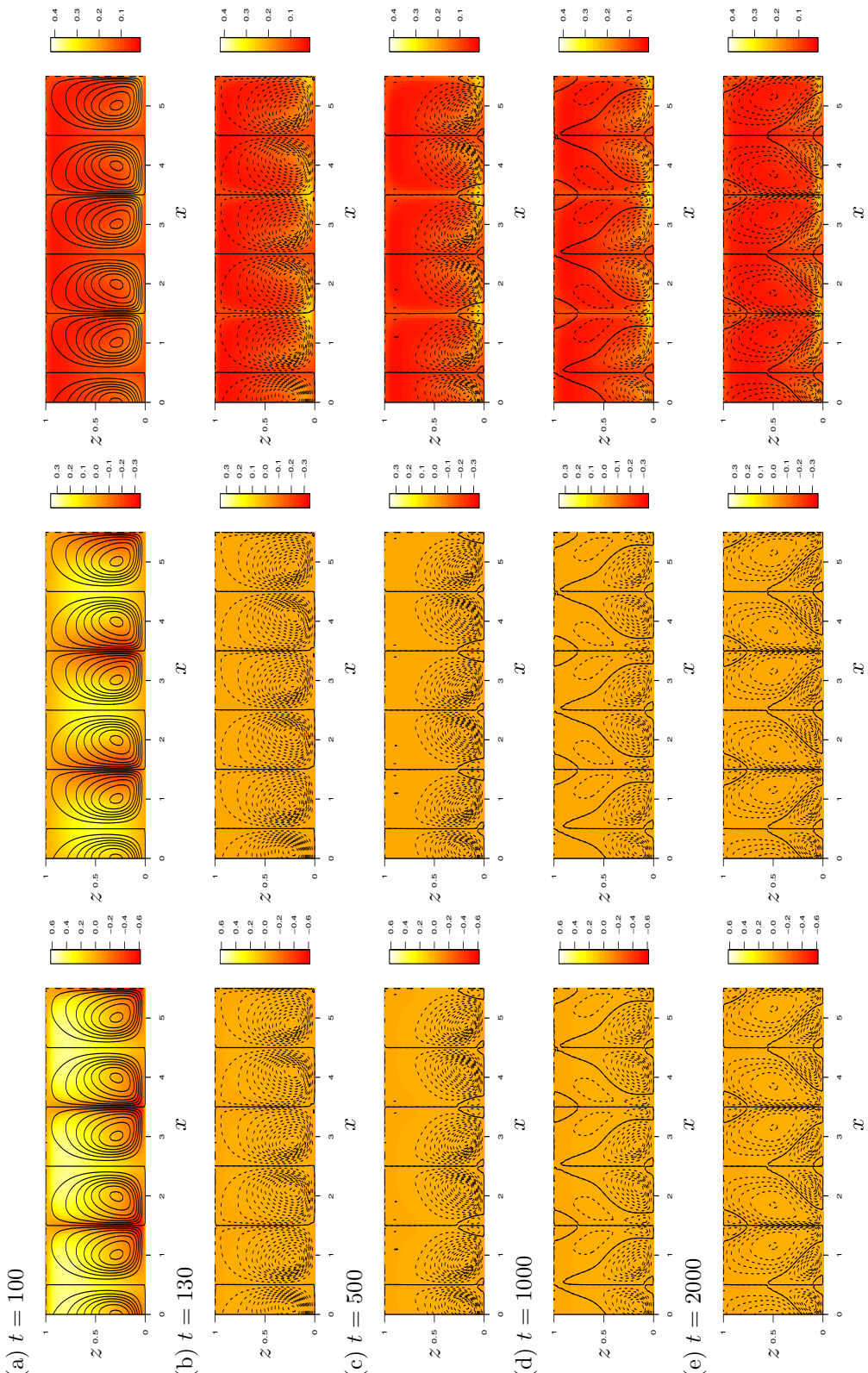
(a) $t = 100$
(b) $t = 130$
(c) $t = 500$
(d) $t = 1000$
(e) $t = 2000$
z
x

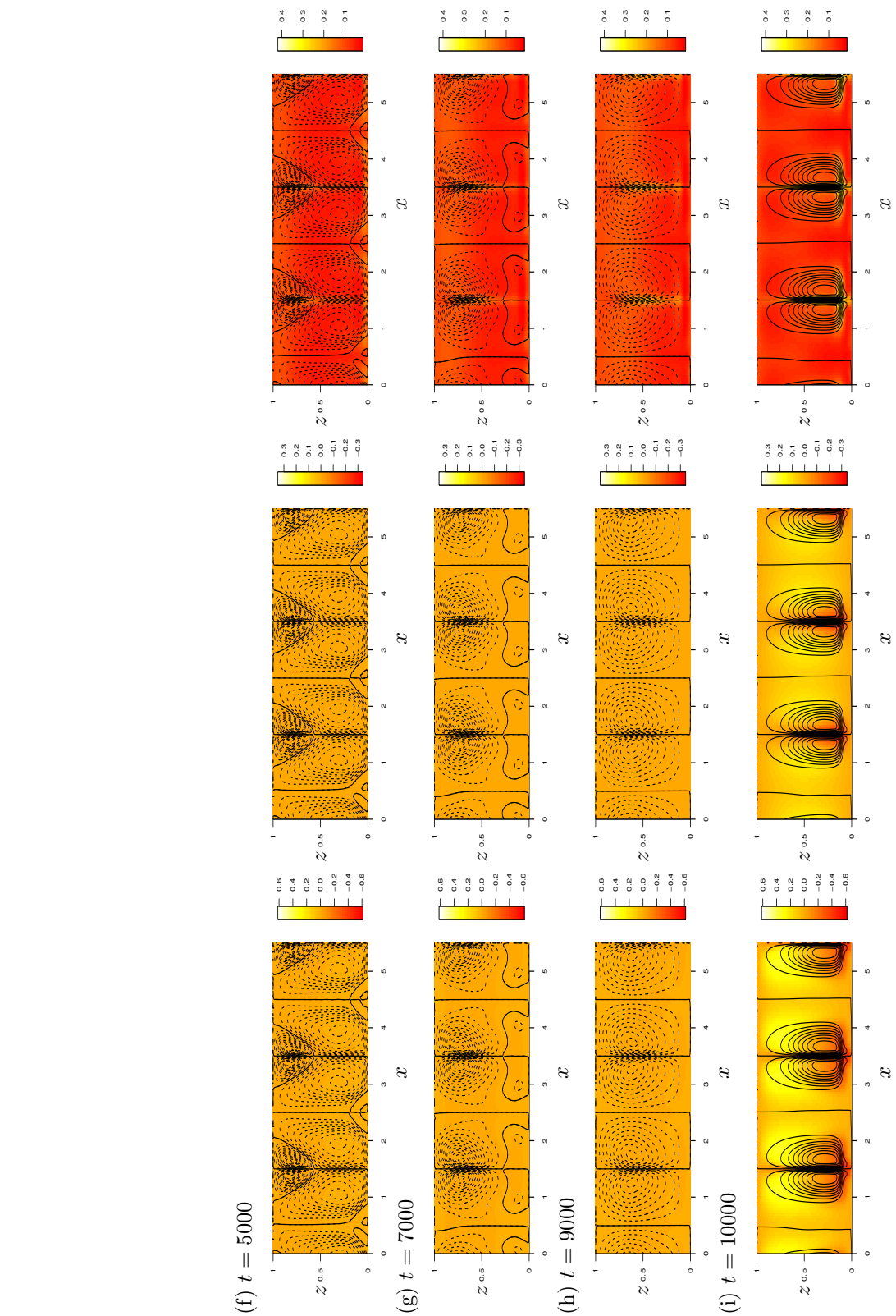

Figure 6.9: Evolution for $\mathcal{R}_C = -15$, $\mathcal{R}_T = 245$, and $k_0 = 20$. Shading indicates solutal concentration perturbation $\tilde{C}$ (left), temperature perturbation $\tilde{T}$ (centre), and porosity ϕ (right). Solid and dashed lines are streamlines.

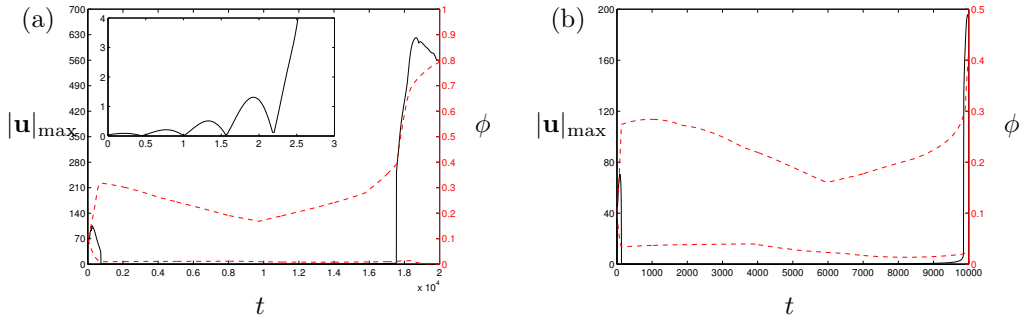

Figure 6.10: Maximum absolute velocity $|\mathbf{u}|$ (solid) and maximum and minimum porosity ϕ (dashed) throughout the whole domain for (a) $k_0 = 5$, $\mathcal{R}_C = -15$, $\mathcal{R}_T = 199$; (b) $k_0 = 20$, $\mathcal{R}_C = -15$, $\mathcal{R}_T = 245$.

6.2 Summary of long-term behaviour

A common feature of all the numerical simulations is the interaction between processes operating at different time scales. The long-term behaviour of the system, however, depends on the strength of the thermal gradient relative to that of the solutal gradient.

In each case, convection is established over dimensionless time scales of order $1 - 10$ and, over a slower time scale of order 100, the cells tend to establish and reinforce an in-phase porosity pattern on the rock matrix. Recall that the matrix evolution parameter $|\delta| = 0.001$ in these simulations. Now, if the solutal gradient dominates, then the longer term behaviour resembles that of reactive solutal convection as seen in chapter 3: the reinforcement results in the clogging of downflow regions, which drives a secondary instability in the form of a phase shift that reverses the direction of the circulation over time scales of order 10. Over extremely long time scales of order 1000, the repeated interaction between the circulation and the concentration and porosity fields results in a layered porosity structure penetrated by high porosity channels but, in contrast to solutal convection, there is an almost continual lateral migration of the circulation and concentration fields.

If the thermal gradient dominates, however, then the reinforcement of the in-phase porosity structure results (over time scales of order 100) in the circulation being

forced into too small a region to be maintained. Once convection is suppressed, a slow porosity evolution over timescales of order 1000 occurs, again resulting in a layered porosity structure penetrated by high porosity channels. However, now there is an almost continual vertical movement of the circulation cells. Eventually, the porosity evolves sufficiently to allow the return of very vigorous, localised convection in regions of high porosity.

Comparing figures 6.10(a) and (b) it appears that there could be a relationship between the reaction rate and the timescale required for the re-emergence of vigorous scaling. In fact, further numerical simulations (not shown) with the porosity evolution parameter δ increased by a factor of ten, reduce the timescale for re-emergence by a factor of ten for both reaction rates. This result suggests that the timescale for the re-emergence of convection depends on both the reaction rate k_0 and the porosity evolution parameter δ.

Higher reaction rates favour a more rapid evolution of the system. In the case of a dominant solutal gradient, they bring forward the onset of the secondary instability, and with a dominant thermal gradient they result in quicker suppression of convection. In both cases they also accelerate the very slow evolution of the rock matrix.

Chapter 7

Conclusions

7.1 Summary of results

In this thesis we have examined two idealised models of reactive convection in a porous medium where the rock matrix is allowed to evolve through precipitation and dissolution as a mineral is lost or gained from the fluid. Rather than studying a detailed geochemical model of a particular system we considered a simple, but physically founded, model with the aim of elucidating the fundamental mechanisms which control the evolution of the porous matrix, through a combination of linear stability analyses and numerical simulations.

We began by considering the simplest model in which interactions between convective circulation and an evolving porous medium may occur: reactive solutal convection, where the solute may be exchanged with the porous matrix by a first-order reaction which attempts to restore the local solute concentration to some local equilibrium value that varies with depth in the medium. This model can be obtained from the full thermosolutal model, in the limit of very high thermal diffusivity and finite solutal diffusivity with negligible thermal expansion.

Although the porosity evolution is slow on the timescale of convection and reaction, we find, through a linear stability analysis, that it exerts an unexpected influence on the stability properties of the system. When the system is strongly buoyantly unstable, the reaction acts to remove destabilising solute and thus

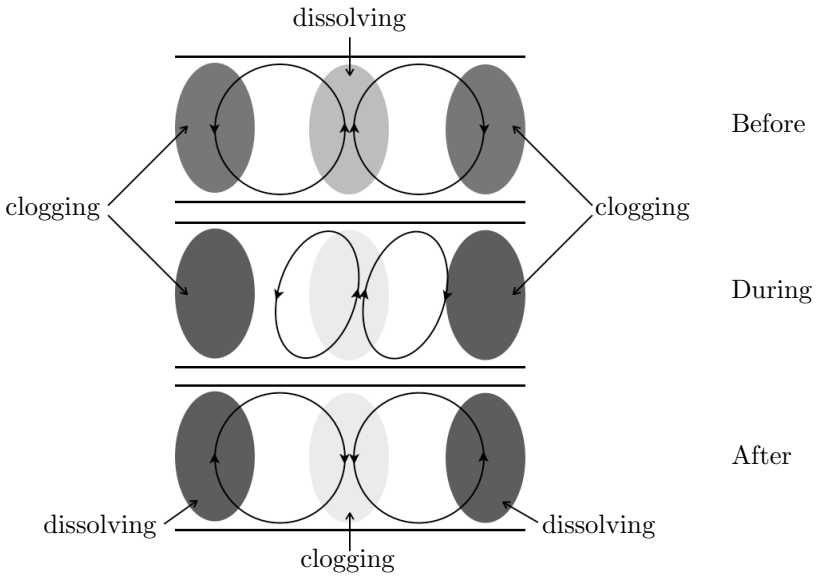

Figure 7.1: Schematic of the phase-shift mechanism. The shading indicates the porosity field with darker shading corresponding to lower values; the solid lines indicate the pattern of fluid flow.

to stabilise the system. However, when the system is close to the threshold of instability (as calculated without porosity evolution), a novel reaction-diffusion instability mode becomes available, which persists even when the Rayleigh number is reduced below the critical value for buoyant instability.

Over longer timescales, the positive feedback between the concentration and porosity fields results in the porosity decreasing in downflow regions, but increasing in upflow regions. These porosity changes become steadily more pronounced, and ultimately trigger a relatively rapid reorganisation of the flow in which the entire pattern of convective cells tilts and shifts sideways by half a wavelength. This phase-shift mechanism is illustrated in figure 7.1.

The repeated interplay between episodes of quasi-steady convection and the rapid reorganisations that punctuate them eventually develops a layered porosity structure, with the centre of the layer being dominated by a low-porosity band broken by occasional higher-permeability vertical channels, and pockets of enhanced porosity occurring nearer the top and the bottom of the layer (figure 7.2(a), cf. figure 3.11(e)). There appears to be no long-term steady convective state

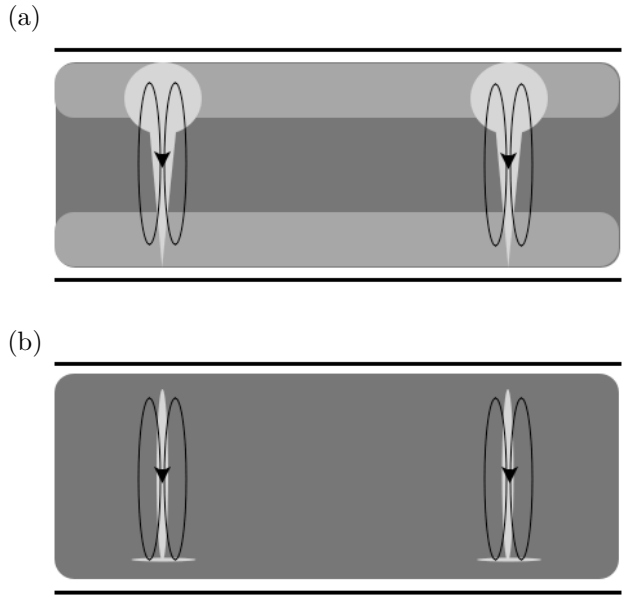

Figure 7.2: Schematic of the long-term pattern of the porosity field for (a) solutally-driven convection, and (b) thermally-driven convection. The shading indicates the porosity field with darker shading corresponding to lower values; the solid lines indicate the pattern of weak fluid flow.

towards which the system asymptotes, although once layering has become established there is a tendency for the strength of convection to decrease.

Similar long-term behaviour was seen when the top and bottom boundary conditions were changed from Dirichlet to Neumann conditions. With Neumann boundary conditions, however, the system underwent fewer phase shifts and settled into a phase of slow evolution at an earlier point in the simulation, suggesting that these boundary conditions stabilise the system against the rapid reorganisations.

The model was extended to consider reactive double-diffusive convection in an evolving porous layer, bounded above and below by impermeable layers held at constant concentration and temperature. After revisiting the stability analysis of Pritchard and Richardson (2007) for non-evolving reactive thermosolutal convection, we performed a linear stability analysis to investigate how the evolution of a reactive porous medium affects the onset of thermosolutal convection.

As with solutal convection, the porosity evolution allows an unstable reaction-

diffusion mode to become available, which persists when the thermal Rayleigh number is reduced below the critical value required for buoyant instability. This reaction-diffusion mode appears regardless of the reaction rate and the exact destabilising nature of the thermal and solutal gradients. With a destabilising solutal gradient the reaction-diffusion instability results in the same tilting of the cells seen with solutal convection. However, with a stabilising solutal gradient the reaction-diffusion instability results in vertical squashing of the entire pattern of convective cells.

If the solutal gradient is destabilising then, regardless of the thermal gradient, the behaviour of the system is qualitatively identical to that seen for solutal convection: the positive feedback between the concentration and porosity fields results in the clogging of downflow regions, which drives a secondary instability in the form of a phase shift that reverses the direction of the circulation (figure 7.1). Over extremely long time scales, the repeated interaction between the circulation and the concentration and porosity fields results in a layered porosity structure penetrated by high porosity channels, with an almost continual lateral migration of the circulation and concentration fields (figure 7.2(a), cf. figure 6.2(i)).

Different behaviour was seen in the solutally stable regime, however. Here, the reaction rate plays an important role at the onset of convection, with a 'slow' subcritical reaction leading to an oscillatory instability, but a 'faster' supercritical reaction leading to a monotonic instability. Over long timescales the reinforcement of the in-phase porosity structure results in the circulation being forced into too small a region to be maintained. Once convection is suppressed, a slow porosity evolution occurs, again resulting in a layered porosity structure penetrated by high porosity channels. However, now there is an almost continual vertical movement of the circulation cells. Eventually, the porosity evolves sufficiently to allow the return of very vigorous, localised convection in regions of high porosity (figure 7.2(b), cf. figure 6.9(i)).

Higher reaction rates favour a more rapid evolution of the system. In the case of a dominant solutal gradient, they bring forward the onset of the secondary instability, and with a dominant thermal gradient they result in quicker suppression of convection. In both cases they also accelerate the very slow evolution of the

rock matrix.

Our results complement the numerical experiments of Bolton *et al.* (1996; 1997; 1999) by demonstrating that geochemical convection can spontaneously give rise to heterogeneous porosity fields, and not merely enhance heterogeneities that already exist. Their wider implication is that in situations where long-term convective transport is simulated in order to determine patterns of mineralisation, such as ore deposition (e.g. Raffensperger and Garven 1995a,b), it may be essential to incorporate flow–reaction–permeability coupling in order to capture even the outline of the mineralisation patterns. Another implication is that, because of the development of instabilities which scale in a nonlinear manner with the matrix evolution rate δ, simulations which accelerate the rock evolution to reduce runtime may thereby distort their results in unexpected ways.

Our results from the full thermosolutal model with a destabilising solutal gradient suggest that a reduced solutal model does capture the fundamental feedback mechanisms which drive the evolution of the rock matrix in solutally driven convection. However, thermal diffusion does play an important role; a lower value of the Lewis number, and hence slower thermal diffusion, results in a weaker restoring force, leading to a continual lateral migration of the pattern of convective cells.

Our simulations with stabilising solutal gradient have shown that there exists the possibility of entirely depleting the rock matrix of reactive mineral in places, resulting in very localised porosity. Finally, we note the importance of running numerical simulations for a sufficiently long time, since our results suggest that vigorous convective circulation can return, even after long quiescent periods.

7.2 Future work

The most natural extension of the work on reactive thermsolutal convection would be to investigate the effect of Neumann boundary conditions. However, the results for solutal convection suggest that any fundamental effect on the long-term behaviour from the boundary conditions is minimal. We could also consider

more complex geometries, for example, horizontal convection or the Elder problem (Elder 1967) which considers convection in a rectangular box heated over the central half of its base. It might also be useful to compare our numerical simulation results to those obtained with a more specialised numerical solver, or with alternative approaches such as spectral methods.

As noted in all our simulations, the porosity evolution allows an unstable reaction-diffusion mode to become available, which persists when the Rayleigh number is reduced below the critical value required for buoyant instability. However, in our analysis we noted that our assumption of a divergence-free velocity field is strictly no longer valid in this regime. Therefore, a more important line of work would be study the reaction–diffusion instability in more detail without this limiting assumption.

Another avenue would be to consider more detailed models of the geochemistry, including multiple species or more complicated reaction laws. In light of the results on thermally-driven reactive thermosolutal convection, the first step would be to remove the assumption of no supply limitation, and instead only allow the porosity to evolve to a fixed value such that $\phi_{\text{final}} < 1$.

The aim of this work would be to determine just how robust our instability and long-term evolution mechanisms are to increased model complexity; that is, we want to determine if our fundamental mechanisms are in fact fundamental to reactive convection with porosity evolution, or if they are particular to our simple idealised models.

Appendix A

Technical details of various mathematical results

A.1 Perturbation amplitudes

We now linearise the dimensionless governing equations (3.9)–(3.12), assuming that the amplitude of the matrix evolution parameter δ is smaller than the amplitude of the perturbations. Hence, the linearised equations are given by

$$\nabla \cdot \mathbf{u}' = 0, \tag{A.1.1}$$

$$\nabla p' = -\mathbf{u}' - \mathcal{R}_C C' \mathbf{e}_z, \tag{A.1.2}$$

$$\frac{\partial C'}{\partial t} + w' = \phi_0 \nabla^2 C' + \frac{\partial \phi'}{\partial z} - k_0 C', \tag{A.1.3}$$

$$\frac{\partial \phi'}{\partial t} = 0. \tag{A.1.4}$$

Since the porosity field is fixed in time, we can split the perturbations into a steady ϕ-dependent part with no flow, plus a time-dependent part, such that

$$C' = C_\phi + \tilde{C}, \quad p' = p_\phi + \tilde{p}, \quad \mathbf{u}' = \tilde{\mathbf{u}}, \tag{A.1.5}$$

where the subscript ϕ denotes the ϕ-dependent part of the perturbation. Therefore (A.1.1)–(A.1.4) can be rewritten into a convective part given by

$$\nabla \cdot \tilde{\mathbf{u}} = 0, \tag{A.1.6}$$

$$\nabla \tilde{p} = -\tilde{\mathbf{u}} - \mathcal{R}_C \tilde{C} \mathbf{e}_z, \tag{A.1.7}$$

$$\frac{\partial \tilde{C}}{\partial t} + \tilde{w} = \phi_0 \nabla^2 \tilde{C} - k_0 \tilde{C}, \tag{A.1.8}$$

and a porosity-dependent part given by

$$\nabla p_\phi = -\mathcal{R}_C C_\phi \mathbf{e}_z, \tag{A.1.9}$$

$$\phi_0 \nabla^2 C_\phi - k_0 C_\phi = -\frac{\partial \phi'}{\partial z}. \tag{A.1.10}$$

Since there is no porosity evolution, the linearised convective and porosity-dependent systems are decoupled. The linearised convection equations are equivalent to those for the reduced case of a reaction but no porosity evolution studied in §3.2.1. Therefore, in this case, the effect of porosity evolution would enter the system as a non-linear effect.

A.2 Principle of the exchange of stabilities when $\delta = 0$

Adapting the approach of Chandrasekhar (1961, §11), we show that for the reduced problem with a reaction but no matrix evolution the principle of the exchange of stabilities is valid, so marginal stability is characterised by $\sigma = 0$. Throughout this appendix we will use the notation $D = \mathrm{d}/\mathrm{d}z$ for brevity.

Let $G(z) = (D^2 - m^2)W(z)$, so equation (3.27), with $\delta = 0$, becomes

$$\left[\phi_0(D^2 - m^2) - (k_0 + \sigma)\right] G(z) = m^2 \mathcal{R}_C W(z). \tag{A.2.1}$$

We multiply equation (A.2.1) by G^*, the complex conjugate of G, and integrate

over the range of z, obtaining

$$\int_0^1 G^*\big[\phi_0(D^2-m^2)-(k_0+\sigma)\big]G\mathrm{d}z = m^2\mathcal{R}_C\int_0^1 G^*W\mathrm{d}z. \tag{A.2.2}$$

Integrating by parts and using $G(z)=(D^2-m^2)W(z)$, this may be rewritten as

$$\int_0^1\{\phi_0|DG|^2+(\phi_0m^2+k_0+\sigma)|G|^2\}\mathrm{d}z - m^2\mathcal{R}_C\int_0^1\{|DW|^2+m^2|W|^2\}\mathrm{d}z=0, \tag{A.2.3}$$

regardless of whether Dirichlet ($W(z)=0$ and $G(z)=0$) or Neumann ($W(z)=0$ and $DG(z)=0$) boundary conditions must be satisfied at the top and bottom of the layer.

The real and imaginary parts of equation (A.2.3) must vanish separately. The imaginary part is given by

$$\Im(\sigma)\int_0^1|G|^2\mathrm{d}z=0 \tag{A.2.4}$$

which is satisfied only if $\Im(\sigma)=0$. Therefore, σ must be real, and marginal stability is characterised by $\sigma=0$.

A.3 Reduction of determinant

The determinant of B, with elements given by (5.34), can be simplified by performing seven column operations. We first subtract the first column from each of the other six columns, and then subtract column three from column four, and column five from column six. The corresponding Maple code for the column operations is given below.

```
B1:=ColumnOperation(B,[2,1],-1):
ColumnOperation(B1,[3,1],-1,inplace):
ColumnOperation(B1,[4,1],-1,inplace):
ColumnOperation(B1,[5,1],-1,inplace):
ColumnOperation(B1,[6,1],-1,inplace):
```

```
ColumnOperation(B1,[4,3],-1,inplace):
ColumnOperation(B1,[6,5],-1,inplace):
```

We then expand the determinant by the first row, and take the first element of each column out as a common factor of that column. Therefore,

$$\det(\mathrm{B}) = (e^{q_2} - e^{q_1})(e^{q_4} - e^{q_3})(e^{q_6} - e^{q_5})(e^{q_3} - e^{q_1})(e^{q_5} - e^{q_1}) \det(\mathrm{C}), \quad \text{(A.3.1)}$$

where the matrix C is given by

$$
C = \begin{bmatrix}
1 & 1 \\
\dfrac{q_2^2 - q_1^2}{e^{q_2} - e^{q_1}} & \dfrac{q_3^2 - q_1^2}{e^{q_3} - e^{q_1}} \\
\dfrac{(q_2^2 - m^2 - \sigma)e^{q_2} - (q_1^2 - m^2 - \sigma)e^{q_1}}{e^{q_2} - e^{q_1}} & \dfrac{(q_3^2 - m^2 - \sigma)e^{q_3} - (q_1^2 - m^2 - \sigma)e^{q_1}}{e^{q_3} - e^{q_1}} \\
\dfrac{(q_2^2 - m^2)(q_2^2 - m^2 - \sigma) - (q_1^2 - m^2)(q_1^2 - m^2 - \sigma)}{e^{q_2} - e^{q_1}} & \dfrac{(q_3^2 - m^2)(q_3^2 - m^2 - \sigma) - (q_1^2 - m^2)(q_1^2 - m^2 - \sigma)}{e^{q_3} - e^{q_1}} \\
\dfrac{(q_2^2 - m^2)(q_2^2 - m^2 - \sigma)e^{q_2} - (q_1^2 - m^2)(q_1^2 - m^2 - \sigma)e^{q_1}}{e^{q_2} - e^{q_1}} & \dfrac{(q_3^2 - m^2)(q_3^2 - m^2 - \sigma)e^{q_3} - (q_1^2 - m^2)(q_1^2 - m^2 - \sigma)e^{q_1}}{e^{q_3} - e^{q_1}}
\end{bmatrix}
$$

$$
\begin{bmatrix}
1 & 1 \\
\dfrac{q_4^2 - q_3^2}{e^{q_4} - e^{q_3}} & \dfrac{q_5^2 - q_1^2}{e^{q_5} - e^{q_1}} \\
\dfrac{(q_4^2 - m^2 - \sigma)e^{q_4} - (q_3^2 - m^2 - \sigma)e^{q_3}}{e^{q_4} - e^{q_3}} & \dfrac{(q_5^2 - m^2 - \sigma)e^{q_5} - (q_1^2 - m^2 - \sigma)e^{q_1}}{e^{q_5} - e^{q_1}} \\
\dfrac{(q_4^2 - m^2)(q_4^2 - m^2 - \sigma) - (q_3^2 - m^2)(q_3^2 - m^2 - \sigma)}{e^{q_4} - e^{q_3}} & \dfrac{(q_5^2 - m^2)(q_5^2 - m^2 - \sigma) - (q_1^2 - m^2)(q_1^2 - m^2 - \sigma)}{e^{q_5} - e^{q_1}} \\
\dfrac{(q_4^2 - m^2)(q_4^2 - m^2 - \sigma)e^{q_4} - (q_3^2 - m^2)(q_3^2 - m^2 - \sigma)e^{q_3}}{e^{q_4} - e^{q_3}} & \dfrac{(q_5^2 - m^2)(q_5^2 - m^2 - \sigma)e^{q_5} - (q_1^2 - m^2)(q_1^2 - m^2 - \sigma)e^{q_1}}{e^{q_5} - e^{q_1}}
\end{bmatrix}
$$

$$
\begin{bmatrix}
1 \\
\dfrac{q_6^2 - q_5^2}{e^{q_6} - e^{q_5}} \\
\dfrac{(q_6^2 - m^2 - \sigma)e^{q_6} - (q_5^2 - m^2 - \sigma)e^{q_5}}{e^{q_6} - e^{q_5}} \\
\dfrac{(q_6^2 - m^2)(q_6^2 - m^2 - \sigma) - (q_5^2 - m^2)(q_5^2 - m^2 - \sigma)}{e^{q_6} - e^{q_5}} \\
\dfrac{(q_6^2 - m^2)(q_6^2 - m^2 - \sigma)e^{q_6} - (q_5^2 - m^2)(q_5^2 - m^2 - \sigma)e^{q_5}}{e^{q_6} - e^{q_5}}
\end{bmatrix}
\tag{A.3.2}
$$

A.4 Minimising $g(M, n)$ over M and n

We wish to minimise $g(M, n)$ over M and n, where $M \geq 0$ and $n \geq 1$, with the extra condition that $n \in \mathbb{N}$. To begin we will ignore the last condition and assume that n varies continuously.

The global minimum of $g(M, n)$ over (M, n) may occur either:
(a) within the (M, n) region of interest and so it must also be a local minimum over M and n simultaneously,
(b) at the boundary of the region, or
(c) in one of the limits $M \to \infty$ or $n \to \infty$.
If the minimum occurs at the boundary $n = 1$, but not in one of the limits of M, then it must correspond to a local minimum of M; while, if it occurs at the boundary $M = 0$, but not in one of the limits of n, then it must correspond to a local minimum of n.

We will deal with option (c) first. In the limit $M \to \infty$, $g \sim M/\lambda$, while in the limits $n \to \infty$ and $M \to 0$, $g \sim n^4\pi^4/(M\lambda)$. Therefore, the global minimum cannot occur in either of these limits. We are left with two possibilities: either the global minimum occurs within the (M, n) region, or on the boundary $n = 1$. We will attempt to locate an internal local minimum in the region $n > 0$, $M > 0$. If no minimum occurs in this region then the global minimum must occur on the boundary $n = 1$, while if a minimum does exist, we will need to determine if it occurs for $n \geq 1$ and if it is a global minimum.

For general values of M, $\partial g/\partial n = 0$ if and only if $F(n) = 0$ where

$$\begin{aligned} F(n) = n^6\pi^6 + (2k_0Le + 3M)n^4\pi^4 + (4k_0LeM + 3M^2 + k_0Le^2)n^2\pi^2 \\ + M(M + k_0Le)^2 + \frac{1}{2}k_0MLe\mathcal{R}_C(\lambda - Le). \end{aligned} \tag{A.4.1}$$

Now $\mathrm{d}F/\mathrm{d}n > 0$ for all $n > 0$, and so $F(n)$ has a root for $n > 0$ if and only if $F(0) < 0$. Hence, $g(M, n)$ has a local minimum over n if and only if

$$M < M_F = \left[\frac{1}{2}k_0Le\mathcal{R}_C(Le - \lambda)\right]^{1/2} - k_0Le. \tag{A.4.2}$$

Therefore, any local minimum over n can be a local minimum over both M and n only if $M < M_F$. If $\mathcal{R}_C < 0$, then $M_F \in \mathbb{C}$ (since $Le > \lambda$) and the global minimum over n must occur on $n = 1$. Also, if $M_F < 0$, then the global minimum over n must occur on $n = 1$ for any physical value of M. We therefore need to worry about a local minimum over n if and only if $M_F > 0$; i.e. if and only if

$$k_0 < k_F = \frac{(Le - \lambda)}{2Le}\mathcal{R}_C. \tag{A.4.3}$$

We now consider the variation of $g(M, n)$ over M, keeping n general. Now, $\partial g/\partial M = 0$ if and only if

$$\begin{aligned}\frac{M^4}{Le^2} + \left(\frac{2k_0}{Le} + \frac{2n^2\pi^2}{Le^2}\right)M^3 + \left(\frac{2k_0n^2\pi^2 + k_0\lambda\mathcal{R}_C}{Le} - \mathcal{R}_Ck_0 + k_0^2\right)M^2 \\ + \left(-\frac{2k_0n^4\pi^4}{Le} - \frac{2n^6\pi^6}{Le^2}\right)M - k_0^2n^4\pi^4 - \frac{2k_0n^6\pi^6}{Le} - \frac{n^8\pi^8}{Le^2} = 0,\end{aligned} \tag{A.4.4}$$

and so there can be at most four local extrema of $g(M, n)$. Since $g(M, n) \to \infty$ as $M \to \infty$ and $M \to 0$, and $g(M, n) \to -\infty$ as $M \to -\infty$, there must be at least one local minimum in the physical range $M > 0$. We can show that

$$\frac{\partial^2 g}{\partial M^2} = \frac{2n^2\pi^2}{\lambda M^3} + \frac{2k_0Le(Le - \lambda)}{\lambda(k_0Le + M + n^2\pi^2)^3}\mathcal{R}_C, \tag{A.4.5}$$

and so, for $\mathcal{R}_C > 0$, $g(M, n)$ cannot have more than a single local minimum in the range $M > 0$. We have already shown that if $\mathcal{R}_C < 0$ then the global minimum must occur on the boundary $n = 1$. Therefore, there is only one minimum over M to be concerned about. We will denote this minimum $M = M_c$.

Now, if we can prove that the unique value of M_c given by (A.4.4) which minimises $g(M_c, n)$ must always be greater than M_F regardless of the value of n, then we will have shown that the global minimum corresponds to $n = 1$. This will follow if we can show that $\partial g/\partial M(M_F, n) < 0$ for all $n > 0$ (when $M = M_c$, $\partial g/\partial M(M_c, n) = 0$ for all $n > 0$, and so if $M_F < M_c$ then $\partial g/\partial M(M_F, n) < 0$ for all $n > 0$).

The sign of $\partial g/\partial M$ is the same as as the sign of $G(M, n)$ where $G(M, n)$ is given

by (A.4.4) multiplied by Le^2. Substituting in $M = M_F$ and rearranging, we find that (correcting Pritchard and Richardson (2007))

$$G(M_F, n) = \frac{16k_0^4}{\beta^4}\left(-P^4 - P^3 - \frac{\beta}{4}(2-\beta)P^2 + \frac{1}{4}(1-\beta)^2 P - \frac{1}{16}(1-\beta)^2\right) \tag{A.4.6}$$

where

$$P = \frac{n^2\pi^2}{\sqrt{2k_0 Le\mathcal{R}_C(Le-\lambda)}}, \quad \beta = \sqrt{\frac{2k_0 Le}{\mathcal{R}_C(Le-\lambda)}}. \tag{A.4.7}$$

Now, $0 < \beta < 1$ for $k_0 < k_F$, and it is simple to show by plotting $G(P, \beta)$ that there are no points in the range $P > 0$, $0 < \beta < 1$ at which $G \geq 0$.

We have shown that there is no local minimum over (M, n) within the range $M > 0$, $n > 0$. Therefore, along with our earlier results, the global minimum of $g(M, n)$ over M and n always occurs on the boundary $n = 1$ and corresponds to a local minimum over M given by M_c. We note that this result is consistent with the extra requirement that $n \in \mathbb{N}$. Hence, $\mathcal{R}_{T,0}^c(\mathcal{R}_C) = g(M_c, 1)$.

Appendix B

Tolerance testing and mesh independence

All numerical simulations in this thesis were performed using Comsol Multiphysics v3.5a, a finite element numerical solver software package designed for various physics and engineering applications. It allows for the direct entry of coupled systems of partial differential equations which are to be solved on a user-specified domain. It has a number of inbuilt numerical solvers, and the user has full control over the size, shape and number of mesh elements used.

However, Comsol is designed to be treated as a 'black box' solver which gives the user only limited access to the numerical methods and tolerances. Therefore, it is important that all models are tested for convergence and mesh independence before their results are believed.

B.1 Solutal convection

The overall performance of the model was verified both for convection with no reaction or porosity evolution and for convection with a reaction but no porosity evolution. In both cases the model reproduced the linear stability results found in §3.2: details are given in §3.3.1.

In order to check the convergence of our numerical model, simulations for $0 \leq t \leq 5000$ were conducted using two different reaction rates, $k_0 = 0$ and $k_0 = 10$, and four different Rayleigh numbers: the critical Rayleigh number given by (3.41), and 10%, 20%, and 50% above this value. Each simulation was conducted using 4480 triangular mesh elements: absolute tolerances were varied between 10^{-3} and 10^{-6} while relative tolerances were varied between 10^{-2} and 10^{-5}. For each simulation we noted the values for the maximum and minimum porosity ϕ, the maximum and minimum concentration perturbation C', and the maximum absolute velocity $|\mathbf{u}|$ over all timesteps (tables B.1 and B.2); we also plotted the maximum absolute velocity against time for each set of tolerances to check for convergence over all time steps (figures B.1 and B.2). A relative tolerance of 10^{-3} and an absolute tolerance of 10^{-4} were found to give convergence of all key quantities to four significant figures while maintaining a reasonable solution time.

The mesh independence of the numerical method was tested similarly by conducting simulations with 1120, 4480, 17920, and 71680 triangular mesh elements and using the same reaction rates and Rayleigh numbers used for the tolerance testing. Each simulation lasted 5000 time units and used a relative tolerance of 10^{-3} and an absolute tolerance of 10^{-4}. The same metrics as before were used to assess convergence.

When no reaction occurred ($k_0 = 0$), the solution was essentially mesh-independent: steady convection developed when the Rayleigh number was above the threshold $R_{C,0}^{\text{crit}}$, and all key quantities converged to three significant figures as long as at least 4480 mesh elements were employed (see table B.3 and figure B.3).

The mesh-dependence at higher reaction rates is more subtle, as illustrated by figure B.4. It is apparent from this that 1120 mesh elements are insufficient to resolve the behaviour consistently, whereas for 4480 or more mesh elements the evolution is qualitatively similar. However, particularly for the convective cases with Rayleigh numbers 10%, 20%, and 50% above the critical value, increasing the number of mesh elements results in the porosity evolving for longer before the first phase shift, signified by the reversal in porosity evolution (figure B.5). We also see that the maximum absolute velocity behaves in a similar way when we use at least 4480 mesh elements (figure B.4). As the number of mesh elements is increased,

$\mathcal{R}_C = \mathcal{R}_{C,0}^{\text{crit}}$							
Relative tol.	Absolute tol.	$\phi_{\max}$	$\phi_{\min}$	$C'_{\max}$	$C'_{\min}$	$\lvert\mathbf{u}\rvert_{\max}$	Solution time (s)
10^{-2}	10^{-3}	0.1025	0.0975	0.0017	-0.0017	0.0032	199.129
10^{-3}	10^{-4}	0.1025	0.0975	0.0017	-0.0017	0.0032	203.590
10^{-4}	10^{-5}	0.1025	0.0975	0.0017	-0.0017	0.0032	319.443
10^{-5}	10^{-6}	0.1025	0.0975	0.0017	-0.0017	0.0032	315.264
$\mathcal{R}_C = 1.1\mathcal{R}_{C,0}^{\text{crit}}$							
10^{-2}	10^{-3}	0.1025	0.0975	0.1903	-0.1908	0.4198	189.759
10^{-3}	10^{-4}	0.1025	0.0975	0.1903	-0.1908	0.4197	242.955
10^{-4}	10^{-5}	0.1025	0.0975	0.1903	-0.1908	0.4197	345.560
10^{-5}	10^{-6}	0.1025	0.0975	0.1903	-0.1908	0.4197	369.354
$\mathcal{R}_C = 1.2\mathcal{R}_{C,0}^{\text{crit}}$							
10^{-2}	10^{-3}	0.1025	0.0975	0.2564	-0.2572	0.6006	239.001
10^{-3}	10^{-4}	0.1025	0.0975	0.2562	-0.2570	0.6001	308.030
10^{-4}	10^{-5}	0.1025	0.0975	0.2562	-0.2570	0.6001	294.580
10^{-5}	10^{-6}	0.1025	0.0975	0.2562	-0.2570	0.6001	271.754
$\mathcal{R}_C = 1.5\mathcal{R}_{C,0}^{\text{crit}}$							
10^{-2}	10^{-3}	0.1025	0.0975	0.3565	-0.3582	1.0037	217.484
10^{-3}	10^{-4}	0.1025	0.0975	0.3566	-0.3584	1.0040	247.962
10^{-4}	10^{-5}	0.1025	0.0975	0.3566	-0.3584	1.0039	269.467
10^{-5}	10^{-6}	0.1025	0.0975	0.3566	-0.3584	1.0040	315.894

Table B.1: Tolerance testing results for $k_0 = 0$.

the resolution of the numerical solution is increased and less numerical noise is encountered. Therefore, the porosity evolution can continue for longer before triggering an instability in the form of a phase shift. Since each solution displayed the same behaviour when at least 4480 elements were used we concluded that 4480 elements were sufficient for mesh independence. However, it is important to note that the inception of the secondary instability is sensitive to the amount of numerical error introduced into the system.

B.2 Thermosolutal convection

In order to check the convergence of our numerical model, simulations were conducted using two reaction rates, $k_0 = 5$ and $k_0 = 20$, and three values of the solutal Rayleigh number, $\mathcal{R}_C = -15$, $\mathcal{R}_C = 10$ and $\mathcal{R}_C = 30$, to cover each convective quadrant of the stability diagram (see figure 5.1). In each case we take the thermal Rayleigh number $\mathcal{R}_T$ to be 10 % above its critical value. Each

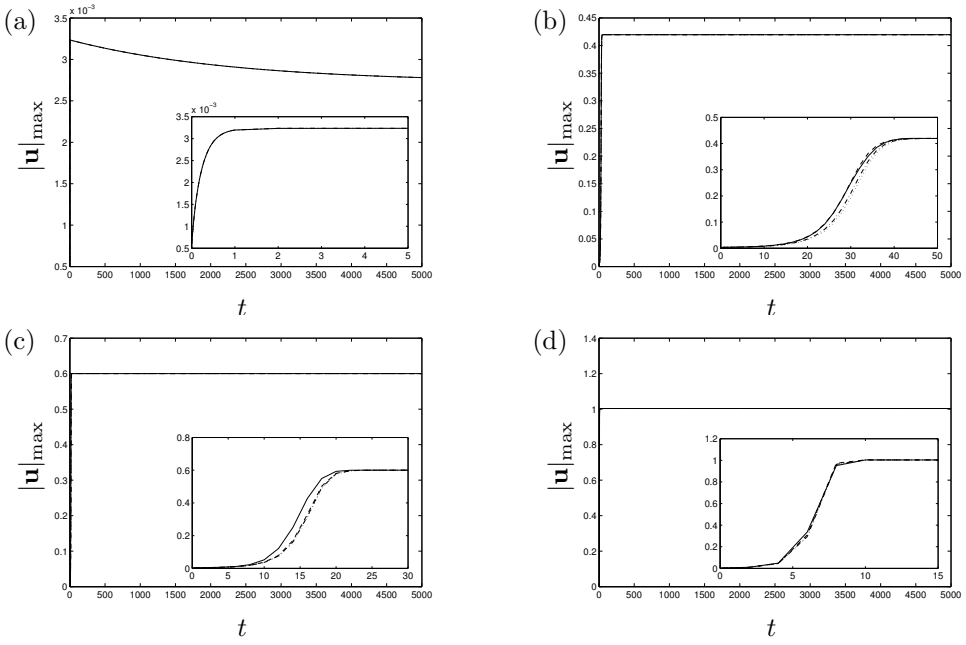

Figure B.1: Maximum $|\mathbf{u}|$ throughout the whole domain when $k_0 = 0$ for (a) $\mathcal{R}_C = \mathcal{R}_{C,0}^{\text{crit}}$, (b) $\mathcal{R}_C = 1.1\mathcal{R}_{C,0}^{\text{crit}}$, (c) $\mathcal{R}_C = 1.2\mathcal{R}_{C,0}^{\text{crit}}$, and (d) $\mathcal{R}_C = 1.5\mathcal{R}_{C,0}^{\text{crit}}$. Here the solid line represents the solution with a relative tolerance of 10^{-2} and an absolute tolerance of 10^{-3}, the dashed line is for a relative tolerance of10^{-3} and an absolute tolerance of 10^{-4}, the dashed-dotted line is for a relative tolerance of 10^{-4} and an absolute tolerance of 10^{-5}, and the dotted line is for a relative tolerance of 10^{-5} and an absolute tolerance of 10^{-6}. The early stage adjustment is shown in each insert.

simulation lasted 5000 time units and was conducted using 4480 triangular mesh elements; absolute tolerances were varied between 10^{-3} and 10^{-6} while relative tolerances were varied between 10^{-2} and 10^{-5}. For each simulation we noted the values for the maximum absolute velocity $|\mathbf{u}|$, maximum and minimum temperature perturbation $\tilde{T}$, maximum and minimum concentration perturbation $\tilde{C}$, and the maximum and minimum porosity ϕ over all timesteps (tables B.5 and B.6); we also plotted the maximum absolute velocity against time for each set of tolerances to check for convergence over all time steps (figures B.6 and B.7). It is apparent from the maximum absolute velocity plots that a relative tolerance of at most 10^{-3} and an absolute tolerance of at most 10^{-4} are required for convergence.

$\mathcal{R}_C = \mathcal{R}_{C,0}^{\text{crit}}$							
Relative tol.	Absolute tol.	$\phi_{\max}$	$\phi_{\min}$	$C'_{\max}$	$C'_{\min}$	$\lvert\mathbf{u}\rvert_{\max}$	Solution time (s)
10^{-2}	10^{-3}	0.1099	0.0901	0.0273	-0.0264	0.3952	234.324
10^{-3}	10^{-4}	0.1099	0.0901	0.0274	-0.0265	0.3965	264.216
10^{-4}	10^{-5}	0.1100	0.0900	0.0275	-0.0265	0.3971	456.089
10^{-5}	10^{-6}	0.1100	0.0900	0.0275	-0.0265	0.3971	677.814
$\mathcal{R}_C = 1.1\mathcal{R}_{C,0}^{\text{crit}}$							
10^{-2}	10^{-3}	0.1878	0.0433	0.1358	-0.1320	3.2947	322.900
10^{-3}	10^{-4}	0.1873	0.0434	0.1358	-0.1320	3.2859	413.828
10^{-4}	10^{-5}	0.1869	0.0435	0.1358	-0.1320	3.2772	567.453
10^{-5}	10^{-6}	0.1869	0.0434	0.1358	-0.1320	3.2786	796.890
$\mathcal{R}_C = 1.2\mathcal{R}_{C,0}^{\text{crit}}$							
10^{-2}	10^{-3}	0.2307	0.0321	0.1898	-0.1865	5.6307	372.950
10^{-3}	10^{-4}	0.2300	0.0322	0.1885	-0.1859	5.6073	397.753
10^{-4}	10^{-5}	0.2283	0.0323	0.1885	-0.1859	5.6026	779.454
10^{-5}	10^{-6}	0.2283	0.0323	0.1885	-0.1859	5.6016	992.461
$\mathcal{R}_C = 1.5\mathcal{R}_{C,0}^{\text{crit}}$							
10^{-2}	10^{-3}	0.4195	0.0109	0.2746	-0.2751	16.9673	525.023
10^{-3}	10^{-4}	0.4191	0.0109	0.2746	-0.2751	16.9487	839.878
10^{-4}	10^{-5}	0.4182	0.0109	0.2746	-0.2751	16.8920	997.964
10^{-5}	10^{-6}	0.4182	0.0109	0.2746	-0.2751	16.8901	1545.282

Table B.2: Tolerance testing results for $k_0 = 10$.

The mesh independence of the numerical method was tested similarly by conducting simulations with 1120, 4480, 17920, and 71680 triangular mesh elements and using the same reaction rates and Rayleigh numbers as used for the tolerance testing. Again, each simulation lasted 5000 time units and used a relative tolerance of 10^{-3} and an absolute tolerance of 10^{-4}. The same metrics as before were used to assess convergence.

As with reactive solutal convection, the mesh independence of the numerical method is hard to discern. Figures B.8 and B.9 show the maximum absolute velocity for $k_0 = 5$ and $k_0 = 20$, respectively. When the solutal gradient dominates, the behaviour is similar to the reactive solutal case with an increase in mesh elements resulting in the porosity evolving for longer before the first phase shift (figures B.8(b,c) and B.9(b,c)). When the thermal gradient dominates, the length of convecting period was very similar regardless of the number of mesh elements used (figures B.8(a) and B.9(a)). Since in both cases the maximum absolute behaviour behaves in a similar way when at least 4480 mesh elements are used, we concluded this was sufficient for mesh independence.

$\mathcal{R}_C = \mathcal{R}_{C,0}^{\text{crit}}$						
No. elements	$\phi_{\max}$	$\phi_{\min}$	$C'_{\max}$	$C'_{\min}$	$\lvert\mathbf{u}\rvert_{\max}$	Solution time (s)
1120	0.1025	0.0975	0.0017	-0.0017	0.0034	56.705
4480	0.1025	0.0975	0.0017	-0.0017	0.0032	203.590
17920	0.1025	0.0975	0.0017	-0.0017	0.0032	1245.031
71680	0.1025	0.0975	0.0017	-0.0017	0.0032	8580.568
$\mathcal{R}_C = 1.1\mathcal{R}_{C,0}^{\text{crit}}$						
1120	0.1025	0.0975	0.1900	-0.1906	0.4314	56.279
4480	0.1025	0.0975	0.1903	-0.1908	0.4197	241.958
17920	0.1025	0.0975	0.1903	-0.1908	0.4164	1743.812
71680	0.1025	0.0975	0.190	-0.191	0.4156	19883.028
$\mathcal{R}_C = 1.2\mathcal{R}_{C,0}^{\text{crit}}$						
1120	0.1025	0.0975	0.2562	-0.2570	0.6172	66.958
4480	0.1025	0.0975	0.2562	-0.2570	0.6001	334.743
17920	0.1025	0.0975	0.2562	-0.2570	0.5953	1997.250
71680	0.1025	0.0975	0.256	-0.257	0.5942	20760.437
$\mathcal{R}_C = 1.5\mathcal{R}_{C,0}^{\text{crit}}$						
1120	0.1025	0.0975	0.3568	-0.3585	1.0294	54.092
4480	0.1025	0.0975	0.3566	-0.3584	1.0040	308.282
17920	0.1025	0.0975	0.3566	-0.3583	0.9969	1654.938
71680	0.1025	0.0975	0.3566	-0.3584	0.9952	22467.623

Table B.3: Mesh independence test results for $k_0 = 0$.

$\mathcal{R}_C = \mathcal{R}_{C,0}^{\text{crit}}$						
No. elements	$\phi_{\max}$	$\phi_{\min}$	$C'_{\max}$	$C'_{\min}$	$\lvert\mathbf{u}\rvert_{\max}$	Solution time (s)
1120	0.1042	0.0958	0.0129	-0.0129	0.1929	52.779
4480	0.1099	0.0901	0.0274	-0.0265	0.3965	256.188
17920	0.1101	0.0901	0.0261	-0.0260	0.3854	1199.540
71680	0.1092	0.0912	0.0247	-0.0247	0.3660	5455.824
$\mathcal{R}_C = 1.1\mathcal{R}_{C,0}^{\text{crit}}$						
1120	0.1778	0.0464	0.1352	-0.1313	3.4370	89.551
4480	0.1872	0.0434	0.1358	-0.1320	3.2830	395.722
17920	0.1868	0.0436	0.1359	-0.1321	3.1870	1938.908
71680	0.1852	0.0440	0.1359	-0.1321	3.1342	9248.919
$\mathcal{R}_C = 1.2\mathcal{R}_{C,0}^{\text{crit}}$						
1120	0.2296	0.0332	0.1880	-0.1852	6.0223	92.654
4480	0.2303	0.0321	0.1885	-0.1859	5.6073	478.448
17920	0.2359	0.0294	0.1885	-0.1860	5.5147	2014.583
71680	0.2479	0.0279	0.1885	-0.1860	5.5361	9385.604
$\mathcal{R}_C = 1.5\mathcal{R}_{C,0}^{\text{crit}}$						
1120	0.4342	0.0123	0.2745	-0.2754	16.1901	174.565
4480	0.4190	0.0109	0.2746	-0.2751	16.9535	751.606
17920	0.4167	0.0108	0.2747	-0.2751	15.3585	4298.313
71680	0.4167	0.0108	0.2747	-0.2751	15.9415	16465.349

Table B.4: Mesh independence test results for $k_0 = 10$.

$\mathcal{R}_C = -15$, $\mathcal{R}_T = 299$								
Relative tol.	Absolute tol.	$\phi_{\max}$	$\phi_{\min}$	$\tilde{C}_{\max}$	$\tilde{C}_{\min}$	$\tilde{T}_{\max}$	$\tilde{T}_{\min}$	$\lvert\mathbf{u}\rvert_{\max}$
10^{-2}	10^{-3}	0.3162	0.0101	0.7463	-0.6514	0.4230	-0.4056	104.8682
10^{-3}	10^{-4}	0.3162	0.0096	0.7604	-0.6492	0.4231	-0.4046	104.5554
10^{-4}	10^{-5}	0.3174	0.0095	0.7585	-0.6493	0.4231	-0.4046	105.7292
10^{-5}	10^{-6}	0.3179	0.0094	0.7592	-0.6493	0.4232	-0.4046	105.5019
$\mathcal{R}_C = 10$, $\mathcal{R}_T = 25$								
10^{-2}	10^{-3}	0.1205	0.0742	0.0932	-0.0866	0.0057	-0.0062	0.8161
10^{-3}	10^{-4}	0.1203	0.0743	0.0789	-0.0684	0.0046	-0.0051	0.6512
10^{-4}	10^{-5}	0.1203	0.0742	0.0731	-0.0678	0.0046	-0.0048	0.6236
10^{-5}	10^{-6}	0.1204	0.0741	0.0731	-0.0678	0.0046	-0.0048	0.6239
$\mathcal{R}_C = 30$, $\mathcal{R}_T = -348$								
10^{-2}	10^{-3}	0.1582	0.0353	0.6834	-0.5983	0.0259	-0.0305	8.0181
10^{-3}	10^{-4}	0.1559	0.0411	0.1307	-0.1313	0.0053	-0.0057	1.6417
10^{-4}	10^{-5}	0.1544	0.0413	0.1283	-0.0963	0.0040	-0.0041	1.4642
10^{-5}	10^{-6}	0.1535	0.0416	0.1286	-0.0958	0.0040	-0.0041	1.4628

Table B.5: Tolerance testing results for $k_0 = 5$.

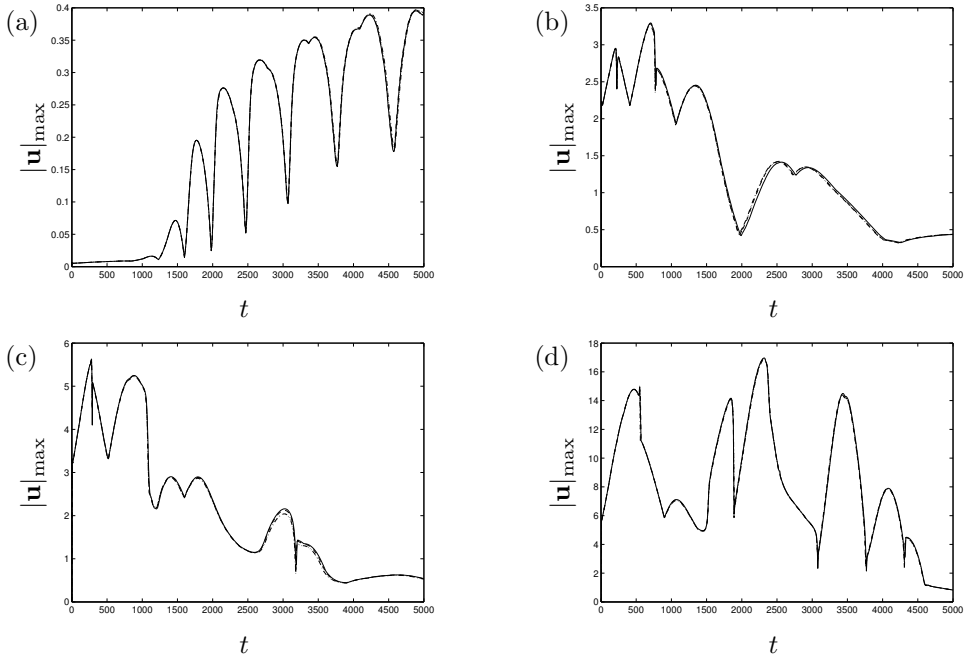

Figure B.2: Maximum $|\mathbf{u}|$ throughout the whole domain when $k_0 = 10$ for (a) $\mathcal{R}_C = \mathcal{R}_{C,0}^{\text{crit}}$, (b) $\mathcal{R}_C = 1.1\mathcal{R}_{C,0}^{\text{crit}}$, (c) $\mathcal{R}_C = 1.2\mathcal{R}_{C,0}^{\text{crit}}$, and (d) $\mathcal{R}_C = 1.5\mathcal{R}_{C,0}^{\text{crit}}$. Here the solid line represents the solution with a relative tolerance of 10^{-2} and an absolute tolerance of 10^{-3}, the dashed line is for a relative tolerance of10^{-3} and an absolute tolerance of 10^{-4}, the dashed-dotted line is for a relative tolerance of 10^{-4} and an absolute tolerance of 10^{-5}, and the dotted line is for a relative tolerance of 10^{-5} and an absolute tolerance of 10^{-6}.

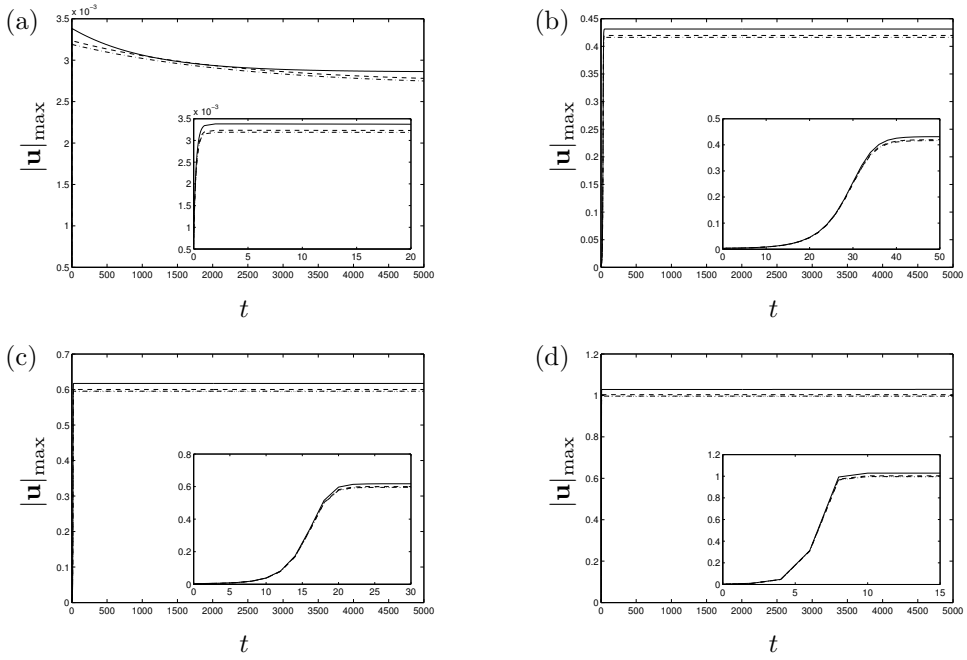

Figure B.3: Maximum $|\mathbf{u}|$ throughout the whole domain when $k_0 = 0$ for (a) $\mathcal{R}_C = \mathcal{R}_{C,0}^{\text{crit}}$, (b) $\mathcal{R}_C = 1.1\mathcal{R}_{C,0}^{\text{crit}}$, (c) $\mathcal{R}_C = 1.2\mathcal{R}_{C,0}^{\text{crit}}$, and (d) $\mathcal{R}_C = 1.5\mathcal{R}_{C,0}^{\text{crit}}$. Here the solid line represents the solution with 1120 mesh elements, the dashed line is for 4480 mesh elements, the dashed-dotted line is for 17920 mesh elements, and the dotted line is for 71680 mesh elements. The early stage adjustment is shown in each insert.

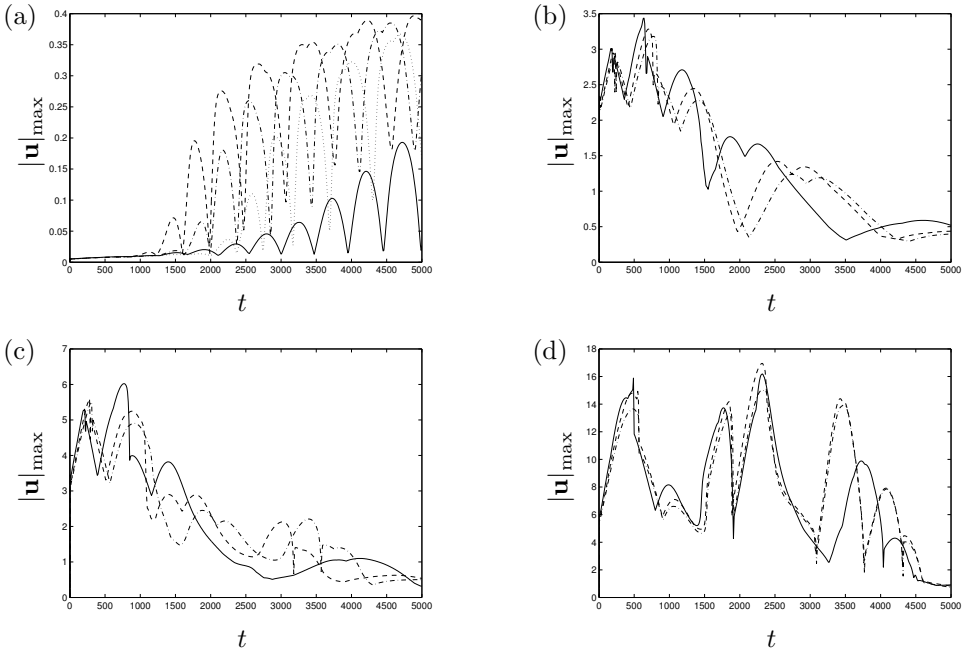

Figure B.4: Maximum $|\mathbf{u}|$ throughout the whole domain when $k_0 = 0$ for (a) $\mathcal{R}_C = \mathcal{R}_{C,0}^{\text{crit}}$, (b) $\mathcal{R}_C = 1.1\mathcal{R}_{C,0}^{\text{crit}}$, (c) $\mathcal{R}_C = 1.2\mathcal{R}_{C,0}^{\text{crit}}$, and (d) $\mathcal{R}_C = 1.5\mathcal{R}_{C,0}^{\text{crit}}$. Here the solid line represents the solution with 1120 mesh elements, the dashed line is for 4480 mesh elements, the dashed-dotted line is for 17920 mesh elements, and the dotted line is for 71680 mesh elements.

$\mathcal{R}_C = -15$, $\mathcal{R}_T = 245$								
Relative tol.	Absolute tol.	$\phi_{\max}$	$\phi_{\min}$	$\tilde{C}_{\max}$	$\tilde{C}_{\min}$	$\tilde{T}_{\max}$	$\tilde{T}_{\min}$	$\lvert\mathbf{u}\rvert_{\max}$
10^{-2}	10^{-3}	0.2862	0.0290	0.6172	-0.6173	0.3491	-0.3426	71.6773
10^{-3}	10^{-4}	0.2843	0.0288	0.6172	-0.6173	0.3491	-0.3426	70.6192
10^{-4}	10^{-5}	0.2844	0.0287	0.6172	-0.6172	0.3491	-0.3426	70.7904
10^{-5}	10^{-6}	0.2849	0.0286	0.6172	-0.6172	0.3492	-0.3426	70.9154
$\mathcal{R}_C = 10$, $\mathcal{R}_T = 122$								
10^{-2}	10^{-3}	0.1445	0.0662	0.4707	-0.7683	0.0850	-0.0931	12.9209
10^{-3}	10^{-4}	0.1894	0.0568	0.3182	-0.3292	0.0844	-0.0816	11.4413
10^{-4}	10^{-5}	0.1909	0.0564	0.3179	-0.3293	0.0845	-0.0815	11.5738
10^{-5}	10^{-6}	0.1908	0.0563	0.3180	-0.3295	0.0845	-0.0816	11.5826
$\mathcal{R}_C = 30$, $\mathcal{R}_T = -13$								
10^{-2}	10^{-3}	0.1464	0.0668	0.2165	-0.1864	0.0236	-0.0163	6.6800
10^{-3}	10^{-4}	0.1346	0.0710	0.0663	-0.0657	0.0078	-0.0078	2.3958
10^{-4}	10^{-5}	0.1374	0.0693	0.0690	-0.0650	0.0082	-0.0078	2.3705
10^{-5}	10^{-6}	0.1361	0.0698	0.0679	-0.0651	0.0080	-0.0078	2.3449

Table B.6: Tolerance testing results for $k_0 = 20$.

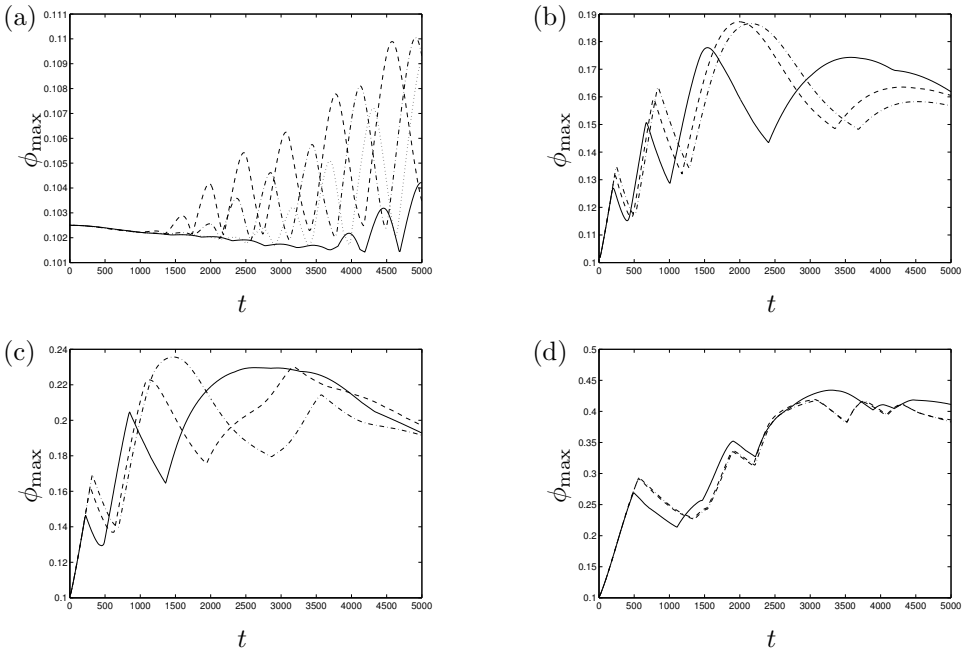

Figure B.5: Maximum porosity ϕ throughout the whole domain when $k_0 = 0$ for (a) $\mathcal{R}_C = \mathcal{R}_{C,0}^{\text{crit}}$, (b) $\mathcal{R}_C = 1.1\mathcal{R}_{C,0}^{\text{crit}}$, (c) $\mathcal{R}_C = 1.2\mathcal{R}_{C,0}^{\text{crit}}$, and (d) $\mathcal{R}_C = 1.5\mathcal{R}_{C,0}^{\text{crit}}$. Here the solid line represents the solution with 1120 mesh elements, the dashed line is for 4480 mesh elements, the dashed-dotted line is for 17920 mesh elements, and the dotted line is for 71680 mesh elements.

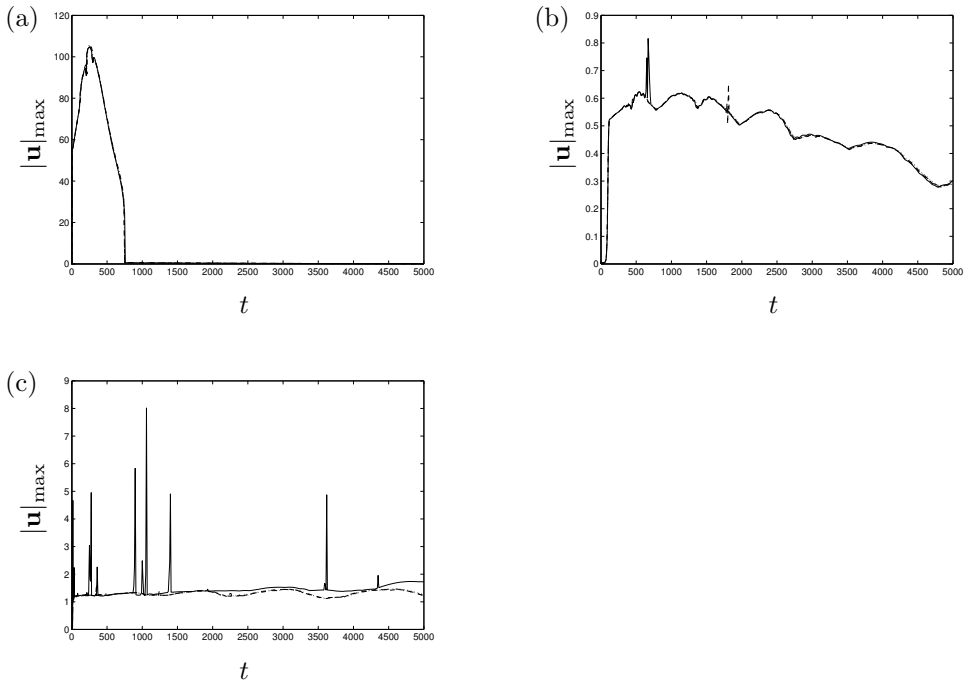

Figure B.6: Maximum $|\mathbf{u}|$ throughout the whole domain when $k_0 = 5$ for (a) $\mathcal{R}_C = -15$, (b) $\mathcal{R}_C = 10$, and (c) $\mathcal{R}_C = 30$. Here the solid line represents the solution with a relative tolerance of 10^{-2} and an absolute tolerance of 10^{-3}, the dashed line is for a relative tolerance of10^{-3} and an absolute tolerance of 10^{-4}, the dashed-dotted line is for a relative tolerance of 10^{-4} and an absolute tolerance of 10^{-5}, and the dotted line is for a relative tolerance of 10^{-5} and an absolute tolerance of 10^{-6}.

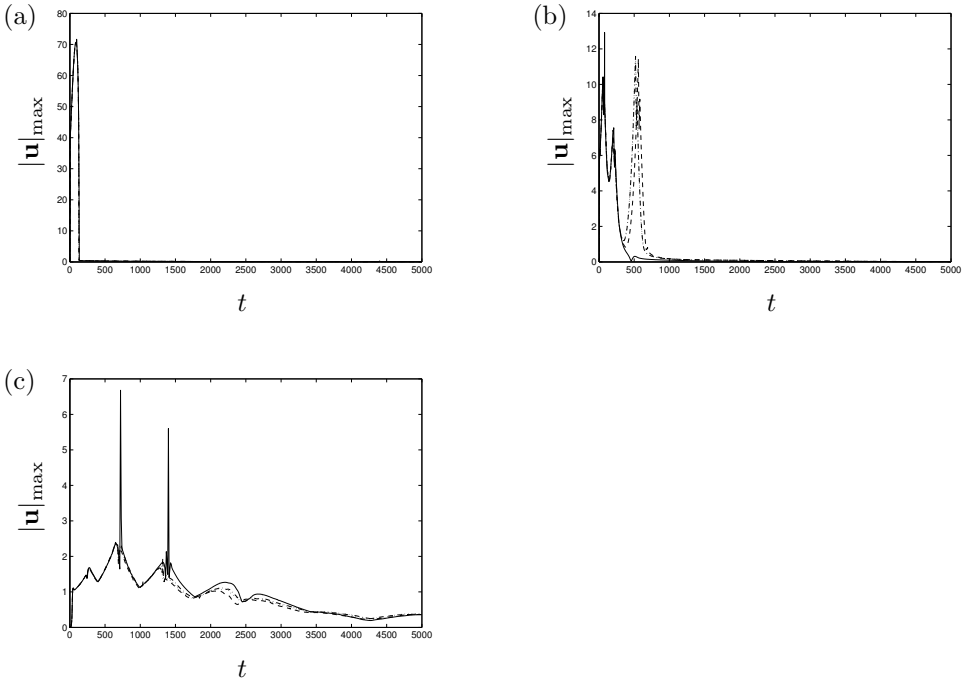

Figure B.7: Maximum $|\mathbf{u}|$ throughout the whole domain when $k_0 = 20$ for (a) $\mathcal{R}_C = -15$, (b) $\mathcal{R}_C = 10$, and (c) $\mathcal{R}_C = 30$. Here the solid line represents the solution with a relative tolerance of 10^{-2} and an absolute tolerance of 10^{-3}, the dashed line is for a relative tolerance of10^{-3} and an absolute tolerance of 10^{-4}, the dashed-dotted line is for a relative tolerance of 10^{-4} and an absolute tolerance of 10^{-5}, and the dotted line is for a relative tolerance of 10^{-5} and an absolute tolerance of 10^{-6}.

$\mathcal{R}_C = -15$, $\mathcal{R}_T = 299$							
No. elements	$\phi_{\max}$	$\phi_{\min}$	$\tilde{C}_{\max}$	$\tilde{C}_{\min}$	$\tilde{T}_{\max}$	$\tilde{T}_{\min}$	$\lvert\mathbf{u}\rvert_{\max}$
1120	0.3185	0.0112	0.7698	-0.7036	0.4204	-0.4045	91.2987
4480	0.3178	0.0094	0.7592	-0.6493	0.4232	-0.4046	105.4822
17920	0.3219	0.0098	0.7177	-0.6462	0.4235	-0.4045	92.5187
71680	0.3222	0.0096	0.7165	-0.6457	0.4237	-0.4045	92.4604
$\mathcal{R}_C = 10$, $\mathcal{R}_T = 25$							
1120	0.1188	0.0765	0.0712	-0.0659	0.0044	-0.0047	0.6232
4480	0.1204	0.0741	0.0731	-0.0679	0.0046	-0.0048	0.6236
17920	0.1201	0.0739	0.0741	-0.0686	0.0046	-0.0049	0.6346
71680	0.1200	0.0741	0.0750	-0.0693	0.0047	-0.0050	0.6476
$\mathcal{R}_C = 30$, $\mathcal{R}_T = -348$							
1120	0.1493	0.0443	0.1270	-0.0956	0.0041	-0.0041	1.5852
4480	0.1534	0.0416	0.1286	-0.0958	0.0040	-0.0041	1.4629
17920	0.1521	0.0429	0.1255	-0.0954	0.0040	-0.0041	1.3893
71680	0.1476	0.0458	0.1234	-0.0954	0.0040	-0.0041	1.3651

Table B.7: Mesh testing results for $k_0 = 5$.

$\mathcal{R}_C = -15$, $\mathcal{R}_T = 245$							
No. elements	$\phi_{\max}$	$\phi_{\min}$	$\tilde{C}_{\max}$	$\tilde{C}_{\min}$	$\tilde{T}_{\max}$	$\tilde{T}_{\min}$	$\lvert\mathbf{u}\rvert_{\max}$
1120	0.2819	0.0142	0.6480	-0.6461	0.3497	-0.3431	72.1939
4480	0.2839	0.0288	0.6172	-0.6172	0.3491	-0.3426	70.6612
17920	0.2770	0.0294	0.6144	-0.6144	0.3491	-0.3426	64.1274
71680	0.2764	0.0293	0.6143	-0.6142	0.3492	-0.3426	61.9186
$\mathcal{R}_C = 10$, $\mathcal{R}_T = 122$							
1120	0.1895	0.0558	0.3089	-0.3210	0.0820	-0.0787	12.0820
4480	0.1879	0.0570	0.3178	-0.3292	0.0844	-0.0815	10.7764
17920	0.1813	0.0593	0.3236	-0.3346	0.0862	-0.0834	10.6712
71680	0.1783	0.0592	0.3289	-0.3392	0.0876	-0.0850	11.0441
$\mathcal{R}_C = 30$, $\mathcal{R}_T = -13$							
1120	0.1343	0.0701	0.0635	-0.0616	0.0075	-0.0073	2.2484
4480	0.1364	0.0698	0.0685	-0.0651	0.0081	-0.0078	2.3627
17920	0.1352	0.0705	0.0678	-0.0645	0.0080	-0.0077	2.1966
71680	0.1354	0.0704	0.0683	-0.0645	0.0080	-0.0077	2.1847

Table B.8: Mesh testing results for $k_0 = 20$.

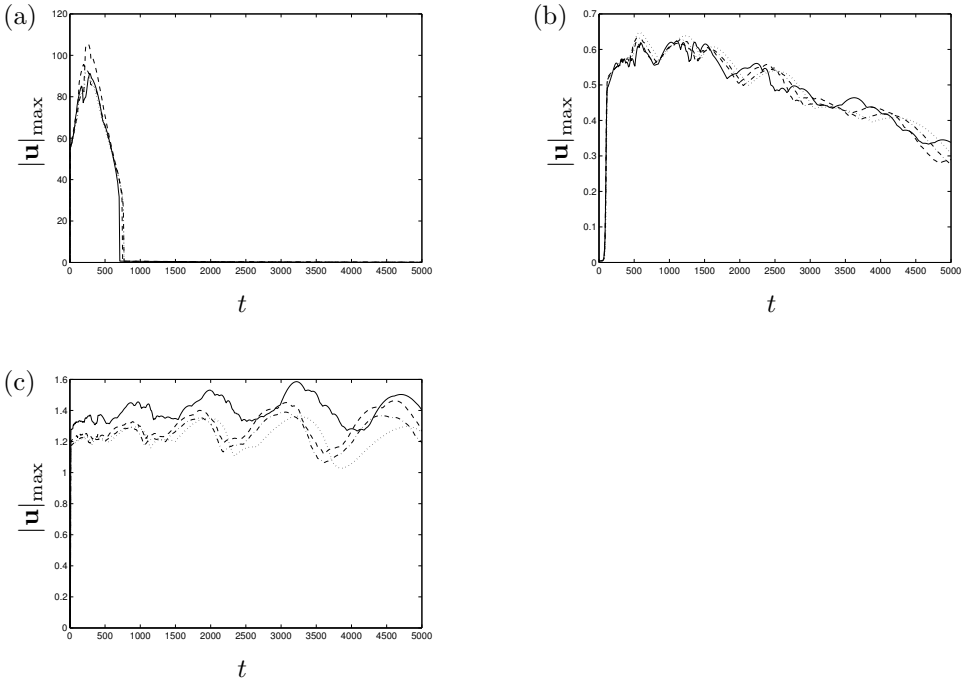

Figure B.8: Maximum $|\mathbf{u}|$ throughout the whole domain when $k_0 = 5$ for (a) $\mathcal{R}_C = -15$, (b) $\mathcal{R}_C = 10$, and (c) $\mathcal{R}_C = 30$. Here the solid line represents the solution with 1120 mesh elements, the dashed line is for 4480 mesh elements, the dashed-dotted line is for 17920 mesh elements, and the dotted line is for 71680 mesh elements.

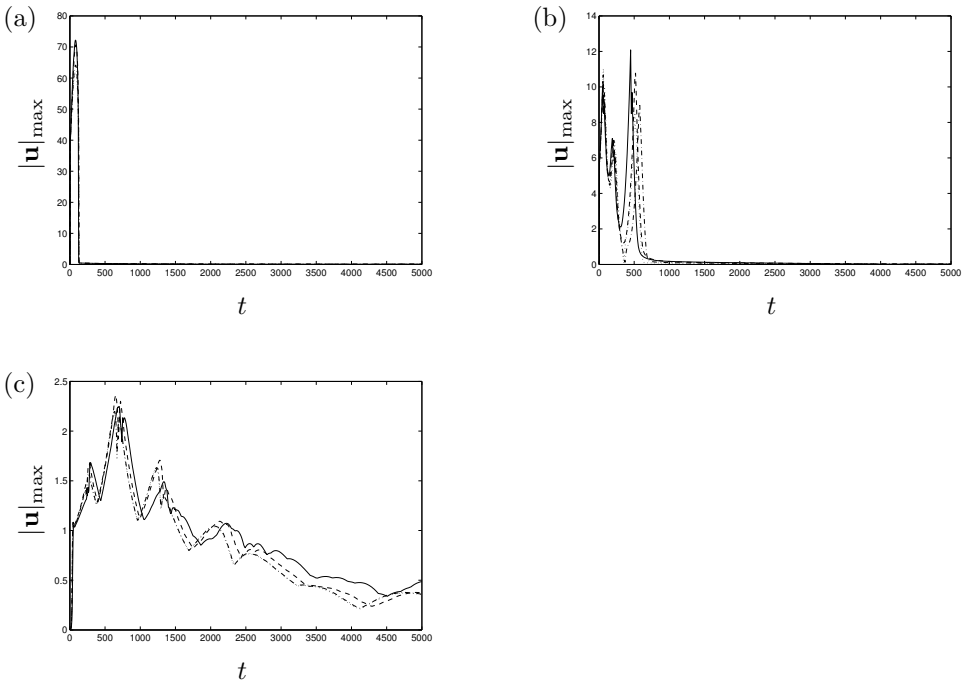

Figure B.9: Maximum $|\mathbf{u}|$ throughout the whole domain when $k_0 = 20$ for (a) $\mathcal{R}_C = -15$, (b) $\mathcal{R}_C = 10$, and (c) $\mathcal{R}_C = 30$. Here the solid line represents the solution with 1120 mesh elements, the dashed line is for 4480 mesh elements, the dashed-dotted line is for 17920 mesh elements, and the dotted line is for 71680 mesh elements.

Bibliography

Anderson, D. M. and M. G. Worster (1996). A new oscillatory instability in a mushy layer during the solidification of binary alloys. *J. Fluid Mech.* **307**, 245–267.

Anderson, G. M. and C. W. Burnham (1965). The solubility of quartz in supercritical water. *Am. J. Sci.* **263**, 494–511.

Bear, J. (2004). Mathematical models of flow and contaminant transport in saturated porous media. In J. Kubik, M. Kaczmarek, and I. Murdoch (Eds.), *Modelling Coupled Phenomena in Saturated Porous Materials*, pp. 86–175.

Bobeck, P. (2004). *The public fountains of the City of Dijon by Henry Darcy (1856)*. Kendall Hunt.

Bodenschatz, E., W. Pesch, and G. Ahlers (2000). Recent developments in Rayleigh-Bénard convection. *Annu. Rev. Fluid Mech.* **32**, 709–778.

Bolton, E. W., A. C. Lasaga, and D. M. Rye (1996). A model for the kinetic control of quartz dissolution and precipitation in porous media flow with spatially variable permeability: Formulation and examples of thermal convection. *J. Geophys. Res.* **101**(B10), 22157–22187.

Bolton, E. W., A. C. Lasaga, and D. M. Rye (1997). Dissolution and precipitation via forced-flux injection in a porous medium with spatially variable permeability: Kinetic control in two dimensions. *J. Geophys. Res.* **102**(B6), 12159–12171.

Bolton, E. W., A. C. Lasaga, and D. M. Rye (1999). Long-term flow/chemistry feedback in a porous medium with heterogenous permeability: kinetic control of dissolution and precipitation. *Am. J. Sci* **299**, 1–68.

Buretta, R. J. (1972). *Thermal convection in a fluid filled porous layer with uniform internal heat sources*. Ph. D. thesis, University of Minnesota, Minneapolis.

Caciagli, N. C. and C. E. Manning (2003). The solubility of calcite in water at 6-16 kbar and 500-800 ∘c. *Contrib. Mineral Petrol* **146**, 275–285.

Chadam, J., D. Hoff, E. Merino, P. Ortoleva, and A. Sen (1986). Reactive infiltration instabilities. *IMA J. Appl. Math.* **36**, 207–221.

Chadam, J., P. Ortoleva, Y. Qin, and R. Stamicar (2001). The effect of hydrodynamic dispersion on reactive flows in porous media. *Eur. J. Appl. Math.* **12**, 557–569.

Chadam, J., A. Peirce, and P. Ortoleva (1991). Stability of reactive flows in porous media: Coupled porosity and viscosity changes. *SIAM J. Appl. Math.* **51**(3), 684–692.

Chandrasekhar, S. (1961). *Hydrodynamic and Hydromagnetic Stability*. Oxford University Press.

Combarnous, M. and B. LeFur (1969). Transfert de chaleur par convection naturelle dans one conche poreuse horizontale. *C. R. Acad. Sci. Paris B* **269**, 1009–1012.

Cooper, C. A., R. J. Glass, and S. W. Tyler (1997). Experimental investigation of the stability boundary for double-diffusive finger convection in a Hele-Shaw cell. *Water Resour. Res.* **33**(4), 517–526.

Daccord, G. (1987). Chemical dissolution of a porous medium by a reactive fluid. *Phys. Rev. Lett.* **58**, 479–482.

Drazin, P. G. (2002). *Introduction to Hydrodynamic Stability*. Cambridge University Press.

Elder, J. W. (1967). Steady free convection in a porous medium heated from below. *J. Fluid Mech.* **27**, 29–48.

Ennis-King, J. and L. Paterson (2007). Coupling of geochemical reactions and convective mixing in the long-term geological storage of carbon dioxide. *Intl J. Greenhouse Gas Control* **1**, 86–93.

Ennis-King, J., I. Preston, and L. Paterson (2005). Onset of convection in anisotropic porous media subject to a rapid change in boundary conditions. *Phys. Fluids* **17**(8), 084107.

Gatica, J. E., H. J. Viljoen, and V. Hlavacek (1989). Interaction between chemical reaction and natural convection in porous media. *Chem. Engng Sci* **44**(9), 1853–1870.

Graham, M. D. and P. H. Steen (1994). Plume formation and resonant bifurcations in porous media convection. *J. Fluid Mech.* **272**, 67–89.

Griffiths, R. W. (1981). Layered double-diffusive convection in porous media. *J. Fluid Mech.* **102**, 221–248.

Hallworth, M. A., H. E. Huppert, and A. W. Woods (2005). Dissolution-driven convection in a reactive porous medium. *J. Fluid Mech.* **535**, 255–285.

Hassanizadeh, S. M. and T. Leijnse (1988). On the modelling of brine transport in porous media. *Water Resour. Res.* **24**(3), 321–330.

Hinch, E. J. and B. S. Bhatt (1990). Stability of an acid front moving through porous media. *J. Fluid Mech.* **212**, 279–288.

Hoefner, M. L. and H. S. Fogler (1988). Pore evolution and channel formation during flow and reaction in porous media. *AIChE J.* **34**(1), 45–54.

Horton, C. W. and F. T. Rogers (1945). Convection currents in a porous medium. *J. Appl. Phys.* **16**, 367–370.

Imhoff, P. T. and T. Green (1988). Experimental investigation of double-diffusive groundwater fingers. *J. Fluid Mech.* **188**, 363–382.

Jupp, T. E. and A. W. Woods (2003). Thermally driven reaction fronts in porous media. *J. Fluid Mech.* **484**, 329–346.

Kadanoff, L. (2001). Turbulent heat flow: Structures and scaling. *Physics Today* **54**, 34–39.

Katto, Y. and T. Masuoka (1967). Criterion for the onset of convective flow in a fluid in a porous medium. *Int. J. Heat Mass Transfer* **10**, 297–309.

Kaufman, J. (1994). Numerical models of fluid flow in carbonate platforms: implications for dolomitization. *J. Sed. Res. A* **64**, 128–139.

Lapwood, E. R. (1948). Convection of a fluid in a porous medium. *Proc. Camb. Phil. Soc.* **44**, 508–521.

Lord Rayleigh (1916). On convection currents in horizontal layer of fluid when the higher temperature is on the under side. *Philos. Mag. Ser. 6* **32**(192), 529–546.

Mamou, M. and P. Vasseur (1999). Thermosolutal bifurcation phenomena in porous enclosures subject to vertical temperature and concentration gradients. *J. Fluid Mech.* **395**, 61–87.

Mamou, M., P. Vasseur, and M. Hasnaoui (2001). On numerical stability analysis of double-diffusive convection in confined enclosures. *J. Fluid Mech.* **433**, 209–250.

Murray, B. T. and C. F. Chen (1989). Double-diffusive convection in a porous medium. *J. Fluid Mech.* **201**, 147–166.

Nield, D. A. (1968). Onset of thermohaline convection in a porous medium. *Water Resour. Res.* **4**(3), 553–560.

Nield, D. A. (1975). The onset of transient convective instability. *J. Fluid Mech.* **71**, 441–454.

Nield, D. A. and A. Bejan (2006). *Convection in Porous Media* (Third ed.). Springer.

Oldenburg, C. M. and K. Pruess (1998). Layered thermohaline convection in hypersaline geothermal systems. *Transport Porous Media* **33**, 29–63.

Otero, J., L. A. Dontcheva, H. Johnston, R. A. Worthing, A. Kurganov, G. Petrova, and C. R. Doering (2004). High-Rayleigh-number convection in a fluid-saturated porous layer. *J. Fluid Mech.* **500**, 263–281.

Palm, E., J. E. Weber, and O. Kvernvold (1972). On steady convection in a porous medium. *J. Fluid Mech.* **54**, 153–161.

Parmigiani, A., C. Huber, O. Bachmann, and B. Chopard (2011). Pore-scale mass and reactant transport in multiphase porous media. *J. Fluid Mech.* **686**, 40–76.

Pearson, J. R. A. (1958). On convection cells induced by surface tension. *J. Fluid Mech.* **4**, 489–500.

Phillips, O. M. (1991). *Flow and Reactions in Permeable Rocks*. Cambridge University Press.

Phillips, O. M. (2009). *Geological Fluid Dynamics: sub-surface flow and reactions*. Cambridge University Press.

Pritchard, D. and C. N. Richardson (2007). The effect of temperature-dependent solubility on the onset of thermosolutal convection in a horizontal porous layer. *J. Fluid Mech.* **571**, 59–95.

Raffensperger, J. P. and G. Garven (1995a). The formation of unconformity-type uranium ore deposits. 1. Coupled groundwater flow and heat transport modelling. *Am. J. Sci* **295**(5), 581–636.

Raffensperger, J. P. and G. Garven (1995b). The formation of unconformity-type uranium ore deposits. 2. Coupled hydrochemical modelling. *Am. J. Sci* **295**(6), 639–696.

Raw, A. W. V. and A. W. Woods (2003). On gravity-driven flow through a reacting porous rock. *J. Fluid Mech.* **474**, 227–243.

Riaz, A., M. A. Hesse, H. Tchelepi, and F. M. O. Jr. (2006). Onset of convection in a gravitationally unstable, diffusive boundary layer in porous media. *J. Fluid Mech.* **548**, 87–111.

Ritchie, L. T. and D. Pritchard (2011). Natural convection and the evolution of a reactive porous medium. *J. Fluid Mech.* **673**, 286–317.

Rudraiah, N. (1984). Linear and non-linear magneto convection in a porous medium. *Proc. Math. Sci.* **93**(2-3), 117–135.

Rudraiah, N. and P. Srimani (1980). Finite-amplitude cellular convection in a fluid-saturated porous layer. *Proc. Roy. Soc. London Ser. A* **373**, 199–222.

Rudraiah, N., P. Srimani, and R. Friedrich (1982). Finite amplitude convection in a two-component fluid saturated porous layer. *Int. J. Heat Mass Transfer* **25**(5), 715–722.

Sharp, J. M. and M. Shi (2009). Heterogeneity effects on possible salinity-driven free convection in low-permeability strata. *Geofluids* **9**, 263–274.

Steinberg, V. and H. Brand (1983). Convective instabilities of binary mixtures with fast chemical reaction in a porous medium. *J. Chem. Phys.* **78**(5), 2655–2660.

Steinberg, V. and H. Brand (1984). Amplitude equations for the onset of convection in a reactive mixture in a porous medium. *J. Chem. Phys.* **80**(1), 431–435.

Stevens, J. D., J. M. Sharp, C. T. Simmons, and T. R. Fenstemaker (2009). Evidence of free convection in groundwater: Field-based measurements beneath wind-tidal flats. *J. Hydrology* **375**, 394–409.

Subramanian, S. and V. Balakotaiah (1994). Convective instabilities induced by exothermic reactions occurring in a porous medium. *Phys. Fluids* **6**, 2907–2922.

Taunton, J. W., E. N. Lightfoot, and T. Green (1972). Thermohaline instability and salt fingers in a porous medium. *Phys. Fluids.* **15**, 748–753.

Turner, J. S. (1985). Multicomponent convection. *Ann. Rev. Fluid Mech.* **17**, 11–44.

Vadasz, P. (2000). Flow and thermal convection in rotating porous media. In K. Vafai (Ed.), *Handbook of Porous Media*, pp. 395–439. Marcel Dekker, New York.

Van Dam, R. L., C. T. Simmons, D. W. Hyndman, and W. W. Wood (2009). Natural free convection in porous media: First field documentation. *Geophys. Res. Lett.* **36**, L11403.

Verdon, J. and A. W. Woods (2007). Gravity-driven reacting flows in a confined porous aquifer. *J. Fluid Mech.* **588**, 29–41.

Viljoen, H. J., J. E. Gatica, and V. Hlavacek (1990). Bifurcation analysis of chemically driven convection. *Chem. Engng Sci* **45**(2), 503–517.

Whitaker, S. (1986). Flow in porous media I: A theoretical derivation of Darcy's law. *Transp. Porous Media* **1**, 3–25.

Worster, M. G. (1997). Convection in mushy layers. *Annu. Rev. Fluid Mech.* **29**, 91–122.

Zhao, C., B. E. Hobbs, A. Ord, P. Hornby, and S. Peng (2008). Morphological evolution of three-dimensional chemical dissolution front in fluid-saturated porous media: a numerical simulation approach. *Geofluids* **8**, 113–127.